Title
Biointerfacing via Cell Membrane-Coated Nanoparticles for Novel Antibacterial Nanotherapeutics

Author
Angsantikul, Pavimol

Publication Date
2018

UNIVERSITY OF CALIFORNIA SAN DIEGO

Biointerfacing via Cell Membrane-Coated Nanoparticles for Novel Antibacterial Nanotherapeutics

A Dissertation submitted in partial satisfaction of the
requirements for the degree
Doctor of Philosophy

in

NanoEngineering

by

Pavimol Angsantikul

Committee in charge:

Professor Liangfang Zhang, Chair
Professor Shaochen Chen
Professor Yi Chen
Professor Lars Eckmann
Professor Marygorret Obonyo

2018

The Dissertation of Pavimol Angsantikul is approved, and it is acceptable in quality and form for publication on microfilm and electronically:

Chair

University of California San Diego

2018

DEDICATION

This dissertation is dedicated to the memory of my beloved grandfather,
Iam Angsantikul, without whom none of my achievements would be
possible; to my parents, Chitti and Somsri Angsantikul who provide
unconditional love and never-ending support; to my sister, Pavinee
Angsantikul who always understand me without words;
to the rest of Angsantikul family for nursing me with love and affection;
and to my fiancé, Yang Yu who has been my pillar of strength.
I am forever grateful to have them in my life.

EPIGRAPH

A scientist in his laboratory is not a mere technician: he is also a child confronting natural phenomena that impress him as though they were fairy tales.

– Marie Curie

TABLE OF CONTENTS

Signature Page . . . iii

Dedication . . . iv

Epigraph . . . v

Table of Contents . . . vi

List of Figures . . . ix

List of Tables . . . xi

Acknowledgements . . . xii

Vita . . . xvi

Abstract of the Dissertation . . . xx

Chapter 1 Nanoparticle approaches against bacterial infections . . . 1
- 1.1 Introduction . . . 2
- 1.2 Targeted Antibiotic Delivery . . . 4
- 1.3 Environmentally Responsive Antibiotic Delivery . . . 7
- 1.4 Combinatorial Antibiotic Delivery . . . 11
- 1.5 Nanoparticle-enabled Antibacterial Vaccination . . . 14
- 1.6 Nanoparticle-based Bacteria Detection . . . 19
- 1.7 Conclusion . . . 22

Chapter 2 Biointerfacing via cell membrane-coated nanoparticles for novel antibacterial drug delivery system . . . 24
- 2.1 Coating nanoparticles with gastric epithelial cell membrane for targeted antibiotic delivery against *Helicobacter pylori* infection . . . 25
  - 2.1.1 Introduction . . . 25
  - 2.1.2 Experimental Methods . . . 28
  - 2.1.3 Results and Discussion . . . 37
  - 2.1.4 Conclusions . . . 50

2.2 Micromotors spontaneously neutralize gastric acid for pH-responsive payload release 51
2.2.1 Introduction 51
2.2.2 Experimental Methods 53
2.2.3 Results and Discussion 57
2.2.4 Conclusions 68
2.3 Micromotor-enabled active drug delivery for *in vivo* treatment of stomach infection 71
2.3.1 Introduction 71
2.3.2 Experimental Methods 74
2.3.3 Results and Discussion 80
2.3.4 Conclusions 94

Chapter 3 Biointerfacing via cell membrane-coated nanoparticles for novel pathologic countermeasure applications 97
3.1 Neutralization of cholera toxin with nanoparticle decoys for treatment of cholera 98
3.1.1 Introduction 98
3.1.2 Experimental Methods 100
3.1.3 Results and Discussion 106
3.1.4 Conclusions 117
3.2 Macrophage-like nanoparticles concurrently absorbing endotoxins and proinflammatory cytokines for sepsis management 122
3.2.1 Introduction 122
3.2.2 Experimental Methods 125
3.2.3 Results and Discussion 133
3.2.4 Conclusions 143
3.3 Biomimetic Platelet-Camouflaged Nanorobots for Binding and Isolation of Biological Threats 146
3.3.1 Introduction 146
3.3.2 Experimental Methods 149
3.3.3 Results and Discussion 155
3.3.4 Conclusions 165

Chapter 4 Conclusions 168

4.1 Coating nanoparticles with gastric epithelial cell membrane for targeted antibiotic delivery against *Helicobacter pylori* infection 169
4.2 Micromotors spontaneously neutralize gastric acid for pH-responsive payload release 170
4.3 Micromotor-enabled active drug delivery for *in vivo* treatment of stomach infection 171
4.4 Neutralization of cholera toxin with nanoparticle decoys for treatment of cholera 172
4.5 Macrophage-like nanoparticles concurrently absorbing endotoxins and proinflammatory cytokines for sepsis management 173
4.6 Biomimetic Platelet-Camouflaged Nanorobots for Binding and Isolation of Biological Threats 175

Bibliography 177

LIST OF FIGURES

Figure 1.1: Schematic illustration of major nanoparticle-based delivery platforms for treating bacterial infections 3
Figure 1.2: Schematic illustration of a phospholipid liposome stabilized by charged gold nanoparticles and its drug release in response to pH change or the presence of bacterial toxin. 9
Figure 1.3: Schematic preparation of nanoparticle-detained toxins, denoted 'nanotoxoid' 16
Figure 1.4: Schematic illustration of interbilayer-crosslinked multilamellar vesicles (ICMVs) for vaccine delivery 18
Figure 1.5: Magneto-DNA assay for the detection of bacterial 16S rRNA. . . 21

Figure 2.1: Schematic illustrations of the preparation of gastric epithelial cell 29
Figure 2.2: Physicochemical characterization of AGS-NPs. 38
Figure 2.3: AGS-NPs targeting to *H. pylori* bacteria. 41
Figure 2.4: Characterization of clarithromycin(CLR)-loaded AGS-NP. 44
Figure 2.5: *In vivo* anti-*H. pylori* therapeutic efficacy of AGS-NP(CLR). . . 46
Figure 2.6: Evaluation in vivo toxicity of AGS-NP. 47
Figure 2.7: Schematic illustrations of Mg-based micromotor and its acid neutralization mechanism 59
Figure 2.8: *In vitro* acid neutralization and pH-triggered payload release. . . 61
Figure 2.9: *In vivo* acid neutralization and pH-triggered payload release. . . 64
Figure 2.10: Recovery of the gastric pH post micromotor treatment. 67
Figure 2.11: Toxicity evaluation of Mg micromotors. 69
Figure 2.12: Synthesis and characterization of drug-loaded Mg-based micromotors. 81
Figure 2.13: Antibiotic drug loading of the Mg-based micromotors and *in vitro* bactericidal activity. 86

Figure 2.14: Retention of the Mg-based micromotors in mouse stomachs. . . . 88
Figure 2.15: *In vivo* anti-H. pylori therapeutic efficacy. 90
Figure 2.16: *In vivo* toxicity evaluation of the Mg-based micromotors. 93

Figure 3.1: Preparation and physical characterization of GM1-coated nanoparticles. 107
Figure 3.2: Specific binding of cholera toxin B subunit to GM1-NPs. 110
Figure 3.3: Neutralization of CT activity with GM1-NPs. 112
Figure 3.4: Functional stability of GM1-NPs in the presence of intestinal luminal factors. 114
Figure 3.5: *In vivo* efficacy of GM1-NPs against CT and live *V. cholerae*. . . 116
Figure 3.6: Model of therapeutic effect of GM1-NPs. 118
Figure 3.7: Formulation and characterization of macrophage membrane-coated nanoparticles (MΦ-NPs). 135
Figure 3.8: *In vitro* LPS and proinflammatory cytokine removal with MΦ-NPs.137
Figure 3.9: *In vitro* and *in vivo* LPS neutralization with MΦ-NPs. 140
Figure 3.10: *In vivo* therapeutic efficacy of MΦ-NPs evaluated with a mouse bacteremia model. 142
Figure 3.11: Preparation and characterization of PL-motors. 150
Figure 3.12: Propulsion performance and anti-biofouling capability of PL-motors.160
Figure 3.13: Shiga toxin (Stx) binding and neutralization study. 162
Figure 3.14: Binding and isolation of platelet-adhering pathogens. 164

LIST OF TABLES

Table 1.1: Combinatorial Nanoparticles for Antibacterial Drug Delivery . . . 12

ACKNOWLEDGEMENTS

First and foremost, I would like to thank my advisor, Professor Liangfang Zhang, who welcomed me to his laboratory and gave me the opportunity to freely explore the frontiers of nanomedicine. He is undoubtedly the best mentor one could ask for. I thank him for his dedication, inspiration, and advice. He showed me all the characters in a great scientist and supported me in pursuing a career in scientific research. His knowledge, values and perspectives have been a great influence in both my academic and personal life. I am forever grateful to have worked under his guidance, it made my graduate life at UCSD an immensely memorable one.

I would like to give my special thanks to my faculty collaborators. I thank Prof. Joseph Wang, who played a crucial role in many of my final projects. His charisma and working style has added new perceptions to the way I do research. I greatly appreciate the research contributions that him and his research team have made, especially the open-mindedness and countless efforts from Jinxing Li, Berta Esteban-Fernández de Ávila, and Ewa Liu, who contributed significant time on developing novel nano/micromotors. I thank Prof. Marygorret Obonyo who kindly shared her expertise in Helicobacter pylori with me. She always made herself available for me and give me great advice. I thank Prof. Lars Eckmann for the valuable experience and numerous insightful discussions from our research collaborations. I thank Prof. Victor Nizet for contributing his time and resources to our shared project. I also acknowledge the collaborative efforts from Dr. Soumita Das, Christine Le, Dr. Yukiko Miyamoto, and Tamara Escajadillo who are great scientists from their labs.

Over the five years of my Ph.D. journey, I have had a wonderful opportunity to work beside and learn from members of the Zhang lab. They have also made a great contribution toward my graduate study. Dr. Weiwei Gao is both a well-rounded scientist and a brilliant artist. He made numerous of wonderful illustration figures and always gave me valuable advice on research. I learned a lot from working with him. Dr. Soracha Thamphiwatana is one of my earliest colleagues in the lab. She is an expert on bacterial culture and antimicrobial studies and kindly trained me those skill sets. She is not only my respected colleague but also a great friend whom I enjoyed working with in the lab days and nights. Her help and advice have been invaluable, and I wish her a great success as a faculty member back in Thailand. Dr. Ronnie Fang is such an inspiring scientist. I highly appreciate and admire his research leadership style, critical thinking and lifelong learning attitude. Dr. Che-Ming Hu, Dr. Brian Luk, Dr. Xiaoli Wei and Dr. Hua Gong contributed to many useful discussions and are always very supportive. I acknowledge the great collaboration with Yue Zhang, Diana Dehaini, Jia Zhuang, Qiangzhe Zhang, and Yijie Chen. I thank the undergraduate researchers, Chih-Ning Yang, Merrick Chai, Kevin Speikermann, Sophia Zhang, Richard Samakapiruk, and Christopher Lo who have worked with me with their enthusiastic efforts and I wish they all have promising careers ahead. Last but not least, I thank all members of Zhang lab for their great friendship. Everyone always shows their willingness to help and gives invaluable suggestion and discussion. I am deeply thankful of being a part of Zhang lab family.

I sincerely thank the Ananda Mahidol Scholarship for the financial support through my entire graduate study. It has given me the freedom to better pursue my interests and focus on what is important to me. I also thank Friends of the

International Center for their fellowship that aided me in the fourth year of my study.

I would like to thank warm friendship offered by Thai community in San Diego. I thank all their supports and fun activities we shared. I am grateful that our paths crossed. Our friendships will never fade.

I offer special thanks to Prof. Shaochen chen, and Prof. Yi Chen for serving on my defense committee. Last but not least, I would like to thank NanoEngineering department at UCSD, their faculty, Dana Jimenez, and many of other fantastic nanoengineering staffs, for giving me the most memorial, inspiring, and illuminating time of my life.

Chapter 1, in full, is a reprint of the material as it appears in WIREs Nanomedicine & Nanobiotechnology, 2014, Weiwei Gao, Soracha Thamphiwatana, Pavimol Angsantikul and Liangfang Zhang. The dissertation author was a major contributor and co-author of this paper.

Chapter 2.1, in full, is a reprint of the material as it appears in Advanced Therapeutics, 2018, Pavimol Angsantikul, Soracha Thamphiwatana, Qiangzhe Zhang, Kevin Spiekermann, Jia Zhuang, Ronnie Fang, Weiwei Gao, Marygorret Obonyo, and Liangfang Zhang. Chapter 2.2, in full, is a reprint of the material as it appears in Angewandte Chemie International Edition, 2017, Jinxing Li, Pavimol Angsantikul, Wenjuan Liu, Berta Esteban-Fernández de Ávila, Soracha Thamphiwatana, Mingli Xu, Elodie Sandraz, Xiaolei Wang, Jorge Delezuk, Weiwei Gao, Liangfang Zhang, Joseph Wang. Chapter 2.3, in full, is a reprint of the material as it appears in Nature Communications, 2017, Berta Esteban-Fernández de Ávila, Pavimol Angsantikul, Jinxing Li, Miguel Angel Lopez-Ramirez, Doris E. Ramírez-Herrera, Soracha Thamphiwatana, Chuanrui Chen, Jorge Delezuk, Richard Samakapiruk, Valentin Ramez, Marygorret Obonyo, Liangfang Zhang, and Joseph Wang. The dissertation author was either the primary investigator or co-primary investigator and co-author of these papers.

Chapter 3.1, in full, is a reprint of the material as it appears in PLOS Neglected Tropical Diseases, 2018, Soumita Das, Pavimol Angsantikul, Christine Le, Denny Bao, Yukiko Miyamoto, Weiwei Gao, Liangfang Zhang, and Lars Eckmann. Chapter 3.2, in full, is a reprint of the material as it appears in Proceedings of the National Academy of Sciences, 2017, Soracha Thamphiwatana, Pavimol Angsantikul, Tamara Escajadillo, Qiangzhe Zhang, Joshua Olson, Brian T. Luk, Sophia Zhang, Ronnie H. Fang, Weiwei Gao, Victor Nizet, and Liangfang Zhang. Chapter 3.3, in full, is a reformatted of the material as it appears in Advanced Materials, 2018, Jinxing Li, Pavimol Angsantikul, Wenjuan Liu, Berta Esteban-Fernández de Ávila, Xiaocong Chang, Elodie Sandraz, Yuyan Liang, Siyu Zhu, Yue Zhang, Chuanrui Chen, Weiwei Gao, Liangfang Zhang, and Joseph Wang.The dissertation author was the co-primary investigator and co-author of these papers.

VITA

2012	B.Eng. *First-class Honours*, Nano-Engineering, Chulalongkorn University, Bangkok Thailand
2015	M.Sc., NanoEngineering, University of California San Diego, USA
2018	Ph.D., NanoEngineering, University of California San Diego, USA

PUBLICATIONS

1. Angsantikul, P.; Thamphiwatana, S.; Zhang, Q.; Spiekermann, K.; Zhuang, J.; Fang, R.; Gao, W.; Obonyo, M.; Zhang, L "Coating nanoparticles with gastric epithelial cell membrane for targeted antibiotic delivery against Helicobacter pylori infection", Advanced Therapeutics 2018, in press.

2. Esteban-Fernandez de Avila, B. *; Angsantikul, P. *; Ramirez-Herrera, D. *; Soto, F.; Teymourian, H.; Dehaini, D.; Chen, Y.; Zhang, L., Wang, J. "Hybrid-biomembrane functionalized nanorobots for concurrent removal of pathogenic bacteria and toxins", Science Robotics 2018, in press. (* co-first author)

3. Esteban-Fernandez de Avila, B.; Angsantikul, P.; Li. J.; Gao, W.; Zhang, L., Wang, J. "Micromotors go in vivo: From petro dishes to live animals", Advanced Functional Materials 2018, in press.

4. Angsantikul, P.; Fang, R.; Zhang, L. "Toxoid vaccination against bacterial infection using cell membrane-coated nanoparticles", Bioconjugate Chemistry 2018, 29, 604-612.

5. Hansen-Bruhn, M.; Esteban-Fernandez de Avila, B.; Beltran-Gastelum, M.; Zhao, J.; Ramirez-Herrera, D.; Angsantikul, P.; Gothelf, K. V.; Zhang, L., Wang, J. "Active intracellular delivery of Cas9-sgRNA complex using ultrasound-propelled nanomotors", Angewandte Chemie International Edition 2018, 57, 2657-2661.

6. Das, S.*; Angsantikul, P.*; Le, C.; Bao, D.; Miyamoto, Y.; Gao, W.; Zhang, L., Eckmann, L. "Neutralization of cholera toxin with nanoparticle decoys for treatment of cholera", PLOS Neglected Tropical Diseases 2018, 12, e0006266.

7. Chen, C.; Chang, X.; Angsantikul, P.; Li, J.; Esteban-Fernandez de Avila, B.; Karshalev, E.; Liu, W.; Mou, F.; He, S.; Castillo, R.; Liang, Y.; Guan, J.;

Zhang, L.; Wang, J. "Chemotactic guidance of synthetic organic/inorganic payloads functionalized sperm micromotors", Advanced Biosystems 2018, 2, 1700160.

8. Li, J.*; Angsantikul, P.*; Liu, W.*; Esteban-Fernandez de Avila, B.*; Chang, X.; Sandraz, E.; Liang, Y.; Zhu, S.; Zhang, Y.; Chen, C.; Gao, W.; Zhang, L., Wang, J. "Biomimetic platelet-camouflaged nanorobots for binding and isolation of biological threats", Advanced Materials 2018, 30, 1704800. (* co-first author)

9. Zhang, X.; Angsantikul, P.; Ying, M.; Zhuang, J.; Zhang, Q.; Wei, X.; Jiang, Y.; Zhang, Y.; Dehaini, D.; Chen, M.; Chen, Y.; Gao, W.; Fang, R.; Zhang, L. "Remote loading of small molecule therapeutics into cholesterol-enriched cell membrane-derived vesicles", Angewandte Chemie International Edition 2017, 56, 14075-14079.

10. Thamphiwatana, S.*; Angsantikul, P.*; Escajadillo, T.*; Zhang, Q.; Olsan, J.; Luk, B.; Zhang, S.; Fang, R.; Gao, W.; Nizet, V.; Zhang, L. "Macrophage-like nanoparticles concurrently absorbing endotoxins and proinflammatory cytokines for sepsis management", Proceedings of the National Academy of Sciences 2017,114, 11488-11493. (* co-first author)

11. Zhang, Y.; Zhang, J.; Chen, W.; Angsantikul, P.; Spiekermann, K.; Fang, R.; Gao, W.; Zhang, L. "Erythrocyte membrane-coated nanogel for combinatorial antivirulence and responsive antimicrobial delivery against Staphylococcus aureus infection", Journal of Controlled Release 2017, 263, 185-191.

12. Wei, X.; Gao, J.; Wang, F.; Ying, M.; Angsantikul, P.; Kroll, A.; Zhou, J.; Gao, W.; Lu, W.; Fang, R.; Zhang, L. "In situ capture of bacterial toxins for antivirulence vaccination", Advanced Materials 2017, 29, 1701644.

13. Esteban-Fernandez de Avila, B.*; Angsantikul, P.*; Li, J.*; Lopez-Ramirez, M.; Ramirez-Herrera, D.; Thamphiwatana, S.; Chen, C.; Delezuk, J.; Samakapiruk, R.;Ramez, V.; Obonyo, M.; Zhang, L.; Wang, J. "Micromotor-enabled active drug delivery for in vivo treatment of stomach infection", Nature Communications 2017, 8, 272. (* co-first author)

14. Huang, Q.; Lee, J.; Arce, F. T.; Yoon, I.; Angsantikul, P.; Liu, J.; Shi, Y.; Villanueva, J.; Thamphiwatana, S.; Ma, X.; Zhang, L.; Chen, S.; Lal, R.; Sirbuly, D. "Nanofiber optic force transducers with sub-piconewton resolution via near-field plasmon-dielectric interactions", Nature Photonics 2017, 11, 352-357.

15. Esteban-Fernandez de Avila, B.; Ramirez-Herrera, D. E.; Campuzano, S.; Angsantikul, P.; Zhang, L., Wang, J. "Nanomotor-enabled pH-responsive intracellular delivery of caspase-3: Towards rapid cell apoptosis", ACS Nano 2017, 11, 5367-5374.

16. Dehaini, D.; Wei, X.; Fang, R.; Masson, S.; Angsantikul, P.; Luk, B.; Zhang, Y.; Ying, M.; Jiang, Y.; Kroll, A.; Gao, W.; Zhang, L. "Erythrocyte-platelet hybrid

membrane coating for enhanced nanoparticle functionalization", Advanced Materials 2017, 29, 1606209.

17. Li, J. *; Angsantikul P.*; Liu, W.*; Esteban-Fernandez de Avila, B. *; Thamphiwatana, S.; Xu, M.; Sandraz, E.; Wang, X.;Delezuk J.; Gao, W.; Zhang, L., Wang, J. "Micromotors spontaneously neutralize gastric acid for pH-responsive payload release", Angewandte Chemie International Edition 2017, 56, 2165-2161. (* co-first author)

18. Li, J.; Thamphiwatana, S.; Liu, W.; Esteban-Fernandez de Avila, B.; Angsantikul, P.; Sandraz, E.; Wang, J.; Xu, T.; Soto, F.; Ramez, V.; Wang, X.; Gao, W.; Zhang, L.; Wang, J. "Enteric micromotor can selectively position and spontaneously propel in the gastrointestinal tract", ACS Nano 2016, 10, 9536-9542.

19. Wang, F.; Fang, R.; Luk, B.; Hu, C-M.; Thamphiwatana, S.; Dehaini, D.; Angsantikul, P.; Kroll, A.; Pang, Z.; Gao, W.; Lu, W.; Zhang, L. "Nanoparticle-Based Antivirulence Vaccine for the Management of Methicillin-Resistant Staphylococcus aureus Skin Infection", Advanced Functional Materials 2016, 26, 1628-1635.

20. Angsantikul, P.; Thamphiwatana, S.; Gao, W.; and Zhang, L.; "Cell membrane-coated nanoparticles as an emerging antibacterial vaccine platform", Vaccines 2015, 3, 814-828.

21. Hu, C-M.; Fang, R.; Wang, K-C.; Luk, B.; Thamphiwatana, S.; Dehaini, D.; Nguyen, P.; Angsantikul, P.; Wen, C.; Kroll, A.; Carpenter, C.; Ramesh, M; Qu, V.; Patel, S.; Zhu, J.; Shi, W.; Hofman, F.; Chen, T.; Gao, W.; Zhang, K.; Chien, S.; Zhang, L.; "Nanoparticle biointerfacing by platelet membrane cloaking", Nature 2015, 526, 118-121.

22. Pang, Z.; Hu, C-M.; Fang, R.; Luk, B.; Gao, W.; Wang, F.; Chuluun, E.; Angsantikul, P.; Thamphiwatana, S.; Lu, W.; Jiang, X.; Zhang, L; "Detoxification of organophosphate poisoning using nanoparticle bioscavengers", ACS Nano 2015, 9, 6450-6458.

23. Wang, F.; Gao, W.; Thamphiwatana, S.; Luk, B.; Angsantikul, P.; Zhang, Q.; Hu, C-M.; Fang, R.; Copp, J; Pornpattananangkul, D.; Lu, W.; Zhang L.; "Hydrogel retaining toxin-absorbing nanosponges for local treatment of methicillin-resistant Staphylococcus aureus infection", Advanced Materials 2015, 27, 3437-3443.

24. Gao, W.; Fang, R.; Thamphiwatana, S.; Luk, B.; Li, J.; Angsantikul, P.; Zhang, Q.; Hu, C-M.; Zhang, L.; "Modulating antibacterial immunity via bacterial membrane-coated nanoparticles", Nano Letters 2015, 15, 1403-1409.

25. Gao, W.; Thamphiwatana, S.; Angsantikul, P.; Zhang, L.; "Nanoparticle approaches against bacterial infections", WIREs Nanomedicine & Nanobiotechnology 2014, 6, 532-547.

ABSTRACT OF THE DISSERTATION

Biointerfacing via Cell Membrane-Coated Nanoparticles for Novel Antibacterial Nanotherapeutics

by

Pavimol Angsantikul

Doctor of Philosophy in NanoEngineering

University of California San Diego, 2018

Professor Liangfang Zhang, Chair

Antibiotic resistance has become an undeniable burden on global health as we move further into the twenty-first century. It is predicted that drug-resistant infections could lead to an annual mortality rate of 10 million people by 2050 and a cumulative cost of up to 100 trillion USD on the world's economy. These unsettling projections have necessitated the exploration of new and more effective ways to manage bacterial infection. This dissertation focuses on novel strategies for addressing this pressing challenge via nanomedicine, particularly the use of natural cell-derived membrane to enhance the biointerfacing of synthetic nanomaterials. The resulting membrane-cloaked platforms exhibit unique, cell-specific properties that can be leveraged for antibacterial therapy. Additionally, novel nano/micromotors are further exploited to design new biomimetic therapeutic modalities capable of active movement.

The first part of this thesis will focus on novel antibiotic delivery systems, including targeted delivery and active delivery platforms. For targeted antibiotic delivery, the native function of the source cells, particularly their natural adhesion property was exploit by the natural cell membranes-coated nanoparticles. Meanwhile, the second delivery platform involves mobile micromotor which are acid-powered and enable active delivery. Not only can the propulsion of antibiotic-loaded motors in gastric media effectively deliver the drug payload, but the motor-based therapy can also rapidly neutralize gastric acid without the need of proton pump inhibitor.

the second portion of this dissertation will focus on the exploitation of biomimicking nanoplatforms as countermeasures against pathologic moieties for the abrogation of bacterial infection. This is demonstrated through a range of bacterial virulence including diarrhea-causing cholera toxin, Shiga toxin, and systemic endotoxin. Ultimately, cell membrane-coated technology has the potential to greatly impact the landscape of nanomedicine and contribute to the management of bacterial infections in the future.

Chapter 1

Nanoparticle approaches against bacterial infections

1.1 Introduction

Despite the profound success achieved by the use of antibiotics against infectious diseases, bacterial infections continue to impose significant challenges on global healthcare. [1, 2] Eradication of certain bacterial infections such as tuberculosis remains difficult due to the complex mechanisms of the pathogen in subverting its host's immune system as well as the delivery barriers that prevent antibiotics from reaching sites of infection. [3, 4] Highly potent antibiotics, including certain aminoglycosides and fluoroquinolones, generate severe adverse effects and are reserved only for serious infections. [5, 6] More significantly, the emergence of antibiotic resistance has generated alarming impact, threatening to set back the progress against a range of infectious diseases to the pre-antibiotic era. [7, 8] The widespread drug resistance is further exacerbated by the retreat of the pharmaceutical sector from new antibiotic development. [9, 10] These challenges, together, highlight the demand for alternative and effective antimicrobial strategies.

Over the last few decades, the application of nanotechnology, particularly the use of nanoparticles for drug delivery, has generated significant impact in medicine. [10, 11] Various nanoparticle delivery platforms, especially liposomes, polymeric nanoparticles, dendrimers, and inorganic nanoparticles, have received significant attention (Figure 1.1). Drug molecules loaded into nanocarriers through physical encapsulation, adsorption, or chemical conjugation exhibit an improved pharmacokinetic profile and therapeutic index when compared to their free drug counterparts. [12] Other advantages of nanoparticle delivery systems, including improved drug solubility, prolonged systemic circulation, sustained and controlled release, precise drug target-

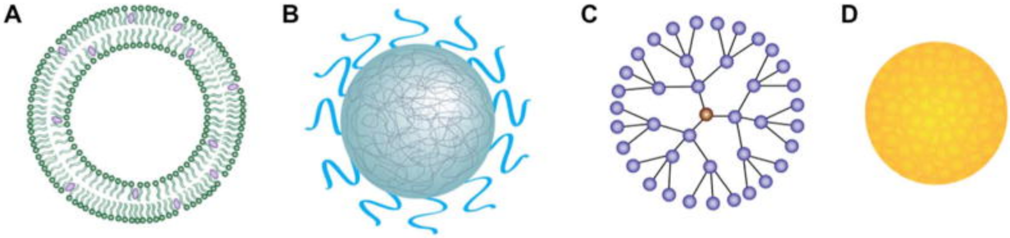

Figure 1.1: Schematic illustration of major nanoparticle-based delivery platforms for treating bacterial infections: (a) liposome, (b) polymeric nanoparticle, (c) dendrimer, and (d) inorganic nanoparticle.

ing, and concurrent delivery of multiple drugs, have also been validated in various studies. [13] As a result, a number of nanoparticle-based drug delivery systems have been approved for clinical use to treat a variety of infectious diseases, and many other antimicrobial nanoparticle formulations are currently under various stages of pre-clinical and clinical tests. [14]

As the ability to engineer multifunctional nanoparticles continually advances, numerous innovative approaches have emerged, further improving on nanoparticle therapeutic efficacy against bacterial infections. In this review article, we select five areas where nanoparticle approaches hold significant potential to improve upon current treatments. These areas include: (1) targeted antibiotic delivery, (2) environmentally responsive antibiotic delivery, (3) combinatorial antibiotic delivery, (4) nanoparticle-enabled antibacterial vaccination, and (5) nanoparticle-based bacterial detection. Progresses made in these areas offer tremendous opportunities for alternative and more effective antimicrobial strategies that alter the pharmacokinetics of existing antibiotics, produce new antibiotics with novel microbial inhibition mechanisms, or allow for more rapid and sensitive microbial detection. Collectively, they address the aforementioned challenges including overcoming antibiotic resistance. Herein, we review each area with highlights of the current and forthcoming nanoparticle platforms against bacterial infections.

1.2 Targeted Antibiotic Delivery

Bacterial infection increases vascular permeability, which makes passive targeting possible. At the infection sites, the release and accumulation of bacterial components such as bacterial protease and lipopolysaccharide from Gram-negative bacteria or lipoteichoic acid from Gram-positive bacteria are known to trigger various inflammatory mediators that directly stimulate vascular permeability. [15, 16] These bacterial components also activate immune cells, which in turn interact with vascular endothelium through multiple inflammatory and vascular media- tors, leading to gap widening, barrier dysfunction, and eventually increased permeability. [17] Moreover, dysfunctional lymphatic drainage has also been reported in bacterial infection, which potentially promotes nanoparticle accumulation at the sites of infection. [18] These features of bacterial infection suggest that the enhanced permeation and retention (EPR) effect can be harnessed by nanoparticles for targeted antibiotic delivery. [19] In fact, both uncoated liposomes and PEGylated liposomes have been shown to accumulate selectively at soft tissues infected by *Staphylococcus aureus* (*S. aureus*), and their retention times correlated closely with size. [20–23] Similar results were observed for superparamagnetic iron oxide nanoparticles (SPIONs) at the soft tissue of rats and in the lungs of mice infected by *S. aureus*. [24]

Pathogenic bacteria maintain a negative surface charge under physiological conditions. Therefore, cationic nanoparticles capable of binding with bacteria via electrostatic interactions have been explored for effective bacterial targeting. [25, 26] This strategy is attractive for its multivalent effect and the ability to target polymicrobial infections. As a result, a diverse range of bactericidal polymers and peptides has been incorporated into various nanoparticle designs for antibacterial applications. [27] More importantly, nanoparticle formulation can increase the local charge and mass densities of the bactericidal components, resulting in enhanced therapeutic index. For example, a self-assembled cationic peptide nanoparticle has shown strong antimicrobial properties while inducing minimal systemic toxicity. [28] Furthermore, improving the biodegradability of the nanoparticles can further reduce cationic charge related toxicity. In this perspective, cationic nanoparticles self-assembled from polycarbonate-based block copolymers with high biodegradability have been shown to kill bacteria without inducing obvious hemolytic activity and systemic toxicity. [29]

Active targeting with pathogen-binding ligands directly conjugated to the surface of nanoparticles is another strategy to target bacteria. For example, small molecules such as vancomycin have been conjugated to the surfaces of dendrimers, [30] iron oxide nanoparticles, [31] gold nanoparticles, [32] and porous silica nanoparticles, [33] resulting in preferential binding of nanoparticles to Gram-positive bacteria. The targeting efficiency of small molecules was also found to be strongly dependent on molecular orientation, surface density, and length of the spacer used in conjugation. [34] In addition to small molecules, lectins, particularly those with selective agglutination activities, have also been used as ligands to target bacteria. [35] Polymeric nanoparticles conjugated with mannose-specific or fucose-specific lectins showed enhanced binding affinity to the carbohydrate receptors on *Helicobacter pylori* (*H. pylori*) surfaces, suggesting a promising approach for site-specific and gastroretentive drug delivery to treat *H. pylori* infection. [36] Besides lectins, other protein ligands such as single-domain antibodies [37] and bacteriophage tailspike proteins [38] are highly specific targeting ligands and their conjugation to nanoparticles has resulted in targeted delivery platforms effective against a variety of bacterial infections. Furthermore, aptamers have also become a class of attractive targeting moieties owing largely to the advancement in bacterium-based aptamer selection techniques, which continually improve aptamer binding affinity and specificity. These targeting molecules have been extensively explored to target nanoparticles to pathogenic bacteria such as *Salmonella typhimurium* and *Mycobacterium tuberculosis* (*M. tuberculosis*). [39, 40]

Moreover, bacteria can survive ingestion by phagocytic cells such as macrophages, hence evading the immune system and the bactericidal action of antibiotics. [3] However, macrophages are able to transport drugs to the site of infection by a chemotactic mechanism. [41, 42] Therefore, targeting antimicrobial nanoparticles to macrophages as opposed to bacteria has become an attractive strategy for improving antibiotic therapy, particularly to treat intracellular bacterial infection. [43] It has been observed that following passive targeting to the infection sites, nanoparticles could preferentially be taken up by macrophages due to the spontaneous scavenging feature of macrophages. [23, 24] Such macrophage uptake could be further enhanced by attaching targeting ligands onto the nanoparticles. [44, 45] In this regard, various ligands, including mannose, maleylated bovine serum albumin, and O-steroyl amylopectin, have been applied to successfully enhance macrophage uptake of nanoparticles for the treatment of intracellular infection. [46,47]

1.3 Environmentally Responsive Antibiotic Delivery

To further improve upon the therapeutic efficacy of antimicrobial nanoparticles, researchers have explored environmentally responsive nanoparticles that remain inactive until they are triggered by cues found in the microenvironment of infection sites. These external stimuli can be physical signals such as temperature, electric field, magnetic field, and ultrasound; they can also be chemical signals such as pH, ionic strength, redox potential, and enzymatic activities. [48]

Among these environmental stimuli, pH gradient has been widely used to design novel, responsive nanoparticles for antibiotic delivery. At the organ level, nanoparticles have been designed to respond to the pH gradient along the gastrointestinal (GI) tract [49] and the acidic environment of human skin [50] for site-specific antibiotic delivery. At the intracellular level, nanoparticles have been formulated to respond to the acidic pH inside the endolysosomal compart-ments for triggered drug release. [51–53] In addition to pH gradient, bacterial enzymatic activities, including those of secreted toxins, have also been used to trigger the release of antimicrobial agents to inhibit the growth of the target bacteria.

Charged polymers have been adsorbed onto liposome surfaces with opposite charge to stabilize the liposomes. [54,55] Such stabilization is pH sensitive and has been extensively used to treat various intracellular bacterial infections including *Salmonella enterica* [56, 57] as well as cases of septic shock. [58, 59] On the basis of a similar mechanism, ionic liposomes can be employed to carry oppositely charged drug molecules for pH-sensitive drug release. In addition, loading liposomes with membrane disrupting toxins such as hemolysin and listeriolysin that are responsive to endosomal acidification has also shown potential for the treatment of intracellular infections. [60, 61]

Recently, a new environment-responsive delivery strategy has emerged that involves the attachment of small charged nanoparticles onto liposome surfaces for liposome stabilization and triggered antimicrobial delivery (Figure 1.2). The nonspecific adsorption of charged nanoparticles onto phospholipid bilayers pro- vided steric repulsion that inhibited liposome fusion. It also reduced liposome surface tension and thus further enhanced liposome stability. [62, 63] Intriguingly, the charge and charge density of both the nanoparticle stabilizers and the liposomes could be precisely tailored to enable stimulus-responsive binding and detachment of the nanoparticles, thereby allowing for an on-demand control over liposome fusion activity for smart drug delivery. For instance, cationic liposomes bound with negatively charged gold nanoparticles only fused with bacteria at acidic pH, which made them suitable for treating various skin pathogens that thrive in acidic infection sites such as the case with *Propionibacterium acnes*. [64] Conversely, anionic liposomes stabilized by positively charged gold nanoparticles were highly stable in gastric acid, but capable of fusing with bacteria at physiological pH, making them suitable to treat gastric pathogens such as *H. pylori*. [65] Even in the absence of such stimulus-induced

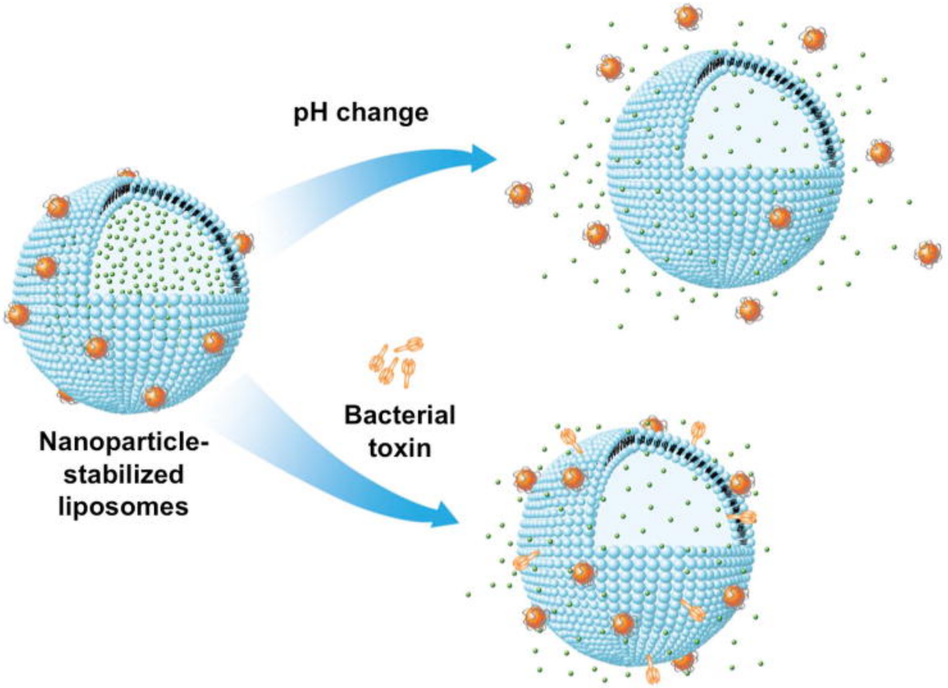

Figure 1.2: Schematic illustration of a phospholipid liposome stabilized by charged gold nanoparticles and its drug release in response to pH change or the presence of bacterial toxin.

detachment of the nanoparticle stabilizers, these liposomes still had a substantial fraction of their surface areas exposed and highly accessible to bacterial toxins. This feature allowed the liposomes to respond to various bacteria such as *S. aureus* that secret pore-forming toxins to trigger drug release from the liposomes. [66] Aimed at improving the topical applications of nanoparticle-stabilized liposomes, a hydrogel form of the delivery system was recently developed, which not only preserved the structural integrity of the nanoparticle-stabilized liposomes, but also allowed for controllable viscoelasticity and tunable liposome release rate. [67]

Meanwhile, polymeric nanoparticles have been extensively studied for responsive antibiotic delivery. For example, tri-block copolymer nanoparticles composed of poly(lactic-co-glycolic acid) (PLGA), poly(l-histidine), and poly(ethylene glycol) (PEG) have been reported for acid-responsive antibiotic delivery. [68] These nanoparticles maintained a negative charge at neutral pH; however, when exposed to an acidic pH, the protonation of the imidazole groups switched the surface charge to a positive one, resulting in enhanced bacterial binding and improved antibacterial efficacy. As another example, heparin and chitosan have been applied to form base-sensitive nanoparticles for treating gastric pathogens such as *H. pylori.* The polymers self-assembled to form nanoparticles at pH 1.2-2.5; however, upon contact with *H. pylori* at the gastric epithelium with physiological pH, the chitosan deprotonated, causing nanoparticle disassembly and release of drugs for bacteria killing. [69] Moreover, by tailoring the pK_a of amphiphilic copolymers, a wide range of polymeric nanoparticles has been engineered, which precisely respond to the subtle changes of pH along the GI tract for site-specific antibiotic delivery. Enzyme-sensitive polymeric nanoparticles have also been developed for intracellular delivery in macrophages. For example, a triple-layered nanogel formulation has been reported, which contained a bacterial lipase-sensitive poly(ϵ-caprolactone) interlayer between the crosslinked polyphosphoester core and the PEG shell. [70] Following macrophage uptake, the presence of bacterial phosphatase or phospholipase triggered rapid drug release, which subsequently inhibited the growth of *S. aureus.* [47]

1.4 Combinatorial Antibiotic Delivery

Combining two or more distinct antibiotics represents a common strategy in treating bacterial infections with the aim to broaden the antimicrobial spectrum, generate synergistic effects, and counteract antibiotic resistance. However, varying pharmacokinetics, biodistributions, toxicity profiles, and membrane transport properties among different drug compounds complicate dosing and scheduling optimization, which in turn compromise drug synergy *in vivo*. [71] In this regard, nanoparticles offer unique properties to enhance combinatorial antibiotic delivery and numerous applications have been investigated to address a variety of bacterial infections (Table 1).

Liposomes are a highly versatile platform for combinatorial delivery. Hydrophilic drugs can be directly encapsulated in the aqueous compartments of liposomes, while hydrophobic drugs can be incorporated into the lipid bilayer membranes. [14] For example, isoniazid and rifampicin, first line antitubercular drugs, have been loaded in the aqueous compartment and the lipid bilayer, respectively. The resulting liposomal formulation has shown increased efficacy compared to free drug counterparts at the same dosages. [72–74] Liposomal formulation can also reduce drug toxicity to the host cells, thereby allowing for co-delivery of combinatorial antibiotics that are otherwise too toxic in their free forms. For example, drug compounds such as gallium (Ga) and bismuth derivatives are antibiotics that inhibit bacterial growth by interrupting their iron uptake. Although they have shown synergetic effects in combination with other antibiotics, their usage has been limited by severe toxicity. [75] To address this challenge, Ga^{3+} was combined with gentamicin and loaded into liposomes. The

Table 1.1: Combinatorial Nanoparticles for Antibacterial Drug Delivery

Platform	Formulation	Drug Combination	Targeted Bacteria	References
Liposomes	DPPC, DMPG and cholesterol	Gallium and gentamicin	*Pseudomonas aeruginosa*	77
	DSPC and cholesterol	Bismuth-ethanedithiol (BiEDT) and tobramycin	*Pseudomonas aeruginosa* and *Burkholderia cenocepacia*	78
	PEGylated liposome	Daptomycin and clarithromycin	MRSA	85
	PG, PC and cholesterol	Clarithromycin and ofloxacin	*Mycobacterium avium*	86
	PC, SA, and cholesterol	Ciprofloxacin and vancomycin	MRSA	84
	PC, PEG-DSPE, and cholesterol	Gentamicin and ceftazidime	*Klebsiella pneumoniae*	83
	DPPC and cholesterol	Isoniazid and rifampicin	*Mycobacterium tuberculosis*	75
	PG, PC and cholesterol	Streptomycinand and ciprofloxacin	*Mycobacterium avium*	87
	PC, PE, SA and cholesterol	Amoxicillin trihydrate and ranitidine bismuth citrate	*Helicobacter pylori*	88
	PAA, PAH, PC, and cholesterol	Amoxicillin and metronidazole	*Helicobacter pylori*	89
Polymeric nanoparticles	PLGA	Rifampin and azithromycin	*Chlamydia trachomatis* and *Chlamydia pneumoniae*	95
	PLGA	Rifampicin, isoniazid, pyrazinamide, and ethambutol.	*Mycobacterium tuberculosis*	99
	Sodium alginate and chitosan	Rifampicin, isoniazid, pyrazinamide, and ethambutol.	*Mycobacterium tuberculosis*	100
	Chitosan and glutamic acid	Amoxicillin, clarithromycin, and omeprazole	*Helicobacter pylori*	97
	Gliadin and Pluronic F-68	Clarithromycin and omeprazole	*Helicobacter pylori*	98
	Gliadin, lectin and Pluronic F-68	Amoxicillin, clarithromycin and omeprazole	*Helicobacter pylori*	96

DPPC, 1,2-dipalmitoyl-sn-glycero-3-phosphocholine; DMPG, 1,2-dimyristoyl-sn-glycero-3-phosphoglycerol; DSPC, 1,2-distearoyl-sn-glycero-3-phosphocholine; DSPE, 1,2-distearoyl-sn-glycero-3-phosphoethanolamine; DPPC, dipalmitoylphosphatidylcholine; PG, egg yolk phosphatidylglycerol; PE, phosphatidylethanolamine; PC, phosphatidylcholine; PLGA, poly(lactic-co-glycolic acid); PAA, poly(acrylic acid); PAH, poly(allylamine hydrochloride); SA, stearylamine.

formulation reduced Ga toxicity and improved efficacy against highly resistant *Pseudomonas aeruginosa* (*P. aeruginosa*). [76] Similarly, bismuth-ethanedithiol (BiEDT) was encapsulated together with tobramycin into liposomes, resulting in the elimination of BiEDT's toxic effect on human lung cells while increasing its antibacterial efficacy against *P. aeruginosa* and *Burkholderia cepacia*. [77–79] A recent *in vivo* study showed that the same drug combination in a liposome formulation enhanced efficacy in reducing bacterial burden in rats chronically infected with *P. aeruginosa*. [80]

Moreover, liposomal formulation of combinatorial antibiotics enables ratiometric control over the drugs and thus unifies the pharmacokinetics of different drug molecules and ensures parallel tissue distribution. These advantages serve to enhance the antimicrobial efficacy of the drugs. For example, using the dosage and dosing schedule derived from *in vitro* studies, the co-administration of gentamicin and ceftazidime only resulted in an additive effect in a rat model of an acute unilateral *Klebsiella pneumoniae* infection. [81] In contrast, the corresponding liposomal formulation encapsulating both gentamicin and ceftazidime showed a synergistic effect that led to a shorter course of treatment at lower cumulative doses. [82] The benefit of ratiometric delivery using liposomes was also reported in other combination therapies in treating *S. aureus*, [83, 84] *M. tuberculosis*, [72, 73] *Mycobacterium avium*, [85, 86] and *H. pylori*. [87, 88] Polymeric nanoparticles represent another emerging platform for combinatorial antibiotic delivery to treat bacterial infection. In general, drug molecules can be directly encapsulated into the polymeric cores. For precise ratiometric loading and controlled drug release, multiple drugs can be covalently conjugated to the polymer backbone followed by nanoparticle preparation. [89–91] In addition, using emulsion techniques, both hydrophobic and hydrophilic drug molecules can be co-encapsulated into the polymeric cores. [92, 93] As a result, several polymeric nanoparticle systems have been reported for delivering antibiotic combinations. For example, the combination of rifampin and azithromycin was delivered with PLGA nanoparticles and showed better efficacy *in vitro* compared to free drugs in treating persistent chlamydial infection. [94] Nanoparticles made of gliadin, a vegetal protein commonly derived as a fraction of wheat gluten, were used to co-encapsulate clarithromycin and omeprazole, which achieved better efficacy against H. pylori bacteria in rats. [95, 96] The gliadin nanoparticles were further conjugated with lectin and used in triple therapy with amoxicillin, clarithromycin, and omeprazole, [97] resulting in superior *in vivo* clearance of *H. pylori* compared to the nonconjugated formulation and free drugs. Moreover, PLGA nanoparticles were also used for oral delivery of anti-tuberculosis drugs (ATDs). [98, 99] In these studies, three or four frontline ATDs, including rifampicin, isoniazid, pyrazinamide, and ethambutol, were co-encapsulated inside PLGA nanoparticles through an emulsion technique, and the resulting nanoparticle formulation improved bacterial clearance in *M. tuberculosis* infected mice and guinea pigs via oral administration.

1.5 Nanoparticle-enabled Antibacterial Vaccination

Vaccines can protect against or treat infections by manipulating the host's immune responses, and their success in controlling former epidemics worldwide has been considered as the most effective public health intervention ever achieved.

[100, 101] The vaccine strategy also holds the promise to halt antibiotic resistance by reducing the exposure of bacteria to widely used antimicrobial agents. [102, 103] However, the majority of existing vaccines predominantly drive the generation of neutralizing or opsonizing antibodies against pathogens, a mechanism that is ineffective against a number of infections. [104] Vaccine development against these diseases is further hampered by incomplete understanding of the enormously complex human immune system and the underlying mechanisms of protection. [105] To address these challenges, nanoparticles offer unique advantages for immune modulation against bacterial infections. [106, 107]

Nanoparticles have been extensively explored to overcome the instability, undesirable systemic biodistribution, and toxicity frequently associated with the administration of soluble molecules. [108, 109] It has been reported that conjugation of antigens to nanoparticle surfaces facilitated B-cell activation, [110] due to a higher quantity of antigens that were delivered to antigen presenting cells (APCs). [111] With the advancement in nanoparticle engineering, fabrication techniques long established for manufacturing nanoparticle-based drug delivery systems including layer-by-layer assembly, [112, 113] facile spray-drying process, [114] and soft lithography-based particle replication in non-wetting templates (PRINT) technology [115] have also been increasingly applied to improve on antigen loading. Recently, natural cellular membrane-coated nanoparticles have also been shown to detain membrane-damaging toxins and divert them away from their cellular targets. [116, 117] Such a toxin-detainment strategy was applied to safely deliver intact staphylococcal α-hemolysin to APCs and induced superior protective immunity against toxin-mediated adverse effects

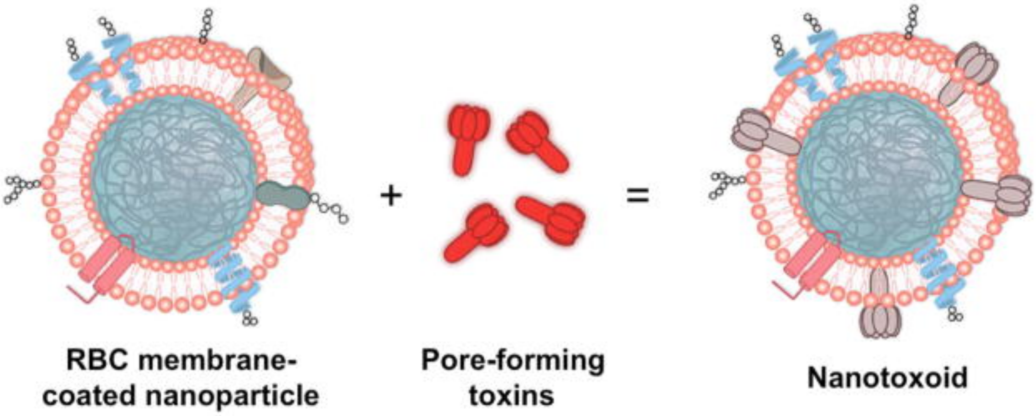

Figure 1.3: Schematic preparation of nanoparticle-detained toxins, denoted 'nanotoxoid', consisting of substrate-supported RBC membranes into which pore-forming toxins can spontaneously incorporate.

in mice when compared to vaccination with heat-denatured toxins (Figure 1.3). [118] This approach maintained a faithful antigenic presentation while removing toxin virulence, therefore avoiding the trade-off between efficacy and safety that remains a major challenge of current toxoid development.

Besides delivering antigens, nanoparticles can concurrently carry adjuvants to mimic natural microbes for enhanced vaccination efficacy. [119, 120] Particularly, various toll-like receptor (TLR) ligands including small molecules, carbohydrates, DNAs, and RNAs, together with antigens have been delivered using nanoparticles, resulting in equivalent immune responses compared to soluble antigen formulations but at significantly reduced dosages. [121–124] More importantly, nanoparticles allow for programmable presentation of adjuvants and antigens to immune cells for desirable responses. For example, combinations of TLR agonists, as opposed to a single adjuvant, have been concurrently loaded into nanoparticles to mimic the combinatorial TLR activation that occurs in natural infections, therefore resulting in more vigorous immune responses. [125–127] In addition, nanoparticles allow for the sequential presentation of antigens and adjuvants to be programmed for optimal immune responses. For example, encapsulation of antigens and TLR agonists into the same nanoparticles has shown advantages for the induction of effector T-cell responses [123, 128] due to the manner in which antigen processing occurs in dendritic cells. [129, 130] In contrast, delivery of antigens and TLR agonists in separate nanoparticles seemed to benefit antibody responses. [131] Recent advancement in controlling the intra-nanoparticle architecture and adjuvant distribution has provided additional capability for programming nanoparticle-based immune modulation. [132] For example, when interbilayer-crosslinked multilamellar vesicles were used as synthetic vaccines, the TLR-4 agonist monophosphoryl lipid A (MPLA) was incorporated throughout the vesicle layers and elicited stronger serum IgG titres as compared to the vesicles carrying the same amount of MPLA but attached only on the vesicle surfaces (Figure 1.4). [133]

Targeting vaccines to desired sites for safe and effective immune responses is another advantage of using nanoparticles for vaccine delivery. For example, a cationic nanogel loaded with a subunit fragment of *Clostridium botulinum* type-A neurotoxin has been shown to facilitate persistent antigen adherence to the nasal epithelium and effective uptake by mucosal dendritic cells. [134] This platform not only elicited strong systemic and mucosal immune responses, but also prevented exposure of the upper respiratory tract and the central nervous system to toxic antigens. As another example, nanoparticles responsive to the pH gradient of the GI tract have been able to protect antigens while in the stomach but release them in the lower GI tract for subsequent translocation across the intestinal epithelium. [135] A similar strategy

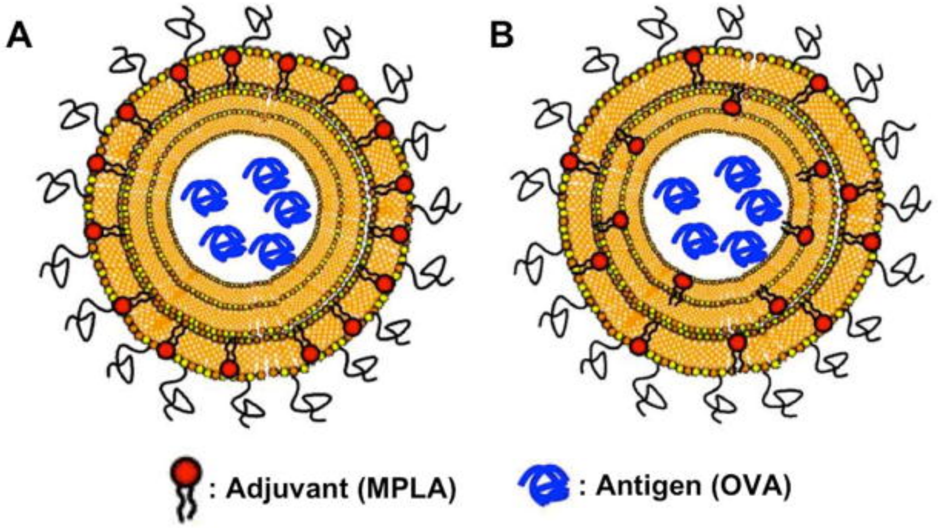

Figure 1.4: Schematic illustration of interbilayer-crosslinked multilamellar vesicles (ICMVs) for vaccine delivery: (a) OVA-loaded ICMVs with MPLA only on the external surface and (b) OVA-loaded ICMVs with MPLA throughout the lipid multilayers.

has also shown promise for targeting antigen-transcytosing M cells overlying Peyer's patches for further enhanced immunity. [136] In addition, nanoparticle-based vaccine platforms can effectively target lymph node-residing immune cells. It has been shown that smaller nanoparticles transport faster to the lymph node, [137] but larger particles are retained longer within the lymph node. [138] Such distinct correlations indicate the importance of size optimization in lymphatic targeting for desired immune responses. At the single-cell level, numerous nanoparticle formulations have been designed to escape endosomes following their uptake by APCs. [139–141] These nanoparticles specifically deposited vaccine payloads into the cytosol and showed promise to enhance CD8+ T-cell priming.

1.6 Nanoparticle-based Bacteria Detection

Rapid and sensitive bacterial detection is crucial for identification of the infection source, allowing for treatment with the appropriate antibiotics and thus preventing the spread of the disease. [142, 143] Bacterial culture and biochemical staining remain the current gold standard in the clinic despite laborious processing, long procedural times, and limitations in identifying certain pathogenic species. Among the various existing diagnostic approaches, those based on polymerase chain reaction (PCR) and sequencing have shown particular promise as highly sensitive tools for microbial identification. [144, 145] However, quantitative real-time PCR-based systems are often too expensive in resource-limited settings, and the current sequencing techniques still lack practical applicability for patient care. [146, 147] In this regard, nanoparticles offer unique opportunities for generic, accurate, and point-of-care detection of pathogens. [148, 149]

Using conventional organic fluorophores for bacterial detection is limited by the molecules' short lifetime and low sensitivity. To overcome these challenges, silica nanoparticles have been used to encapsulate thousands of fluorescent molecules in a single particle, resulting in significantly stronger fluorescence signals. [150] This strategy has resulted in ultra sensitive bacterial detection at a single-cell level. Meanwhile, semiconductor quantum dots (QDs) have also emerged as a promising class of fluorophores for bacterial detection. Compared to organic fluorophores, QDs are brighter and more stable; they also exhibit broad absorption and narrow emission spectra, a property useful for simultaneous excitation and detection. [151] Ligand-conjugated QDs have been extensively explored for the detection of various bacteria, including *Escherichia coli* (*E. coli*), *S. typhimurium*, *Mycobacterium bovis*, and oral bacteria. [152–154] Additional strategies have been explored to further improve the sensitivity of QD-based bacterial detection systems. For example, the binding affinity of QDs coated with zinc(II)-dipicolylamine coordination complexes, a bacterial ligand, has been shown to correlate to the size of the QDs. [155] Based on this observation, QDs with tailored sizes have been developed to distinguish different mutants of the same bacterial species. As another example, streptavidin-coated QDs have been used to label engineered bacteriophages following an *in vivo* amplification and biotinylation process. [156] This method enabled specific detection of as few as 10 bacteria per milliliter in testing samples.

Besides fluorescence-based detection techniques, iron oxide nanoparticles have received much attention, owing largely to their intrinsic magnetic properties. [157,158] Iron oxide nanoparticles coated with pathogen-specific antibodies have been widely used to isolate living bacteria from human blood samples under a magnetic field. [159,160] More recently, this technique has been coupled with microfluidic technology and has resulted in high-throughput bacterial detection under various clinical settings. [161–163] Meanwhile, paramagnetic iron oxide nanoparticles that allow for signal readout with magnetic resonance imaging (MRI) systems have become an attractive new option for ultrasensitive bacterial detection. For *in vitro* diagnosis, iron oxide nanoparticles with a diameter of 21 nm have been coupled with a DNA hybridization technique to enhance the capturing of bacterial 16S rRNAs with a miniaturized micro-NMR system, resulting in rapid and specific pathogen profiling in clinical samples (Figure 1.5). [164] For *in vivo* diagnosis, iron oxide nanoparticles have also

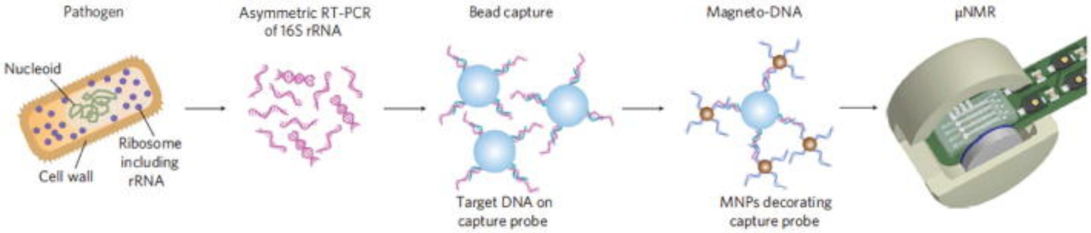

Figure 1.5: Magneto-DNA assay for the detection of bacterial 16S rRNA. Total RNA is extracted from the specimen, and the 16S rRNA is amplified by asymmetric RT-PCR. Single-strand DNA of the amplified product is then captured by beads conjugated with capture probes, followed by hybridizing with MNPs to form a magnetic sandwich complex. Samples are subsequently analyzed using a miniaturized micro-NMR (μNMR) system.

been explored to detect a variety of pathogenic bacteria in animal models, where the high spatial resolution and excellent soft tissue contrast of MRI provided information on both bacterial localization and corresponding host responses. [165]

Gold nanoparticles are another emerging nanoparticle platform for bacterial detection. These nanoparticles possess strong light scattering properties and change their plasmon resonance spectrum upon aggregation. This phenomenon has been widely explored for the detection of bacteria-specific DNAs, proteins, and live bacteria. [166] For example, individual gold nanoparticles have been precisely crosslinked with switchable linkers, which were designed to break in the presence of target subjects. [167] As a result, this design amplified the pathogen-induced nanoparticle aggregation-dispersion process and allowed for visible detection of *E. coli* at a concentration of 100 CFU/mL. In addition, gold nanoparticles can nonspecifically quench fluorescent molecules. Based on this phenomenon, a fluorophore displacement strategy has been developed for bacterial detection. [168] In this strategy, gold nanoparticles adsorbed with fluorescent polymers such as poly(paraphenyleneethynylene) and polylysine selectively interacted with bacteria and released the bound fluorescent polymers which were initially quenched by the gold nanoparticles. The recovered polymer fluorescence allowed for the effective identification of bacteria within minutes.

Recently, rapid progress has been made by integrating nanoparticle-based microbial detection into miniaturized devices such as microfluidic systems and lab-on-a-chip for broader applications. [169] These devices potentially perform assays with adequate sensitivity, specificity and reproducibility, yet demand little user input. [162, 170] The combination of nanoparticle-based detection principles with such devices provide unprecedented opportunities in under-developed regions to perform routine tests, detect the presence of an infectious agent with epidemic potential, and provide guidance for the regional disease control.

1.7 Conclusion

The advent of nanotechnology, particularly nanoparticle engineering, together with the accumulation of knowledge on infectious diseases, has allowed for significant advancement in the field of antibacterial drug delivery. Major efforts have been devoted to developing various nanoparticle-based delivery platforms including liposomes, polymeric nanoparticles, dendrimers, and inorganic nanoparticles. These nanoparticle approaches have shown excellent out- comes in treating and detecting bacterial pathogens by enabling targeted, responsive, and combinatorial delivery of antibiotics, effective antibacterial vaccination, and rapid detection of bacteria. It is expected that nanotechnology will continue bringing improvements to antimicrobial delivery systems for efficacious, patient-compliant, and cost effective therapeutics as well as the specific and sensitive detection of various infectious diseases.

Chapter 1, in full, is a reprint of the material as it appears in WIREs Nanomedicine & Nanobiotechnology, 2014, Weiwei Gao, Soracha Thamphiwatana, Pavimol Angsantikul and Liangfang Zhang. The dissertation author was a major contributor and co-author of this paper.

Chapter 2

Biointerfacing via cell membrane-coated nanoparticles for novel antibacterial drug delivery system

2.1 Coating nanoparticles with gastric epithelial cell membrane for targeted antibiotic delivery against ***Helicobacter pylori*** infection

2.1.1 Introduction

Helicobacter pylori (*H. pylori*) is one of the most prevalent bacterial pathogens that infects more than half of the human population. [171,172] *H. pylori* infection has been considered the major cause responsible for peptic ulcer disease, inflammatory gastritis, and gastric cancer, posing a significant healthcare burden worldwide. [173, 174] Currently, triple therapy based on clarithromycin (CLR) in combination with a proton pump inhibitor (PPI) and an antibiotic (either amoxicillin or metronidazole) is the recommended treatment for *H. pylori* infection. However, mutations in *H. pylori* has led to resistance to CLR and other macrolides, causing a large number of treatment failures. [175] Meanwhile, resistance to other antibiotics including amoxicillin, metronidazole, and levofloxacin, is also rising rapidly. As a result, *H. pylori* eradication rates with standard triple therapy have declined significantly. [176,177] Alternative agents and treatment regimens to address resistance development are being actively studied, but the results remain mixed. [178,179] Clearly, new and effective anti-*H. pylori* treatments are urgently needed.

Unmet clinical needs in controlling *H. pylori* infection has prompted the development of anti-*H. pylori* nanoparticles with distinct therapeutic advantages. For example, nanoparticles have been made to encapsulate multiple antibiotics for concurrent delivery. [180, 181] With better controls over antibiotic release kinetics, the nanotherapeutics were able to minimize resistance development through additive or synergistic drug actions. Meanwhile, nanoparticles responsive to pH changes in the stomach or enzymatic activities have been developed. [182–184] They increased drug potency by only releasing drug payloads in the proximity of *H. pylori* infectious site Meanwhile, nanoparticles have also been conjugated with targeting ligands such as mannose-specific or fucose-specific lectins to target the carbohydrate receptors on *H. pylori* bacteria. [185] These targeted nanoparticles offered site-specific release and gastro-retentive properties, which together boosted local drug levels for a higher bactericidal efficacy. More recently, novel liposomes containing free fatty acids, which were prone to fusion with *H. pylori* bacteria, have been developed. [186, 187] These liposomes disrupted bacterial membrane and compromised the structural integrity of the bacteria for bioactivity, and thus showed a much lower rate to elicit drug resistance compared to conventional antibiotics. [188]

While therapeutic nanoparticles are increasingly applied to treat *H. pylori* infection, technologies for nanoparticle engineering and functionalization have also advanced significantly. [189–191] In particular, using natural cell membranes to coat nanoparticles has recently gained much attention. This strategy combines natural cell membranes with synthetic nanomaterials to leverage native cell functions for therapeutic applications. [192] One area is to harness the natural adhesion property of the source cells for targeted drug delivery. [193] For example, nanoparticles coated with cancer cell membranes inherited homotypic adhesion and showed an innate ability to bind with source cells for drug targeting. [194] In addition, nanoparticles coated with platelet membranes were shown to mimic the binding of platelets with pathogens such as methicillin-resistant Staphylococcus aureus for targeted antibiotic delivery. [195] Meanwhile, platelets also recognize tumor cells including circulating tumor cells through ligand binding interactions. Therefore, platelet membrane-coated nanoparticles were also developed for site-specific delivery of anticancer drugs. [196] These compelling applications inspire us to develop cell membrane-coated nanoparticles for targeted antibiotic delivery against *H. pylori* infection.

The adherence of *H. pylori* in the stomach is a pre-requisite for the bacteria to establish persistent infection. [197] Specifically, *H. pylori* bacteria display a preferential affinity through adherence pedestals to gastric epithelial cells of the gastric antrum. Various surface receptors on gastric epithelial cells have been identified as receptors for *H. pylori* binding. For example, *H. pylori* were shown to bind with integrin $\beta 1$ (CD29) in gastric epithelia cells. [198, 199] An increased expression of CD29 correlated with enhanced invasion of the bacteria. In addition, the fucosylated Lewis blood group antigens (Leb) on gastric epithelia cells are also known as receptors for *H. pylori* binding mediated through bacterial adhesin BabA. [200, 201] Furthermore, *H. pylori* is also known to gain adhesion through defined members of the carcinoembryonic antigen-related cell adhesion molecules (CEACAMs) on gastric epithelial cells via HopQ for adherence and subsequent translocation of cytotoxin-associated gene A (CagA) for virulence. [202]

Based on these adhesion mechanisms, we hypothesize that drug-loaded nanoparticles coated with plasma membranes derived from gastric epithelial cells will inherit the native pathogen-host adhesion and therefore are capable of *H. pylori* targeting. Herein, we derived membranes from AGS cells, a model gastric epithelia cell line, and coated them onto polymeric cores made from poly(lactic-co-glycolic acid) (PLGA, Figure 2.1). The resulting AGS membrane-coated nanoparticles (denoted 'AGS-NPs') present an external membrane coating for bacterial targeting and an internal polymeric core for drug encapsulation and controlled release. We further loaded AGS-NPs with CLR and demonstrated an enhanced bactericidal effect *in vitro* attributable to preferential binding of AGS-NPs with *H. pylori.* In a mouse model of *H. pylori* infection, CLR-loaded AGS-NPs showed superior anti-*H. pylori* efficacy when compared to free CLR or a non-targeted nanoparticle formulation. Overall, we demonstrated that AGS-NP formulation was effective in delivering antibiotics to *H. pylori* bacteria in an actively targeting manner and thus achieved high therapeutic efficacy.

2.1.2 Experimental Methods

AGS cell culture and membrane derivation

AGS cell line (human gastric adenocarcinoma, ATCC CRL-1739) was purchased from the American Type Culture Collection (ATCC) and maintained in Ham F-12K Medium (Invitrogen) supplemented with 10% fetal bovine serum (FBS, Hyclone) and 1% penicillin-streptomycin (100 U/mL penicillium and 100 μg/mL streptomycin, Invitrogen) at 37°C in a humidified atmosphere containing 5% CO2. For cell membrane derivation, AGS cells were grown in T-175 culture flasks to 70-80% confluency and detached with 2 mM ethylenediaminetetraacetic acid (EDTA, USB Corporation) in phosphate buffered saline (PBS, Invitrogen) and washed in PBS

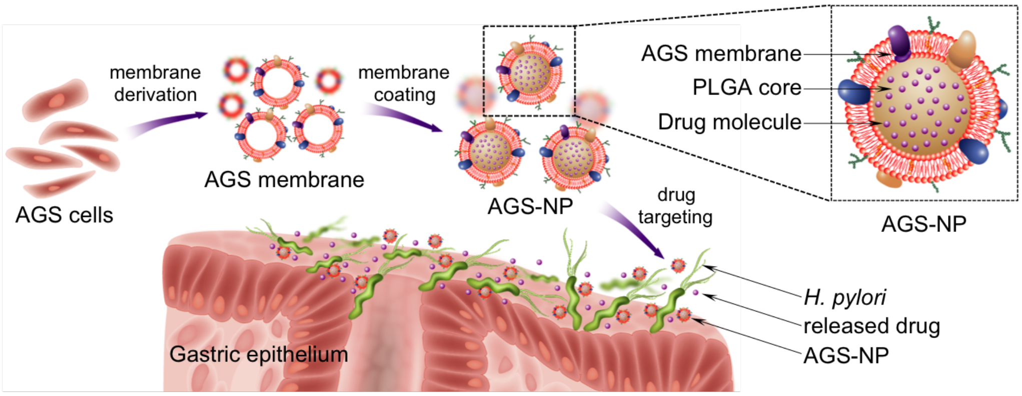

Figure 2.1: Schematic illustrations of the preparation of gastric epithelial cell (e.g. AGS cell) membrane-coated nanoparticles (denoted 'AGS-NPs') and their use for targeted antibiotic delivery to treat Helicobactor pylori (*H. pylori*) infection. To prepare AGS-NPs, cellular membranes are first derived from AGS cells, a human stomach adenocarcinoma cell line. AGS-NPs are then fabricated by coating poly(lactic-co-glycolic acid) (PLGA) polymeric cores with AGS membranes, which contain key antigens for *H. pylori* binding. The resulting AGS-NPs mimic natural pathogen-host binding interactions. Following the administration into the stomach, the AGS-NPs are expected to preferentially bind with *H. pylori* bacteria and release antibiotic payload onsite for enhanced antibacterial efficacy.

three times by centrifuging at 500 × g for 10 min. The pellet was suspended in homogenization buffer (HB) consisting of 75 mM sucrose, 20 mM Tris-HCl pH 7.5 (Mediatech), 2 mM $MgCl_2$ (Sigma Aldrich), 10 mM KCl (Sigma Aldrich), and protease/phosphatase inhibitors cocktails. Cells were disrupted by a dounce homogenizer (20 passes), then spun down at 3,200 × g for 5 min. The supernatant was saved while the pellet was resuspended in HB and the homogenization and centrifugation were repeated again. The supernatants were pooled and centrifuged at 7,600 × g for 25 min, after which the pellet was discarded and the supernatant was centrifuged at 29,600 × g for 35 min. The supernatant was discarded and the pellet was resuspend in 10 mM Tris-HCl pH = 7.5 and 1 mM EDTA and centrifuged again at 29,600 × g for 35 min. The pellet containing the plasma membrane material was then collected and resuspended in DI water. Samples were aliquoted and stored in -80°C fridge for subsequent studies.

Nanoparticle synthesis and characterization

To synthesize polymeric nanoparticle cores, 0.67 dl/g acid (carboxyl)- terminated 50:50 poly (lactic-co-glycolic acid) (PLGA) (LACTEL Absorbable Polymers) in acetone was nanoprecipitated in aqueous solution. To prepare fluorescently labeled PLGA cores, 1,19-dioctadecyl-3,3,3',3'-tetramethylindodicarbocyanine perchlorate (DiD, $\lambda_{\text{excitation/emission}} = 644/665$ nm, 0.1 wt%, Life Technologies) was dissolved together with PLGA in acetone followed by the nanoprecipitation process. The nanoparticle solution was then put under vacuum to remover organic solvent with continuous stirring for 2h. To synthesize AGS cell membrane-coated nanoparticles

(AGS-NPs), PLGA nanoparticles cores were mixed with membrane vesicles at 1:2 membrane protein to polymer weight ratio, and sonicated using a bath sonicator (FS30D, Fisher Scientific, with a frequency of 42 kHz and a power of 100 W for 5 min) to coat membranes on to polymeric cores. Following the coating, AGS-NPs were purified by centrifugation at 16,000 × g for 10 mins to remove unbound membrane fragments. AGS membrane-derived vesicles (AGS-vesicles) were prepared by sonicating collected cell membranes without PLGA cores for 2 min. As a control group, PLGA nanoparticles coated with polyethylene glycol (PEG-NPs) were fabricated through a nanoprecipitation method previously described. Briefly, a solution of PLGA in acetone was nanoprecipitated into an aqueous phase containing 1,2-distearoyl-sn-glycero-3-phosphoethanolamine-N-[methoxy(polyethylene glycol)- 2000] (DSPE-mPEG2000, average Mw = 2.8 kDa, Laysan Bio, Inc., AL, 10 wt% of PLGA). The nanoparticle solution was then placed under vacuum to remover organic solvent with continuous stirring for 2h. Following the nanoparticle synthesis, dynamic light scattering (DLS) studies were performed to measure the hydrodynamic size and surface zeta potential (Malvern ZEN 3600 Zetasizer). All measurements were carried out in triplicate at room temperature. To examine the nanoparticle miscroscopic morphology, AGS-NP samples were visualized with transmission electron microscopy (TEM, Tecnai G2 Sphera FEI 200 kV). Briefly, AGS-NP samples (1 mg/mL) were dropped onto carbon-coated copper grid and left for 1 min, and then washed off with DI water. The sample was then stained with 1 wt% uranyl acetate (Sigma Aldrich) before imaging.

Membrane protein characterization

An SDS-PAGE assay (Thermo Fisher Scientific) was carried out to examine the protein profile of AGS cell lysates, AGS membranes, and AGS-NPs. Specifically, all samples were adjusted to equivalent total protein concentrations in lithium dodecyl sulfate (LDS) loading buffer. The samples were then separated on a 4-12% Bis-Tris 17-well minigel in MOPS running buffer using a Novex Xcell SureLock Electrophoresis System. The protein bands were stained with InstantBlue Protein Stain (Expedeon) for observation according to manufacturer's protocol. Western blotting was conducted to identify membrane proteins on AGS-NPs. Specifically, gels from the SDS-PAGE study were transferred onto a nitrocellulose membranes (Thermo Scientific) and probed with primary antibodies including mouse anti-human CD29 (Biolegend), mouse anti-human Blood Group Lewis b (Santa Cruz Biotechnology), and mouse anti-human CD66e (CEACAM5, Santa Cruz Biotechnology). Horseradish peroxidase (HRP)-conjugated secondary antibodies including goat anti-mouse IgG (Biolegend) and goat anti-mouse IgM (Southern Biotech) were used as secondary staining based on the isotype of the primary antibodies. The nitrocellulose membrane was then incubated with ECL western blotting substrate (Pierce) and developed with the Mini-Medical/90 Developer (ImageWorks).

AGS-NP targeting to *H. pylori* bacteria

H. pylori Sydney strain 1 (SS1) was maintained on Columbia agar supplemented with 5% horse blood (Hardy Diagnostics) at 37°C under microaerobic conditions (10% CO2, 85% N2, and 5% O2). Before the experiments, a single colony of

H. pylori from the agar plate was inoculated into Brain Heart Infusion (BHI) broth containing 5% FBS and incubated overnight at 37°C under microaerobic conditions with moderate reciprocal shaking. Following the culture, the bacteria were harvested by centrifugation at 5,000 × g for 10 min, washed with sterile 1X PBS twice, and suspended to a concentration of 1×10^8 CFU/mL (OD600 = 1.0) in PBS. For the targeting study, 500 μL of *H. pylori* SS1 (5×10^7 CFU) was added with 200 μL DiD-labeled AGS-NPs or PEG-NPs (250 μg/mL in 1X PBS) and the samples were allowed to mix for 30 min at room temperature. Unbound nanoparticles were removed from the bacteria by repeated centrifugal and washing steps (5,000 × g and 1X PBS). The bacteria were then suspended in 1X PBS and fixed with 2% glutaraldehyde (Sigma Aldrich) for 2 h at room temperature. For imaging by deconvolution scanning fluorescence microscope (DeltaVision System, Applied Precision), post-fixed bacterial suspension was mixed at 1:1 ratio with Vectashield mounting medium containing DAPI. Then 5 μL of the bacterial suspension was dropped on a poly-L-lysine coated glass slide, sealed with coverslip and the fluorescence images were obtained. To quantify DiD fluorescence intensity, bacterial samples were added to a 96-well plate and read with a plate reader (Biotek Spectroscopy). AGS-NP targeting to *H. pylori* was also observed with scanning electron microscopy (SEM, FEI/Philips XL30 ESEM). Briefly, 5 μL of the post-fixed bacterial suspension was dropped onto a polished silicon wafer and allowed to dry overnight in a biosafety cabinet. The sample was then coated with chromium and imaged. In all experiments, bacterial sample without adding the nanoparticles was used as a control.

Drug loading and release studies

To load clarithromycin (CLR) into AGS-NPs, CLR and PLGA were mixed and dissolved in acetone, followed by precipitation into water containing 1 wt% of F68 (Invitrogen). Solutions were stirred for 4 h to evaporate the organic solvent. Loading efficiency was studied by varying the weight ratio of CLR to PLGA from 5 to 30 wt%. Following the preparation, nanoparticles were washed with Amicon Ultra-4 centrifugal filters (Millipore, 10 kDa cut-off) and then used for membrane coating as described above. To measure CLR loading yield, 1 mL of AGS-NPs (6 mg/mL) was lyophilized. Dried AGS-NPs were first dissolved in 200 μL acetronitrile, and then added with 200 μL methanol to extract CLR. Samples were then centrifuged at 21,000 × g. The supernatants were collected and the pellets were discarded. The concentration of CLR in the supernatant samples was measured by high performance liquid chromatography (HPLC, with a PerkinElmer Brownlee C18 analytical column, 4.6 × 100 mm, 3 μm particle size). The mobile phase contained methanol and 0.067 M monobasic potassium phosphate (13:7) and pH was adjusted to 4.0 with phosphoric acid. The flow rate was kept at 1.0 mL/min and the detector wavelength was set as 205 nm.

To study the release kinetics of CLR from AGS-NPs, the samples (6 mg/mL, 200 μL) were loaded into Slide-A-Lyzer mini dialysis devices (10K MWCO, Thermo Scientific Pierce) and then dialyzed against 2L of 1X PBS. PBS buffer was replaced every 12 h during the dialysis process. At each predetermined time point, AGS-NP solutions in three mini dialysis cups were collected and CLR concentration was measured as described above.

Bactericidal activity of CLR-loaded AGS-NPs against *H. pylori*

Bacteria were pelleted from liquid culture with centrifugation at 3000 × g for 7 min and resuspended in fresh BHI to a concentration of 5×10^7 CFU/mL. Then 200 μL of the bacterial solution was mixed with 1000 μL free CLR, CLR-loaded PEG-NPs, CLR-loaded AGS-NPs with a final drug concentration ranging from 0 to 8 μg/mL. Mixtures were first cultured at 37°C under microaerobic condition on reciprocal shaker for 30 min and then centrifuged at 3,000 × g for 7 min. Bacterial pellets were washed twice with PBS to remove unbound drugs and NPs and then resuspended with fresh BHI, followed by an overnight incubation. After the incubation, the samples were serial diluted 10 to 10^7-fold with 1X PBS. The bacterial suspensions were spotted onto Columbia agar plates with 5% laked horse blood. The agar plates were incubated for 3-5 days for bacterial enumeration.

Induction of *H. pylori* infection in mice

Six-week-old C57BL/6 male mice were purchased from the Jackson Laboratory (Bar Harbor, ME). Mice were housed in the Animal Facility at the University of California San Diego under federal, state, local, and National Institutes of Health guidelines for animal care. To induct infection, each C57BL/6 mouse received 0.3 mL of 1×10^9 CFU/mL *H. pylori* in BHI broth administered intragastrically through oral gavage every 48 h, repeated three times (on day 3, 5, and 7, respectively), and the infection was allowed to develop for 2 weeks.

In vivo anti-*H. pylori* efficacy of CLR-loaded AGS-NPs

Infected mice were randomly divided into four treatment groups (n=8) and orally administered with CLR-loaded AGS-NPs, CLR-loaded PEG-NPs, free CLR, (with 30 mg/kg CLR dosage) or PBS. Administration was performed once daily for 5 consecutive days. Before the treatment, mice were first administered with omeprazole (a proton pump inhibitor) through oral gavage at a dose of 400 μmol/kg body weight, followed by a lag time of 30 min before administration of different treatment groups. Forty-eight hours after last administration, mice were sacrificed and the stomachs were excised from the abdominal cavity. The stomachs were cut along the greater curvature, and the gastric content was removed. Stomach tissues were rinsed with 1X PBS and weighed. Then samples were suspended in 200 μL 1X PBS and homogenized with Bullet Blender homogenizer (Next Advance). The homogenate was serially diluted and spotted onto Columbia agar plate with 5% laked horse blood and Skirrow's supplement (10 μg/mL vancomycin, 5 μg/mL trimethoprim lactate, 2,500 IU/L polymyxin B, Oxiod). The plates were then incubated at 37°C under a microaerobic condition for 5 days and then bacterial colonies were enumerated.

Evaluation of AGS-NP toxicity *in vivo*

To evaluate the acute toxicity of the AGS-NPs in vivo, uninfected C57BL/6 male mice (n=6, 25-30 g each) were orally administered with AGS-NPs once daily for 5 consecutive days using the procedure as described above. Control mice were administered with PBS. During the experimental period, the mouse body weight was monitored daily. On day 6, mice were sacrificed and sections of the mouse stomach tissues were processed for histological examination. The stomach was cut open along the greater curvature, and the gastric content was removed. The longitudinal tissue sections were fixed in neutral-buffered 10 v/v% formalin for 15 h, transferred into 70% ethanol, and then embedded in paraffin. The tissue sections were cut with 5 μm thickness and stained with hematoxylin and eosin (H&E). The stained sections were visualized by Hamamatsu NanoZoomer 2.0HT and the images processed using NDP viewing software.

Statistical Analysis

DLS and plate reader data represent averaged values (obtained from 3 replicates) with standard deviation shown as error bars. For Western blot studies, the experiments were performed in triplicate and a representative image was shown. To examine the statistical significance, unpaired two-tailed t-tests were performed in GraphPad Prism 7 with confidence level P = 0.05 deemed significant.

2.1.3 Results and Discussion

The formulation process of AGS-NPs consists of three steps. In the first step, cytoplasm membranes of AGS cells were derived based on a previously established process, which involves hypotonic lysis, mechanical disruption, and differential centrifugation. [194, 203] In the second step, polymeric cores of PLGA were synthesized with a nanoprecipitation method, where acetone solution containing PLGA was added dropwise to an aqueous phase followed by evaporation. The nanoprecipitation process also allows for encapsulation of dye molecules or antibiotics by co-dissolving these

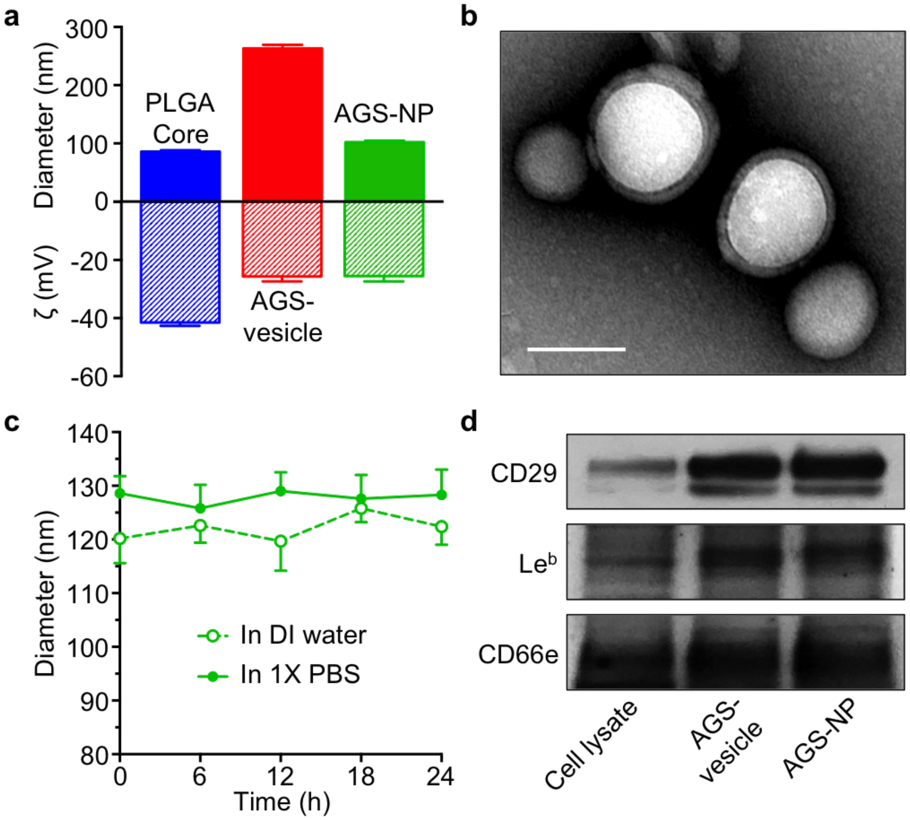

Figure 2.2: Physicochemical characterization of AGS-NPs. (A) Dynamic light scattering (DLS) measurements of hydrodynamic size (diameter, nm) and surface zeta potential (ζ, mV) of PLGA cores, AGS membrane vesicles (AGS-vesicle), and AGS-NPs ($n = 3$). (B) Translation electron microscopy (TEM) image of AGS-NPs stained with uranyl acetate. Scale bar = 100 nm. (C) Stability of AGS-NPs in DI water or 1X PBS, determined by monitoring particle size (diameter, nm), over a span of 24 h (n=3). (D) Western blotting analysis for AGS membrane-specific protein markers. Samples were run at equal protein concentrations and immunostained against membrane markers including CD29, Leb, and CD66e.

molecules with PLGA in acetone. In the third step, AGS cell membranes were fused onto PLGA cores by mixing the cores with AGS membrane followed by sonication. Following the synthesis, dynamic light scattering (DLS) measurements on AGS-NPs showed that the diameter of the nanoparticles increased from 85.8 ± 4.4 nm of the PLGA cores to 102.2 ± 4.0 nm after the cell membrane coating (Figure 2.2A). Meanwhile, the surface zeta-potential increased from -41.5 ± 2.0 to -25.5 ± 3.3 mV. An increase of approximate 16 nm of nanoparticle diameter and a change of about 20 mV of the surface zeta-potential are attributable to the addition of a bilayer membrane onto the exterior of the PLGA cores. [194, 203] Following the fabrication, AGS-NPs were also examined under transmission electron microscopy (TEM) for morphology. Under the microscope, AGS-NPs present a typical core-shell structure, where a spherical core is surrounded by a unilamellar membrane coating (Figure 2.2B). AGS-NPs were suspended in water or 1X PBS and monitored for hydrodynamic sizes measured with DLS for 24 h. Herein, 1X PBS simulated the pH level in stomach after proton pump inhibitor was also administered in anti-*H. pylori* treatment. [187] In PBS, AGS-NPs maintained stable sizes comparable to those in water, indicating an enhanced colloidal stability due to the membrane coating (Figure 2.2C). AGS-NPs were further analyzed with Western blot for antigenic information (Figure 2.2D). Specifically, we verified the presence of key membrane proteins responsible for *H. pylori* binding, including CD29 (integrin $\beta1$), blood group Lewis b (Leb), and CD66e (carcinoembryonic antigen-related cell adhesion molecule-5 or CEACAM5). Compared to cell lysate, membrane derivation also enriched membrane protein concentration, reflected by higher protein immunoblot intensity for AGS membrane vesicles (denoted

AGS-vesicles) and AGS-NPs compared to that of the cell lysate. Overall, these results show the successful coating of AGS cell membranes onto polymeric cores.

After the nanoparticle synthesis, we tested the preferential targeting of AGS-NPs to *H. pylori* bacteria. As shown in Figure 2.3A, *H. pylori* (blue) showed a typical rod shape when observed under a fluorescence microscope. The image of the bacteria obtained with scanning electron microscopy (SEM) confirms the morphology and further reveals the polar sheathed flagella. Next, we mixed the bacteria with fluorescence-labeled AGS-NPs (red). The mixture was incubated at 37°C for 30 min. Following the incubation, the bacteria were thoroughly washed and then observed with a fluorescence microscope. In this case, sporadic red dots in the peripheral area of the bacteria were visible, suggesting AGS-NP retention and co-localization with the bacteria. Under SEM, the presence of individual nanoparticles on the bacteria was revealed, further verifying *H. pylori*-AGS-NP co-localization. To confirm AGS-NP targeting, we formulated polyethylene glycol (PEG)-coated PLGA nanoparticles (denote PEG-NPs), which are inert to bacterial binding, as a negative control. Although PEG-NPs were also fluorescence-labeled and had comparable sizes to AGS-NPs, they were not detected under either fluorescence microscope or SEM after incubation with the bacteria, therefore confirming the critical role played by AGS membrane coating for *H. pylori* targeting. We further quantified the overall fluorescence intensity of the bacterial samples. As shown in Figure 2.3B, *H. pylori* bacteria incubated with AGS-NPs showed a nearly 10-fold increase in fluorescence intensity compared to that of the bacteria incubated with PEG-NPs, confirming the occurrence of a prominent binding between AGS-NPs and *H. pylori* bacteria.

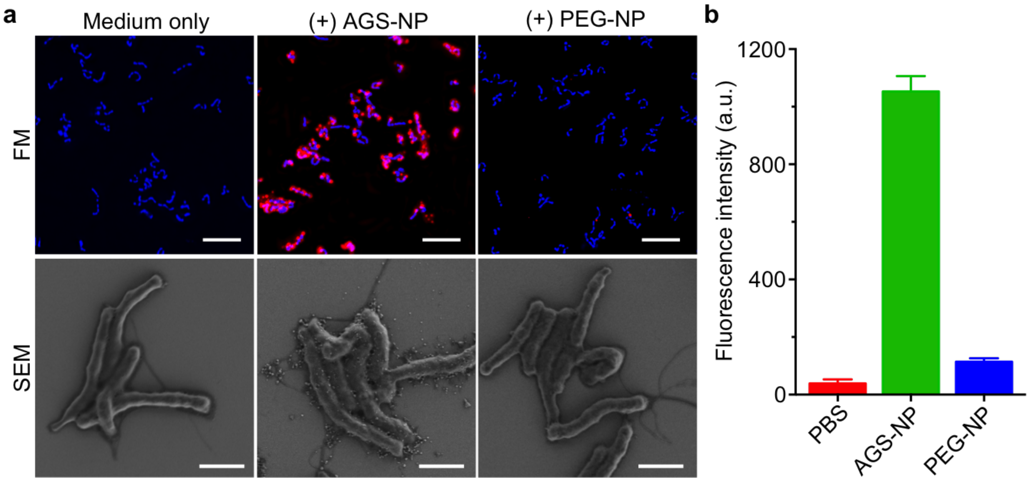

Figure 2.3: AGS-NPs targeting to *H. pylori* bacteria (A) Fluorescence microscopy (FM, top row) and scanning electron microscopy (SEM, bottom row) images of *H. pylori* bacteria after incubation with medium only, AGS-NPs, and corresponding pegylated PLGA nanoparticles (PEG-NPs), respectively. Scale bar = 5 μm in FM and 1 μm in SEM, respectively. (B) Fluorescence intensity at 665 nm measured from the *H. pylori* bacterial samples incubated with PBS, AGS-NPs, and PEG-NPs, respectively. In FM images and fluorescent intensity measurements, AGS-NP and PEG-NP were labeled with DiD dye (red) and *H. pylori* were stained with DAPI (blue). Bars represent means ± SD (n = 3).

After having confirmed the preferential binding between AGS-NPs and *H. pylori* bacteria, we proceeded to examine whether AGS-NPs could carry CLR, one of the first-line antibiotics in anti-*H. pylori* treatment, and specifically deliver CLR to *H. pylori*. In the study, drug loading was achieved by co-dissolving CLR with PLGA polymer in acetone at desired ratios prior to nanoprecipitation. Following evaporation of the organic solvent, the cores were coated with AGS membrane, resulting in CLR-loaded AGS-NP (denoted AGS-NP(CLR)). In the study, we fixed PLGA amount and varied the initial CLR input from 0 to 30 w/w% of the polymer weight, a range where the resulting PLGA cores maintained comparable sizes and stability. As shown in Figure 2.4A, CLR loading yield increased when drug initial input was increased. The highest CLR loading yield of 12.43 ± 0.98% was achieved when drug initial input was kept at 30 w/w%. We selected this formulation for the following studies. Following drug loading, samples of free CLR and CLR released from AGS-NP(CLR) were analyzed with high performance liquid chromatography (HPLC). As shown in Figure 2.4B, CLR molecules released from nanoparticles elute at the same time as that of free CLR and peak shapes of the both are similar, suggesting that drug encapsulation and membrane coating did not cause drug degradation. The release kinetics of CLR from AGS-NPs or bare PLGA cores were also examined (Figure 2.4C).The study was carried out in 1X PBS to simulate the pH level in stomach as proton pump inhibitor was also administered to block gastric acid. [187] Without membrane coating, PLGA cores showed a prominent burst release of CLR. In contrast, burst release was minimized when release from AGS-NP(CLR) was measured. In addition, CLR release rate from AGS-NPs stayed lower than that from uncoated PLGA cores. Specifically, a cumulative 83% of CLR was release from PLGA cores in 24 h, whereas only 68% was released from AGS-NP(CLR). A more prolonged drug release from AGS-NP(CLR) is likely due to the coated membranes, which acts as a barrier for drug diffusion out of the polymer matrix. [204]

After successful loading of CLR into AGS-NP, we next investigated the bactericidal activity of AGS-NP(CLR) against *H. pylori*. In the study, *H. pylori* was first incubated with free CLR, AGS-NP(CLR), or CLR-loaded PEG-NP (denoted PEG-NP(CLR)), followed by washing steps to remove free CLR and unbound PEG-NP(CLR), respectively. Bacteria were cultured and then enumerated. As shown in Figure 2.4D, under the experimental conditions, neither free CLR nor PEG-NP(CLR) was able to eradicate *H. pylori* bacteria. In contrast, bacteria incubated with AGS-NP(CLR) showed a nonlinear correlation between bacterial viability and nanoparticle concentrations. A drastic enhancement in bacterial killing of AGS-NP(CLR) compared to control formulations demonstrated a superior antibiotic targeting effect. For this study, we defined minimal bactericidal concentration (MBC) as the minimum concentration of the bactericidal agent required to kill 3 logs (99.9%) of the bacteria during a 30-min incubation. Accordingly, the value of MBC of AGS-NP(CLR) was determined to be 4 μg/mL.

Next, we evaluated the in vivo therapeutic efficacy of AGS-NP(CLR) against *H. pylori*. To this end, we first established a mouse model of infection with *H. pylori* SS1 strain. [205,206] Specifically, we administered each C57BL/6 mouse with 3×10^8 CFU bacteria through oral gavage once every two days for four times (Figure 2.5A). After bacterial administration, infection was allowed to develop for two weeks and

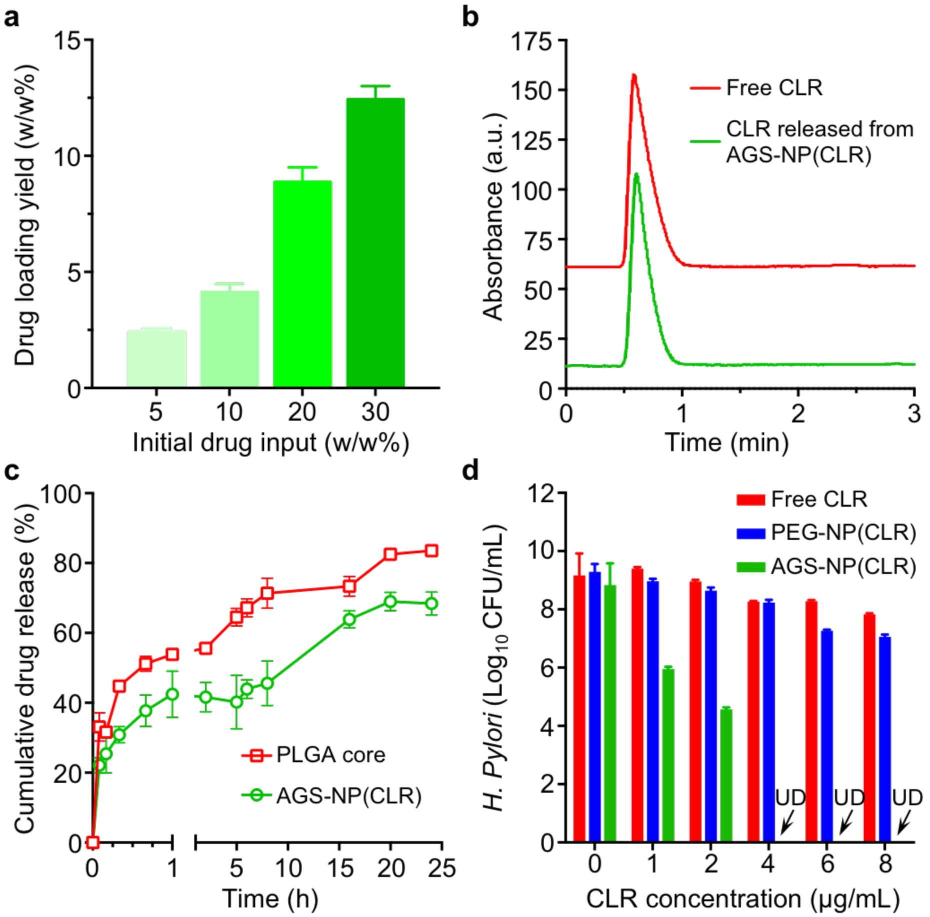

Figure 2.4: Characterization of clarithromycin(CLR)-loaded AGS-NP (denoted 'AGS-NP(CLR)'). (A) Quantification of CLR loading yield of AGS-NP(CLR) when initial drug input was varied from 0 to 30 w/w%. (B) Chromatogram of free CLR and CLR released from AGS-NP(CLR). The flow rate was kept 1.0 mL/min and a detector wavelength at 205 nm. (C) CLR release profiles from PLGA core without membrane coating (red) and from AGS-NP(CLR). Data points represent means ± SD (n = 3). (D) *In vitro* bactericidal activity of free CLR, PEG-NP(CLR), and AGS-NP(CLR) against *H. pylori* bacteria, respectively. Bars represent means ± SD (n = 3). UD = undetectable.

then infected mice were randomly divided into four groups (n=8 for each group) and treated with PBS, free CLR, PEG-NP(CLR), or AGS-NP(CLR). In the study, a CLR dosage of 30 mg/kg body weight was chosen based on existing studies. [207, 208] To avoid potential drug degradation, all mice were given proton pump inhibitor through oral gavage 30 min prior to the administration of all formulations to neutralize gastric acid in the stomach. Each formulation was administered once a day for five consecutive days. On day 6, mice were sacrificed and stomach tissues were processed for bacterial quantification. Therapeutic efficacy was evaluated by enumerating and comparing *H. pylori* colonies. As shown in Figure 2.5B, mice treated with PBS showed a high bacterial burden of 1.58×10^5 CFU/g of stomach tissue. Meanwhile, mice treated with free CLR and PEG-NP(CLR) carried a bacterial burden of 5.01×10^4 and 6.45×10^3 CFU/g of stomach tissue, respectively. These values correspond to a bacterial reduction of approximately 0.53 and 1.43 orders of magnitude, respectively. In contrast, the bacterial burden in mice treated with AGS-NP(CLR) was found to be 1.46×10^2 CFU/g of stomach tissue, approximately 3.08 orders of magnitude reduction. The superior anti-*H. pylori* efficacy found with AGS-NP(CLR) demonstrates the effectiveness of AGS membrane coating for drug targeting.

Lastly, we evaluated the toxicity of AGS-NP with uninfected C57BL/6 mice. In the study, mice were orally administered with AGS-NP once daily for 5 consecutive days with the same dosing regimen as the one used in above efficacy study. Mice administered with PBS buffer were used as a control group. During the study, mice administered with AGS-NPs maintained the same body weight compared to mice administered with PBS and all mice showed stable body weight and steady growth

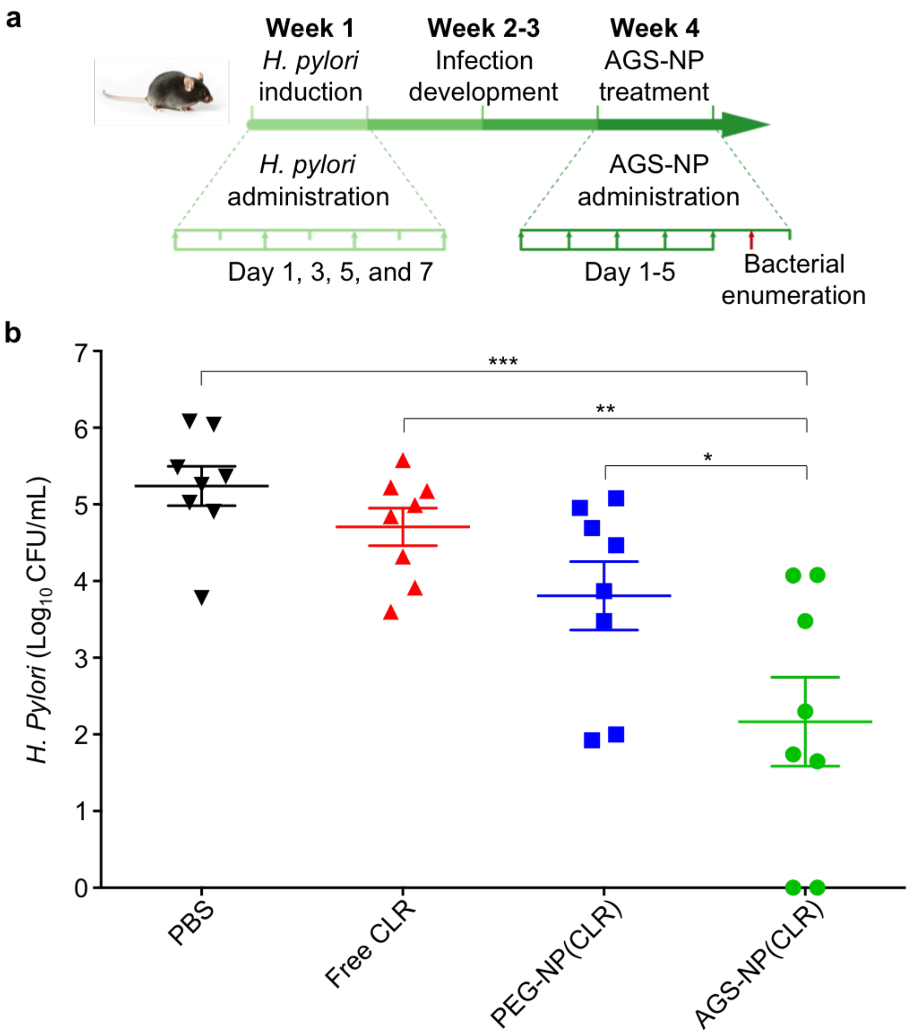

Figure 2.5: *In vivo* anti-*H. pylori* therapeutic efficacy of AGS-NP(CLR). (A) The study protocol using a C57BL/6 mouse model of *H. pylori* infection, which includes *H. pylori* inoculation (week 1), infection development (week 2-3), and treatment (week 4). (B) Quantification of *H. pylori* bacterial burden in the stomach of infected mice treated with PBS, free CLR, PEG-NP(CLR), or AGS-NP(CLR) (n = 6 per group). Bars represent median values. $*P < 0.05$, $**P < 0.01$, $***P < 0.001$.

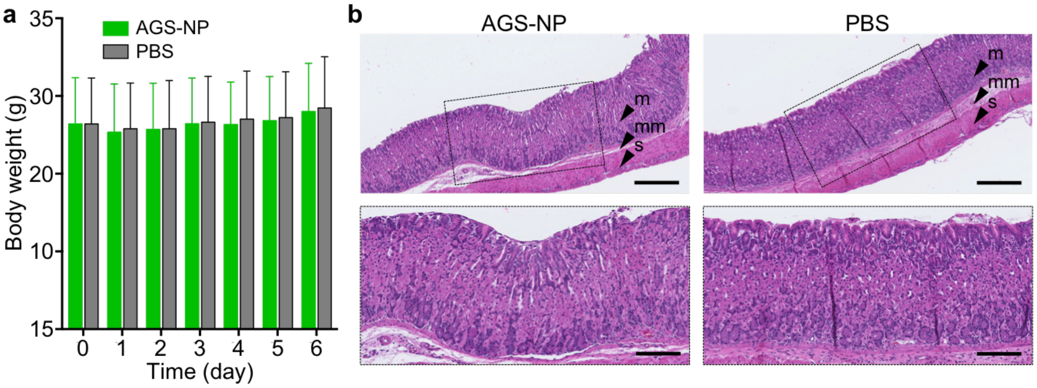

Figure 2.6: Evaluation in vivo toxicity of AGS-NP. Uninfected mice were orally administered with the AGS-NP or PBS once daily for five consecutive days. (A) Mouse body weight log from day 0 to day 6 during study. Error bars represent the standard deviation of the mean (n = 6). (B) On day 6, mice were sacrificed and sections of the stomach were processed for histological staining with hematoxylin and eosin (H&E). Scale bars represent 250 μm in the top row and 100 μm in the bottom row). In the images on the top row, m: mucosa, mm: muscularis mucosa, and s: submucosa.

(Figure 2.6A). On day 7, all mice were sacrificed and the longitudinal sections of gastric tissues obtained from the mice were collected and stained with hematoxylin and eosin (H&E). Under microscope, tissue samples of mice from both groups show clear layers of mucosa, muscularis mucosa, and submucosa (Figure 2.6B). When zoomed-in, the gastric tissues from mice treated with AGS-NPs maintained an undisturbed structure with a clear layer of epithelial cells and well-organized gastric pits, which was similar to the gastric samples treated with PBS only. The absence of any detectable gastric histopathologic changes or toxicity within a five-day treatment suggests that orally administered AGS-NPs is safe.

Targeted delivery can promote drug-pathogen localization and minimizes drug systemic exposure, therefore reducing the risk of drug resistance. [191] To achieve effective drug targeting, one common method is to conjugate nanoparticles with bacterium-specific ligands including small molecules, peptides, antibodies, and aptamers. [189] However, the application of such ‘bottom-up’ strategy may be limited by the availability of reliable ligands for pathogen binding as well as the robustness of the conjugation process. In contrast, cell membrane coating approach represents an alternative ‘top-down’ method that leverages native cell-pathogen adhesion mechanisms for targeting without ligand selection and conjugation. Like *H. pylori*, various opportunistic pathogens, such as strains of staphylococci, streptococci, and *Escherichia coli*, are also known to exploit complex adhesion mechanisms for host cell adhesion and colonization. [209, 210] Cell membrane coating is an effective approach to harnessing these biological mechanisms and replicate the binding. Using membranes from their host cells to coat nanoparticles is expected to be applicable for antibiotic targeting against the pathogen infections. In addition, harnessing patient’s host cell functions for pathogen targeting may open new opportunities to enable patient-specific and disease-specific precision medicine. [211]

In this study, we selected CLR as a model antibiotic to demonstrate the targeted delivery ability of the AGS-NPs. As PLGA nanoparticles have extensive applications in drug encapsulation and delivery, AGS-NPs are expected to load and deliver other antibiotics or antibiotic combinations to further improve anti-*H. pylori* efficacy. [212] Herein, AGS-NPs are designed with a diameter of approximately 100 nm and a negative surface charge, as nanoparticles with a comparable size and surface charge are known to effectively penetrate mucus layer. [187, 213] In addition, cell membrane coated onto PLGA is known to neutralize bacterial toxins for antibacterial efficacy [214, 215]. For H. pylori infection, such activity may also exist and can benefit from a bacterial targeting effect that reduces nanoparticle stomach clearance and brings nanoparticles to the proximity of the bacteria. [187] Meanwhile, nanoparticle cores made with materials such as mesoporous silica, macromolecule gelatin, and crosslinked acrylamide have been coated with cell membranes. [192] New coating processes, such as cell membrane vesicle-templated in situ gelation, have also been developed. [216] Furthermore, the furture development of AGS-NPs toward clinical use needs to address cell membrane supply issue. In this regard, the rapid advances in methods of *ex vivo* cell expansion may address the large quantity of cell membrane materials demanded for clinical studies. [217, 218] Meanwhile, genetic engineering aimed at modifying primary human cells have also advanced significantly, offering on-demand membrane function in combination with rapid and large-scale cell expansion. [219] These breakthroughs together offer a promising prospect to the translation of AGS-NPs and cell membrane-coating technology in general.

These technological advances can be also applied to enable new antimicrobial strategies beyond antibiotic delivery. For instance, cell membrane-coated nanoparticles have been developed to neutralize bacterial toxins based on toxins' virulent mechanisms rather than their structures, therefore enabling broad-spectrum and 'drug free' antivirulence therapy. [220, 221] As another 'drug free' strategy to combat infection, cell membrane-coated nanoparticles have also been developed as antibacterial vaccines. In this case, nanoparticles coated with bacterial outer membranes not only present the natural antigen presentation by bacteria to the immune system, but also modulate the host immune response through size-controlled lymphatic targeting. Meanwhile, bacterium-secreted virulent toxins have been entrapped using cell membrane-coated nanoparticles, resulting in multivalent nanotoxoids capable of delivering diverse virulence factors in a natural, concurrent, and safe fashion for immunity. [222,223] The nanotoxoid formulation consistently outperformed traditional vaccine formulations prepared from denatured proteins. Overall, these developments illustrate the promise and strength of using cell membrane coating technology to address the therapeutic challenges of bacterial infections.

2.1.4 Conclusions

In summary, we derived natural membranes of AGS cells, a gastric epithelial cell line, and coated them onto PLGA polymeric cores. The resulting AGS-NPs preserved cell surface antigens used by *H. pylori* bacteria to adhere and colonize the host. AGS-NPs showed preferential binding and retention with *H. pylori* when compared to control nanoparticles coated with synthetic PEG. We further loaded CLR into AGS-NPs and achieved high drug loading yield and prolonged drug release profile from the nanoparticles. The resulting CLR-loaded AGS-NPs showed superior bactericidal effect *in vitro* and were able to effectively reduce bacterial burden in a mouse model of *H. pylori* infection. In addition, mouse body weight and stomach histology in a toxicity test showed no adverse effects from the AGS-NPs. Collectively, these results demonstrate that AGS-NPs are an effective and safe approach for targeted antibiotic delivery to treat *H. pylori* infection.

2.2 Micromotors spontaneously neutralize gastric acid for pH-responsive payload release

2.2.1 Introduction

Gastric acid, consisting primarily of hydrochloric acid produced by parietal cells in the gastric glands, plays a crucial role in maintaining the stomach's digestive function. It enables gastric proteolysis by denaturing proteins from food for break down by digestive enzymes. It also inhibits the growth of many microorganisms which enter the stomach and thus reduces the risk of pathogen infection. However, the harsh gastric environment becomes a double-edged sword under certain circumstances. For example, it creates a physiological barrier for the use and delivery of therapeutic drugs, such as protein-based drugs and some antibiotics to the stomach. In these cases, the drugs are exclusively combined with a proton pump inhibitor (PPI), which reduces the production of gastric acid. The effectiveness of PPIs is attributed to the irreversible binding to the proton pumps to suppress acid secretion for approximately 12 to 24 hours. [224, 225] Long-term use of PPIs can cause adverse effects such as headache, diarrhea, and fatigue, and in more serious scenarios cause anxiety and depression, as well as severe reaction rhabdomyolysis. [226–231] Therefore, it would be highly desirable to develop alternative approaches which can temperately neutralize gastric acid while not causing adverse drug effects.

Recent advances in nanotechnology has led to the design of a variety of nanocarrier systems which can respond to various biological stimuli, such as pH, for triggered release of their payload. [232–235] In particular, the emerging synthetic nano/ micromotors, which are tiny devices that convert locally supplied fuels or externally provided energy into force and movement, [236–245] have shown considerable promise as delivery vehicles because of their active transport capacity and ability to dynamically respond to their surroundings. [246–253] For example, recent *in vivo* evaluations of synthetic micromotors demonstrated that these artificial motors can self-propel in the stomach and intestinal fluids for enhanced retention and targeted delivery in the gastrointestinal tract. [254, 255] These prior studies demonstrate that the motor-based active transport systems offer attractive features for localized targeted delivery.

In this work, we introduce a new magnesium (Mg)-based micromotor, covered by a pH-sensitive polymer coating, which can rapidly yet transiently neutralize the acidity of the stomach fluid *in vitro* and *in vivo*. By using acid as fuel, these synthetic motors quickly deplete protons while propelling within the stomach, which can effectively elevate the gastric pH to neutral in less than 20 minutes after the motors are applied. More importantly, the motor-induced neutralization of the stomach fluid further triggers the autonomous payload release from the pH-sensitive polymer coating. In contrast to acid suppression by PPIs, the micromotors temporally alter the local environment without blocking the function of the proton pumps. Therefore, this approach has minimal interference upon the function of the stomach and completely eliminates all possible adverse effects associated with conventional PPIs. Since the micromotors are made of biocompatible materials without biological activities, they are safe to use and will not cause acute toxicity. Compared to conventional pH-responsive nanocarriers which passively respond to the local environment, these micromotors can actively adjust their surroundings to reach desired conditions for triggered payload release. Therefore, the use of micromotors, with built-in dual capabilities of acid neutralization and pH-responsive payload release, is a unique and highly promising platform for drug delivery to treat various gastric diseases.

2.2.2 Experimental Methods

Synthesis of EUDRAGIT® L100-55/Au/Mg micromotors

Magnesium (Mg) microparticles (catalog # FMW20, TangShan WeiHao Magnesium Powder Co.; 20± 5 μm) were used as the core to prepare the Mg-based Janus micromotors. The Mg microparticles were initially dispersed onto glass slides coated with a thin film of Poly(vinylpyrrolidinone) template followed by sputtering a gold layer using a Denton Discovery- 18 sputter system. After that, the Janus micromotors were coated with a film of a commercial pH-responsive polymer (EUDRAGIT® L100-55; Evonik Industries, Germany), forming the outermost layer coated on the Mg micropsheres, using a polymer concentration of 0.67% (w/v) in ethanol. After the ethanol was completely evaporated, the EUDRAGIT® L100-55/Au/Mg micromotors were collected by lightly scratching the particles off the glass slide and weighed for use.

Synthesis of R6G-loaded Mg micromotors

For performing the *in vitro* studies, fluorescent Mg-based micromotors were prepared by using a mixture of EUDRAGIT® L100-55 polymer solution (0.67% (w/v) in ethanol) and 20 μg/mL of rhodamine 6G dye (83697, SIGMA, USA). To compare with the Mg-based micromotors, inert polystyrene (PS) microparticles (Bangs Laboratories, Fisher, IN, USA) were used as core particles, following the same protocols for the Au and polymer coatings as described above.

In vitro **pH neutralization study**

In vitro pH neutralization study was performed by measuring the pH values of a gastric fluid simulant (initial pH=1.3; 01651-Sigma-Aldrich) with a pH meter (Seven Easy, Mettler-Toledo, Switzerland) at 1-minute intervals after adding varying amounts of Mg micromotors. The commercial pH indicator BCECF (catalog# B1151, Thermo Fisher, USA) was also used for the pH neutralization study. The fluorescence intensity of BCECF in gastric fluid (pH 1.3), PBS buffer (pH 7.4), and neutralized gastric fluid was measured at excitation/emission = 508/532 nm using a Tecan Infinite M200 microplate reader. The *in vitro* triggered release of R6G dye used as a drug- loaded model and as an indicator of the pH responsive polymer dissolution was followed by monitoring the fluorescence intensity of the gastric fluid simulant solution.

Micromotor propulsion studies

For recording the bright field microscopy videos and capturing the bright field and fluorescent images, an inverted optical microscope (Nikon Instrument Inc. Ti-S/L100) coupled with a 20× and 40× microscope objectives and a Hamamatsu digital camera C11440 was used. The NIS-Elements AR 3.2 software was employed to characterize the movement of the Mg micromotors. For the fluorescence microscopy videos, an identical setup was used in conjunction with a Sola Light Engine (SM5-

LCR-VA, Lumencor) for fluorescence excitation. Nikon fluorescence filter cubes 96312 were used for green light excitation.

In vivo pH neutralization and release study

Six-week-old male ICR mice purchased from Harlan Laboratories (Indianapolis, IN) were fasted for 6 h with free access to water prior to the experiment. For the *in vivo* pH measurement of gastric content, mice were divided into 4 groups (n=3) to be orally administered with 2.5 mg, 5 mg, or 10 mg of Mg micromotors suspended in 0.2 mL DI water. Mice administered with 0.2 mL DI water were tested in parallel as a control. After 20 min of administration, mice were sacrificed and stomachs were excised. The pH of the gastric content was immediately measured using a pre-calibrated pH meter (Seven Easy, Mettler-Toledo, Switzerland). A miniaturized pH microsensor probe (InLab® 423 Combination pH Micro Electrode), with tip diameter 3 mm, was used to ensure a full immersion of the probe tip in the stomach lumen without touching the gastric mucosa. Three separated pH measurements were taken from each stomach, the pH probe was removed, washed with DI water and calibrated between measurements.

For *in vivo* release study, mice were fed with alfalfa-free food from LabDiet (St. Louis, MO, USA) for 2 weeks prior to the experiment. 1,19-dioctadecyl-3,3,3',3'-tetramethylindodicarbocyanine perchlorate (DiD, excitation/emission = 644/665 nm, Life Technologies) was used as a model drug. The DiD dye (20 μg/ml) was loaded into the pH-sensitive polymer EUDRAGIT® L100-55. A 0.2 mL suspension of Mg micromotors or PS microparticles coated with DiD-loaded EUDRAGIT® L100-55 was administered orally. 0.2 mL DI water was given to control mice. 20 mins after administration, the stomachs were cut open along the greater curvature, excess gastric content was removed, and then imaged using an intelligent visual inspection system (IVIS).

Toxicity evaluation of Mg micromotors, pH neutralization and recovery

To assess the recovery of gastric pH after Mg micromotor treatment. Mice were intragastrically administered (n=3) with 0.2 mL suspension of 5 mg Mg micromotors. At 20 min and 24 h after administration, mice were sacrificed and stomachs were removed from the abdominal cavity. The pH of the gastric content was immediately measured using a precalibrated pH meter. The probe tip was carefully positioned to avoid contact with the stomach mucosa. Control mice were orally administered with DI water.

For *in vivo* imaging of pH change, mice were fed with alfalfa-free food from LabDiet (St. Louis, MO, USA) for 2 weeks prior to the experiment. 20 mins and 24 h after administration of 5 mg Mg micromotors, the stomachs were cut open along the greater curvature, excess gastric content was removed. 40 micro L of 2 mg/mL pH indicator BCECF was evenly distributed onto the opened stomach. The fluorescence imaging of the whole stomach labeled with pH indicator was performed using IVIS. Control mice were orally administered with DI water. To evaluate the acute toxicity of Mg micromotor *in vivo*, six-week-old ICR male mice were orally administered with 0.2 mL suspension of 5 mg Mg micromotor. Mice treated with DI water were used as a control. 24 hours after the oral administration, mice were euthanized and the stomachs were removed for histological analysis. The longitudinal sections of gastric tissue were fixed in neutral-buffered 10% (vol/vol) formalin for 15 h, transferred into 70% ethanol, and embedded in paraffin. The tissue sections were cut with 5 μm thickness stained with hematoxylin and eosin (H&E) assay. Epithelial cell apoptosis was evaluated by the terminal deoxynucleotidyl transferase-mediated deoxyuridine triphosphate nick end labeling (TUNEL) assay (Boehringer Mannheim, Indianapolis, IN). Sections were visualized by Hamamatsu NanoZoomer 2.0HT and the images processed using NDP viewing software.

2.2.3 Results and Discussion

Figure 2.7 a schematically illustrates the structure of a Mg-based micromotor along with its gastric acid neutralization process (through proton depletion enabled by the micromotor reaction and propulsion) and consequent payload release from the pH-responsive polymer coating. The new microvehicle thus consists of the Mg motor, the pH-sensitive polymer coating, and the encapsulated cargo. It offers multiple capabilities and functions, including movement, acid neutralization, cargo transport, and release. The Mg engine converts the acid fuel into a propulsion force and simultaneously alters the local pH, thus causing payload release from the pH-sensitive coating. The core of the micromotor is made of a Mg microsphere with a diameter of about 20 mm. For the fabrication of the micromotors, a layer of Mg microparticles was dispersed onto a glass slide, followed by an asymmetrical coating of the microspheres by sputtering with a thin (10 nm) gold (Au) layer, which is responsible for efficient propulsion through the macrogalvanic corrosion of the Mg surface. [256] After sputtering the Au layer, the Janus microspheres were coated with a pH-sensitive polymeric (EUDRAGIT® L100-55, dissolves at pH > 5.5) film containing the payload. Finally, the well-separated Mg Janus micromotors were obtained after soft mechanical scratching of the glass slide, thus leaving a small opening which exposes the Mg surface to react with the gastric fluid, and leads to the hydrogen-bubble generation and propulsion. The presented micromotor design is highly biocompatible, as magnesium is an essential mineral needed for variety of physiological functions. [257] The enteric polymer coating has been extensively used for drug delivery and release, [255] while gold is commonly employed for imaging and therapeutic applications. [258] The bottom section of Figure 2.7A illustrates the *in vivo* acid neutralization process associated with the propulsion of the Mg-based Janus micromotors along with the corresponding payload release from the pH-sensitive polymer layer. Upon contact with the gastric fluid, a spontaneous reaction between the Mg microsphere motor surface and the surrounding protons (top left of Figure 2.7A) generates hydrogen bubbles, and efficient micromotor thrust. Such a reaction and acid neutralization are facilitated by the presence of the Au layer, which boosts proton depletion through macrogalvanic corrosion.

Figure 2.7B shows the characterization of the Mg-based Janus micromotors. The scanning electron microscopy (SEM) image shows a small opening (ca. 2 μm), produced during the coating process of the micromotors, on the spherical Mg-based micromotor to expose the Mg surface for reaction with the surrounding acidic fluid. The presence of Mg, Au, and carbon (from the polymer coating) is also confirmed by the corresponding energy-dispersive X-ray spectroscopy (EDX) mapping. The

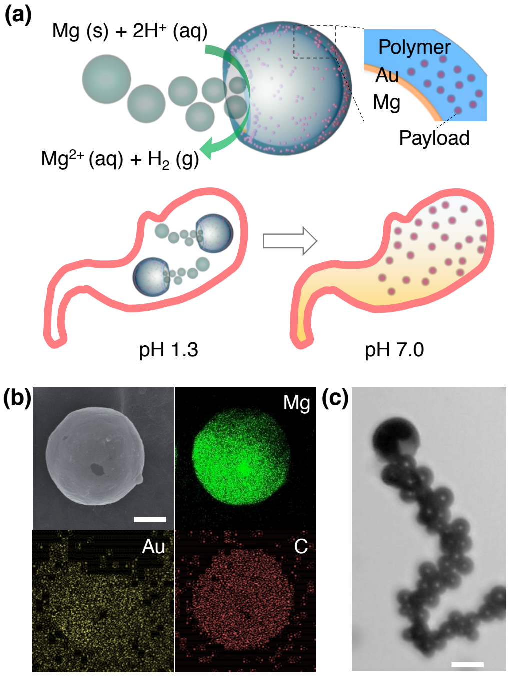

Figure 2.7: Schematic illustrations of Mg-based micromotor and its acid neutralization mechanism (A) Illustrations of an acid-powered Mg-based micromotor and its acid neutralization mechanism. The micromotor is made of a Mg microsphere coated with a thin gold (Au) layer and a payload-encapsulated pH-sensitive polymer layer. At acidic pH, the Mg reacts with acids and generates hydrogen bubbles, thus propelling the motors and depleting protons in the solution. (B) SEM and EDX characterizations of the Mg-based micromotor. Scale bar: 5 μm. (C) Microscopy image illustrating the bubble propulsion of a micromotor in gastric fluid. Scale bar: 20 μm.

microscopy image in Figure 2.7C illustrates the micromotor movement in gastric fluid simulant (pH 1.3). Efficient hydrogen-bubble generation propels the micromotor with an average speed of 60 μm s^{-1}, thus indicating that these micromotors can rapidly react and move in gastric fluid.

The ability of Mg micromotors to neutralize gastric acid and trigger release of their payload was first tested *in vitro*. Figure 2.8A displays the time-dependent pH neutralization process associated with the built-in proton consumption during the reaction and propulsion of Mg micromotors in simulated gastric fluid (initial pH1.3), using 2.75mg of micromotors and 3 mL gastric fluid. The pH of the fluid increases rapidly from 1.3 to 6.2 within 12 minutes, and then more slowly, stabilizing around pH 7.5 after 18 minutes. These data confirm that a fast neutralization of gastric acid can be realized within less than 20 minutes, compared to the 0.5- 1 hour typically required by using PPIs to reach the same level of neutralization. [224] The fluorescent pH indicator BCECF was also used to verify the fast pH neutralization of the gastric fluid by the micromotors. As displayed in Figure 2.8B, in the absence of Mg micromotors, the gastric fluid containing the BCECF indicator displays a light yellow color and very weak fluorescence intensity, and is indicative of acidic conditions. In contrast, an obvious color change to red is observed 20 minutes after adding the Mg micromotors to the gastric fluid. The fluorescence intensity drastically increases to a similar level to that observed in a PBS buffer (pH 7.4), which was used as a control solution. These results demonstrate that the Mg micromotors can rapidly neutralize the gastric fluid through fast proton depletion and efficient propulsion. The fast neutralization process reflects the dramatic fluid convection induced by the collective motion of micromotors in the gastric fluid and the corresponding bubble generation. Such motor-induced “self-stirring” has been shown to accelerate environmental decontamination processes. [259]

To study the pH-responsive release, enabled by the active neutralization of the gastric fluid, R6G dye was used as a model payload encapsulated within the pH-sensitive EUDRAGIT® L100-55 polymeric coating of the Mg micromotors. Inert

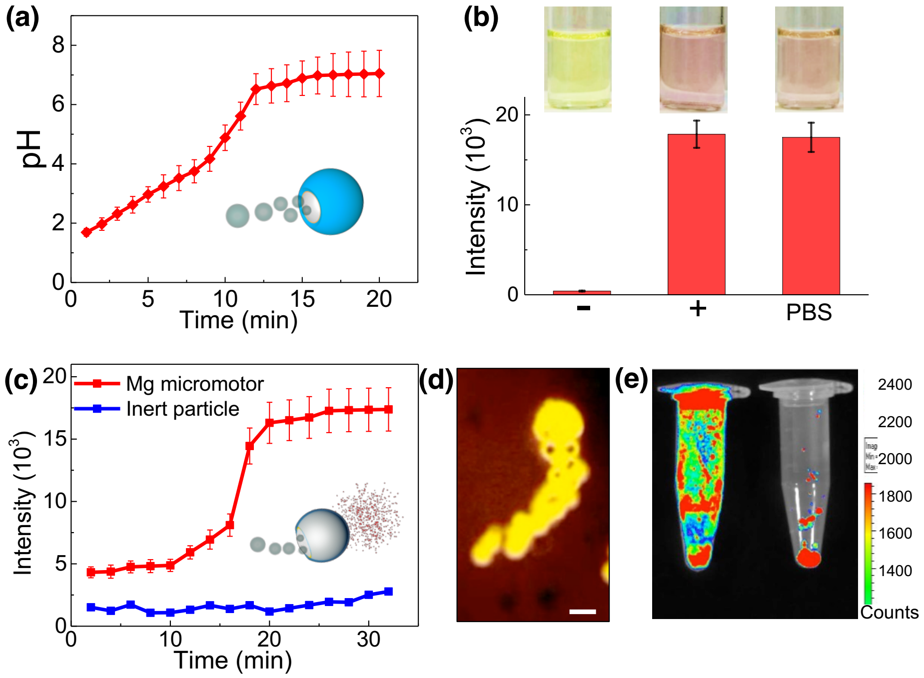

Figure 2.8: *In vitro* acid neutralization and pH-triggered payload release. (A) Time-dependent pH value of gastric fluid (3 mL, pH 1.3) in the presence of Mg micromotors (2.75 mg). (B) Fluorescence intensity of the pH indicator BCECF in gastric fluid (pH 1.3), gastric fluid containing 2.75 mg of the Mg micromotor, and PBS buffer (pH 7.4). Insets: images of the corresponding solutions. (C) Time-dependent fluorescence intensity of released rhodamine 6G (R6G) in the supernatant of 3 mL gastric fluid. R6G dye is loaded in the pH-sensitive polymer coating (starts to dissolve at pH > 5.5) as a model payload. Polystyrene (PS)-based inert microparticles with a similar size as the Mg micromotors were used as a negative control. (D) Fluorescence image showing the propulsion and release processes of an R6G-loaded Mg micromotor. Scale bar: 20 μm. (E) Fluorescence images of the released R6G in the supernatant of gastric fluid containing Mg micromotors (left) or PS microparticles (right).

polystyrene (PS) microspheres (diameter : 10 μm) coated with the R6G dye-loaded polymer layer was used as a control group. Figure 2.8C displays the payload release profile, which obtained by measuring the supernatant fluo- rescence intensity, using the micromotors and inert (control) particles placed in the acidic gastric fluid (initial pH 1.3). The pH change associated with the presence of the Mg micromotors results in sustained release of R6G from the pH- sensitive polymeric coating. The fluorescence of the gastric fluid solution thus increases gradually and reaches a plateau at 20 minutes. In contrast, no such R6G release is observed using the inert PS microparticles which do not react with the protons to cause a pH change, and thus the pH-sensitive polymer coating remains stable.

The fluorescence microscopy image of Figure 2.8D displays the real-time propulsion and payload release of R6G from a Mg micromotor in the gastric fluid. The strong fluorescence signals observed on the micromotor body and the yellow bubble tail confirm the gradual dissolution of the polymer and consequent release of R6G. Figure 2.8E shows the corresponding fluorescence photographs of R6G in 1mL bulk gastric solution in the presence of Mg micromotors and an inert control with microparticles (both coated with R6G-loaded, pH-sensitive polymer). These images clearly show that the dye is released to the solution using micromotors but resides in the sediment at the bottom (containing the inert microparticles). This behavior indicates that the Mg micromotors, which actively neutralize the gastric fluid, can trigger drug release. This behavior represents a distinct advantage of the based on the *in vitro* study which showed that the Mg micromotors were able to effectively neutralize gastric acid within this time window. As shown in Figure 2.9B, this experiment resulted in a clear dose-dependent gastric pH change. Herein, 5 milligrams of the Mg micromotor were able to neutralize gastric acid in the mouse stomach, thus resulting in pH 7.81 ± 0.38. This motor concentration was higher than the 2.75 mg per 3 mL gastric acid as observed in the *in vitro* study. Such an increase of the motor amount was likely due to the continuous secretion of gastric acid from gastric glands in the mouse stomach, as well as the dynamic peristalsis wave of the stomach tissue which counteracts and dilutes the pH neutralization efficacy of the micromotors. Lower and higher doses of Mg micromotors resulted in slightly acidic and alkaline stomach environments (pH 4.24 for 2.5 mg Mg micromotors and pH 9.43 for 10 mg Mg micromotors, respectively). Using deionized (DI) water as a control resulted in a constant acidic stomach pH (1.88), which further supports the fact that no pH neutralization occurs in the absence of Mg micromotors. Since 5 milligrams of the Mg micromotor can neutralize the gastric acid to about neutral value in the mouse stomach, this motor dosage was chosen for further studies.

Next, we studied the *in vivo* pH-responsive payload release by orally administrating fluorescently labeled Mg micromotors. DiD (1,1'-dioctadecyl-3,3,3',3'-tetramethyl-indodicarbocyanine perchlorate, Life Technologies) was chosen as a model drug, and was loaded onto the pH-sensitive polymer coating. After 20 minutes of administration, the entire stomach was excised and cut opened along the greater curvature for fluorescence imaging. As shown in Figure 2.9C, the stomach from mice treated with 5 milligrams of the Mg micromotor displays strong and evenly distributed fluorescence intensity over the entire stomach, thus reflecting the pH change resulting from the proton depletion by the active Mg micromotors. Apparently,

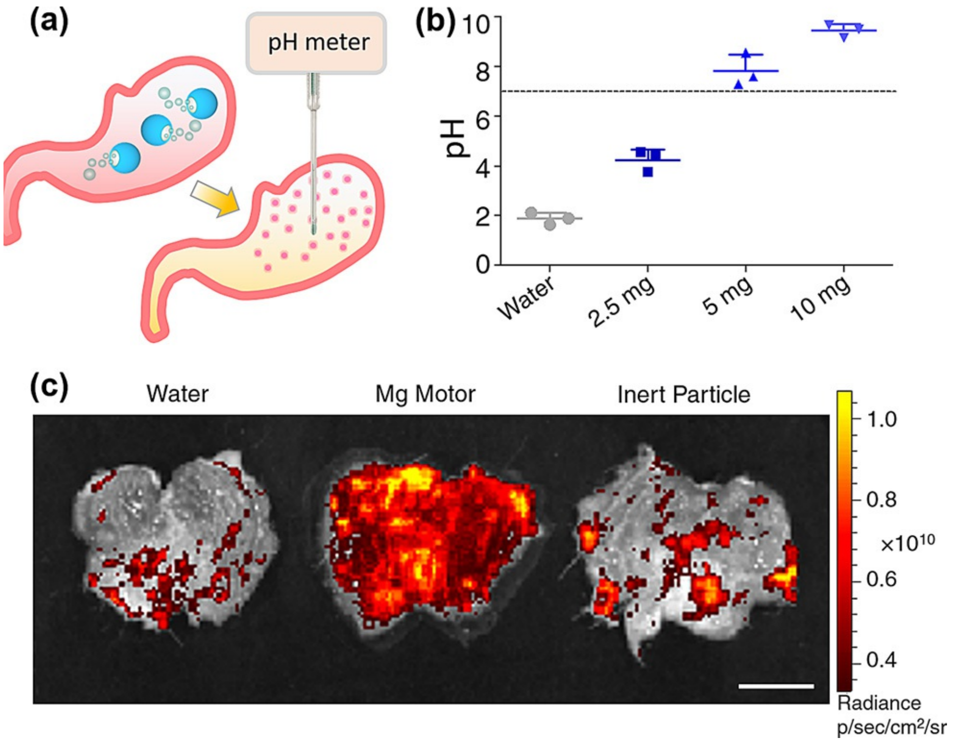

Figure 2.9: *In vivo* acid neutralization and pH-triggered payload release. (A) Schematic illustration of *in vivo* gastric acid neutralization process by Mg micromotors and pH measurement using a microelectrode-enabled pH meter. (B) *In vivo* gastric pH values using a mouse model (n = 3) measured 20 min post administration of different amounts of Mg micromotors. DI water was used as a negative control. (C) Superimposed fluorescent images, of the whole stomach of mice, collected 20 min post administration of DI water, Mg micromotors, and inert PS microparticles (both Mg micromotors and PS microparticles are loaded with DiD dye, which is encapsulated within the pH-sensitive polymer coating as a model drug). Scale bars: 5 mm.

the Mg micromotor delivery system can actively tune the stomach environment to facilitate dissolution of pH-sensitive polymer and release of the payload. In contrast, mice treated with an equal amount of inert PS microparticles displays only some small local areas of the stomach with low fluorescence signal, similar to the fluorescence signal observed using the DI water control, thus reflecting the self-fluorescence of the administered food. As expected, the inert PS microparticles do not alter the stomach pH, and hence cannot trigger dissolution of the pH-sensitive polymer and consequent payload release. Overall, in agreement with the early *in vitro* results, the data in Figure 2.9 demonstrate the ability of Mg micromotors to neutralize gastric acid in the stomach of live animals and trigger the dissolution of the pH-responsive polymer coating with subsequent payload release. The micromotor thus serves as a motile carrier which enhances transport of its payload to different locations. The efficient local propulsion, along with the corresponding bubble tail, have been shown to generate an effective convective fluid transport to substantially enhance the delivery of cargo compared to passive-diffusion systems. [259, 260] Furthermore, the propulsion of Mg micromotors provides a driving force to penetrate the mucus layer and enhance the payload retention in the stomach, and has been illustrated in early micromotor studies within the stomach and GI tract. [254, 255]

To ensure the recovery of gastric pH after Mg micromotor treatment, the pH of the stomach content was measured at 20 minutes and 24 hours after administration of the motors (Figure 2.10A). After the pH change induced by the Mg micromotor, the mean gastric pH returned to 2.16 within 24 hours post-treatment and is close to pH 1.88 of the control group which was treated with DI water. To further confirm the *in vivo* recovery of gastric pH, the pH indicator BCECF, with a $\mathrm{pK_a} \approx 6.98$, was employed. The stomachs were dissected along the greater curvature and excess gastric content was removed. BCECF fluorescence dye was evenly distributed and mixed with the gastric content on the stomach tissues. Fluorescence imaging of BCECF was performed on the different treatment groups (Figure 2.10B). When the environmental pH is greater than its $\mathrm{pK_a} \approx$, BCECF exhibits strong fluorescence emission, as shown by the stomach sample treated with micromotors for 20 minutes. In contrast, 24 hours after administrating the Mg micromotors, the gastric content labeled with BCECF indicator showed weak fluorescence intensity, thus reflecting the low pH conditions. The results from Figure 2.10 A,B designate the transient pH neutralization effect of the Mg micromotors and show that the normal acidity of gastric content can be recovered following the motor treatment.

Finally, the gastric toxicity of the administrated Mg micromotors was evaluated. 5 milligrams of either the Mg micromotor or DI water were orally administered to mice and they were monitored for general toxicity symptoms every 2 hours for the first 10 hours post-administration. No observable signs of pain such as hunched posture, unkempt fur, or lethargy were observed in either group. The Mg micromotor's toxicity was further investigated by histological analysis. Hematoxylin and eosin (H&E) stained cross-sections of glandular stomach from the micromotor-treated group showed intact glandular mucosa with no signs of superficial degeneration of columnar epithelial cells or erosion (Figure 2.11A). There was no observable difference in the either the crypt and villus size and number, or mucosal thickness between the motor-treated and water-treated groups. Moreover, lymphocytic infiltration into

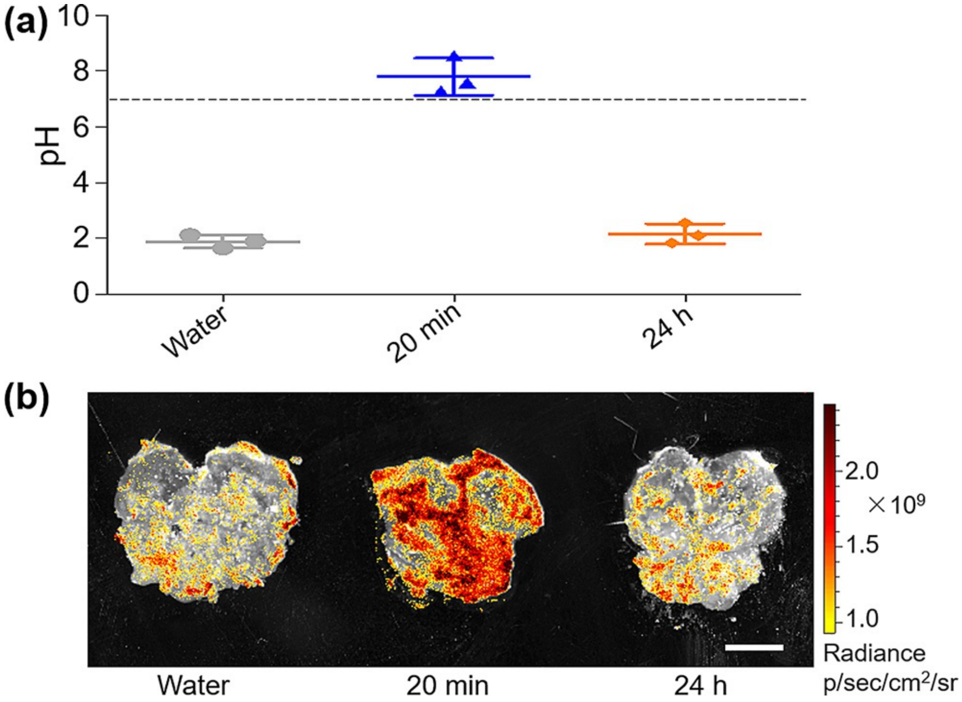

Figure 2.10: Recovery of the gastric pH post micromotor treatment. (A) *In vivo* gastric pH values using a mouse model (n = 3) measured 20 min and 24 h post administration of 5 mg of the Mg micromotor. Mice treated with water were used as a control. (B) Fluorescent images of the pH indicator BCECF superimposed on the entire stomach for the samples in (A).

the mucosa and submucosa was not apparent, thus implicating no sign of gastric inflammation. The potential toxicity of the Mg micromotors was further evaluated using gastric tissue sections in a terminal deoxynucleotidyl transferase mediated deoxyuridine triphosphate nick end labeling (TUNEL) assay to examine the level of gastric epithelial apoptosis as an indicator of gastric mucosal homeostasis. No apparent increase in gastric epithelial apoptosis was observed for micromotor-treated groups when compared to the water control group (Figure 2.11B). Overall, the *in vivo* toxicity studies demonstrate no interfer- ence in gastric pH homeostasis, and no apparent gastric histopathologic change or inflammation, thus suggesting that the oral administration of Mg micromotors is safe in a mouse model. The Mg micromotors can thus temporarily adjust the stomach pH without adverse effects, thus making them an attractive vehicle for gastric drug delivery.

2.2.4 Conclusions

We have demonstrated that acid-powered micromotors can operate as an active microdevice to efficiently and temporarily adjust local physiological parameters *in vivo* for diverse biomedical applications. In particular, the reaction of the motor's magnesium core with the gastric fluid leads to rapid proton depletion and thus acid neutralization without affecting the normal stomach function or causing adverse effects, thus making these synthetic micromotors an attractive alternative to proton pump inhibitors. The fast and efficient neutralization reflects the localized fluid convection generated by the micromotor movement. When coupled to a pH-sensitive payload-containing polymer coating, this pH change can lead to autonomous release

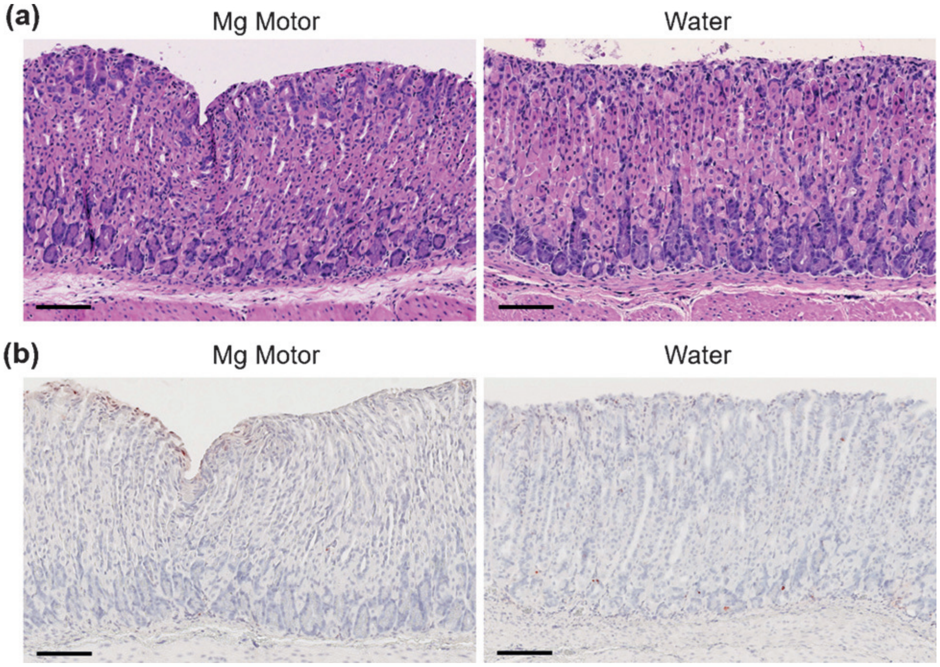

Figure 2.11: Toxicity evaluation of Mg micromotors. 5 mg of the Mg micromotor and DI water were orally administered to mice. After 24 h, mice were sacrificed and sections of the mouse stomach were processed and stained with (A) H&E assay and (B) TUNEL assay. Scale bars, 100 μm.

of the encapsulated cargo. The new microvehicle thus combines self-propulsion and acid neutralization along with cargo transport and release. Its Mg engine converts the acid fuel into a propulsion force and simultaneously alters the local pH to lead to payload release from the pH-sensitive coating. Such a micromotor-based delivery vehicle can thus actively adjust the local environment to achieve desired conditions for triggered payload release.

2.3 Micromotor-enabled active drug delivery for *in vivo* treatment of stomach infection

2.3.1 Introduction

Recent advances in the nano and micromotor field [261–264] in terms of improvement of biocompatibility and biological function have led to their growing use in biomedicine [265–267], including therapeutic payload delivery [268–273], microsurgery [274, 275], isolation of biological targets [276], operation within living cells [277, 278], and removal of toxicant molecules and organisms [279–281]. Although significant progress has been accomplished to demonstrate the *in vitro* capabilities of nano/micromotors to transport therapeutic cargos to target destinations, tremendous effort is still required to translate the proof-of-concept research to *in vivo* biomedical applications.

In recent years, the utility and performance of these motor-based active transport systems have been tested in live animals. For example, our group has demonstrated the attractive *in vivo* performance of zinc-based and magnesium (Mg)-based micromotors under *in vivo* conditions [282–284]. These studies have shown that artificial micromotors can self-propel in the stomach, and intestinal fluids for enhanced retention in the gastric mucous layer [282] and targeted delivery in the gastrointestinal (GI) tract [283]. Walker et al. [285] presented the ability of magnetic micropropellers to move through gastric mucin gels, by mimicking the mucus penetration strategy of *Helicobacter pylori* (*H. pylori*). In addition, Nelson's group has demonstrated that magnetically actuated microswimmers can swarm *in vivo* [271], whereas Martel's group has shown that microorganisms can be transformed into natural robots under magnetic guidance towards therapeutic cargo delivery into deep tumor regions [272]. These prior *in vivo* studies of synthetic motors have significantly advanced motor research and cleared a path towards direct evaluation of disease-oriented therapeutic efficacy associated with motor-enabled active drug delivery. However, this still remains an alluring but unmet goal for biomedical researchers.

This work demonstrates, to the best of our knowledge, the first attempt to apply Mg-based micromotors, loaded with antibiotic drug clarithromycin (CLR), for *in vivo* treatment of *H. pylori* infection in a mouse model. Given the built-in proton depletion function, this motor-based therapy is able to undergo the harsh gastric environment to achieve antibacterial efficacy without involving the commonly used proton pump inhibitors (PPIs). The *H. pylori* bacteria, found in about half of the world's population, can cause stomach infection and subsequently lead to diverse gastric and extragastric diseases [286, 287]. In most cases, the administration of antibiotics for the treatment of *H. pylori* infection is combined with the use of PPIs to reduce the production of gastric acid [288], because the gastric acid could make antibiotics less effective. The effectiveness of PPIs is attributed to the irreversible binding to proton pumps and thus to suppress acid secretion [289, 290], which in long term use can lead to adverse effects such as headache and diarrhea and in more serious scenarios cause anxiety or depression [291–294]. Therefore, it would be highly beneficial to develop an alternative therapeutic regimen with equivalent or advantageous therapeutic efficacy as the current antibiotic treatments while excluding the use of PPIs.

The reported Mg-based micromotors rely on the combination of a CLR-loaded poly(lactic-co-glycolic acid) (PLGA) layer and a chitosan polymer layer covering on a propellant Mg core to offer high drug-loading capacity, along with biodegradability. The positively charged chitosan outer coating enables adhesion of the motor onto the stomach wall [295], facilitating efficient localized autonomous release of CLR from the PLGA polymer coating. In contrast to acid suppression by PPIs, Mg-based micromotors can temporally and physically alter the local acidic environment by quickly depleting protons while propelling within the stomach [284]. By using acid as fuel, these synthetic motors rapidly deplete protons while propelling within the stomach, which can effectively elevate the gastric pH to neutral in < 20 min after the motors are applied [284]. Testing in a mouse model has demonstrated that these motors can safely and rapidly neutralize gastric acid without causing noticeable acute toxicity or affecting the stomach function, and that the normal stomach pH can be restored within 24h post motor administration. Such elimination of the PPI administration is coupled with significant reduction of bacteria burden, as demonstrated *in vivo* in a mouse model. Using a mouse model of *H. pylori* infection, the propulsion of the drug-loaded Mg-based micromotors in gastric fluid along with their outer chitosan layer are shown to greatly enhance the binding and retention of the drug-loaded motors on the stomach wall. As these micromotors are propelled in the gastric fluid, their Mg cores are dissolved, leading to self-destruction of these motors without harmful residues, as is demonstrated by the toxicity studies.

Overall, we take advantage of the efficient propulsion of Mg-based micromotors in the acidic stomach environment, their built-in proton depletion ability, their active and prolonged retention within the stomach wall, and their high drug-loading capacity, to demonstrate to the best of our knowledge the first actual *in vivo* therapeutic application of chemically powered micromotors. *in vivo* studies examine the therapeutic efficacy, distribution, and retention of the micromotors in the mouse stomach compared with passive drug-loaded microparticles and other control groups, along with the corresponding *in vivo* toxicity profile. These results illustrate the attractive therapeutic capabilities of acid-driven micromotors, which open the door for *in vivo* therapeutic applications of body-fluid propelled micromotors towards the treatment of a variety of diseases and disorders.

2.3.2 Experimental Methods

Synthesis of Mg-based micromotors.

The Mg-based micromotors were prepared using magnesium (Mg) microparticles (catalog # FMW20, TangShan WeiHao Magnesium Powder Co.; average size, 20 ± 5 μm) as the core. The Mg microparticles were initially washed with acetone to eliminate the presence of impurities. After being dried under a N_2 current, the Mg microparticles were dispersed onto glass slides (2 mg of Mg microparticles per glass slide), followed by ALD of TiO_2 (at 100 °C for 120 cycles) using a Beneq TFS 200 system. As such an ALD process utilizes gas phase reactants, it leads to uniform coatings over the Mg microparticles, whereas still leaving a small opening at the contact point of the particle to the glass slide. After that, the Janus micromotors were coated with 120 μL of 1% (w/v) PLGA (Sigma-Aldrich, P2191) prepared in ethyl acetate (Sigma-Aldrich, 270989) and containing 40 mg mL $^{-1}$ CLR (TCI CO., Ltd. C220). It should be noted that different CLR amounts (between 4 mg and 6 mg) were tested to optimize the drug-loading. The PLGA@CLR coating was dried fast to avoid crystallization of the drug. Finally, the Janus micromotors were coated with a thin layer of 0.05% (w/v) Chit (Sigma-Aldrich, C3646) prepared in water and containing 0.1% (w/v) sodium dodecyl sulfate (SDS) (Sigma-Aldrich, 62862) and 0.02% (v/v) acetic acid (Sigma-Aldrich, 695092), forming the outermost layer coated on the Mg microparticles. Finally, the Mg-based micromotors were collected by lightly scratching the microparticles off the glass slide.

Synthesis of dye-loaded Mg-based micromotors.

For performing the characterization of the Mg-based micromotors along with the *in vivo* retention studies, fluorescent Mg-based micromotors were prepared by combining both 1% PLGA and 0.05% Chit solutions with 5 μg mL $^{-1}$ 1,1'-dioctadecyl-3,3,3',3'-tetra- methylindodicarbocyanine, 4-chlorobenzenesulfonate salt (DiD, $\lambda_{\text{ex}} = 644$ nm/ $\lambda_{\text{em}} = 665$ nm, Life Technologies, D7757) and 1 μg mL $^{-1}$ fluorescein isothiocyanate- dextran (FITC, $\lambda_{\text{ex}} = 492$ nm/$\lambda_{\text{em}} = 520$ nm, Sigma-Aldrich, 46945) dyes, respectively. To compare with the Mg-based micromotors, inert silica (Si) microparticles (Nanocs, Inc., Cat. No. Si01-20u-1; 20 μm size) were used as core particles, following the same protocol described above.

Micromotor characterization.

Bright-field and fluorescent images of the Mg-based micromotors and inert silica microparticles were captured using a EVOS FL microscope coupled with a

20× and 40× microscope objectives and fluorescence filters for red and green light excitation. Scanning electron microscopy (SEM) images of the Mg-based micromotors were obtained with a Phillips XL30 ESEM instrument, using an acceleration voltage of 10 kV. EDX mapping analysis was performed using an Oxford EDX detector attached to SEM instrument and operated by INCA software.

Micromotor propulsion studies.

Autonomous Mg-based micromotors propulsion in simulated gastric fluid (Sigma-Aldrich, 01651) was obtained by diluting 25 times the simulated gastric fluid according to the commercial specifications (final pH 1.3), and adding 1% Triton X-100 (Fisher Scientific, FairLawn, NJ, USA) as surfactant. An inverted optical microscope (Nikon Eclipse 80i upright microscope) coupled with different microscope objectives (10× , 20× , and 40×) and a QuantEM:512SC camera were used for recording the autonomous micromotor propulsion in the gastric fluid simulant. The speed of the Mg-based micromotors was characterized using the MetaMorph 7.1 software (Molecular Devices, Sunnyvale, CA, USA).

***In vitro* anti-*H. pylori* activity.**

H. pylori Sydney strain 1 (HPSS1) was cultured from frozen stock and routinely maintained on Columbia agar supplemented with 5% (vol/vol) laked horse blood at 37 °C under microaerobic conditions (10% CO_2, 85% N_2, and 5% O_2). For experiments, broth cultures of *H. pylori* were prepared by subculturing fresh colonies from agar plates into brain-heart infusion (BHI) supplemented with 5% fetal bovine serum (FBS) and incubated overnight at 37 °C under microaerobic conditions with moderate reciprocal shaking. An overnight broth culture of *H. pylori* was centrifuged at 5000× g for 10 min to obtain a bacterial pellet. After removal of culture medium by centrifugation, the obtained bacteria pellet was then suspended in an appropriate amount of fresh BHI with 5% FBS for future use. The bactericidal activity against *H. pylori* of free CLR and CLR-loaded Mg-based micromotors (PLGA@CLR-TiO_2-Mg) were tested *in vitro*. All samples were treated in 0.1 N HCl for 1 h and serially diluted to desired concentrations with PBS (pH 7). Bare Mg-based micromotors (PLGA-TiO_2-Mg) with corresponding amount of micromotors were used as negative control. The samples were added with 1×10^6 CFU mL^{-1} *H. pylori* in BHI with 5% FBS to make final concentrations of 0-16 μg mL^{-1} CLR, followed by incubation at 37 °C under microaerobic conditions with moderate reciprocal shaking for 24 h. Then, a series of 10-fold dilutions of the bacterial suspension was prepared, and inoculated onto a Columbia agar plates supplemented with 5% laked horse blood. The plates were cultured for 4 days before the colony-forming unit (CFU) of *H. pylori* was quantified. All measurements were made in triplicate.

***in vivo* micromotor retention.**

Prior to the experiment, C57BL/6 mice (n = 3) were fed with alfalfa-free food from LabDiet (St Louis, MO, USA) for 2 weeks. The *in vivo* retention study was performed by using dye-loaded Mg-based micromotors prepared by the protocol described above. A 0.3 mL suspension of Mg-based micromotors with DiD-labeled PLGA and FITC-labeled chitosan coatings were intragastrically administered. A group of mice was administered with DI water as a negative control. Following 30 min and 2 h of oral administrations, the mice were killed and their entire stomachs were excised and cut opened along the greater curvature. Then, the tissues were rinsed with PBS, flattened, and visualized using a Keyence BZ-X700 fluorescence microscope. The bright-field and corresponding fluorescence images were obtained at 665 and 520 nm (DiD and FITC, respectively) for each sample. Subsequently, the tissues were transferred to 1 mL PBS and homogenized. Analysis of the amount of micromotors retained in the stomachs was carried out by measuring the fluorescence intensity of their embedded DiD-labeled PLGA and FITC-labeled chitosan using Synergy Mx fluorescent spectrophotometer (Biotek, Winooski, VT, USA). All animal experiments were in compliance with the University of California San Diego Institutional Animal Care and Use Committee (IACUC) regulations.

in vivo therapeutic efficacy against *H. pylori* infection.

Six-week-old C57BL/6 male mice were purchased from the Jackson Laboratory (Bar Harbor, ME, USA). Each C57BL/6 mouse received 0.3 mL of 1×10^6 CFU mL $^{-1}$ *H. pylori* in BHI broth administered intragastrically through oral gavage every 48 h, repeated three times (on day 3, 5, and 7, respectively), and the infection was allowed to develop for 2 weeks [296]. For the *in vivo* anti-*H. pylori* therapeutic study, mice were randomly divided in five treatment groups (n = 6) to be orally administered once daily for five consecutive days with CLR-loaded Mg-based micromotors, CLR-loaded inert silica microparticles, free CLR+PPI, blank Mg-based micromotors or DI water. For free CLR+PPI group, each day of treatment mice were first administered with omeprazole (a PPI) through oral gavage at a dose of 400 μmol kg^{-1} [296–299], followed by a lag time of 30 min before administration of CLR. CLR-loaded Mg-based micromotors, CLR-loaded inert silica microparticles and free CLR (with 30 mg kg $^{-1}$ CLR dosage) were also administered through oral gavage once daily for five consecutive days [296]. Blank Mg-based micromotors and DI water served as movement control and negative control, respectively. Forty-eight hours after last administration39, [300–302], mice were killed and stomachs were excised from the abdominal cavity. The stomachs were cut along the greater curvature, and the gastric content were removed and rinsed with PBS. For *H. pylori* recovery, each gastric tissue was weighed before suspended in 200 μL PBS and homogenized. The homogenate was serially diluted and spotted onto Columbia agar plate with 5% laked horse blood and Skirrow's supplement (10 μg mL $^{-1}$ vancomycin,5 μg mL $^{-1}$ trimethoprim lactate, and 2500 IU/L polymyxin B; Oxiod). The plates were then incubated at 37 °C under microaerobic conditions for 5 days, and bacterial colonies were enumerated. Statistical analysis was performed using one-way ANOVA. No statistical methods were used to predetermine sample size. Studies were done in a non-blinded fashion. Replicates represent different mice subjected to the same treatment (n = 6). All animal experiments were in compliance with the University of California San Diego Institutional Animal Care and Use Committee (IACUC) regulations.

Toxicity evaluation of Mg-based micromotors.

To evaluate the acute toxicity of the Mg-based micromotors *in vivo*, uninfected C57BL/6 male mice (n = 6) weighing 25-30 g were orally administered with CLR-loaded micromotors once daily for five consecutive days. Mice administered with DI water were tested in parallel as a negative control. During the experimental period, the mouse body weight was monitored by weighing the mice daily. On day 6, mice were killed and sections of the mouse stomach, small and large intestine tissues were processed for histological examination. The stomach was cut open along the greater curvature, and the gastric content was removed. The small and large intestines were cut to small sections as duodenum, jejunum, ileum, proximal, and distal colon and rinsed inside with PBS to remove internal residues. The longitudinal tissue sections were fixed in neutral-buffered 10% (vol/vol) formalin for 15 h, transferred into 70% ethanol, and embedded in paraffin. The tissue sections were cut with 5 μm thickness and stained with H&E assay. The stained sections were visualized by Hamamatsu NanoZoomer 2.0HT and the images processed using NDP viewing software. All animal experiments were in compliance with the University of California San Diego Institutional Animal Care and Use Committee (IACUC) regulations.

2.3.3 Results and Discussion

Drug-loaded Mg-micromotors preparation and characterization.

Figure 2.12A schematically illustrate the preparation steps of the drug-loaded Mg-based micromotors. The cores of the micromotors are made of Mg microparticles with an average size of 20 μm. In the study, a layer of Mg microparticles was dispersed onto a glass slide, followed by an asymmetrical coating of the microspheres with a thin TiO_2 layer using atomic layer deposition (ALD). The ALD process leads to a TiO_2 uniform coating over the Mg-microspheres, while leaving a small opening (essential for

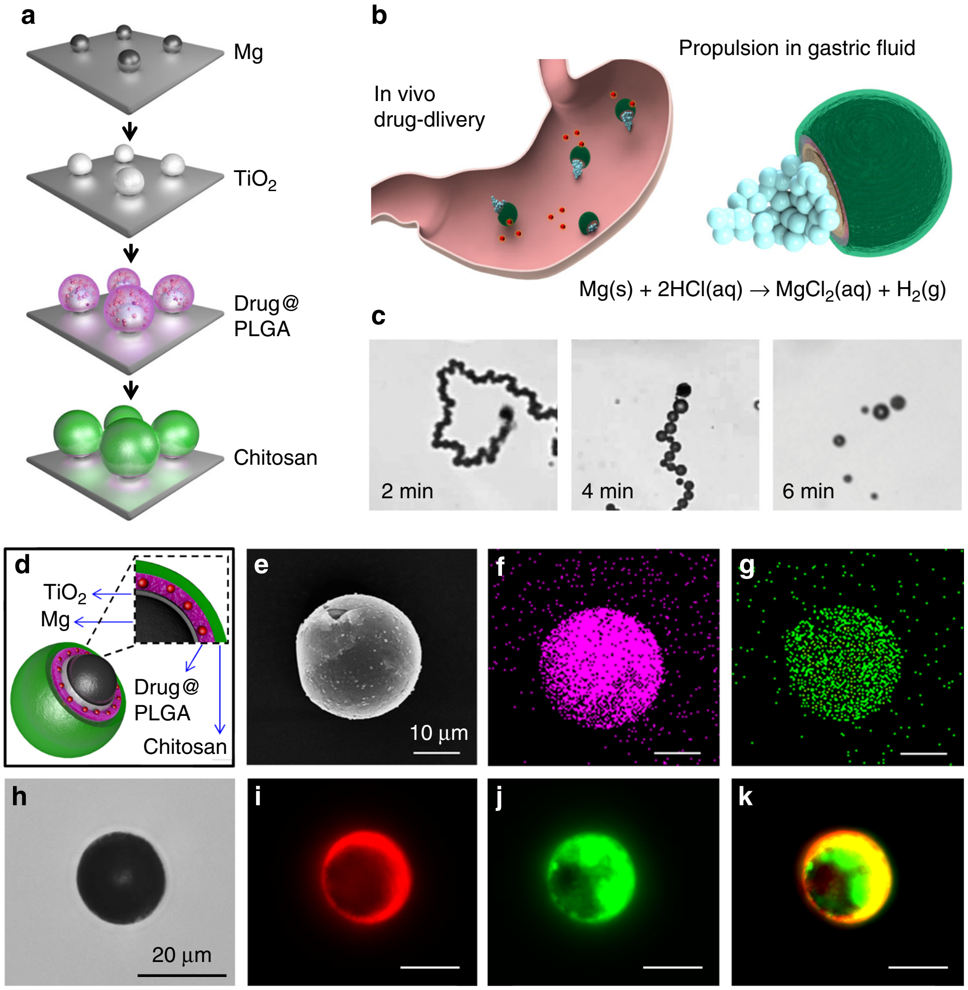

Figure 2.12: Synthesis and characterization of drug-loaded Mg-based micromotors. (A) Schematic preparation of the micromotors: Mg microparticles dispersion over a glass slide, TiO_2 atomic layer deposition (ALD) over the Mg microparticles, drug-loaded PLGA deposition over the Mg-TiO_2 microparticles, and Chitosan polymer deposition over the Mg-TiO_2-PLGA microparticles. (B) Schematic of in vivo propulsion and drug delivery of the Mg-based micromotors in a mouse stomach. (C) Time-lapse images of the propulsion of the drug-loaded Mg-based micromotors in simulated gastric fluid (pH 1.3). (D) Schematic dissection of a drug-loaded micromotor consisting of a Mg core, a TiO_2 shell coating, a drug-loaded PLGA layer, and a chitosan layer. (E) Scanning electron microscopy (SEM) image of a drug-loaded Mg-based micromotor. (F), (G) Energy-dispersive X-ray spectroscopy (EDX) images illustrating the distribution of (F) magnesium and (G) titanium in the micromotor. (H)-(K) Microscopy images of dye-loaded Mg-based micromotor: (H) optical image and fluorescence images showing the dye-loaded Mg-based micromotors in the (I) DiD channel (PLGA layer),(J) FITC channel (chitosan layer), along with an overlay of the two channels (K)

contact with the acid fuel) at the sphere-glass contact point [303], which forms a Janus microstructure. Such TiO_2 layer acts as a shell scaffold that maintains the micromotor spherical shape and the opening size during the propulsion, leading to consistent and prolonged operation. The Mg- TiO_2 Janus microparticles were then coated with a PLGA film containing the CLR antibiotic payload. After the drug-loading step, the microparticles were coated with an outer thin chitosan layer (thickness 100nm) that ensures efficient electrostatic adhesion of the micromotors to the mucosal layer on the stomach wall while protecting the CLR-loaded PLGA layer. Finally, the resulting CLR-loaded Mg-based micromotors were separated and collected by soft mechanical scratching of the glass slide, leaving a small opening for spontaneous Mg-acid reaction when the motors are placed in an acidic solution. This reaction generates hydrogen microbubbles and leads to efficient propulsion in the stomach fluid [284]. The small opening enables also a slow reaction process and gradual dissolution of the Mg core, leading to a prolonged micromotor lifetime of 6 min. The *in vivo* self-propulsion in the gastric fluid of a stomach and the corresponding drug delivery process from the PLGA layer of the Mg-based micromotors are illustrated schematically in Figure 2.12B. The ability of drug-loaded Mg-based micromotors to efficiently propel in gastric acid was first tested *in vitro* by using a simulated gastric fluid (pH 1.3). The microscopic images in Figure 2.12C illustrate the fast and prolonged autonomous propulsion of a CLR-loaded Mg-based micromotor in the gastric fluid simulant. The efficient hydrogen bubble generation propels the micromotors rapidly, with an average speed of 120 μm s $^{-1}$ (corresponding to a relative speed of 6 body lengths $^{-1}$), and indicates that the Mg-based micromotors can react and move fast in the gastric fluid. Such efficient micromotor propulsion is essential for the motors to reach stomach wall and thus achieving significant therapeutic efficacy. Importantly, the acid-Mg reaction responsible for the autonomous propulsion also spontaneously depletes protons in gastric fluid and thus neutralizes the stomach pH without using PPIs [284]. Figure 2.12D schematically illustrates the structure of a drug-loaded Mg-based micromotor, showing the Mg core, covered mostly with the TiO_2 shell layer, drug-loaded PLGA layer, and an outer chitosan layer. The drug-loaded Mg-based micromotors were carefully characterized. The scanning electron microscopy (SEM) image of a drug-loaded micromotor (shown in Figure 2.12E) confirms the presence of a small opening (2 μm) on the spherical micromotor, produced during the coating process, that exposes the Mg core of the micromotor to the gastric fluid and facilitates the hydrogen bubble thrust. Energy-dispersive X-ray (EDX) spectroscopy mapping analysis was carried out to confirm the motor composition. The resulting EDX images, shown in Figure 2.12F and 2.12G, illustrate the presence and distribution of magnesium and titanium, respectively. A fluorescence study was carried out to confirm efficient drug-loading within the PLGA layer, and the coating of the micromotor with the protective and adhesive chitosan layer. This was accomplished by preparing Mg-based micromotors with the PLGA and chitosan coatings containing the fluorescent dyes 1,1'-dioctadecyl-3,3,3',3'-tetramethylindodicarbocyanine, 4-chlorobenzenesulfonate salt (DiD, $\lambda_{\mathrm{ex}} = 665$ nm), and fluorescein isothiocyanate-dextran (FITC, $\lambda_{\mathrm{ex}} = 520$ nm), respectively. An optical image of a dye-loaded micromotor is displayed in Figure 2.12H. The corresponding fluorescence images show the dye-loaded Mg-based micromotor in the DiD and FITC channels (Figure 2.12I and 2.12J, respectively);

an overlay of the two channels is displayed in Figure 2.12K. The high-fluorescent intensity of the loaded dyes confirms the successful coating of the micromotor with both PLGA and chitosan layers, along with the high cargo-loading capacity of the micromotor.

Drug-loading optimization and *in vitro* bactericidal activity.

The CLR-loading onto the Mg-based micromotors was optimized to achieve a clinically relevant therapeutic concentration of the drug (15-30 mg kg $^{-1}$ day $^{-1}$)37. Figure 2.13A shows a schematic displaying the loading of CLR onto the micromotors. Briefly, the Mg- TiO_2 microparticles dispersed onto a glass slide (2 mg of Mg microparticles per glass slide) were coated with a PLGA solution prepared in ethyl acetate, which was mixed with CLR (see detailed experimental protocol in “Experimental Methods” section). Rapid evaporation under nitrogen current leads to the formation of a homogeneous PLGA-CLR coating over the Mg-TiO_2 microparticles (microscope images of the coated micromotors are displayed in Figure 2.13B). The microparticles were further coated with chitosan before quantifying the CLR-loading efficiency of the micromotors. To optimize the drug-loading, Mg-based micromotors were coated with PLGA solutions containing different amounts of CLR (between 4 and 6 mg). By studying different combinations of the PLGA-CLR solution volume and CLR concentration, the highest CLR-loading efficiency (26%), corresponding to 1032 ± 37 μg per 2 mg micromotor, was obtained when coating the microparticles with 120μL of the PLGA solution containing 4.8 mg of CLR (Figure 2.13C, II). This formulation offered optimal CLR-loading and was selected for subsequent *in vitro* and *in vivo* anti-*H. pylori* studies.

Once confirmed that the micromotors were capable to load antibiotic cargo with high-loading efficiency, an *in vitro* bactericidal activity of CLR-loaded Mg-based micromotors against *H. pylori* was performed. To mimic the gastric environment, samples were treated in 0.1 N HCl for 1 h prior to incubation with bacteria. This also ensured the dissolution of micromotors and consecutive drug release. Figure 2.13D shows the enumerated amount of bacteria after being treated by CLR-loaded Mg-based micromotors or free CLR solution with varying concentrations of CLR. According to the results, drug-loaded micromotors exhibited a comparable bactericidal activity to free drug solution over the whole range of concentrations used in the study. Specifically, we determined the minimal bactericidal concentration (MBC) values of the samples, defined as the minimal concentration of an antimicrobial agent that kills 3 logs (99.9%) of the bacteria. The MBC value for CLR-loaded Mg-based micromotors was found to be 0.25 μg mL $^{-1}$, which was unaltered from the MBC value of free CLR. Moreover, bare Mg-based micromotors, with corresponding amount of motors and treated under the same conditions as the free CLR and CLR-loaded Mg-micromotors, were used as negative controls. From Figure 2.13D, the bare motors had negligible effect on the viability of *H. pylori* over the studied range, which supports that the bactericidal effect of CLR-loaded Mg-based micromotors is solely due to the loaded antibiotics, and not due the other compositions of the micromotor carrier or the micromotor acidic environment. Overall, Figure 2.13D verifies that the activity of the loaded drug was not compromised compared to free drug. Our *in vitro* results verified also that drug-loaded micromotors, made of Mg and other degradable materials, eventually

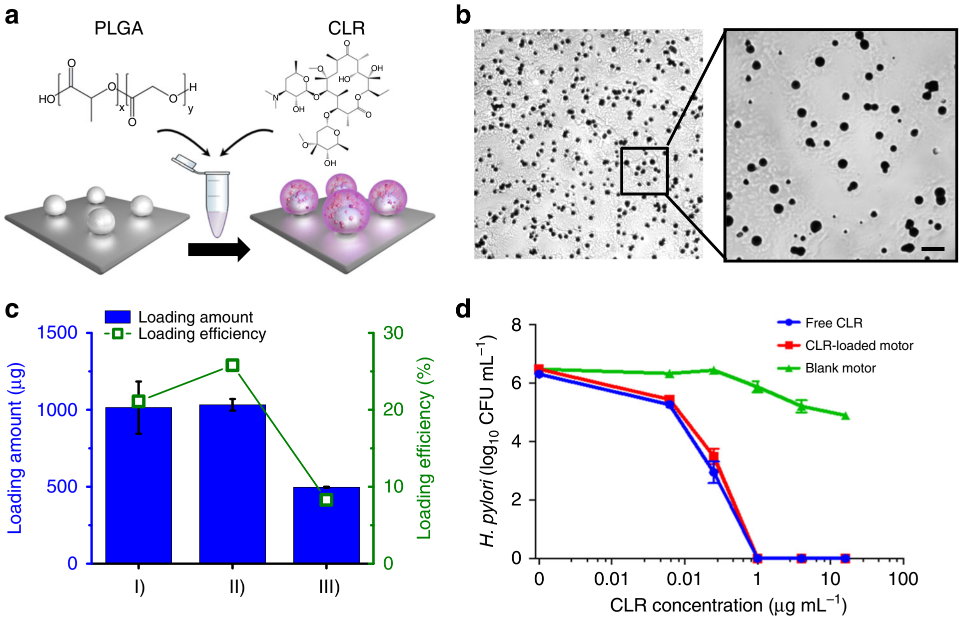

Figure 2.13: Antibiotic drug loading of the Mg-based micromotors and *in vitro* bactericidal activity. (A) Schematic displaying the loading clarithromycin (CLR) onto the Mg-based micromotors. PLGA polymer dissolved in ethyl acetate is mixed with CLR, and the solution is deposited over the Mg-TiO_2 microparticles resulting in the formation of a thin PLGA-CLR coating. (B) Microscope images showing the PLGA-CLR film over the Mg-based micromotors. Scale bars 100 μm and 40 μm, respectively. (C) Quantification of CLR-loading amount and yield of the micromotors prepared with different CLR solutions: (I) 100 μL of 40 mg mL^{-1} CLR solution, (II) 120 μL of 40 mg mL^{-1} CLR solution, and (III) 200 μL of 30 mg mL^{-1} CLR solution. All the CLR-loaded Mg-based micromotors were coated with a thin chitosan layer; all samples were dissolved in acid for 24 h before the drug-loading measurement. (D) In vitro bactericidal activity of free CLR, CLR-loaded Mg-based micromotors, and blank Mg-based micromotors (without CLR drug) against *H. pylori* bacteria. Error bars estimated as a triple of s.d. ($n = 3$)

destroy themselves and disappear in the acidic environment after releasing the CLR, with no apparent residues in the tissue. The findings validate the potential use of these drug-loaded micromotors for therapeutic applications.

In vivo **micromotor retention in mouse stomach.**

After the optimization of drug-loading onto the Mg-based micromotors and the confirmation of effective *in vitro* bactericidal activity, the micromotors were further investigated under *in vivo* setting. First, the *in vivo* retention properties of the Mg-based micromotors on stomach tissue were examined at different post-administration times, and compared with control groups administered with DI water (Figure 2.14). For this purpose, Mg-based micromotors prepared with DiD-labeled PLGA and FITC-labeled chitosan coatings were administered to a group of mice (n = 3), and following 30 min and 2 h of the samples administration, the mice were killed and the entire stomach was excised and opened. Subsequently, the luminal lining was rinsed with PBS and flattened for imaging. Accordingly, Figure 2.14A shows bright-field and fluorescence images of the luminal lining of freshly excised mouse stomach at 0 min after oral gavage of DI water, and at 30 min and 2h after oral gavage of Mg-based micromotors. As can be observed, the images corresponding to the dye-loaded Mg-based micromotors show an intense fluorescent signal in both red and green light channels, which indicates efficient distribution and retention of the micromotors in the mouse stomach. The continuous propulsion of the micromotors and the adhesive properties of the chitosan coating help to achieve a homogeneous distribution of the micromotors in the stomach. The corresponding fluorescence

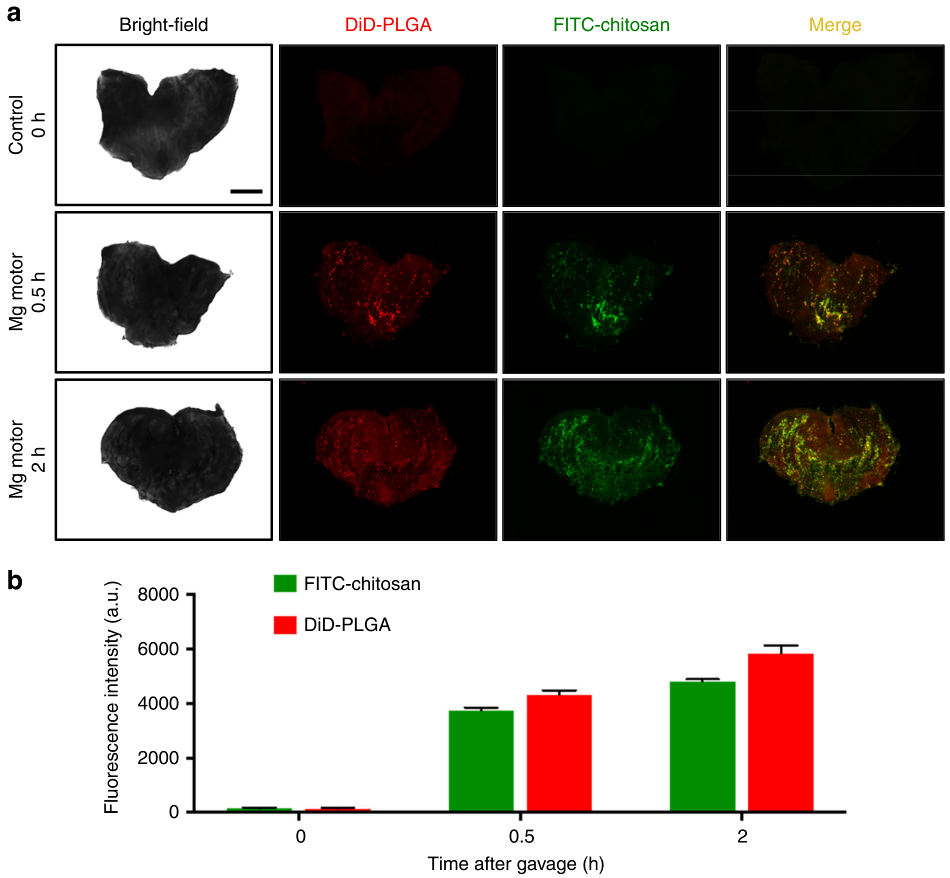

Figure 2.14: Retention of the Mg-based micromotors in mouse stomachs. (A) Bright-field and fluorescence images of the luminal lining of freshly excised mouse stomachs at 0 min after oral gavage of deionized (DI) water (control), and at 30 min and 2 h after oral gavage of the Mg-based micromotors. Scale bar 5 mm. (B) Corresponding fluorescence quantification of all the images shown in (A). Error bars estimated as a triple of s.d. (n = 3)

quantification of the dye-loaded micromotors retained in the mouse stomach after 30 min and 2 h oral gavage of the sample is displayed in Figure 2.14B. The graphic represents the higher fluorescence signals obtained at 665 and 520 nm (corresponding to DiD and FITC dyes, respectively) for each sample. These results indicate that the micromotors can effectively propel in gastric fluid and are retained in the stomach wall, including the antrum, where the *H. pylori* bacteria reside. Such highly enhanced retention in the stomach, which is a major advantage of motor-enabled delivery, has been carefully examined in our early studies [282–284]. The powerful propulsion leads to tissue penetration and binding, so that the drug-loaded motor could reach the whole stomach wall for enhanced retention.

***In vivo* anti-*H. pylori* therapeutic efficacy.**

We proceeded to test the *in vivo* therapeutic efficacy of the drug-loaded Mg-based micromotors against *H. pylori* infection. Prior to the therapeutic study, we developed *H. pylori* infection in a mouse model using C57BL/6 mice. Each mouse was inoculated with 3×10^8 CFU *H. pylori* SS1 in brain-heart infusion (BHI) broth by oral gavage three times on day 3, 5, and 7 (Figure 2.15A) [296, 304]. Two weeks after inoculation, the *H. pylori*-infected mice were divided into five groups ($n = 6$, for each group) and orally administered with DI water, blank Mg-based micromotors (without CLR drug), free CLR drug with PPI (CLR+PPI), CLR-loaded silica microparticles, or CLR-loaded Mg-based micromotors once a day for five consecutive days. On each day of treatment, mice in the free CLR+PPI group received 400 μmol kg $^{-1}$ of omeprazole (as PPI treatment) 30min before administrating CLR, to neutralize gastric acid and

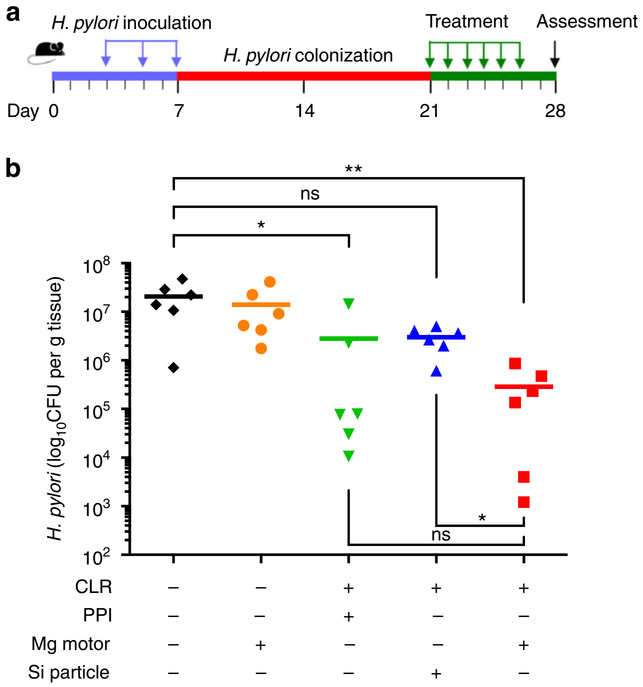

Figure 2.15: *In vivo* anti-H. pylori therapeutic efficacy. (A) The study protocol including *H. pylori* inoculation and infection development in C57BL/6 mice, followed by the treatments. (B) Quantification of bacterial burden in the stomach of H. pylori-infected mice treated with DI water (black color), bare Mg-based micromotors (orange color), free CLR+PPI (green color), CLR- loaded silica microparticles (blue color), and CLR-loaded Mg-based micromotors (red color), respectively ($n = 6$ per group). Bars represent median values. $*P < 0.05$, $**P < 0.01$, ns no statistical significance

prevent potential degradation of CLR. Such PPI dosage has been reported to be effective both in reducing the gastric acidity in mouse models [297], as well as in preserving the effectiveness of co-administered antibiotics [296, 298, 299]. After the treatment course, the bacterial burden was evaluated by enumerating and comparing *H. pylori* counts recovered from each mouse stomach. The mean bacterial burden from two negative control groups treated with DI water and blank Mg-based motors were 2.1×10^7 and 1.4×10^7 CFU g $^{-1}$ of stomach tissue, respectively (Figure 2.15B, black and orange color, respectively). Meanwhile, a bacterial burden of 3×10^6 CFU g $^{-1}$ was measured from the mice treated with CLR-loaded silica microparticles, which did not show statistical difference to the negative controls. In contrast, when the mice were treated with CLR-loaded Mg-based micromotors, the bacterial burden was quantified as 2.9×10^5 CFU g $^{-1}$, a significant reduction compared with the negative control and CLR-loaded silica microparticle groups. The substantial improvement in *H. pylori* reduction demonstrates the benefit of acid-powered Mg-based micromotors compared with static micron-sized carriers. A bacterial burden of 2.8×10^6 CFU g $^{-1}$ was obtained for the positive control mice with free CLR+PPI treatment. Although the difference between CLR-loaded Mg-based micromotors and the free CLR+PPI groups was not statistically significant, the CLR-loaded micromotors reduced the *H. pylori* burden in mice compared with in the negative controls by 1.8 orders of magnitude, whereas the free CLR+PPI group reduced it only by 0.8 orders of magnitude. These results might be derived from the benefit of the propulsion-enabled active drug delivery performed by the Mg-based micromotors in the stomach. These results demonstrate that the Mg-based micromotors can effectively propel and distribute throughout the stomach of living mice to significantly reduce *H. pylori* levels.

***In vivo* toxicity evaluation of Mg-based micromotors**

Finally, the toxicity profile of the Mg-based micromotors in the stomach as well as in the lower GI tract was evaluated. Healthy mice were orally administered with Mg-based micromotors or DI water once daily for five consecutive days. Throughout the treatment, no signs of distress such as squinting of eyes, hunched posture, unkempt fur, or lethargy were observed in both groups. Initially, the toxicity profile of the Mg-micromotors in the mouse was evaluated through changes in body weight. During the experimental period, mice administered Mg-micromotors maintained a constant body weight compared with the mice administered DI water (Figure 2.16A). On day 6, mice were killed and their stomachs and lower GI sections were processed for histological staining. Longitudinal sections of the glandular stomach (Figure 2.16B), three major segments of small intestine (duodenum, jejunum, and ileum, Figure 2.16C-2.16E, respectively) and the two major segments of large intestine (proximal and distal colon, Figure 2.16F-2.16G, respectively) were stained with hematoxylin and eosin (H&E). The stomach and lower GI sections of the micromotor-treated group showed undamaged structure of columnar epithelial cells with no signs of superficial degeneration or erosion (Figure 2.16B-2.16G, left). There was no noticeable difference in the gastric and intestinal mucosal integrity, in terms of thickness as well as size and number of crypt and villus, between the motor-treated and DI water-treated groups (Figure 2.16B-2.16G, left vs. right part). No lymphocytic infiltration into

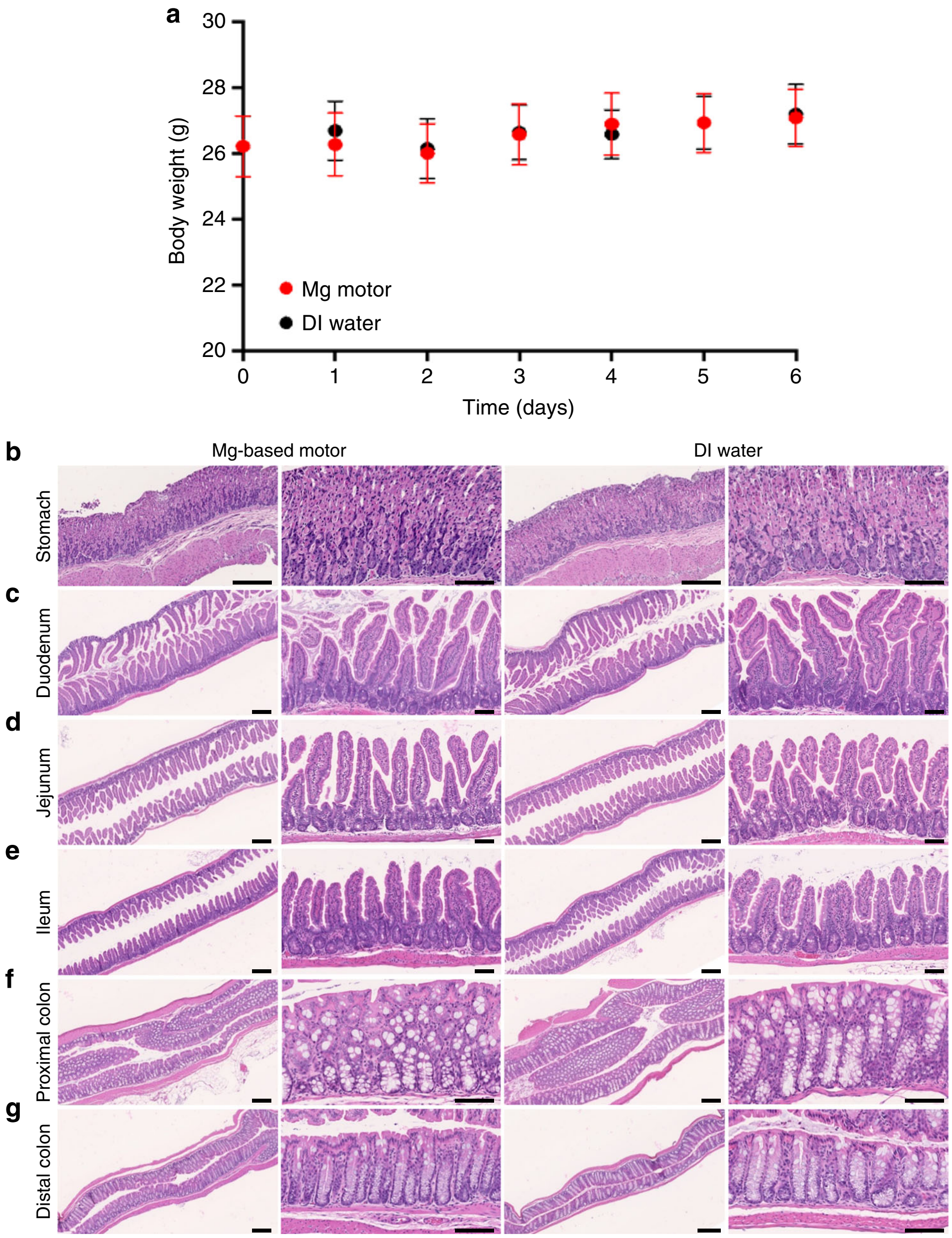

Figure 2.16: *In vivo* toxicity evaluation of the Mg-based micromotors. Uninfected mice were orally administered with the Mg-based micromotors or DI water once daily for five consecutive days. (A) Mouse body weight log from day 0 to day 6 of the toxicity study. Error bars represent the s.d. of the mean (n = 6). On day 6, mice were killed and sections of the mouse stomach (B), small (C)-(E) and large (F), (G) intestine tissues were processed for histological staining with hematoxylin and eosin (H&E). Scale bars Mg-motor, 250 and 100 μm (left and right column, respectively); DI water, 250 and 100 μm (left and right column, respectively)

the mucosa and submucosa was observed, indicating no sign of gastric inflammation. The *in vivo* toxicity studies of Mg-based micromotors showed no effect on the mouse body weight, apparent alteration of GI histopathology or observable inflammation, suggesting that the treatment of Mg-based micromotors is safe in the mouse model.

2.3.4 Conclusions

In this work we conducted the first, to the best of our knowledge, study to evaluate the therapeutic efficacy of a drug-loaded Mg-based micromotor for *in vivo* treatment of *H. pylori* infection in a mouse model. Through these *in vivo* experiments, we demonstrated that acid-powered Mg-based micromotors could efficiently be loaded with clinical doses of drugs, retain in the mouse stomach wall, and perform an appreciable *in vivo* bactericidal activity. Our results showed that the active propulsion of drug-loaded Mg-based micromotors in the acidic media of the stomach and motor-tissue interaction lead to efficient drug delivery and hence to a significant reduction of bacteria burden compared to passive drug carriers. Furthermore, such drug-loaded micromotors function in gastric condition for the *H. pylori* infection treatment without the need of PPIs. We also demonstrated that there were no toxicological con- sequences of the micromotors in the mouse models. Overall, our results indicate that micromotors may be adapted to the development of new and safe therapeutic treatments against stomach diseases such as *H. pylori* infection. As our early studies have shown that the Mg-based micromotors can propel efficiently and position precisely in the GI tract [283, 284], we believe the presented motor-enabled delivery approach is promising to treat diverse GI tract diseases. Extending the propulsion methods with new alternative biocompatible fuels [305, 306] or fuel-free actuation [271–273] might be able to expand the active-delivery concept to different parts of the body. We also envision that the micromotor approach will be useful for eliminating hard-to-treat bacterial biofilms, [307, 308] with the efficient motor propulsion leading to biofilm penetration towards enhanced antibiotic delivery. Although the present results are promising, this work is still at its early stage. As a new active gastric delivery technology, future studies are required to further elucidate the micromotor's *in vivo* delivery performance and functions, and to compare with other standard therapies against *H. pylori* infection or other gastric diseases. Nonetheless, this work opens the door to the use of synthetic motors as an active-delivery platform for *in vivo* treatment of diseases and will likely trigger intensive research interests in this area.

Chapter 2.1, in full, is a reprint of the material as it appears in Advanced Therapeutics, 2018, Pavimol Angsantikul, Soracha Thamphiwatana, Qiangzhe Zhang, Kevin Spiekermann, Jia Zhuang, Ronnie Fang, Weiwei Gao, Marygorret Obonyo, and Liangfang Zhang. Chapter 2.2, in full, is a reprint of the material as it appears in Angewandte Chemie International Edition, 2017, Jinxing Li, Pavimol Angsantikul, Wenjuan Liu, Berta Esteban-Fernández de Ávila, Soracha Thamphiwatana, Mingli Xu, Elodie Sandraz, Xiaolei Wang, Jorge Delezuk, Weiwei Gao, Liangfang Zhang, Joseph Wang. Chapter 2.3, in full, is a reprint of the material as it appears in Nature Communications, 2017, Berta Esteban-Fernández de Ávila, Pavimol Angsantikul, Jinxing Li, Miguel Angel Lopez-Ramirez, Doris E. Ramírez-Herrera, Soracha Thamphiwatana, Chuanrui Chen, Jorge Delezuk, Richard Samakapiruk, Valentin Ramez, Marygorret Obonyo, Liangfang Zhang, and Joseph Wang. The dissertation author was either the primary investigator or co-primary investigator and co-author of these papers.

Chapter 3

Biointerfacing via cell membrane-coated nanoparticles for novel pathologic countermeasure applications

3.1 Neutralization of cholera toxin with nanoparticle decoys for treatment of cholera

3.1.1 Introduction

Diarrheal diseases are a major cause of morbidity and mortality in developing regions, with an estimated 3-5 million cases and over 100,000 deaths per year [309,310]. Diarrhea accounts for 1 in 9 childhood deaths worldwide, making it the second leading cause of death among children under the age of five. As an example, in diarrheal patients attending a hospital in Mirpur, Bangladesh, *Vibrio cholerae* was found to be the causative agent of diarrheal disease in 23% of patients [311]. Current treatments involve rehydration with oral or intravenous replacement electrolyte solutions [312, 313]. While this method has reduced mortality rates in children with acute diarrheal diseases, in general, stool volume and diarrheal durations are not decreased [314]. Administration of antibiotics in conjunction with electrolyte solutions can reduce the volume and duration of diarrhea [315], but extensive use of antibiotics may lead to the emergence of antibiotic-resistant strains of bacteria, threatening the utility of existing antibiotics [316]. Therefore, an urgent need exists to develop alternative treatments.

V. cholerae is usually contracted through ingestion of contaminated water or food in which the bacterium is present [313]. While bacterial colonization is limited to the lumen and epithelial surface of the intestinal tract, the disease symptoms are primarily caused by bacterially produced toxins. Most prominently, *V. cholerae* secretes cholera toxin (CT), which is composed of an A subunit responsible for toxicity and a pentameric B subunit (CTB) responsible for receptor binding [317]. CTB binds to GM1 gangliosides on the surface of intestinal epithelial cells, which subsequently leads to endocytosis of the entire protein complex [318]. The A1 subunit (CTA1) is cleaved from the rest of the toxin through the reduction of a disulfide bond [319]. CTA1 then catalyzes ADP-ribosylation of the $G_{S\alpha}$ protein [320], leading to its activation, stimulation of adenylyl cyclases, and a sustained increase in epithelial cyclic AMP levels [321]. This series of events culminates in a massive efflux of chloride ions and an inhibition of sodium absorption by the epithelium, which leads to the rapid outflow of water into the intestinal lumen, and the attending severe diarrhea and dehydration [322].

Since the GM1 ganglioside host receptors play a key role in the CT-mediated pathogenesis of cholera, it constitutes an attractive target for novel antimicrobial strategies [323]. The recent emergence of nanotechnology is beginning to have a profound impact on modern medicine [324]. Nanoparticle systems have shown to be superior in facilitating drug solubility, systemic circulation, and drug release, and in their ability for differential cell targeting compared to free drugs [325, 326]. In addition, nanoparticles can be engineered to serve as decoys or sinks for microbial toxins, opening up new possibilities for treating toxin-mediated diseases [327, 328]. To determine whether this concept can be applied to cholera as a prototypic model for intestinal diseases caused by enterotoxins, we set out to develop a nanotechnology-based strategy for CT neutralization and treatment of cholera. The work described here demonstrates that nanoparticle decoys are a promising new therapeutic avenue for toxin-mediated diarrheal diseases.

3.1.2 Experimental Methods

Ethics statement

Laboratory mice were used for parts of the study. Anesthesia was done with isoflurane inhalation, and buprenorphine was given before surgery for preventive pain management. Mice were euthanized by CO_2 inhalation and cervical dislocation. All animal studies were reviewed and approved by the UC San Diego Institutional Animal Care and Use Committee.

Preparation of nanoparticles

GM1 ganglioside-coated poly(lactic-co-glycolic acid) (PLGA) hybrid nanoparticles (GM1-NPs) were prepared by nanoprecipitation as previously described [326,329] with several modifications. Briefly, a PLGA stock solution was prepared by dissolving PLGA pellets (LACTEL Absorbable Polymers, Pelham, AL) in acetonitrile at a concentration of 2.5 mg/mL. A GM1 ganglioside stock solution was prepared by dissolving GM1 (Carbosynth, San Diego, CA) in deionized water at 10 mg/mL. To prepare the aqueous phase for GM1-NP synthesis, the desired amount of GM1 stock solution was added into deionized water to yield a final GM1 concentration of 10% (w/v) of the PLGA polymer. A predetermined volume of the PLGA solution was then added dropwise (1 ml/min) into the aqueous GM1 solution under gentle stirring. The nanoparticles were allowed to self-assemble for 2 h with continuous stirring while the organic solvent was allowed to evaporate under vacuum. To remove the remaining free molecules and organic solvent, the nanoparticle suspensions were washed in deionized water three times using an Amicon Ultra centrifuge filter

(Millipore, Billerica, MA) with a molecular weight cut-off of 100 kDa. Nanoparticles were resuspended in deionized water and used immediately or stored at 4°C (up to 4 weeks) for later use. As a control, PLGA nanoparticle cores (PLGA-NPs) were prepared with the nanoprecipitation method described above, but without GM1 in the aqueous solution. As another control, polyethylene glycol (PEG) modified PLGA nanoparticles (PEG-NPs) were fabricated with a coat of 1,2-distearoyl-sn-glycero-3-phosphoethanolamine-N-[methoxy(polyethylene glycol)- 2000] (DSPE-mPEG2000; average molecular weight 2.8 kDa, Laysan Bio, Inc., AL) through nanoprecipitation as previously described [329]. The aqueous phase contained a DSPE- mPEG2000 concentration of 10% (w/v) of the PLGA polymer. All stated concentrations for nanoparticles refer to the concentration of the PLGA polymer in the respective formulation.

Physical characterization of nanoparticles

Nanoparticle stability was analyzed in deionized water and phosphate-buffered saline (PBS). For stability in water, nanoparticles were synthesized as described above at a final polymer concentration of 1 mg/mL. To test the stability in PBS, nanoparticles at 2 mg/mL in water were added to an equal volume of 2 × PBS. Particle size distribution and zeta-potential were measured by dynamic light scattering using a Malvern ZEN 3600 Zetasizer. Transmission electron microscopy of nanoparticles was done by depositing a suspension (2 mg/mL) on a glow-discharged, carbon-coated 400-mesh copper grid. The grid was washed with distilled water and stained with 1% (w/v) uranyl acetate. Imaging was carried out on a Zeiss Libra 120 PLUS energy filter transmission electron microscope.

Cholera toxin binding studies

Binding of FITC-labeled CTB (Sigma-Aldrich, St. Louis, MO) was tested by incubating the different nanoparticle suspensions with 10 μg/mL CTB in in 400 μl of PBS (pH 7.2) for 30 min. Each sample was transferred to an Amicon Ultra centrifuge filter and centrifuged at 8,000 rpm in a Beckman Coulter microfuge 22R centrifuge for 5 min. Fluorescence was determined using a Synergy Mx fluorescent spectrophotometer (Biotek, Winooski, VT). Bound CTB was calculated with the formula: CTB bound (%) = (1 - CTB in supernatant/total CTB input) × 100%. All experiments were performed in triplicate. Bound CTB was plotted against nanoparticle concentrations, and a curve was fitted with the binding-saturation equation in GraphPad Prism.

To investigate the CT binding and neutralization capability, 400 μl of PBS solution containing 1 or 0.25 mg/mL of nanoparticles was mixed with 5 μl of different concentrations of FITCTB, and incubated for 30 min at 37°C . Each sample was processed as described above, and bound CTB was calculated, plotted against CTB input concentrations, and fitted with a binding-saturation equation. To determine the binding capacity of different nanoparticle formulations, 400 μl of PBS solution containing 1 mg/mL of GM1-NPs or PEG-NPs were incubated with 10 μg/mL CTB for 30 min at 37°C . CTB incubated in PBS solution was used as the negative control. Each sample was processed and analyzed as described above, and the bound CTB was calculated.

To determine stability of toxin binding to the nanoparticles, 1 ml of a PBS solution containing 1 mg/mL of GM1-NPs was incubated with 10 μg/mL FITC-CTB for 30 min at 37°C . The sample were transferred to an Amicon Ultra centrifuge filter and centrifuged at 8,000 rpm for 5 min, and the CTB-loaded nanoparticles were resuspended in 1 ml of a pool of undiluted luminal content obtained from the small intestine of several male and female adult C57BL/6 mice. After 24 h incubation at 37°C , particles were dialyzed for 24 h against a PBS solution using a PTFE Dialyzer (Harvard Apparatus) and Nucleopore hydrophilic membrane (Whatman) with a molecular weight cut-off of 200 kDa. Retention of FITC-CTB on the nanoparticles was measured by fluorescence spectroscopy. GM1-NPs incubated in PBS and free CTB incubated in luminal content were used as positive and negative (background) control, respectively. Data are expressed as bound FITC-CTB after 24 h relative to the initial amount bound before incubation. Experiments were done in triplicate.

Confocal microscopy of nanoparticles

To visualize nanoparticles and toxin colocalization, fluorescently-labeled GM1-NPs and PEG-NPs were prepared using 1,1'-dioctadecyl-3,3,3',3'-tetramethylindodicarbocyanine perchlorate fluorescent dye (DiD; excitation/emission 644/665 nm; Life Technologies, Carlsbad, CA) for incorporation into the polymer solution at a concentration of 10 μg/mL during the preparation. Labeled GM1-NPs and PEG-NPs (1 mg/mL) were then incubated with 10 μg/mL CTB as described for the toxin binding studies. After 30 min incubation, nanoparticle solutions were washed three times in deionized water using an Amicon Ultra centrifuge filter, and the samples were visualized by confocal fluorescence microscopy using an Olympus FV1000 microscope with a 100x oil objective. To obtain stable images, the particles were dispersed in glycerol to significantly decrease their spontaneous movements.

Cell culture studies

Vibrio cholerae strain N16961 (serogroup O1, biovar El Tor; ATCC) was grown overnight at 37°C in Luria Bertani broth supplemented with trimethylamine N-oxide without agitation at 37°C in an atmosphere of 5% CO_2 and 95% air. These conditions have been shown to induce CT expression [330]. Human HCA7 colon cancer cells (ATCC) were grown in 75-cm^2 culture flasks in Dulbecco's modified Eagle's medium (DMEM) supplemented with 10% fetal bovine serum and 1% penicillin-streptomycin at 37°C in 5% CO_2 and 95% air. Cells were plated into 48-well plates at 5×10^5 cells/well, and monolayers were grown overnight before experiments.

For toxin neutralization, we mixed different concentrations of CT (List Biological Laboratories, Campbell, CA) and nanoparticles, incubated for 1 h, and added the mixture to the cell monolayers. After 2 h, supernatants were collected and assayed for cAMP by enzyme immunoassay (Cyclic AMP ELISA Kit, Cayman Chemical Co., Ann Arbor, MI). All cAMP measurements were done without additional acetylation.

For neutralization experiments with live bacteria, nanoparticles were added to epithelial cell monolayers, which were then immediately inoculated with *V. cholerae* at a multiplicity-of- infection of 30, as determined by measuring optical density at 600 nm (OD_{600}). After 2 h of infection, cAMP levels were determined in the supernatants by enzyme immunoassay.

Intestinal ligated loops

Ligated loops of the middistal small intestine were prepared in anesthetized adult C57BL/6 mice as described previously [331]. Briefly, mice were fasted for 4-6 h before anesthesia and surgery, and given 0.1% buprenorphine for preventive pain management. After shaving and disinfection of the abdomen, a small abdominal incision was made, and a small intestinal loop was identified and ligated with two small surgical clips placed 2-3 cm apart. Agents were injected into the loop with a 30G needle in a 200 μl volume, and the abdominal cavity was closed with sutures. Loops were excised at different times, and the luminal loop volume was determined and related to the length of the loop. For CT tests, a solution of 12.5 μg/mL CT was incubated with and without 250 μg/mL GM1-NPs or PEG-NPs for 1 h at room temperature, and the mixture, or PBS as a control, was injected into the ligated loops. For tests with live bacteria, *V. cholerae* were prepared as described above, and injected in modified Luria Bertani broth at 10^5 bacteria per loop, either alone or with 1.8 mg/loop of GM1-NPs or PEG-NPs. Broth alone was used as a control.

Statistics

Data were analyzed using Prism 5 (GraphPad Software, La Jolla, USA). Means were compared with Student's t-test or analysis of variance (Anova). P values <0.05 were considered as significant.

3.1.3 Results and Discussion

Construction and physical characterization of GM1-coated nanoparticle decoys

Hybrid nanoparticles, comprised of a polymeric core and a lipid shell, combine the merits of both polymeric nanoparticles and liposomes while avoiding some of their limitations [326]. Compared to the aqueous cores of conventional liposomes, a solid polymeric core provides better control over the mechanical stability, particle morphology, size distribution, and drug release kinetics [329]. Therefore, we applied hybrid nanoparticle fabrication to the formulation of GM1-NPs as schematically outlined in Figure 3.1A. Briefly, an organic solution of PLGA as the polymeric core constituent was added dropwise under gentle stirring to a solution of GM1 in water to yield a final 1:2 volume ratio of organic to aqueous solution. The mixture was vortexed vigorously for 3 min followed by solvent evaporation under reduced pressure. The remaining organic solvent and free molecules were removed by centrifugation. As controls, two other types of nanoparticles were prepared: PLGA-NPs and PEG-NPs. PEG-NPs have a PLGA core coated with DSPE-mPEG2000 [332], a lipid modified with polyethylene glycol that is not expected to bind CT. PLGA-NPs are comprised of only a PLGA core without a lipid shell.

Analysis of the nanoparticles by dynamic light scattering revealed a narrow size distribution of the GM1-NPs, with a measured hydrodynamic diameter of 100 nm (Figure 3.1B), which was similar to the previously reported size of the control PEG-NPs [329]. By comparison, the bare PLGA core had a slightly smaller diameter of 75 nm (Figure 3.1B), suggesting that the increased size of the GM1-NPs was due

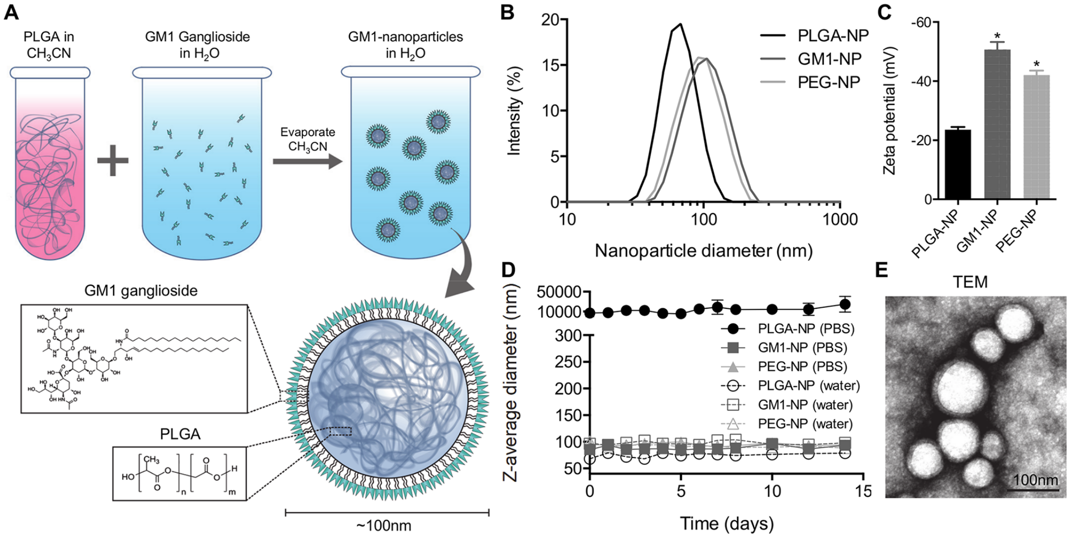

Figure 3.1: Preparation and physical characterization of GM1-coated nanoparticles. (A) Schematic of GM1-NP fabrication. Poly(lactic-co-glycolic acid) (PLGA) dissolved in acetonitrile (CH_3CN) is added to an aqueous solution containing GM1. After acetonitrile evaporation, nanoparticles with a polymeric core and a lipid shell are formed. (B) Intensity-weighted size distribution of representative preparations of GM1-NPs and control PEG-NPs, and PLGA-NPs with a PLGA core but without a lipid shell. (C) Zeta potential of the indicated nanoparticle preparations (n = 3; mean ± SD; $*p<0.05$ vs. PLGA-NPs). (D) Nanoparticle size measurements over two weeks of incubation in distilled water or PBS (n = 3; mean ± SD). (E) Transmission electron micrograph of GM1-NPs.

to the additional GM1 gangliosides coated as an exterior layer onto the PLGA core. Furthermore, GM1-NPs as well as the control PEG-NPs, had a significantly more negative surface zeta-potential of -40 to -50 mV compared to -25 mV of PLGA-NPs (Figure 3.1C), which is also indicative of a difference in the nanoparticle surface characteristics due to the lipid coating of the GM1-NPs compared to the bare PLGA cores.

To test the stability of the nanoparticles in aqueous solution, they were incubated in water or PBS for up to two weeks and analyzed by dynamic light scattering. All three nanoparticle preparations were stable in water for the entire test period, but only the two lipid-coated preparations were stable in PBS, while the bare PLGA-NPs rapidly formed aggregates (Figure 3.1D). These findings clearly distinguished GM1-NPs from the uncoated PLGA-NPs and suggested that the GM1 layer surrounding the GM1-NPs can provide steric and electronic repulsion to prevent detrimental particle aggregation that would interfere with *in vitro* and *in vivo* studies. Transmission electron microscopy confirmed that the GM1-NPs were dispersed as single particles with a core/shell structure characteristic of a unilamellar membrane coating around a nanoparticle core (Figure 3.1E).

Binding characteristics of cholera toxin to GM1 nanoparticle decoys

To determine the ability of GM1-NPs to bind CT, we incubated them, as well as control PEG-NPs, with fluorescently (FITC)-labeled CTB. Unbound CTB was removed by centrifugal filtration, and bound FITC was assayed by fluorescence spectroscopy. Over 95% of input CTB was bound to GM1-NPs, whereas the control

PEG-NPs had only background levels of fluores-cence (Figure 3.2A), showing the specificity of CTB binding to the GM1-NPs. We also constructed GM1-NPs and PEG-NPs in which a far-red fluorescent dye, DiD, was encapsulated in the PLGA core, and incubated them with FITC-CTB under the same conditions. Fluorescence imaging revealed co-localization of DiD and FITC in the GM1-NPs, whereas no FITC staining was observed in the PEG-NPs (Figure 3.2B). These results confirm that CTB binds specifically to GM1-NPs.

Toxin binding was concentration-dependent in regard to CTB and GM1-NPs (Figure 3.2C and 3.2D). Fitting of a one-site specific binding model revealed a maximal binding capacity (Bmax) of $\sim 10^{-7}$ mol CTB per mg GM1-NP (equivalent to $\sim$ mg CTB/mg NP). Taken together, these results show that GM1-NPs are stable in a physiologically relevant salt solution, and can bind CTB in a specific and a high-capacity manner.

Functional neutralization of cholera toxin by GM1 nanoparticle decoys

Having shown specific CTB binding to GM1-NPs, we next investigated whether the particles could block the functional impact of CT holotoxin on intestinal epithelial cells. A fixed concentration of CT was mixed with different concentrations of GM1-NPs or PEG-NPs, and the mixtures were added to monolayers of human HCA7 intestinal epithelial cells. As a functional read-out for CT bioactivity, we determined levels of secreted cAMP in the supernatants, which correlate closely with intracellular cAMP levels [333]. GM1-NPs neutralized the ability of CT to activate cAMP production and secretion in a concentration-dependent fashion, while the GM1-free control PEG-

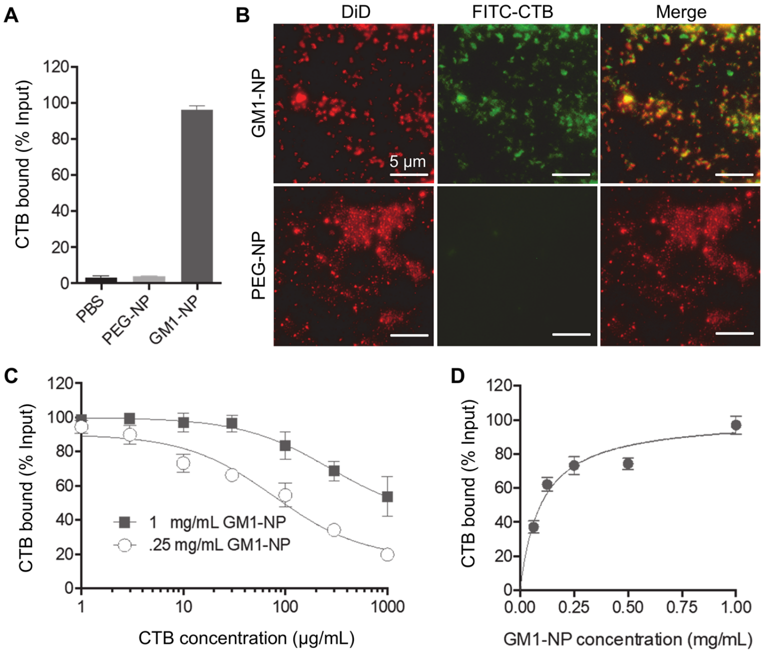

Figure 3.2: Specific binding of cholera toxin B subunit to GM1-NPs. (A) GM1-NPs and control PEG-NPs were incubated with FITC-labeled CTB for 30 min, washed by centrifugation, and analyzed by fluorescence spectroscopy for bound CTB. PBS without nanoparticles served as a background control (n = 3; mean ± SD). (B) DiD-labeled GM1-NPs and PEG-NPs were incubated with FITC-CTB, and imaged by fluorescence microscopy. (C) Increasing concentrations of FITC-CTB were incubated with the indicated fixed amounts of GM1-NPs, and specific binding was analyzed by fluorescence spectroscopy (n = 3; mean ± SD). (D) Increasing amounts of GM1-NPs were incubated with a fixed amount (10 μg/mL) of CTB, and specific binding was analyzed by fluorescence spectroscopy (n = 3; mean ± SD).

NPs had no effect (Figure 3.3A). Half-maximal neutralization of 10 ng/mL CT was achieved at 28 ng/mL GM1-NPs (as measured by their PLGA content). As a further demonstration of the specificity and saturability of the CT/GM1-NP interaction, we observed that increased CT concentrations could overwhelm the neutralizing capacity of GM1-NPs, so a CT concentration of 361 ng/mL was required in the presence of 1,000 ng/mL of GM1-NPs to recover 50% of the maximal CT response seen in the absence of nanoparticles (Figure 3.3B). Control PEG-NPs had no neutralizing effect under these conditions (although decreasing CT concentrations led to the expected diminishment of the epithelial cAMP response).

Neutralization of purified CT was a necessary precondition for practical utility of GM1-NPs, but the particles must be effective against CT produced by live bacteria to have therapeutic potential. Therefore, we infected HCA7 epithelial monolayers with live, CT-secreting *V. cholerae* in the absence or presence of nanoparticles, and measured cAMP secretion in the culture supernatants. GM1-NPs significantly attenuated the cAMP response compared to PEG-NPs, although attenuation was incomplete (Figure 3.3C). Nanoparticles alone without bacteria had no effect on cAMP production. Given the intense exposure of the epithelial monolayers to high numbers of bacteria without physiological mixing that occur with normal intestinal motility and the absence of a normal mucus layer, these data strongly suggest that the GM1-NPs can significantly neutralize CT produced by live bacteria in close contact with epithelial cells.

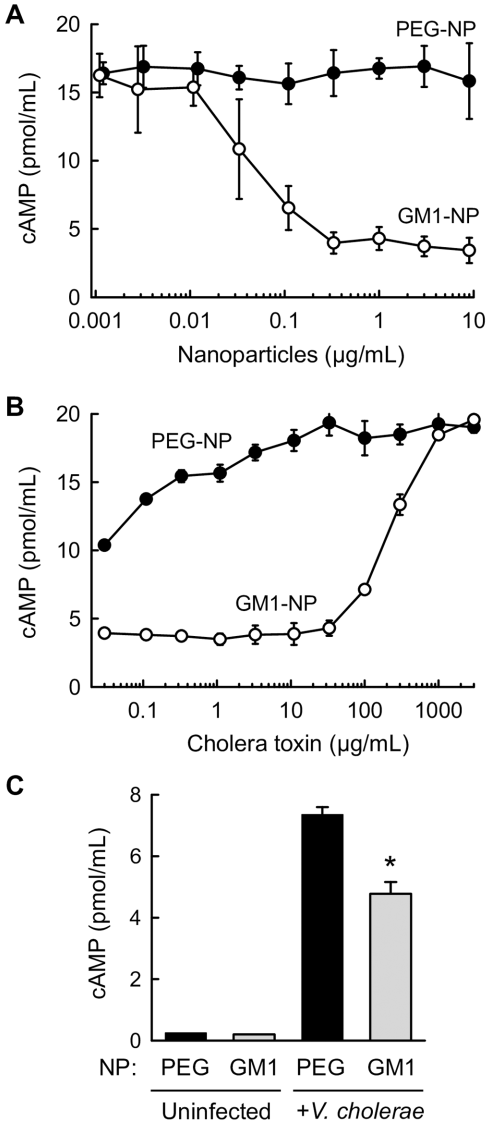

Figure 3.3: Neutralization of CT activity with GM1-NPs. (A) A fixed concentration (10 ng/mL) of CT was combined with increasing amounts of the indicated nanoparticles, and the mixtures were added to confluent monolayers of human HCA7 intestinal epithelial cells. After 2 h, levels of secreted cAMP were determined in the supernatants by ELISA (n = 3; mean ± SD). (B) A fixed amount (1 μg/mL) of the indicated nanoparticles were combined with increasing concentrations of CT, the mixtures were added to HCA7 monolayers for 2 h, and levels of secreted cAMP levels were measured by ELISA (n = 3; mean ± SD). (C) GM1-NPs or control PEG-NPs were added to HCA7 monolayers, which were then infected for 2 h with live *V. cholerae* or left uninfected, and secreted cAMP was determined (n = 3; mean ± SD; $*p<0.05$ vs PEG-NPs).

Stability of GM1 nanoparticle decoys under physiologically relevant conditions

To be effective in the intestinal lumen, where *V. cholerae* resides and secretes CT, nanoparticles have to be stable and functional in the presence of the relevant physiological factors at that site. Of particular importance are bile acids whose amphoteric nature promotes lipid solubilization and digestive enzymes that can break down lipids and other complex molecules. Therefore, we tested whether GM1-NPs remained intact and active upon exposure to these luminal factors. Incubation of GM1-NPs in a solution containing concentrated porcine bile had no impact on particle size or their ability to bind FITC-labeled CTB (Figure 3.4A and 3.4B). Furthermore, incubation of CTB-loaded GM1-NPs for 24 h with luminal fluid (containing bile acids, various digestive enzymes, and some commensal bacteria) from the small intestine of mice did not detach the toxin, indicating that toxin binding to the nanoparticles was stable and not affected by luminal factors (Figure 3.4C; similar observations were made after 48 h of incubation). This conclusion was confirmed by the observation that exposure of the nanoparticles to fecal homogenates (which also contain bile acids and digestive enzymes, as well as large numbers of commensal bacteria and their enzymatic products) did not compromise the ability of GM1-NPs to functionally neutralize CT in respect to epithelial cAMP induction (Figure 3.4D). Together, these results demonstrate that the GM1-NPs display stable and prolonged functionality in the presence of intestinal luminal factors, suggesting that they are suitable for *in vivo* applications to neutralize CT.

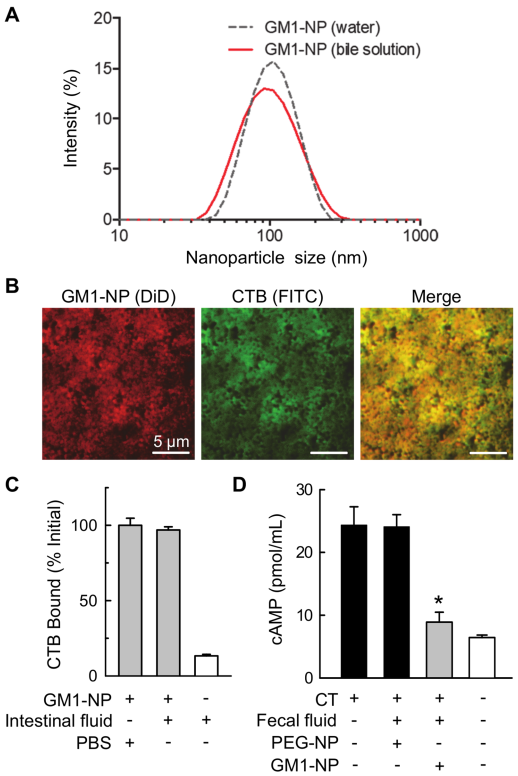

Figure 3.4: Functional stability of GM1-NPs in the presence of intestinal luminal factors. (A) Intensity-weighted size distribution of GM1-NPs incubated 30 min in distilled water or diluted porcine bile solution (1:16 dilution in water). (B) Fluorescence imaging of DiD-labeled GM1-NPs absorbed with FITC-CTB and incubated for 30 min in 1:16 diluted porcine bile solution. (C) GM1-NPs were loaded with FITC-CTB for 30 min, washed, and resuspended in luminal fluid from the small intestine of normal adult mice, or PBS as a control. After incubation for 24 h at 37°C , particle-bound and free FITC-CTB were separated by dialysis, and bound FITC-CTB was measured by fluorescence spectroscopy and related to the initial amount bound (mean ± SD, n = 3). Background readings were obtained with free FITC-CTB without GM1-NPs. (D) Fecal homogenates from mice were mixed 1:1 with GM1-NPs or PEG-NPs in culture media, and incubated for 1 h at 37°C , after which CT (10 ng/mL) was added for an additional 1 h before addition to HCA7 monolayers. After 2 h, cAMP levels in the supernatants were determined by ELISA (mean ± SD, n = 3; $*p<0.05$ vs PEG-NPs).

Attenuation of intestinal secretory response to CT and live *V. cholerae* by GM1 nanoparticle decoys *in vivo*

To evaluate the therapeutic efficacy of the nanoparticles *in vivo*, we utilized ligated intestinal loops in adult mice as a model. Constructed in the distal small intestine, these loops allow undisturbed exposure of the intestine to defined microbial stimuli and therapeutic interventions in the physiologically relevant environment without confounding variables related to intestinal motility or variable susceptibility of adult mice to sustained infection with the target microbe. In a first test, we injected the loops with CT in the absence or presence of GM1-NPs or PEG-NPs. CT alone induced a robust fluid response in the lumen of the loops, which was not affected by the control PEG-NPs (Figure 3.5A). In contrast, GM1-NPs completely blocked the fluid response to CT, indicating that the nanoparticles were as effective *in vivo* as they were *in vitro*. Subsequently, we infected the loops with live *V. cholerae* with and without nanoparticles. Increased fluid secretion was observed after infection, which was significantly attenuated by treatment with GM1-NPs but not with control PEG-NPs (Figure 3.5B and 3.5C). In parallel to the attenuated fluid response, levels of secreted cAMP in the intestinal lumen were significantly decreased with GM1-NP treatment compared to control PEG-NPs after *V. cholerae* infection (Figure 3.5D). Neither of the nanoparticles had an impact on baseline fluid secretion without infection.

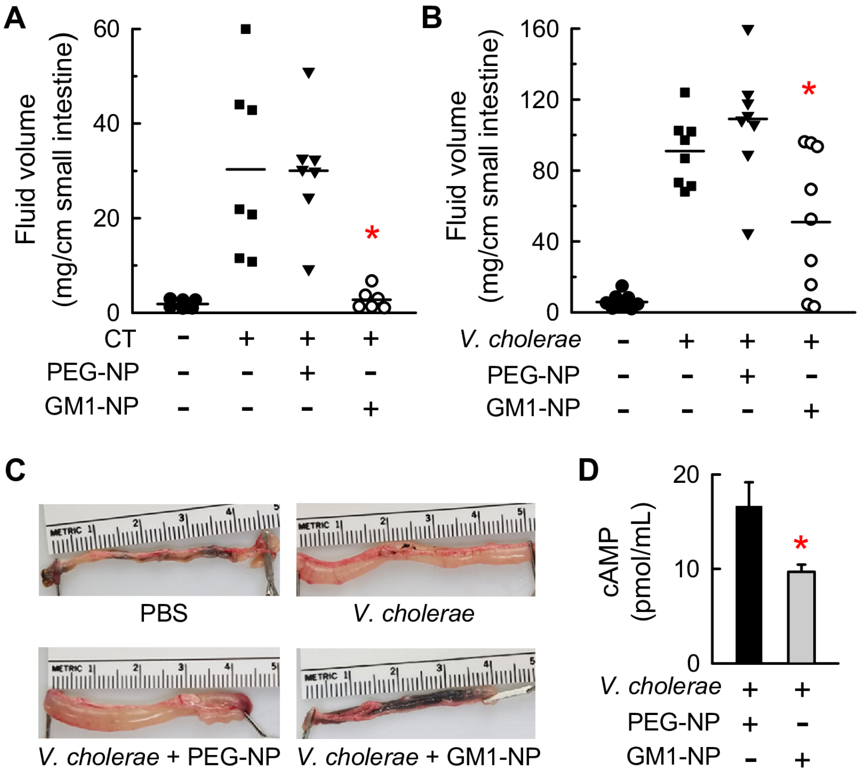

Figure 3.5: *In vivo* efficacy of GM1-NPs against CT and live *V. cholerae*.(A) Ligated intestinal loops were prepared in the distal small intestine of adult C57BL/6 mice, and injected with PBS as a control, or with 2.5 μg CT, without and with prior addition of GM1-NPs or control PEG-NPs. Fluid accumulation in the loops was determined after 4 h, and related to loop length (each point represents one animal, horizontal lines are geometric means; $*p<0.05$ vs PEG-NPs). (B) Loops were injected with PBS as a control, or live *V. cholerae* with GM1-NPs or control PEG-NPs. Fluid accumulation was determined after 16 h (each point represents one animal, horizontal lines are geometric means; $*p<0.05$ vs PEG-NPs). (C) Images of representative intestinal loops. (D) cAMP was measured in the luminal fluid collected from loops after injection of live *V. cholerae* with GM1-NPs or control PEG-NPs (n = 3; mean ± SD; $*p<0.05$ vs PEG-NPs).

3.1.4 Conclusions

Cholera continues to be a major public health challenge in many regions of the world [313]. Medical strategies to combat this scourge can be divided into preventive approaches, which seek to protect individuals from infection, and therapeutic approaches, which attenuate disease symptoms in infected persons. For prevention, the FDA recently approved the first cholera vaccine, Vaxchora, composed of attenuated live bacteria, but the vaccine is currently only effective for *V. cholerae* serogroup 01 and, as a live agent, has the potential to cause disease itself, either in attenuated form in predisposed individuals or potentially upon reversion to a more virulent form [334]. In this regard, quality controls of live microbial agents as therapeutic agents can be challenging. As an alternative, attenuating medical strategies employ well-controlled interventions to ameliorate symptoms and assure survival while allowing mucosal immune defenses to clear the infection. The classical treatment is oral or intravenous rehydration [312], in which bacterially-induced diarrheal processes proceed unhindered, but the devastating systemic consequences of dehydration are prevented by providing sufficient electrolytes and water during the acute disease stage. Although usually effective for promoting survival, severe disease symptoms can still occur for days.

As an alternative attenuation strategy, we show here that a nanotechnology-based intervention can be effective at targeting the bacterially-produced CT, which is the primary cause of diarrheal symptoms in cholera [313]. By coating nanoparticles with the CT-binding lipid, GM1, the particles were able to bind and neutralize the toxin, thereby preventing its effects on epithelial electrolyte and fluid secretion

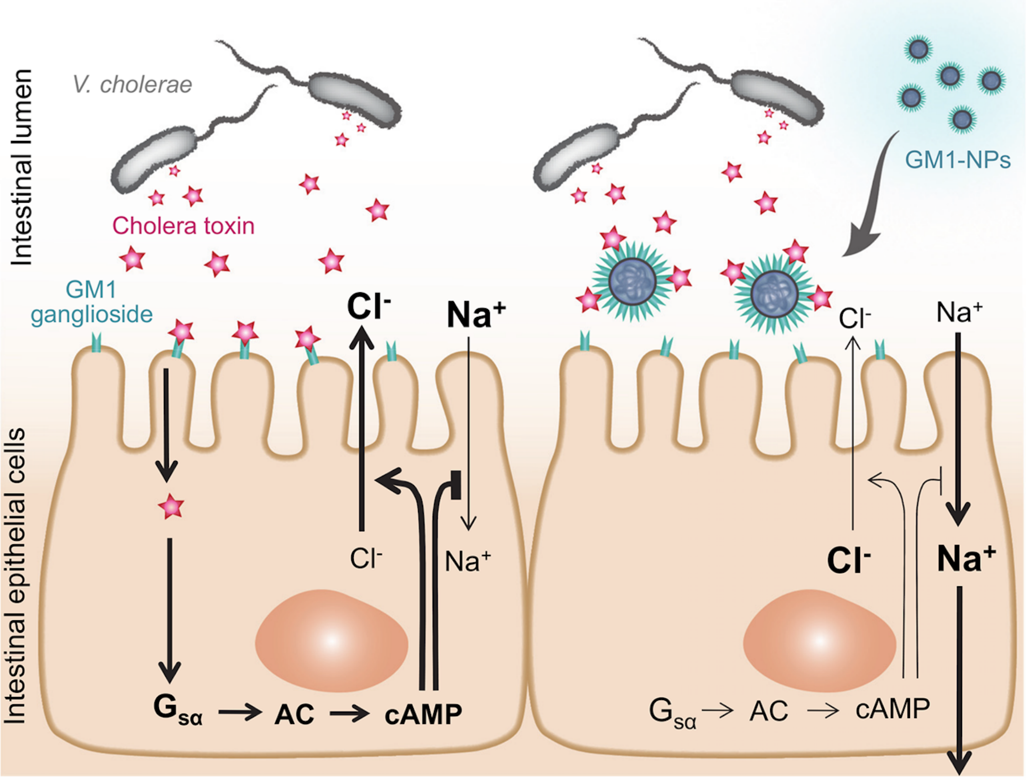

Figure 3.6: Model of therapeutic effect of GM1-NPs.GM1-coated nanoparticles act as decoys to absorb CT produced by *V. cholerae* before it can bind to epithelial cells to stimulate cAMP production and epithelial chloride secretion, and inhibit sodium absorption.

in vitro and *in vivo* (Figure 3.6). This strategy represents a novel interventional approach whose mechanisms of action are physiologically distinct from vaccination, rehydration, or antibiotics, thus significantly broadening the medical armamentarium against cholera.

Neutralization strategies for microbial toxins have been proposed and implemented with different technological means, including antibodies and live bacteria. For cholera, *Escherichia coli* has been engineered to produce GM1 lipid on its surface [335].

The recombinant *E. coli* was shown to bind CT and attenuate *V. cholerae*-induced disease in animal models [323, 335], thus underlining our findings. However, live microbes as therapeutic agents are problematic due to the difficulties in performing quality controls in manufacturing [336]. Furthermore, genetically engineered live bacteria, particularly those that belong to the normal intestinal microbiota, may colonize the intestine permanently [337], raising concerns about long-term microecological consequences of such interventions. In contrast, our nanoparticles were constructed exclusively from tractable reagents that can be readily quality-controlled. The fabrication process is effective and high-yield, thereby minimizing potentially offensive by-products and the accompanying need for extensive purification schemes. Furthermore, the nanoparticles do not replicate and are thus not retained for extended periods in the intestine beyond the treatment period.

In the nanoparticle design, we considered that many glycosylated lipid derivatives, such as gangliosides, contain sialic acid residues on their sugar chains that are prominently positioned and critical for attachment of cholera toxin [338]. Consequently, it was important that the GM1-oligosaccharides were located on the outside of the nanoparticle core in the proper orientation, so the lipid arrangement would resemble as much as possible the naturally occurring cell-surface location and affinity of GM1 to which CT normally binds. We were able to achieve the desired lipid location and orientation on the polymeric nanoparticle surface through a modified nanoprecipitation method [326, 329], in which GM1-gangliosides with their inherent amphiphilic property self-assembled in a single-step synthesis on the hydrophobic nanoparticle surface to produce a lipid monolayer on the interface of the nanoparticle core and the hydrophilic GM1-oligosaccharides present on the outer shell.

The fabricated GM1-nanoparticles represent a novel class of core-shell structured lipid- polymer hybrid nanoparticles, which are known for combining the strengths of both liposomes and polymeric nanoparticles [326]. The lipid shell incasing the core mimics biological membranes and can mediate specific interactions with the environment, such as the reported interaction between the shell GM1 and soluble CT. Meanwhile, the nanoparticle core serves as structural support that provides controlled morphology, size tunability, and narrow size distribution [339]. In addition, lipid-polymeric nanoparticles have excellent physical stability [329, 340, 341], making GM1-NPs promising for their use in tropical environments. In terms of safety, PLGA polymer, which makes up the GM1-NP core, is a safe and FDA-approved biodegradable polymer [342], and GM1-ganglioside is extracted from natural cell membranes. Hence, it is likely that the GM1-nanoparticles are biocompatible and safe for prospective clinical translation.

Since cholera is often a disease affecting poor people in developing countries, cost-effective manufacturing is critical for clinical utility. PLGA has long been produced for pharmaceutical applications [343, 344], and a variety of manufacturing processes have been used in industry for nanoparticle formulations [345–347]. Such processes could be adapted to large-scale GM1-NP production, facilitating downstream translational development. Optimal formulation will require further development, but the platform technology has great flexibility. For example, nanoparticles can be administered directly, as shown for formulations such as poly (lactic-co-glycolic acid) nanoparticles and polyacrylic acid nanoparticles to treat colitis or hypercalcemia

[348, 349]. Alternatively, nanoparticles could be loaded into capsules [350, 351] or a pH-responsive polymer matrix for targeting to specific sections of the intestinal tract [352].

Our nanoparticle strategy has implications for treating other enteric infections in which microbially-produced toxins play an important and central pathophysiological role. For example, the heat-labile enterotoxin of enterotoxigenic *E. coli*, the most common cause of traveler's diarrhea, also binds GM1 ganglioside [353]. Structural analysis of CTB and the binding subunit of LT bound to GM1-pentasaccharide revealed that the residues contacting the terminal galactose sugar are conserved between the two toxins [354], suggesting that nanoparticle-based intervention would predictably also be effective in enterotoxigenic *E. coli*-induced disease. For other toxin-mediated enteric diseases, such as those caused by shiga toxin from *Shigella dysenteriae* [355], similar nanotechnology strategies using the appropriate lipids may also be a promising new therapeutic avenue.

3.2 Macrophage-like nanoparticles concurrently absorbing endotoxins and proinflammatory cytokines for sepsis management

3.2.1 Introduction

Sepsis is a life-threatening complication of bacterial infection characterized by uncontrolled systemic inflammatory response [356]. Sepsis precipitates a collapse of cardiovascular function, leading to multiple organ dysfunction or failure [357, 358]. Despite many efforts devoted to finding an effective treatment, the mortality rate in sepsis is very high, and the number of hospitalizations resulting from the condition continues to rise [359, 360]. Endotoxin, an important pathogenic trigger of Gram-negative bacterial sepsis, induces a systemic inflammatory response characterized by production of proinflammatory cytokines and nitric oxide, fever, hypotension, and intravascular coagulation, culminating in septic shock [361]. Emerging evidence suggests that the systemic spread of endotoxin from sites of infection, rather than bacteremia itself, is crucial in the pathogenesis of this dramatic immune dysregulation [362, 363]. Since higher levels of endotoxin correlate to worsened clinical outcomes [364, 365], effective endotoxin removal is a critical component of successful sepsis management.

Endotoxin neutralization and elimination present various challenges. While all endotoxins share a common architecture, they vary greatly in their structural motifs across bacterial genus, species, and strain [366, 367]. Accordingly, endotoxin interactions with ligands can differ substantially, which poses challenges for structure-based neutralization strategies. Antibiotics effective in neutralizing endotoxin such as polymyxins have limits on their clinical utility due to their strong nephrotoxicity and neurotoxicity [368, 369]. Attaching these molecules to solid-phase carriers for hemoperfusion can retain their endotoxin-binding properties while minimizing the toxic effects, but clinical evidence of therapeutic efficacy has yet to be established [370,371]. In addition, such solid-phase perfusion strategies are impractical in resource-limited environments [372].

Recently, cell membrane-coated nanoparticles have emerged as a biomimetic nanomedicine platform, enabling a broad range of biodetoxification applications [373,374]. In particular, nanoparticles coated with membranes derived from red blood cells (denoted RBC nanosponges) have taken advantage of functional similarities shared by various bacterial pore-forming toxins to neutralize their cytolytic activity regardless of molecular structure [375, 376]. These unique core-shell nanoparticles exhibit prolonged systemic circulation, preventing further bioactivity of the absorbed toxins and diverting them away from their intended cellular targets. RBC nanosponges have also been developed as therapeutic detoxification agents to neutralize pathological antibodies in autoimmune diseases [377] and organophosphate nerve agents [378].

The therapeutic potential of membrane-coated nanoparticles for broad-spectrum detoxification inspired us to develop biomimetic nanoparticles for endotoxin removal, potentially enabling effective sepsis management. In sepsis, endotoxin, also referred to as lipopolysaccharide (LPS), is released from the bacteria during cell division, cell death, or under antibiotic treatment, whereupon it is recognized as a pathogen-associated molecular pattern (PAMP) by sentinel immune cells, including monocytes and macrophages [379,380]. In the bloodstream, LPS-binding protein (LBP) binds with high affinity to LPS via lipid A, and the LPS-LBP complex subsequently engages the pattern recognition receptor (PRR) CD14 present on the macrophage cell surface [381,382]. Following this binding interaction, LPS can induce various changes in immune cell activity. For example, LPS induces a dose-dependent production of nitric oxide (NO), which can be cytotoxic at high levels [365]. LPS binding to macrophages also activates the PRR Toll-like receptor 4 (TLR4), which plays a significant role in the regulation of bacterial phagocytic uptake [383], intracellular trafficking, and macrophage cell death [384,385]. Furthermore, LPS-induced engagement of TLR4 activates the nuclear factor-κB (NF-κB) transcription factor, resulting in the production and release of potent proinflammatory cytokines, such as tumor necrosis factor (TNF), interleukin 6 (IL-6), and IFN-γ [386,387].

Compelled by the critical roles played by macrophages and their PRR in endotoxin signaling, here we develop biomimetic nanoparticles consisting of a biodegradable polymeric nanoparticle core coated with cell membrane derived from macrophages (denoted MΦ-NPs, Figure 3.7A). MΦ-NPs possess an antigenic exterior identical to the source macrophage cells, thus inheriting their capability to bind to endotoxins. In addition, MΦ-NPs act as decoys to bind to cytokines, inhibiting their ability to potentiate downstream inflammation cascades, i.e., pathological “cytokine storm.” These two functionalities together enable effective intervention during uncontrolled immune activation, providing a therapeutic intervention with significant potential for the management of sepsis.

3.2.2 Experimental Methods

Macrophage Membrane Derivation.

The murine J774 cell line was purchased from the American Type Culture Collection (ATCC) and maintained in Dulbecco's modified Eagle medium (DMEM) (Invitrogen) supplemented with 10% FBS (HyClone) and 1% penicillin-streptomycin (pen-strep) (Invitrogen). Plasma membrane was collected according to a previously published centrifugation method [388]. Specifically, cells were grown in T-175 culture flasks to full confluency and detached with 2 mM EDTA (USB Corporation) in PBS (Invitrogen). The cells were washed with PBS three times (500 × g for 10 min each) and the cell pellet was suspended in homogenization buffer containing 75 mM sucrose, 20 mM Tris-HCl (pH = 7.5, MediaTech), 2 mM $MgCl_2$ (Sigma-Aldrich), 10 mM KCl (Sigma-Aldrich), and one tablet of protease/phosphatase inhibitors (Pierce, Thermo Fisher Scientific). The suspension was loaded into a Dounce homogenizer and the cells were disrupted with 20 passes. Then the suspension was spun down at 3,200 × g for 5 min to remove large debris. The supernatant was collected and centrifuged at 20,000 × g for 25 min, after which the pellet was discarded and the supernatant was centrifuged at 100,000 × g for 35 min. After the centrifugation, the supernatant was discarded and the plasma membrane was collected as an off-white pellet for subsequent experiments. Membrane protein content was quantified with a Pierce BCA assay (Life Technologies).

MΦ-NP Preparation and Characterization.

MΦ-NPs were formulated in two steps. In the first step, ∼80-nm polymeric cores were prepared using 0.67 dL/g carboxyl-terminated 50:50 PLGA (LACTEL absorbable polymers) through a nanoprecipitation method. The PLGA polymer was first dissolved in acetone at a concentration of 10 mg/mL. Then 1 mL of the solution was added rapidly to 3 mL of water. For fluorescently labeled PLGA cores, 1,1'-dioctadecyl-3,3,3',3'- tetramethylindodicarbocyanine perchlorate (DiD, excitation/emission = 644 nm/ 665 nm; Life Technologies) was loaded into the polymeric cores at 0.1 wt%. The nanoparticle solution was then stirred in open air for 4 h to remove the organic solvent. In the second step, the collected macrophage membranes were mixed with nanoparticle cores at a membrane protein-to-polymer weight ratio of 1:1. The mixture was sonicated with a Fisher Scientific FS30D bath sonicator at a frequency of 42 kHz and a power of 100 W for 2 min. Nanoparticles were measured for size and size distribution with DLS (ZEN 3600 Zetasizer, Malvern). All mea surements were done in triplicate at room temperature. Serum and PBS stabilities were examined by mixing 1 mg/mL of MΦ-NPs in water with 100% FBS and 2× PBS, respectively, at a 1:1 volume ratio. Membrane coating was confirmed with transmission electron microscopy (TEM). Briefly, 3 μL of nanoparticle suspension (1 mg/mL) was deposited onto a glow-discharged carbon-coated copper grid. Five minutes after the sample was deposited, the grid was rinsed with 10 drops of distilled water, followed by staining with a drop of 1 wt% uranyl acetate. The grid was subsequently dried and visualized using an FEI 200 kV Sphera microscope.

Membrane Protein Characterization.

MΦ-NPs were purified from free vesicles, membrane fragments, and unbound proteins by centrifugation at 16,000 × g. Macrophage cell lysates, membrane vesicles, and MΦ-NPs were mixed with lithium dodecyl sulfate (LDS) loading buffer to the same total protein concentration of 1 mg/mL as determined with a Pierce BCA assay (Life Technologies). Electrophoresis was carried out with NuPAGE Novex 4-12% Bis-Tris 10-well minigels in Mops running buffer with an XCell SureLock Electrophoresis System (Invitrogen). Western blot analysis was performed by using primary antibodies including rat anti-mouse CD14, rat anti-mouse CD126, rat anti-mouse CD130, rat anti-mouse CD284, Armenian hamster anti-mouse CD120a, Armenian hamster anti-mouse CD120b, and Armenian hamster anti-mouse CD119 (BioLegend). Corresponding IgG-horseradish peroxidase (HRP) conjugates were used for the secondary staining. Films were developed with ECL Western blotting substrate (Pierce) on a Mini-Medical/90 Developer (ImageWorks).

LPS and Cytokines Binding Studies.

To study whether LPS binding with MΦ-NPs was dependent on LBP, CD14, or TLR4, the mixture of MΦ-NPs (1 mg/mL) and FITC-LPS (from *E. Coli* O111:B4, 125 ng/mL; Sigma) in 1× PBS was added with FBS (10% as the source of LBP), anti-CD14 (10 μg/mL; BioLegend), or anti- TLR4 (10 μg/mL; Invivogen), respectively. The solution was incubated at 37 °C for 30 min. Following the incubation, MΦ-NPs were spun down with ultracentrifugation (16,000 × g). The fluorescence intensity from FITC-LPS remaining in the supernatant was measured. The fluorescence intensity from a FITC-LPS solution of 125 ng/mL served as 100%. The mixtures without adding FBS or antibodies were used as the controls. An equivalent amount of MΦ-ghost (protein mass) was used as a control to assess the loss of membrane function during coating. The mixture added with nonspecific IgG from human serum was also included as a negative control to exclude the effect of the nonbinding domains of the antibody that may contribute to LPS inhibition. All experiments were performed in triplicate.

To quantify LPS removal with MΦ-NPs, MΦ-NPs (0.4 mg, 4 mg/mL) were mixed with LPS from *E. Coli* K12 (Invivogen) with varying amount of 5, 10, 25, and 50 ng (50, 100, 250, and 500 ng/mL), respectively, in 1× PBS containing 10% FBS. In a parallel experiment, the removal was studied by fixing LPS amount at 50 ng (250 ng/mL) but varying the amount of MΦ-NPs at 0.1, 0.2, 0.3, and 0.4 mg (0.5, 1, 1.5, and 2 mg/mL), respectively. In both cases, the mixtures were incubated for 30 min and then spun down at 16,000 × g for 15 min to pellet the nanoparticles. The free LPS content in the supernatant was quantified by using limulus amebocyte lysate (LAL) assay (Thermo Fisher Scientific) per manufacturer's instructions. All experiments were performed in triplicate.

To determine MΦ-NP binding with cytokines, including IL-6, TNF-α, and IFN-γ 100 μL of MΦ-NP samples (1 and 4 mg/mL) mixed with IL-6 (2,000 pg/mL), TNF-α (370 pg/mL), or IFN-γ (880 pg/mL) in PBS containing 10% FBS were incubated at 37 °C for 30 min. Following the incubation, the samples were centrifuged at 16,000 × g for 15 min to pellet the nanoparticles. Cytokine concentrations in the supernatant were quantified by using ELISA (BioLegend). All experiments were performed in triplicate.

LPS Neutralization in Vitro.

Murine TLR4 reporter cells (HEK-Blue mTLR4 cells, Invivogen) were first used to determine LPS neutralization by MΦ-NPs. Cells were cultured in DMEM supplemented with 10% FBS, 1% pen-strep, 100 μg/mL normocin, 2 mM L-glutamine, and 1× HEK-Blue selection (Invivogen). In the study, 2.5 × 104 cells were seeded in each well of a 96-well plate with 160 μL HEK-Blue detection medium, followed by adding 20 μL of 100 ng/mL LPS in PBS. Then 20 μL of nanoparticle solution of MΦ-NPs, RBC-NPs, or PEG-NPs (all at a concentration of 10 mg/mL), was added into each well. Control wells were added with 20 μL PBS. Cells without any treatment served as the background. The mixture was incubated for 12 h. SEAP was quantified by measuring the absorbance at 630 nm with an Infinite M200 multiplate reader (Tecan). All experiments were performed in triplicate.

Production of iNO was also used to evaluate LPS neutralization with MΦ-NPs. Briefly, 2 × 104 J774 cells were seeded in each well of a 96-well plate. The cells were incubated with 10 μM of 2, 7'-dichlorofluorescin-diacetate (DCFH-DA) (Sigma) in culture medium for 1 h and then washed three times with the culture medium. Then the wells were added with 180 μL of medium containing 10 ng/mL of LPS. Then 20 μL of nanoparticle solution of MΦ-NPs, RBC-NPs, or PEG-NPs (all at a concentration of 10 mg/mL), was added into each well. Twenty microliters of PBS was added to control wells. Cells without any treatment served as the background. The plate was incubated at 37 °C for 5 h. The production of iNO was quantified by measuring the fluorescence intensity at 520 nm using an excitation wavelength of 485 nm (Infinite M200 multiplate reader, Tecan). All experiments were performed in triplicate.

LPS neutralization with MΦ-NPs was further evaluated by examining E-selectin expression on HUVECs. Specifically, HUVECs were cultured to confluence in a 96-well plate. Then 200 μL of LPS (250 ng/mL) mixed with MΦ-NPs, RBC-NPs, or PEG-NPs (4 mg/mL) in culture medium was added to the cells and the plate was incubated at 37 °C . Cells added with LPS and PBS were used as controls. Three wells were used per sample. After 1, 2, 3, and 4 h of incubation at 37 °C , medium was removed and cells were washed with PBS. Then the cells were fixed with 4% paraformaldehyde (Sigma) at room temperature for 15 min. Following the fixation, cells were washed twice with PBS and blocked with 1% BSA (Sigma). Subsequently, the reagent was decanted and 50 μL of primary antibody (mouse anti-human E-selectin, 1:10 dilution in 1% BSA; BioLegend) was added to each well and incubated at 37 °C for 45 min. Wells were then rinsed three times with 1× PBS before the addition of 50 μL of secondary antibody (HRP-conjugated anti-mouse IgG, 1:10 dilution in 1% BSA; BioLegend) followed by an incubation for 45 min at 37 °C . After this, wells were again rinsed three times with 1× PBS and after the final rinse, 100 μL of 3,3',5,5'- tetramethylbenzidine (TMB) substrate solution was added to each well. The plate was incubated at 37 °C followed by measuring the absorbance at 450 nm. To visually examine E-selectin expression, cells following the same treatment as the above experiment were incubated at 37 °C for 4 h and rinsed twice with PBS, fixed with 4% paraformaldehyde for 15 min, permeabilized in

0.2% Triton X-100 (Sigma) in buffer for 10 min, and then incubated with 1% BSA in PBS for 30 min. Cells were then stained with mouse anti-human E-selectin for 1 h, washed three times with 1× PBS, and then incubated with anti-mouse IgG Alexa 488 conjugates in 1% BSA in PBS for 1 h. Cell nuclei were stained with DAPI (1 mg/mL stock solution; Thermo Fisher Scientific). Fluorescence images were taken with an EVOS fluorescence microscope (Thermo Fisher Scientific).

Animal Care and Injections. All animal studies were approved under the guidelines of the University of California San Diego (UCSD) Institutional Animal Care and Use Committee. Mice were housed in an animal facility at UCSD under federal, state, local, and NIH guidelines for animal care. In the study, no inflammation was observed at the sites of injection.

Pharmacokinetics and Biodistribution Studies.

The experiments were performed on 6-wk-old male ICR mice (Harlan Laboratories). To determine the circulation half-life, 150 μL of DiD-labeled MΦ-NPs (3 mg/mL) was injected i.v. through the tail vein. At 1, 15, and 30 min, and 1, 2, 4, 8, 24, 48, and 72 h postinjection, one drop of blood (~30 μL) was collected from each mouse via submandibular puncture with heparin-coated tubes. Then 20 μL of blood was mixed with 180 μL PBS in a 96- well plate for fluorescence measurement. Pharmacokinetic parameters were calculated to fit a two-compartment model. For biodistribution study, 150 μL of DiD-labeled MΦ-NPs (3 mg/mL) was injected i.v. through the tail vein. At 24, 48, and 72 h postinjection, organs including the liver, kidneys, spleen, brain, lungs, heart, and blood were collected from six randomly selected mice. The collected organs were weighed and then homogenized in PBS for fluorescence measurement. All fluorescence measurements were carried out with an Infinite M200 multiplate reader (Tecan).

LPS Neutralization *in vivo.*

The efficacy of MΦ-NPs in neutralizing LPS was first evaluated with a mouse endotoxemia model with 6-wk-old male BALB/c mice (Harlan). To evaluate the efficacy through cytokine production, mice were injected with 5 μg/kg LPS through the tail vein. After 15 min, MΦ-NPs, RBC-NPs, or PEG-NPs were injected at 200 mg/kg. Following the injections, blood samples (<30 μL) were collected at predetermined time points via submandibular puncture. Untreated mice and mice injected with LPS alone were used as controls. Cytokines, including IL-6 and TNF-α, in the plasma were quantified by ELISA as described above. In each group, six mice were used. To evaluate efficacy through survival, mice were first sensitized with D-galactosamine hydrochloride (Sigma-Aldrich) via i.p. injection at a dosage of 800 mg/kg. After 30 min of sensitization, LPS and nanoparticles were injected intravenously. Ten mice were used in each group.

LPS neutralization efficacy was also evaluated with a mouse bacteremia model.

Specifically, 6-wk-old female C57BL/6 (The Jackson Laboratory) mice were injected intraperitoneally with 1×10^7 CFU of uropathogenic *E. Coli* (UPEC) CFT073 suspended in 100 μL of 1× PBS. After 30 min, mice were randomly placed into two groups (n = 10), and each mouse was injected with 500 μL of MΦ-NPs at a concentration of 10 mg/mL in 10% sucrose solution intraperitoneally. Mice were killed 4 h after the injection. Blood and organs were collected and homogenized with a Mini Beadbeater-16 (BioSpec) in 1 mL of PBS. Proinflammatory cytokines in the blood, including IL-6, TNF-α, and IFN-γ, were quantified by a cytometric bead array per manufacturer's instructions (BD Biosciences). For bacterial enumeration, homogenized samples were serially diluted with PBS (from 10- to 10^7-fold) and plated onto agar plates. After 24 h of culture, bacterial colonies were counted. To evaluate efficacy through survival, the same experimental procedure was carried out and survival was monitored over a period of 60 h (n = 10).

3.2.3 Results and Discussion

The preparation of MΦ-NPs was divided into two steps. In the first step, cell membranes from J774 mouse macrophages were derived and purified using a process involving hypotonic lysis, mechanical disruption, and differential centrifugation. In the second step, we used a sonication method to form membrane vesicles and subsequently fused them onto poly(lactic-co-glycolic acid) (PLGA) cores to create MΦ-NPs. Following membrane fusion, the diameter of the nanoparticles measured with dynamic light scattering (DLS) increased from 84.5 ± 1.9 nm to 102.0 ± 1.5 nm, corresponding to the addition of a bilayered cell membrane onto the polymeric cores (Figure 3.7B). Meanwhile, the surface zeta potential changed from -41.3 ± 3.6 mV to -26.7 ± 3.1 mV, likely due to charge screening by the membrane. The engineered MΦ-NPs were stained with uranyl acetate and visualized with transmission electron microscopy (TEM), revealing a spherical core-shell structure, in which the PLGA core was wrapped with a thin shell (Figure 3.7C). Following their formulation, MΦ-NPs were suspended in 1× PBS and 50% serum, respectively, and demonstrated excellent stability in size and membrane coating over 72 h, as monitored by DLS (Figure 3.7D). Improved colloidal stability is attributable to the stabilizing effect of hydrophilic surface glycans on the macrophage membrane. Together, these results demonstrate the successful coating of PLGA cores with unilamellar macrophage membranes.

Through membrane coating, MΦ-NPs inherit key biological characteristics of the source cells. By Western blot analysis, we verified that MΦ-NPs maintained critical membrane proteins responsible for LPS binding, including CD14 and TLR4 (Figure 3.7E). Representative cytokine-binding receptors were also preserved, including CD126 and CD130 for IL-6, CD120a, and CD120b for TNF, and CD119 for IFN-γ. Indeed, the membrane derivation process resulted in significant protein enrichment for these molecules. Following i.v. administration, the systemic circulation time of MΦ-NPs was measured by labeling the nanoparticles with a hydrophobic DiD fluorophore (Figure 3.7F). At 24 h and 48 h, respectively, MΦ-NPs showed 29% and 16% retention in the blood. Based on a two-compartment model applied in previous studies to fit nanoparticle circulation results, the elimination half-life was calculated as 17.2 h [389, 390]. To further evaluate their potential for systemic applications, we investigated the *in vivo* tissue distribution of the MΦ-NPs (Figure 3.7G). When analyzed per organ, MΦ-NPs were distributed mainly in the blood and the liver. Per gram of tissue, MΦ-NPs were principally contained in the liver and spleen, two primary organs of the reticuloendothelial system (RES). Meanwhile, significant fluorescence

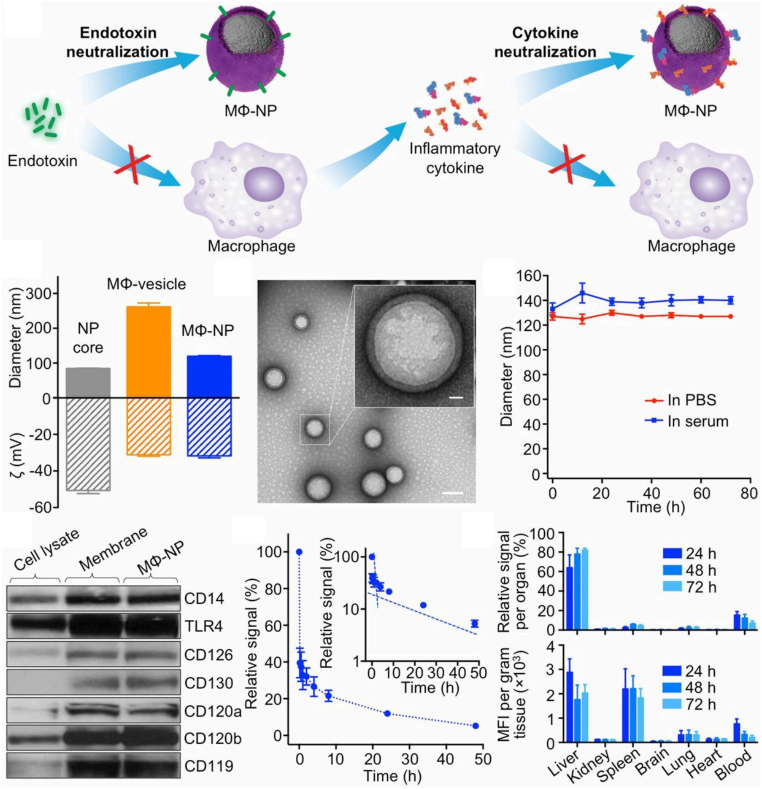

Figure 3.7: Formulation and characterization of macrophage membrane-coated nanoparticles (MΦ-NPs). (A) Schematic representation of using MΦ-NPs to neutralize endotoxins and proinflammatory cytokines as a two-step process for sepsis management. (B) Hydrodynamic size (diameter, nanometers) and surface zeta potential (ζ, millivolts) of PLGA polymeric cores before and after coating with macrophage membrane as measured by dynamic light scat- tering (n = 6). (C) TEM images of MΦ-NPs negatively stained with uranyl acetate. (Scale bar: 100 nm.) (Inset) The zoomed-in view of a single MΦ-NP. (Scale bar: 10 nm.) (D) Stability of MΦ-NPs in 1× PBS or 50% FBS, determined by monitoring particle size (diameter, nanometers), over a span of 72 h. (E) Representative protein bands of macrophage cell lysate, membrane vesicles, and MΦ-NPs resolved using Western blotting. (F) DiD-labeled MΦ- NPs were injected i.v. via the tail vein of mice. At various time points, blood was collected and measured for fluorescence (excitation/emission = 644/ 670 nm) to evaluate the systemic circulation lifetime of the nanoparticles (n = 6). (Inset) The semilog plot of fluorescence signal at various time points. (G) Biodistribution of the MΦ-NPs collected by injecting DiD-labeled MΦ-NPs i.v. into the mice. At each time point (24, 48, and 72 h), the organs from a randomly grouped subset of mice were collected, homogenized, and quantified for fluorescence. Fluorescence intensity per gram of tissue and relative signal per organ were compared (n = 6).

was also observed in the blood. As the blood fluorescence decreased, a corresponding increase in signal was observed in the liver, suggesting the uptake of MΦ-NPs by the RES over time.

We next examined the ability of MΦ-NPs to bind to LPS, which is known to first form high-affinity complexes with LBP. These complexes then bind to TLR4 through CD14, which are both present on the cell surface of macrophages. To test the effect of LBP on LPS binding to MΦ-NPs, we mixed the nanoparticles with FITC-LPS conjugate, incubated the mixture at 37 °C , then collected the MΦ-NPs by ultracentrifugation to compare their FITC fluorescence intensity to that of the supernatant. As shown in Figure 3.8A, in the absence of LBP, nearly 80% of LPS remained in the solution. However, with addition of LBP, 90% of LPS was pelleted into the supernatant, indicating a significant increase in binding to MΦ-NPs. Meanwhile, when MΦ-ghost instead of MΦ-NPs was used (equivalent protein amount), the reduction of LPS was comparable, indicating the preservation of membrane activity during nanoparticle formulation. In addition, while nonspecific IgG from human serum showed no effect to LPS binding, the amount of unbound LPS remaining in the supernatant increased upon addition of anti-CD14 or anti-TLR4 antibodies, indicating that both macrophage PRRs mediated binding interactions between LPS and MΦ-NPs (Figure 3.8B). Overall, compared with macrophages, MΦ-NPs showed similar dependence on LBP, TLR4, and CD14 in binding with LPS, suggesting that MΦ-NPs inherit the biological characteristics of the source cells.

Next, we quantified the LPS removal capacity of MΦ-NPs through two sets of experiments. First, we fixed the quantity of MΦ-NPs at 0.4 mg and incubated them

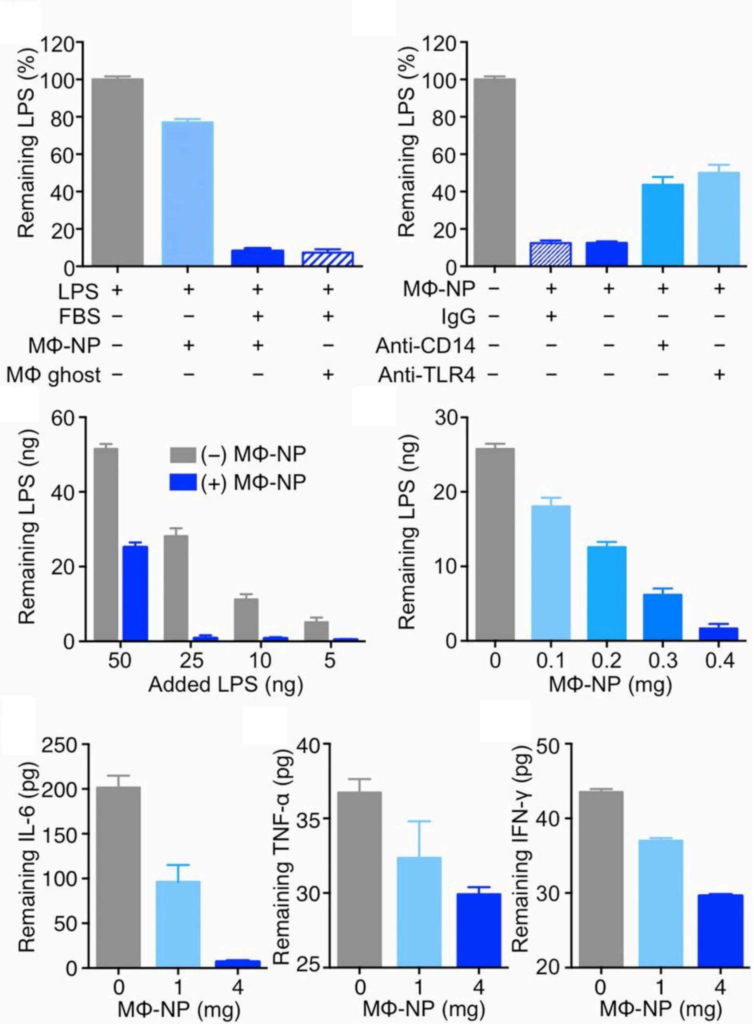

Figure 3.8: *In vitro* LPS and proinflammatory cytokine removal with MΦ-NPs. (A) LPS removal with MΦ-NPs with and without LPS binding protein (LBP) supplemented from FBS. MΦghost with an equivalent amount of protein was included as a control to assess membrane activity loss. (B) LPS removal with MΦ-NPs with and without nonspecific IgG and antibodies blocking CD14 and TLR4, respectively. (C) Quantification of LPS removal with a fixed amount of MΦ-NPs (0.4 mg) while varying the amount of added LPS. (D) Quantification of LPS removal with a fixed amount of LPS (25 ng) while varying the amount of added MΦ-NPs. (E-G) Removal of proinflammatory cytokines, including (E) IL-6, (F) TNF-α, and (G) IFN-γ, with MΦ-NPs. In all studies, three samples were used in each group.

with varying amounts of LPS (5, 10, 25, and 50 ng, respectively). After collecting nanoparticles with ultracentrifuge, it was found that 0.4 mg MΦ-NPs neutralized up to 25 ng LPS (Figure 3.8C). In the second experiment, we fixed the total amount of LPS at 25 ng and varied the amounts of MΦ-NPs (0, 0.1, 0.2, 0.3, and 0.4 mg, respectively). When the MΦ-NP concentration was increased from 0.1 to 0.4 mg, a linear decrease of LPS remaining in the supernatant was observed, with 0.4 mg MΦ-NPs again required to neutralize 25 ng LPS (Figure 3.8D). Together, the dual assays indicate a removal capacity of 62.5 ng LPS per milligram of MΦ-NPs.

The ability of MΦ-NPs to sequester proinflammatory cytokines, including IL-6, TNFα, and IFN-γ, was also investigated. Solutions with known initial concentrations of the cytokines were added to different concentrations of MΦ-NPs and incubated at 37 °C for 30 min, at which time nanoparticles were removed by ultracentrifugation and the amount of cytokine remaining in the supernatant was quantified. As shown in Figure 3.8 E-G, 1 mg of MΦ- NPs removed 105.1 pg of IL-6, 4.3 pg of TNF, and 6.5 pg of IFN-γ from the mixture, corresponding to cytokine removal efficiencies of 52.6%, 11.6%, and 14.8%, respectively. When 4 mg of MΦ-NPs was added, 194.4 pg of IL-6, 6.7 pg of TNFα, and 13.9 pg of IFN-γ were removed from the mixture, corresponding to cytokine removal yields of 97.2%, 18.1%, and 31.6%, respectively. Thus, MΦ- NPs can effectively sequester various types of proinflammatory cytokines in a concentration-dependent manner.

To evaluate functional neutralization of LPS, we used engineered HEK293 TLR4 reporter cells that produce secreted embryonic alkaline phosphatase (SEAP) in response to TLR4 activation (Figure 3.9A). When free LPS was added into the cell culture, pronounced TLR4 activation was observed within 5 h. However, when LPS was incubated with MΦ-NPs before their addition to the culture, TLR4 activation was abrogated. Incubation of LPS with RBC-NPs and PLGA nanoparticles functionalized with synthetic polyethylene glycol (PEG-NPs) were ineffective in inhibiting TLR4 activation, confirming that LPS neutralization was specific to MΦ-NPs. LPS induces macrophage overproduction of intracellular nitric oxide (iNO) by inducible NO synthase [365], which triggers further inflammatory cascades in activated cells. Macrophages incubated with free LPS showed a continual increase of iNO, whereas LPS incubated with MΦ-NPs was unable to enhance iNO production, revealing a clear inhibitory effect (Figure 3.9B); control RBC-NPs or PEG-NPs had no such activity.

Endothelial cells respond to minute LPS exposures by rapidly inducing expression of the cell adhesion molecule E-selectin [391]. We incubated cultured human umbilical vein endothelial cells (HUVECs) with LPS and quantified E-selectin expression by enzyme immunoassay. As shown in Figure 3.9C, 10 ng/mL LPS caused a continuous increase in HUVEC E-selectin expression; but this increase was completely blocked by coincubation with 1 mg/mL of MΦ-NPs. Control RBC-NPs and PEG-NPs did not inhibit the overexpression of E-selectin by HUVECs, confirming the specificity of MΦ-NPs in LPS neutralization. Three hours after adding LPS, cells were also stained with antibodies to fluorescently label E- selectin. Under the microscope, HUVECs incubated with LPS alone, LPS with RBC-NPs, and LPS with PEG-NPs, showed strong labeling in the cytoplasmic and nuclear peripheral regions with a fluorescent anti-E-selectin antibody; in contrast, little expression was observed on

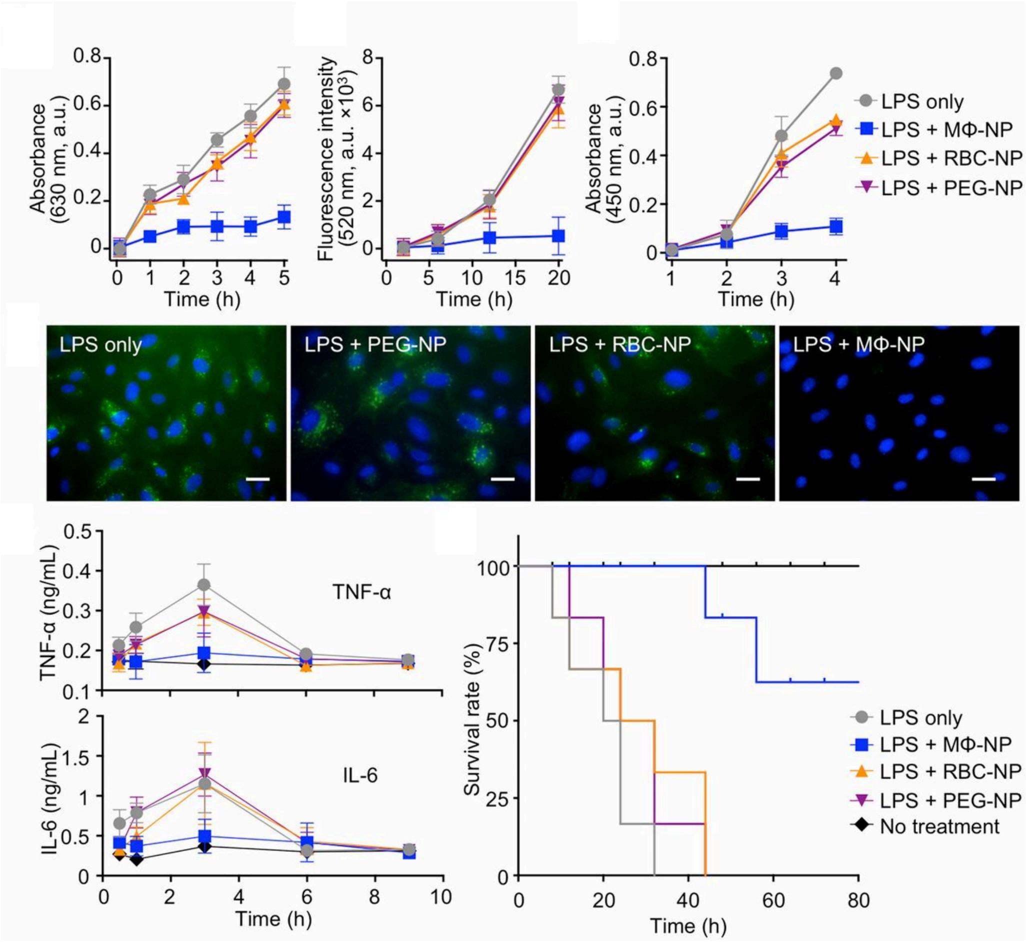

Figure 3.9: *In vitro* and *in vivo* LPS neutralization with MΦ-NPs. (A-C) LPS-inducible cell functions, including (A) TLR4 activation on HEK293 cells, (B) intracellular nitric oxide (iNO) production from J774 macrophages, and (C) E-selectin expression of HUVECs, were studied by stimulating corresponding cells with LPS alone or LPS mixed with MΦ-NPs, RBC-NPs, or PEG-NPs, respectively. (D) Fluorescent images collected from samples in C after 4 h of in- cubation. Cells were stained with mouse anti-human E-selectin, followed by staining with anti-mouse IgG Alexa 488 conjugates (green) and DAPI (blue). (Scale bars: 5 μm.) Three samples were used in each group. (E and F) For *in vivo* evaluation, (E) levels of proinflammatory cytokines, including TNF-α and IL-6, in plasma (n = 6) and (F) survival (n = 10) were studied after injecting mice with LPS alone or LPS mixed with MΦ-NPs, RBC-NPs, or PEG-NPs. Untreated mice were also included as a control group.

HUVECs incubated with LPS together with MΦ-NPs (Figure 3.9D). These results further confirm the capability of MΦ-NPs to functionally neutralize LPS.

LPS neutralization by MΦ-NPs *in vivo* was evaluated in mice by examining inhibition of acute inflammatory responses to endotoxin. LPS (5 μg/kg) was injected via tail vein and blood collected at various time points to measure the level of proinflammatory cytokines, including TNFα and IL-6 by ELISA. Cytokine levels reached maximums 3 h following injection of LPS alone, returning to baseline levels by 6 h. In the treatment group where MΦ-NPs at a dosage of 80 mg/kg were injected immediately after LPS, no increase in cytokine levels was observed. In contrast, when MΦ-NP treatment was replaced with RBC-NPs or PEG- NPs, cytokine levels followed similar kinetics to the LPS-only group. These studies demonstrate potent and specific LPS neutralization by the MΦ-NPs *in vivo*.

To further validate the *in vivo* LPS neutralization capability of MΦ-NPs, we sensitized mice to lethal effects of LPS using 800 mg/kg D-galactosamine hydrochloride [392], 30 min before LPS ± nanoparticle injection. A single dose of LPS (5 μg/kg) caused 100% mortality in the D-galactosamine-sensitized mice within 32 h of injection. Mice in the treatment groups (n = 10) received an i.v. injection of MΦ-NPs, RBC-NPs, or PEG-NPs at a dose of 200 mg/kg. In the group treated with MΦ-NPs, 60% of mice survived the lethal LPS challenge, whereas RBC-NPs and PEG-NPs failed to significantly improve survival rate in the LPS-challenged mice. These results together validate the potential of MΦ-NPs as endotoxin bioscavengers.

Finally, the therapeutic potential of MΦ-NPs was examined in a live infection model of Gram-negative bacterial sepsis. Mice were challenged intraperitoneally with

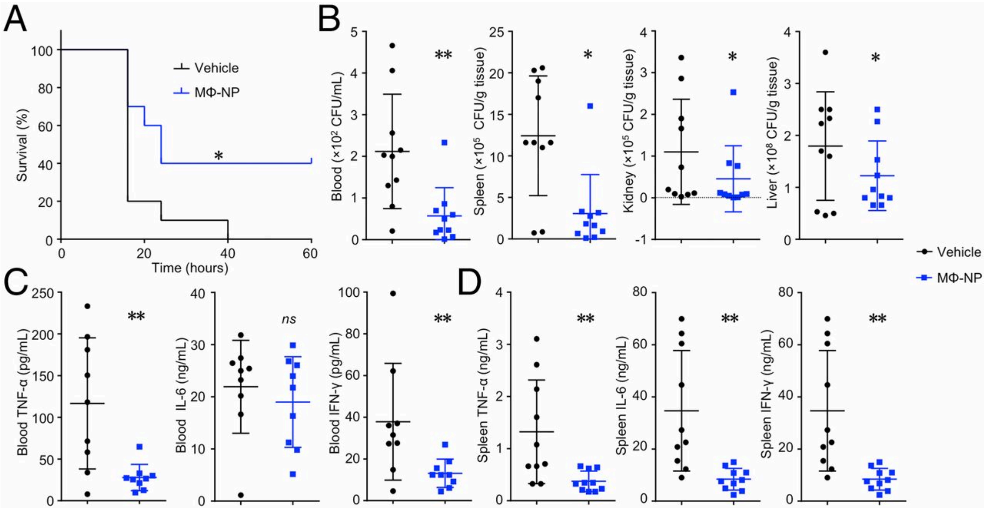

Figure 3.10: *In vivo* therapeutic efficacy of MΦ-NPs evaluated with a mouse bacteremia model. (A) Survival curve of mice with bacteremia after treatment with MΦ-NPs (n = 10). (B) Bacteria enumeration in blood, spleen, kidney, and liver at 4 h after MΦ-NPs were intraperitoneally injected. (C and D) Proinflammatory cytokines, including IL-6, TNF-α, and IFN-γ, from the blood and spleen were quantified with a cytometric bead array (ns, not significant; $*P < 0.05$, $**P < 0.01$).

a lethal dose of *Escherichia coli* (1×10^7 cfu) and treated with either MΦ-NPs (300 mg/kg) or 10% sucrose solution as the vehicle control 30 min after bacterial challenge. In this lethal challenge model, all animals in the control group treated with sucrose solution died, whereas 4 of 10 animals treated with a single dose of MΦ-NPs reached the experimental endpoint of 60 h, revealing a significant survival benefit ($P < 0.05$, Figure 3.10A). In another cohort of mice, we examined acute bacterial dissemination to key organs, including the blood, spleen, kidney, and liver, 4 h after bacterial challenge ± MΦ-NP treatment. In the blood and spleen of the mice treated with MΦ-NPs, bacterial counts were significantly lower compared with those of the control group, whereas the kidney and liver from mice of both groups showed comparable bacterial counts (Figure 3.10B). Reduction of bacterial burden in the blood and spleen conferred by MΦ-NPs corresponded to a significant reduction of proinflammatory cytokines, including IL-6, TNF-α, and IFN-γ, in these organs (Figure 3.10C). Reversal of the pathologic processes of septicemia and cytokine storm to favor improved bactericidal clearance is certainly multifactorial, but may include reduced development of macrophage LPS tolerance by its sequestration, competitive inhibition of immunosuppressive cytokines such as IL-10, and absorption of bacterial cytotoxins (e.g.,*E. Coli* pore-forming α-hemolysin) or immunosuppressive factors [e.g.,*E. Coli* TIR-containing protein C (TcpC)].

3.2.4 Conclusions

In summary, we have demonstrated a therapeutic potential of MΦ-NPs for sepsis control through an apparent two-step neutralization process: LPS neutralization in the first step followed by cytokine sequestration in the second step. MΦ-NPs function as an LPS and cytokine decoy, binding the proinflammatory factors through their cognate PRR and cytokine receptors in a manner decoupled from signal transduction and transcriptional activation of macrophage inflammatory cascades. By thus inhibiting the systemic inflammatory response, MΦ-NPs confer a significant survival benefit during septic shock. Unlike conventional endotoxin neutralization agents that compete with endotoxin binding pathways and may be associated with significant clinical toxicity, MΦ-NPs take advantage of the common functionality of endo- toxin binding to macrophages, allowing for a "universal" neutralization approach across different Gram-negative bacterial genus, species, and strains. The top-down fabrication of MΦ-NPs effecively replicates endotoxin-binding motifs on the target cells that are otherwise difficult to identify, purify, and conjugate. Coating macrophage membranes onto nanoparticle surfaces significantly increases the surface-to-volume ratio of given membrane materials, which is critical for efficient endotoxin neutralization.

In theory, similar first-step benefits as an adjunctive therapeutic agent could be afforded by MΦ-NPs against Gram-positive bacterial sepsis pathogens, by scavenging lipoteichoic acids and peptidoglycan via cognate PRRs TLR2/6, or fungal sepsis pathogens, by scavenging cell wall β-glucans with cognate PRR Dectin-1; although these indications remain to be studied in the manner undertaken with LPS/*E. coli* in the current paper. Moreover, in septic shock caused by any pathogen, second-step cytokine sequestration properties could be seen to mitigate the pathologic damage of cytokine storm. Given a likely i.v. route of administration, however, the pharmacodynamics efficacy of MΦ-NPs against tissue foci of infection such as pneumonia, peritonitis, or bone/soft tissue infections would have to be validated. Meanwhile, novel LPS-binding ligands have been engineered and applied for endotoxin neutralization and detoxification in sepsis [393]. With a lipid-like structure, they can be introduced onto MΦ-NPs through methods such as lipid insertion [394] or membrane hybridization [395], both of which have been validated for functionalizing nanoparticles coated with different cell membranes. Overall, MΦ-NPs represent a promising biomimetic detoxification strategy that may ultimately improve the clinical outcome of sepsis patients, potentially shifting the current paradigm of clinical detoxification therapy.

3.3 Biomimetic Platelet-Camouflaged Nanorobots for Binding and Isolation of Biological Threats

3.3.1 Introduction

Robots have become commonplace in today's world through their application to diverse domains such as manufacturing, service, defense, and healthcare. These automated devices can locomote themselves and perform different tasks in various environments across different scales. The efficient locomotion capacity and advanced biological functionality of natural microscopic subjects, such as motile cells like leukocyte and spermatozoa, have inspired scientists to recreate this form of locomotion and function using artificial robots with similar dimensions. Over the last decade, considerable progress in materials science and nanotechnology has led to remarkable advances in the development and operation of manmade nanorobots mimicking their natural counterparts. [396–405] Synthetic nanorobots based on a variety of materials and nanostructures have demonstrated efficient locomotion capacity by harvesting thrust from either localized chemical reactions or from external stimuli. [406–412] Like their natural counterparts, these versatile manmade nanorobots possess advanced locomotive capabilities, including precise speed egulation and spatial motion control, along with self-organization and collective movement, allowing for tremendous potential applications, ranging from targeted drug delivery, [413–415] to environmental remediation, [416, 417] and nanoscale manipulations for lithography and imaging. [418, 419] As advanced nanorobot capabilities are being developed, proper attention must be given to overcome key challenges for their operation in real-life biological environments. [420,421] Although some types of nanorobots have been functionalized with various bioreceptors for imparting specific recognition of target biomolecules, [422] the viability of these nanorobots relies largely on synthetic nanomaterials, which are susceptible to immune response or biofouling processes in physiological systems, and may eventually hinder their effectiveness. Therefore, new bioinspired and bioengineered approaches, based on the incorporation of natural materials into the nanorobot design, may provide a unique and robust means to address these limitations associated with synthetic materials.

Biomimetic design approaches have recently emerged as a novel paradigm to address the aforementioned limitations of synthetic nanomaterials for biomedical operation. [423,424] By taking inspiration from nature, especially the circulating cells such as erythrocytes, leukocytes, and platelets, essential biological functions of these natural cells can be potentially imparted into synthetic systems. One exciting research area is to mimic cellular membranes, which play very important roles in cells' biointerfacing with the incredibly complex biological environment. Particularly, human platelets have inspired the design of functional nanocarriers owing to their many functions responsible for immune evasion, [425,426] subendothelium adhesion, [427,428] pathogen interactions, [429,430] as well as their essential role in hemostasis. [431] Therefore, the platelet membrane cloaking method, that is wrapping natural platelet cell membranes onto the surface of synthetic nanostructures and nanodevices, has provided a new attractive approach for developing functional nanoparticles with a bioengineered interface for diverse biomedical applications. [432]

Here we demonstrate the preparation of platelet-membrane- cloaked nanomotors (denoted “PL-motors”), by enclosing magnetic helical nanomotors with the plasma membrane of human platelets, for adsorption and isolation of platelet-targeted biological agents (Figure 3.11A). The PL-motors are synthesized using a template-assisted electrochemical deposition method followed by a cell membrane cloaking technique. The prepared PL-motors possess a membrane coating containing a wide variety of functional proteins associated with platelets. Magnetic propulsion offers fuel-free remote actuation and navigation abilities desired of biomimetic nanomotors. [398] Bridging the biological functions of platelet membrane with the locomotion capacity of synthetic nanomotors thus results in a powerful dynamic biomimetic system. The PL-motors offer remarkable biocompatibility and efficient propulsion in various untreated biological fluids. Significantly, these platelet-mimicking nanomotors can evade the body’s immune system and display a rapid locomotion in whole blood with no apparent biofouling, mimicking the movement of natural motile cells. Moreover, coupling the efficient propulsion of these biomimetic nanomotors with the unique surface chemistry properties of natural platelets enables attractive detoxification capabilities. To exemplify their biological function, we demonstrate that the PL-motors can be used to effectively adsorb Shiga toxin (Stx) using a Vero cell assay (VCA), resulting from the strong platelet-Stx binding enabled by the protein receptors presented on the platelet membrane. The PL-motors display also enhanced binding to platelet- adhering pathogens, which can be used for rapid bacteria isolation or targeted drug delivery. These platelet-membrane- camouflaged nanomotors with advanced fuel-free locomotion capabilities are thus expected to dramatically expand the domain of biomedical nanorobotic operations in physiological systems and to open new opportunities to nanomedicine.

3.3.2 Experimental Methods

Preparation and Characterization of PL-Motors

The PL-motors were prepared by enclosing magnetic helical nanomotors with the plasma membrane of human platelets. Platelet membrane derivation was performed as previously described. [432] Briefly, platelets were isolated from whole blood and then resuspended in PBS mixed with protease inhibitor tablets. The whole blood we used was human type O-blood with 1.5 mg mL^{-1} EDTA purchased from BioreclamationIVT. The platelet membrane was derived by a repeated freeze-thaw process and washed by centrifugation in PBS solution mixed with protease inhibitor tablets. Aliquots of platelet suspensions were first frozen at -80 °C , thawed at room temperature, and pelleted by centrifugation at 4000 × g for 3 min. Following three repeated washes, the pelleted platelet membranes were suspended in water and stored at -80 °C until use.

Helical nanomotors were synthesized using a template-assisted electrochemical deposition method. Before electrochemical deposition, a 75 nm gold film was sputtered on one side of a 400 nm pore size polycarbonate (Millipore, HTTP02500) membrane to serve as a working electrode using the Denton Discovery 18 (Moorestown, NJ, USA). A Pt wire and an Ag/AgCl (with 1 M KCl) were used as counter and reference electrodes, respectively. The sputtered membrane was then assembled in a plating cell with an aluminum foil serving as a contact. All electrochemical deposition steps were carried out at room temperature (22°C). Pd/Cu nanorods were deposited at -0.1

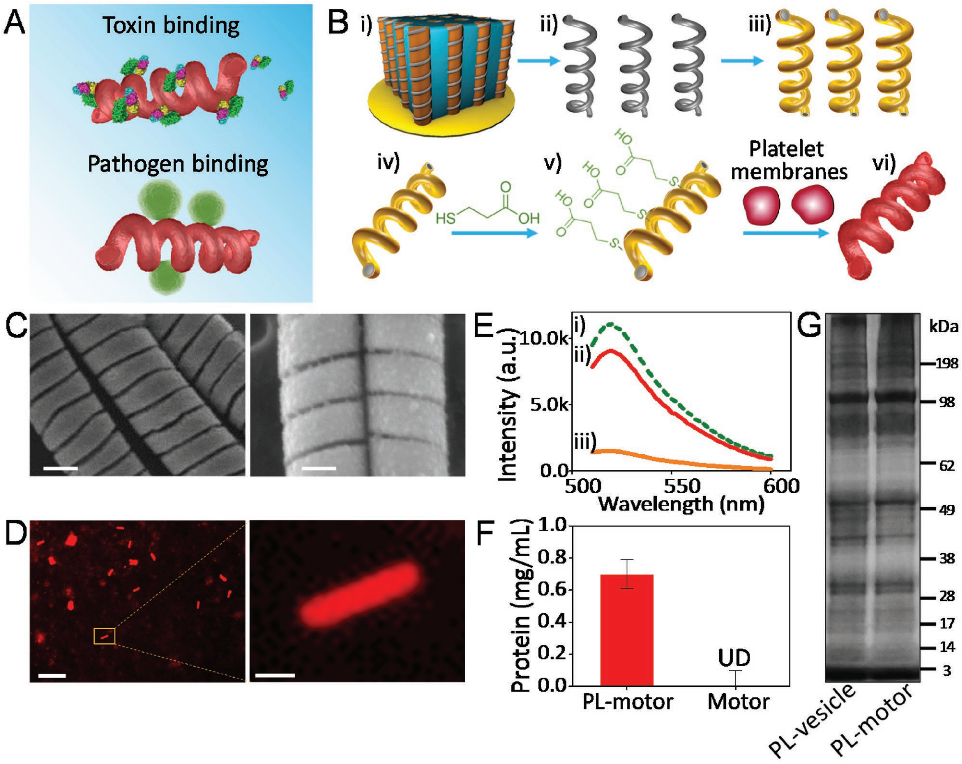

Figure 3.11: Preparation and characterization of platelet-membrane-cloaked magnetic helical nanomotors (denoted “PL-motors”). (A) Schematic of PL-motors for binding and isolation of platelet-specific toxins and pathogens. (B) Preparation of PL-motors: i) Pd/Cu co-electrodeposition in a polycarbonate membrane with pore size of 400 nm. ii) Dissolution of Cu using nitric acid and release of the helical Pd nanostructures. iii) Deposition of Ni/Au bilayer on the Pd helical nanostructure. iv) Collection of the helical nanostructures. v) Modification of the bare helical nanomotor surface with 3-mercaptopropionic acid (MPA). vi) Fusion of platelet-membrane-derived vesicles (denoted “PL-vesicles”) to the MPA-modified surface of the helical nanomotor. (C) Representative SEM images of the fabricated bare nanomotors without platelet coating (left) and PL-motors (right). Scale bars, 100 nm. (D) Fluorescent images of PL-motors covered with rhodamine-labeled platelet membranes. Scale bars, 20 μm (left) and 1 μm (right). (E) Fluorescence quenching assay to determine the platelet membrane coverage of the PL-motors. Fluorescence spectra of i) FITC-thiol only, ii) FITC-thiol and PL-motor mixture, and iii) FITC-thiol and bare motor mixture. (F) The measured weight of protein content on bare motors and PL-motors (both 10 mg mL^{-1}) stored in 1X PBS at 4 °C for 24 h. Error bars represent the standard deviation from three different measurements. UD, undetectable. (G) Sodium dodecyl sulfate polyacrylamide gel electrophoresis (SDS-PAGE) analysis of proteins presents on the PL-vesicles and the PL-motors. The samples were run at equal protein content and stained with Coomassie Blue.

V from the $PdCl_2$/Cu Cl_2 plating solution mixture containing 20×10^{-3} M Cu Cl_2, 30×10^{-3} M Pd Cl_2, and 0.1 M HCl with a total charge of 3C. After electrochemical deposition, the sputtered gold layer was completely removed by hand polishing with 3-4 micro m alumina slurry. The templates were dissolved in methylene chloride for 10 min to completely release the nanostructures. The latter were collected by centrifugation at 9000 rpm for 3 min and washed three times with methylene chloride, ethanol, and deionized water each, with a 3 min centrifugation after each wash. Then the Cu (of the Pd/Cu nanorods) was dissolved using an 8 M HNO_3 solution for 10 min, resulting in the formation of Pd nanohelices with 400 nm diameter and 3-5 μm length. The Pd nanostructures were then dispersed on glass slides, and coated with a 5 nm thick Ni layer by electron beam evaporation (using a deposition speed of 0.05 nm s^{-1}), and sputtered with a 5 nm Au layer. Afterward, the resulting magnetic nanomotors were incubated overnight with MPA (Sigma-Aldrich). Then, the MPA-modified helical nanomotors were incubated with platelet-membrane-derived vesicles (diameter 50-100 nm) under ultrasonication for 20 min. Scanning electron microscopy (SEM) images of bare helical nanomotors and PL-motors were obtained with a Phillips XL30 environmental scanning electron microscope (ESEM) instrument, using an acceleration voltage of 10 kV.

To further confirm the presence and cloaking of platelet membrane onto the surface of the motors, Platelet vesicles were labeled with DMPE-RhB (Avanti Polar Lipids, Inc.) and then incubated with the helical nanomotors. Fluorescence microscopy images were captured using EVOS FL, fluorescence microscope coupled with a 20× and 40× microscope objectives and fluorescence filter with red light excitation.

The fluorescence quenching assay to determine the platelet membrane coverage of the PL-motors was performed by incubating the PL-motors with a thiolated fluorescent ligand made of a synthesized FITC-thiol conjugate probe, and measuring the fluorescence spectra of the FITC-thiol, FITC-thiol, and PL-motor mixture, and FITC-thiol and bare motor mixture, at 520 nm by a Tecan Infinite M200 microplate reader. The thiolated fluorescent probe was prepared by first conjugating FITC to cysteamine 4-methoxytrityl resin (EMD Millipore) through N-hydroxysuccinimide (Thermo Scientific)-mediated amine coupling, followed by trifluoroacetic acid treatment to cleave the conjugate from the resin. To determine the protein content of the PL-motors, 10 mg mL^{-1} of both bare motors and PL-motors were centrifuged and resuspended with 1X PBS for three times, and a BCA colorimetric assay (Thermo Scientific) was used to determine the protein content. Briefly, the purple-colored reaction product of this assay is formed by the chelation of two molecules of BCA with one cuprous ion, and this water-soluble complex exhibits a strong absorbance at 562 nm that is nearly linear with increasing protein concentrations. Gel electrophoresis followed by protein staining with Coomassie Blue was also performed. The PL-vesicle and PL-motor samples containing equivalent total proteins were prepared in lithium dodecyl sulfate sample loading buffer (Invitrogen). The samples were then separated on a 4-12% Bis-Tris 17-well minigel in 3-(N-Morpholino)propanesulfonic acid (MOPS) running buffer using a Novex Xcell SureLock Electrophoresis System (Life Technologies). Finally, the protein columns were stained according to manufacturer's protocol.

Propulsion of PL-Motors

A Helmholtz coil pair was used to generate the magnetic rotation field for remote actuation. The frequency of the rotating magnetic field (15 mT) can be changed from 1 to 1000 Hz by a sinusoidal wave generator. The above magnetic nanohelices were dispersed in water droplets for rotation and translation motion tests. An inverted optical microscope (Nikon Instrument Inc. Ti-S/L100), coupled 20× and 40× objectives, a Hamamatsu digital camera C11440 and NIS Elements AR 3.2 software, were used for capturing movies of the swimming motion. The speed of the nanoswimmers was tracked using an NIS Elements tracking module ($n = 20$).

Shiga Toxin (Stx) Binding and Neutralization

To examine the adhesion of PL-motors with Shiga toxin (Stx), Stx (Toxin Technology, INC, lot# 62411V1) was labeled with fluorescein dye (FITC) following the specifications of a commercial FITC Labeling kit (MarkerGene, M0955). To evaluate the adhesion of Stx-FITC to PL-motors, 1 mg of PL-motors were immersed in the FITC-labeled Stx solution or in FITC dye solution (used as negative control) for 20 min under magnetic actuation (55 Hz, 15 mT). The fluorescence intensity corresponding to the Stx-FITC or FITC solutions was then measured (at 495 nm), before and after the PL-motors binding process, in order to calculate the amount of bound toxin. After the 20 min magnetic actuation, fluorescence microscopy images of the Stx-FITC@PL-motors and FITC dye solutions were taken, using EVOS FL microscope coupled with a 20× and 40× microscope objectives and a fluorescence filter with green light excitation. Furthermore, cellular toxicity was studied using a

Vero cell assay. To perform this experiment, fixed amounts of Stx (150 μL of 100 μg mL^{-1} dissolved in PBS buffer were mixed with equal amounts of PBS buffer containing 1 mg PL-motors, 1 mg bare motors (without platelet coating), or 0.07 mg PL-vesicles (containing equivalent proteins to 1 mg PL-motors). The positive and negative controls were PBS buffer with and without Stx, respectively. All the added toxin formulations have a final Stx concentration of 100 μg mL^{-1} along with a final volume of 150 μL. All samples were treated for 20 min under magnetic field (55 Hz, 15 mT), after which each formulation was added to Vero cell cultured wells (1.2×10^5 cells per well, n = 3 for each formulation) and incubated for 48 h. After the 48 h incubation, the cell viability was assessed using the CellTiter 96 Cell Proliferation Assay (Promega Corporation), based on an MTS tetrazolium compound. In brief, 10 μL of the MTS reagent were added into each well, mixed gently, and incubated at 37 °C for 4 h in a humidified CO_2 incubator. This was followed by reading the absorbance of the 96 well- plate at 490 nm using a plate reader. The quantity of formazan product as measured by Abs at 490 nm was directly proportional to the number of living cells. Microscopy images of Vero cells after the corresponding 48 h incubations were captured using an EVOS FL microscope coupled with a 20× and 40× microscope objectives.

Staphylococcus Aureus **(MRSA252) Bacteria Adherence and Isolation**

MRSA252 obtained from the American Type Culture Collection was cultured on tryptic soy broth (TSB) agar (Becton, Dickinson and Company) overnight at 37 °C . A single colony was inoculated in TSB medium at 37 °C in a rotary shaker. Overnight culture was refreshed in TSB medium at a 1:100 dilution at 37 °C under shaking for another 3 h until the OD600 of the culture medium reached ≈ 1.0 (logarithmic growth phase). The bacteria were washed and suspended in sterile PBS to a concentration of 1×10^8 CFU mL^{-1}. For the nanomotor adhesion study, aliquots of 0.8 mL of 1×10^8 CFU mL^{-1} MRSA252 were mixed with 1 mL of 100 mg mL^{-1} PL-motor, 1 mL of 100 mg mL^{-1} bare motors, 1 mL of 7.5 mg mL^{-1} PL-vesicle, or 1 mL of PBS for 20 min magnetic actuation at room temperature. The suspensions were then left 30 min at room temperature to have the precipitate settle down with a magnet placed below the suspension. After removal of the supernatant, the collected pellets were resuspended in PBS buffer and then fixed with formalin and stained with DAPI subsequently for fluorescence analysis, fluorescence microscopy imaging, and SEM imaging.

3.3.3 Results and Discussion

To obtain the nanostructures with desired geometric configuration and material components, we combine template-assisted electrodeposition and cell membrane cloaking techniques to prepare the PL-motors (Figure 3.11B). First of all, Pd nanohelices, with a diameter of 400 nm and length of 3-5 μm, were synthesized by a template-assisted electrochemical deposition method, followed by segment-selective chemical etching. [433, 434] The Pd nanohelices were then coated with a 5 nm thick nickel layer and a 5 nm gold layer by electron beam evaporation and sputter, respectively. The resulting bare magnetic nanomotors undergo an ex situ stabilization by overnight incubation with 3-mercaptopropionic acid (MPA) to introduce negative charges onto the gold surface, thus allowing the platelet membranes to coat on the negatively charged gold surface of the nanomotor. [435] The resulting nanomotors were subsequently incubated with platelet-membrane-derived vesicles (diameter 50-100 nm) under ultrasonication. The small nanoscale platelet vesicles, with high surface energy, tend to bind and fuse onto the negatively charged gold surface to minimize the free energy of the system. The ultrasonic mixing further enhanced the adsorption of platelet vesicles onto the gold surface of the nanomotors. This fusion process allowed for the retention of the bilayer structure of the platelet membrane and for the preservation of its protein function. In addition, due to the large asymmetric negative charge between the ectoplasmic and cytoplasmic surfaces of the platelet membranes, the outer surface of the platelet membrane is much more negatively charged than the inner surface. Therefore, electrostatic repulsion allowed the platelet vesicles to fuse onto the negatively charged motors at the right-side-out orientation of the membranes, which was similar to what has been observed using platelet-membrane-coated polymeric nanoparticle system. [432]

Figure 3.11C shows the scanning electron microscopy (SEM) images of bare helical nanomotors and PL-motors. The characteristic shape of the PL-motors, with their periodic helical structure, is not affected by the platelet coating, which is expected from the negligible thickness of the lipid bilayer on 400 nm diameter gold nanomotors. To further confirm the presence and cloaking of platelet membrane onto the surface of the motor, platelet-membrane-derived vesicles were labeled with 1,2-dimyristoyl-sn-glycero-3-phosphoethanolamine-N-lissamine rhodamine B sulfonyl (DMPE-RhB) prior to being coated on the nanomotors. Full coverage of the helical motors is illustrated in the fluorescence microscopy images in Figure 3.11D, indicating the successful incorporation of DMPE-RhB-labeled platelet vesicles onto the PL-motors. To further evaluate the completeness of membrane coverage on the motor surface, we studied the interactions between the PL-motors and a thiolated fluorescent ligand using a synthesized fluorescein isothiocyanate (FITC)-thiol conjugate probe. [436] As shown in Figure 3.11E, at the emission peak of 520 nm of the FITC-thiol, the bare motors incubated with the fluorescent probe exhibited a greatly reduced fluorescence intensity in comparison with free FITC-thiol, indicating the presence of fluorescence quenching resulted from the bare gold surface of the motors. Such a noticeable quenching effect is absent in the PL-motors incubated with the FITC-thiol. These results clearly indicate high coverage of platelet membrane on the surface of the nanomotors, which effectively shields the FITC-thiol probe from being quenched by the gold layer on the bare motors.

Next, the platelet membrane coating on the nanomotors was investigated in terms of its protein content. PL-motors were centrifuged and resuspended with 1X phosphate buffer saline (PBS) for three times to remove uncoated vesicles and obtain purified PL-motors. A bicinchoninic acid (BCA) protein assay was used to quantitatively measure the level of the membrane protein on the nanomotor surface. As shown in Figure 3.11F, PL-motors exhibited an increase in absorbance at 562 nm indicating the presence of protein content, which was further quantified to be 0.72 ± 0.10 mg mL^{-1} using a protein standard curve. In contrast, no detectable absorbance was observed for the bare nanomotors at the same motor concentration (10 mg mL^{-1}), suggesting no protein was found. Furthermore, gel electrophoresis followed by protein staining showed the protein profile of the purified platelet vesicles and PL-motors (Figure 3.11G). The protein profile of PL-motors matched closely to the platelet membrane vesicles which evidently demonstrated that platelet membrane can translocate to the nanomotors and that the preparation of PL-motors did not alter the profile of platelet membrane proteins.

An important feature of the platelet-mimicking nanomotors is their ability to resist biofouling, thus ensuring lasting and efficient propulsion of the motor in biological fluids. After having evaluated the preparation and characteristics of PL-motors, it is important to test their propulsion performance and antifouling property in various complex biological environments. The 5 s tracking of PL-motor movement in Figure 3.12A showcases the motor's propulsion performance in water, plasma, serum, and whole blood, respectively. Although the viscosity of each environment affects the propulsion, the resulting movement remains effective for PL-motor operation in biological environments, including whole blood. Figure 3.12B compares the propulsion performance of the PL-motors and of bare nanomotors in different media. It is observed that although their speeds are almost equal in water, the speeds of PL-motors in plasma, serum, and whole blood are significantly faster than the speeds of the bare nanomotors in the same solutions. The layer of natural platelet membrane covering the nanomotors enables their biocompatible and stable operation in whole blood with no apparent biofouling effects over prolonged periods of time. The 10 s tracking trajectory, shown in Figure 3.12C, illustrates the movement of a bare nanomotor in whole blood, which displays slow propulsion at a speed of ≈ 6 μs^{-1}. The propulsion is further hindered after incubation of the bare nanomotors in whole blood for 1 h. Apparently the bare nanomotors undergo severe protein fouling, which dramatically hinders their propulsion effiency. In contrast, the PL-motors display long-term efficient magnetic propulsion in whole blood. The 10 s tracking trajectories in Figure 3.12D (demonstrate the magnetic propulsion of PL-motors in whole blood at 0 and 60 min, respectively. These images illustrate no apparent diminution of the propulsion efficiency over the prolonged actuation in whole blood. Such effective resistance to biofouling and propulsion behavior of the PL-motors were further evaluated by incubating them in undiluted whole blood for 48 h. The 10 s tracking trajectories in Figure 3.12E illustrate the movement of the PL-motors before and after such 48 h incubation. These data indicate that the PL-motors maintain efficient propulsion at similar speeds after such prolonged incubation, indicating that biofouling effects are negligible. Apparently, the platelet membrane coating shields the nanomotor from biofouling effects in untreated biological fluids.

The therapeutic potential of PL-motors was first evaluated by assessing their selective binding and rapid isolation of Shiga toxin (Stx), a toxin produced by *Escherichia coli* that can induce hemolytic uremic syndrome. [437, 438] Shiga and Shiga-like toxins can bind platelets via specific glycosphingolipid receptors, while such binding further contributes to the thrombocytopenia, platelet activation, and microthrombus formation observed in hemolytic-uremic syndrome. [439] To characterize the binding of the Stx with the PL-motors, Stx is labeled with fluorescein (FITC) and then incubated with PL-motors for a 20 min magnetic actuation. Equal amount of FITC dye (without Stx conjugation) for nonspecific staining was used as a negative control. The amount of Stx absorbed on the PL-motors was calculated

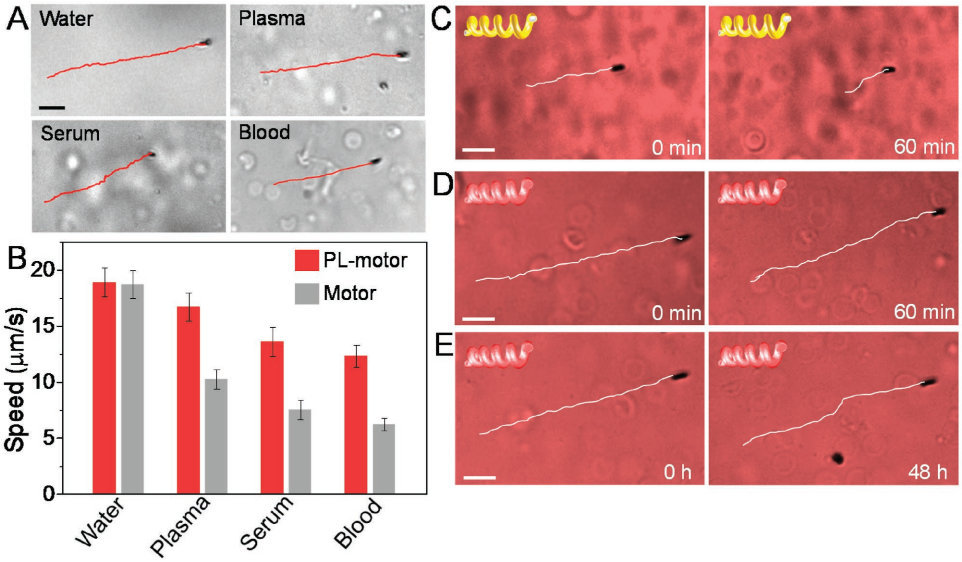

Figure 3.12: Propulsion performance and anti-biofouling capability of PL-motors. (A) Tracking trajectories showing the propulsion of PL-motors in various media over a timeframe of 5 s. (B) Speed comparison of PL-motors with bare helical nanomotors (without platelet membrane coating) in various media. (C) 10 s tracking showing the propulsion of a bare motor in whole blood at the beginning and after 60 min. (D) 10 s tracking showing the propulsion of a PL-motor in whole blood at the beginning and after 60 min. (E) 10 s tracking showing the propulsion of a PL-motor in whole blood without being incubated in the blood and with a 48 h incubation in the blood. Scale bars, 10 μm. The nanomotors were propelled using a frequency of 55 Hz and a magnetic field strength of 15 mT. Speed data are averaged for 20 nanomotors under the same conditions.

by measuring the Stx-FITC fluorescence intensity before and after incubation with PL-motors. As displayed in Figure 3.13A, a 51% of fluorescence intensity decrease in the Stx-FITC conjugate solution was measured, compared to only 15% decrease in the FITC dye with same amount of PL-motors. Figure 3.13B displays fluorescence microscopy images of the PL-motors after 20 min propulsion in the Stx-FITC and FITC solution, respectively. A significantly stronger fluorescence binding was observed for the PL-motors in the Stx-FITC solution. These results confirm the effective and selective binding of the PL-motors to the Shiga toxin.

To further examine the binding of Stx to PL-motors and the successful toxin neutralization, cellular cytotoxicity was studied using a Vero cell assay, as Stx is cytotoxic in the VCA from 10 pg mL^{-1} and above. [440] Experiments were performed by mixing the Stx toxin solution with equal amounts of PBS buffer containing 1 mg PL-motors, 1 mg bare motors (without platelet coating), or 0.07 mg platelet vesicles. Based on the protein weight measurement displayed in Figure 3.11F, 0.07 mg platelet vesicles, which contain equivalent proteins to those in 1 mg PL-motors are used as static control (without magnetic actuation) of PL-motors. The resulting Stx toxin concentration in the above three solutions was 100 μg mL^{-1}. PBS buffer with and without toxin was also added as positive and negative control, respectively. After 20 min of magnetic operation, all of the five formulations were added to Vero cell cultured wells for 48 h incubation. Cell viability was then accessed by an (3-(4,5-dimethylthiazol-2-yl)-5-(3- carboxymethoxyphenyl)-2-(4-sulfophenyl)-2H-tetrazolium) (MTS) assay following the manufacturer's protocol. As illustrated in Figure 3.13C, the PL-motors treated formulation displayed a cell viability of 92%, which is comparable with the

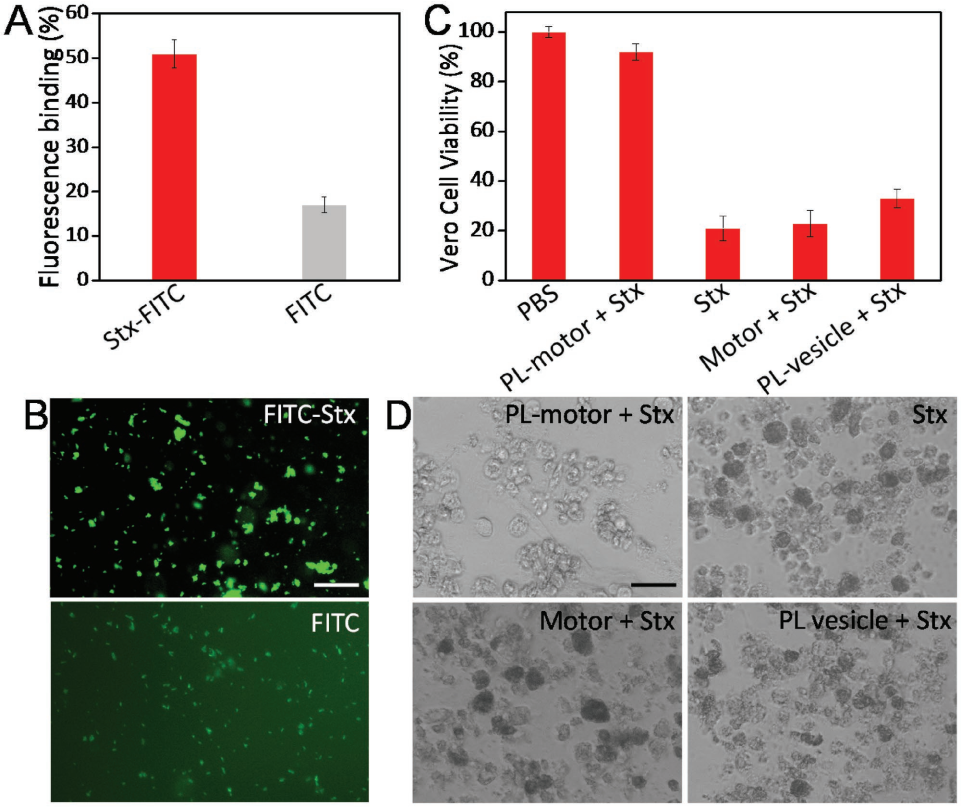

Figure 3.13: Shiga toxin (Stx) binding and neutralization study. (A) Fluorescence binding percentage (measured at 495 nm) of the FITC-Stx conjugate and FITC dye only with PL-motors (red and gray bars, respectively). (B) Fluorescence images of PL-motors after 20 min incubation in whole blood and propulsion in FITC-Stx and FITC dye solution only. (C) Vero cell viability (1.2×10^5 cells per well, n = 3) after 48 h of incubation with Stx solution, PL-motors + Stx, bare motors + Stx, and PL-vesicles + Stx. In all experiments the toxin concentration used was 100 μg mL $^{-1}$ along with a final volume of 150 μL. PBS without Stx was used as a control. One mg of PL-motors (âĽĹ1.3×10^8 motors) was used for the detoxification process along with 20 min of propulsion time. Vero cell viability was measured by using an MTS assay. (D) Microscopy images showing the morphologies of the corresponding Vero cells treated with different formulations. Each image is representative of five examined sections. Scale bars, 50 μm.

PBS buffer control without toxin. In contrast, the viability of bare nanomotors and static platelet vesicles (containing equivalent proteins to those in the PL-motors, but without active motion) was only 21% and 31%, respectively. Figure 3.13D displays the microscopy images showing the morphology of the Vero cells after 48 h incubation with the four formulations. It is clearly observed that the Vero cells are healthy for the formulation treated by the PL-motors, while all other three formulations induce severe damage and lysis to the cells. By cloaking platelet vesicles on the magnetic nanomotors, the PL-motors can serve as moving decoys that attract toxins for cell protection by diverting the toxins away from the cell target and rendering the environment nontoxic to cells. It is estimated that each PL-motor could adsorb $\approx 1.9 \times 10^{3}$ units of Stx. In addition, under magnetic actuation, the large-scale collective location of the PL-motors can dramatically accelerate their binding with Stx, thus enhancing the adsorption process.

We further examined the therapeutic potential of PL-motors for binding and isolation of platelet-adhering pathogens. Oppounistic bacteria, including several strains of staphylococci and streptococci, are able to bind to platelets either directly through a bacterial surface protein or indirectly by a plasma bridging molecule that links bacterial and platelet surface receptors. [441, 442] Such bacteria-platelet interactions further lead to immune evasion and bacteremia. [430] MRSA252, a strain of methicillin-resistant *Staphylococcus aureus* (MRSA) expressing a serine-rich adhesin for platelets (SraP) which can bind to platelets, [443] was used as a model pathogen for PL-motor adhesion study. After 20 min of incubation and magnetic actuation of the PL-motors (1 mg) in MRSA252 suspension (1×10^{5} colony-forming units (CFU)

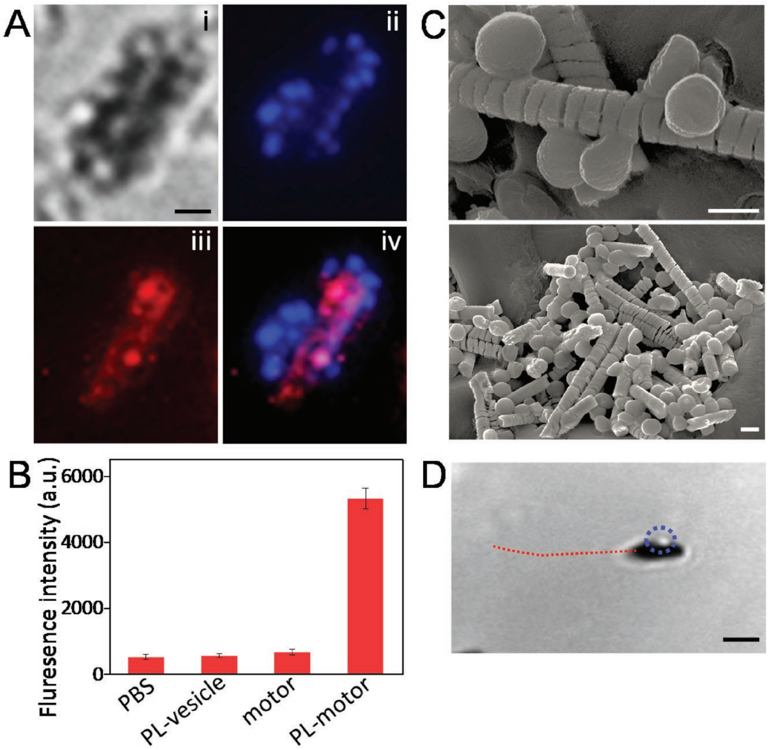

Figure 3.14: Binding and isolation of platelet-adhering pathogens. (A)Microscopic images showing the binding of MRSA252 bacteria with PL-motors: i) bright field, ii) blue fluorescence channel showing the DAPI stained bacteria, iii) red fluorescence channel showing the DMPE-RhB-labeled platelet membrane, and iv) the overlay. (B) Normalized fluorescence intensity of DAPI stained MRSA252 bacteria retained on the PL-motors (n = 3). Bare nanomotors, PL-vesicles, and PBS were used as controls. Scale bars, 500 nm. (C) SEM images of MRSA252 bacteria attached to PL-motors. Scale bars, 500 nm. (D) Microscopy image showing one-the-fly isolation of a bacterium (labeled with blue circle) with a PL-motor. Scale bar, 2 μm.

mL^{-1}), the PL-motors were recollected through precipitation with a magnet. Bare motors and PL-vesicles were used as negative and static (without magnetic actuation) controls. The retained bacteria on the collected pellets were fixed with formalin and stained with 4',6-diamidino-2-phenylindole (DAPI) subsequently. Figure 3.14A displays microscopy images, showing the binding of the DAPI-stained bacteria on a DMPE-RhB- labeled PL-motor. Bare motors and PL-vesicles showed negligible increase of the DAPI signal compared to the PBS control of Figure 3.14B. On the other hand, PL-motors exhibit a tenfold increase in DAPI fluorescence intensity compared to all other groups, which manifests a significant adhesion of the bacteria to PL-motors. It is estimated that each PL-motor can capture ≈ 15 bacteria. The SEM images in Figure 3.14C also clearly show the preferential binding of the bacteria to the PL-motors, while the microscopy image in Figure 3.14D displays "on-the-fly" isolation of a bacterium by a PL-motor. This new nanorobot platform thus presents a unique approach for achieving rapid, direct, and real-time isolation of pathogens.

3.3.4 Conclusions

In summary, we have developed a unique PL-motor system, based on a magnetically actuated helical nanomotor cloaked with a natural platelet membrane, as a new type of biomimetic nanorobot possessing efficient locomotion and distinct biological functions. The intrinsic antifouling properties of the platelet membrane coating shield the synthetic nanomotor from biological environments. A study of the propulsion of PL-motors in whole blood clearly demonstrated their distinct antifouling properties due to platelet membrane coating, which led to efficient propulsion in real complex biological environment, as compared to the uncoated nanomotor counterpart. The platelet membrane coating of these biomimetic nanomotors imparts also strong affinity to platelet-adhering toxins and pathogens, which along with the efficient motor movement leads to efficient detoxification capacity, as illustrated by the rapid binding and isolation of Shiga toxin and MRSA252 bacteria. This study demonstrates that biomembrane coating can significantly enhance the binding of nanorobots to bacterial toxins and pathogens, which may provide a new means of using nanorobots for biodetoxification and for targeted treatment of infectious diseases. Magnetic actuation of a large amount of PL-motors can further enhance the binding and isolation process of these biothreats. Overall, the PL-motors represent a powerful biomimetic platform based on the fusion of biological materials and synthetic nanorobots. Such bioinspired nanorobots are expected to open a variety of new attractive opportunities for both nanomedicine and nanomotor communities.

Chapter 3.1, in full, is a reprint of the material as it appears in PLOS Neglected Tropical Diseases, 2018, Soumita Das, Pavimol Angsantikul, Christine Le, Denny Bao, Yukiko Miyamoto, Weiwei Gao, Liangfang Zhang, and Lars Eckmann. Chapter 3.2, in full, is a reprint of the material as it appears in Proceedings of the National Academy of Sciences, 2017, Soracha Thamphiwatana, Pavimol Angsantikul, Tamara Escajadillo, Qiangzhe Zhang, Joshua Olson, Brian T. Luk, Sophia Zhang, Ronnie H. Fang, Weiwei Gao, Victor Nizet, and Liangfang Zhang. Chapter 3.3, in full, is a reformatted of the material as it appears in Advanced Materials, 2018, Jinxing Li, Pavimol Angsantikul, Wenjuan Liu, Berta Esteban-Fernández de Ávila, Xiaocong Chang, Elodie Sandraz, Yuyan Liang, Siyu Zhu, Yue Zhang, Chuanrui Chen, Weiwei

Gao, Liangfang Zhang, and Joseph Wang. The dissertation author was the co-primary investigator and co-author of these papers.

Chapter 4

Conclusions

4.1 Coating nanoparticles with gastric epithelial cell membrane for targeted antibiotic delivery against *Helicobacter pylori* infection

Helicobacter pylori (*H. pylori*) infection with its vast prevalence is responsible for various gastric diseases including gastritis, peptic ulcers, and gastric malignancy. While effective, current treatment regimens are challenged by a fast-declining eradication rate due to the increasing emergence of *H. pylori* strains resistant to existing antibiotics. Therefore, there is an urgent need to develop novel antibacterial strategies against *H. pylori.* Inspired by the natural pathogen-host interactions and adhesion, we report the development of a novel targeted nanocarrier for *H. pylori* infection treatment. The plasma membranes of AGS cells (a gastric epithelial cell line) are coated onto antibiotic-loaded polymeric cores, the resulting biomimetic nanoparticles (AGS-NPs) carries the same surface antigens as the source AGS cells and thus have inherent adhesion to *H. pylori* bacteria. The AGS-NPs demonstrated preferential binding and retention with *H. pylori* when compared to control nanoparticles coated with synthetic PEG. Furthermore, the AGS-NPs loaded with model drug, showed superior bactericidal effect *in vitro* and were able to effectively reduce bacterial burden in a mouse model of *H. pylori* infection. In addition, mouse body weight and stomach histology in a toxicity test showed no adverse effects from the AGS-NPs. Overall, the results demonstrate that AGS-NPs are an effective and safe approach for targeted antibiotic delivery to treat *H. pylori* infection.

4.2 Micromotors spontaneously neutralize gastric acid for pH-responsive payload release

Magnesium(Mg)-based micromotors are of considerable interest for biomedical applications, as they can utilize both the Mg-acid or Mg-water reactions for their propulsion and can potentially operate in different biological environments (e.g. serum, whole blood or gastric acid). We have demonstrated that acid-powered Mg-based micromotors can efficiently induce a transient change in local physiological pH. Specifically, the reaction of the micromotor with gastric fluid leads to rapid proton depletion and micromotor propulsion which concurrently generate localized fluid convection and prompt efficient acid neutralization without affecting the normal stomach function or causing adverse effects. When coupled to a pH-sensitive payload-containing polymer coating, this pH change can lead to autonomous release of the encapsulated cargo. This approach represents a distinct advantage over conventional stimuli-responsive drug release systems, as the micromotors themselves actively create the desired local pH essential to trigger the release. The "built-in" micromotor strategy could potentially be used to adjust physiological environment *in vivo* to achieve desired conditions for triggered payload release.

4.3 Micromotor-enabled active drug delivery for *in vivo* treatment of stomach infection

While synthetic micromotors have been extensively investigated under *in vitro* conditions for over a decade, their *in vivo* function has rarely been explored. Recent research effort has resulted in micromotors that display fast movement in complex biological media, and possess efficient cargo loading, transport, and release, along with good biocompatibility. These new capabilities have made synthetic micromotors promising active delivery tools for *in vivo* applications including treatment of gastrointestinal diseases. In this work we conducted the first, to the best of our knowledge, study to evaluate the therapeutic efficacy of a drug-loaded Mg-based micromotor for *in vivo* treatment of *H. pylori* infection in a mouse model. This pioneering study demonstrated that Mg micromotors, loaded with clinical doses of drugs, can be retained efficiently in the mouse stomach wall, and hence significantly reduced bacteria burden compared to passive drug carriers. The enhanced drug delivery capability is coupled with a built-in neutralization of the gastric fluid, hence eliminating the needs for PPIs. Additionally, no acute adverse consequences were detected from the micromotor treatment in the mouse models. Consequently, this early work of micromotor for *in vivo* infection treatment opens the door to a new line of micromotor-based therapeutic platforms for *in vivo* treatment of GI diseases.

4.4 Neutralization of cholera toxin with nanoparticle decoys for treatment of cholera

Despite the advancement in medicine, cholera remains a major public health challenge in many regions of the world. Current medical strategies to combat this infection can be divided into preventive and therapeutic measures. Although immunization could offer individuals the protection from infection, but the only current FDA-approved cholera vaccine comprises live bacterial agent which has the potential for reversion and cause disease itself. On the other hand, the conventional treatment, which involves supportive rehydration, could improve survival but severe disease symptoms can still persist for days during the treatment course. As an alternative therapeutic strategy, we developed a nanoparticulate intervention to serve as a decoy to neutralize cholera toxin, which is the primary cause of diarrheal symptoms in cholera. The nanoparticles surface-functionalized with GM1 ganglioside, cholera toxin-binding lipid, were fabricated by a robust single-step synthesis. The GM1-coated nanoparticles (GM1-NPs) demonstrated the capability to bind and divert cholera toxin from interacting to their target host cells, thereby preventing its effects on epithelial electrolyte and fluid secretion *in vitro* and *in vivo*. This detoxification strategy represents a novel interventional approach whose mechanisms of action are physiologically distinct from vaccination, rehydration, or antibiotics, hence significantly broadening the medical treatment options against cholera. Furthermore, a similar nanoparticle platform coated with an appropriate toxin-binding receptor may also offer a promising therapeutic opportunity for other toxin-mediated diseases.

4.5 Macrophage-like nanoparticles concurrently absorbing endotoxins and proinflammatory cytokines for sepsis management

Clinical evidence has indicated that the systemic spread of endotoxins from septic infection plays a crucial role in the pathogenesis of Gram-negative bacterial sepsis. However, currently there are no effective ways to manage the diverse endotoxins released by different bacteria. The emerging cell-membrane coated nanoparticle technology allows the inclusion of natural cell membrane on the surface nanoparticles and opens up a new range of biomedical applications that would otherwise be extremely difficult for synthetic platforms to achieve. One such use is to serve as a decoy for harmful molecules within the body. For instance, endotoxins exploit the receptors on macrophage membranes to induce responses on the host cells, and by directly using a toxin's natural substrate as a coating material, it is possible to target the working mechanism of the toxin in a manner that doesn't require specifically tailoring the nanoparticle to the toxin. This work demonstrates the therapeutic potential of a macrophage-like nanoparticle for sepsis control through a powerful two-step neutralization process: endotoxin neutralization in the first step followed by cytokine sequestration in the second step. The biomimetic nanoparticles possess an antigenic exterior identical to macrophage cells. The inherited capability to bind to endotoxins and proinflammatory cytokines has been demonstrated *in vitro* and conferred a significant survival advantage in a mouse *E. coli* bacteremia model. Unlike conventional endotoxin neutralization agents that compete with endotoxin binding pathways and may be associated with significant clinical toxicity, MΦ-NPs take advantage of the common functionality of endotoxin binding to macrophages, allowing for a "universal" neutralization approach across different Gram-negative bacterial genus, species, and strains. This detoxification strategy may provide a first-in-class treatment option for sepsis and ultimately improve the clinical outcome of patients.

4.6 Biomimetic Platelet-Camouflaged Nanorobots for Binding and Isolation of Biological Threats

Manmade nanorobots based on a variety of materials and nanostructures have demonstrated efficient locomotion capacity by harvesting propulsion from either localized chemical reactions or from external stimuli. These nanorobots possess advanced locomotive capabilities, including precise speed regulation and spatial motion control, which has significant implication for a variety of biomedical use. By taking inspiration from nature, especially the circulating cells such as erythrocytes, leukocytes, and platelets, essential biological functions of these natural cells can be potentially imparted into synthetic systems. One exciting research area is to mimic cellular membranes, which play very important roles in cells' biointerfacing with the incredibly complex biological environment. Particularly, human platelets have inspired the design of functional nanocarriers owing to their many biological functions including complex interactions with bacteria and bacterial toxins. We report a biologically interfaced nanorobot made of magnetic helical nanomotors cloaked with the plasma membrane of human platelets. The resulting biomimetic nanorobots possess a biological membrane coating consisting of diverse functional proteins associated with human platelets. The biointerfaced nanorobots display platelet-mimicking properties, including adhesion and binding to toxins and platelet-adhering pathogens, such as Shiga toxin and *Staphylococcus aureus* bacteria. The locomotion capacity and platelet-mimicking biological function of the biomimetic nanomotors offer efficient binding and isolation of these biological threats. The

PL-motors represent a powerful biomimetic platform that merges the biointerfacing advantages from the biological membrane and the advanced locomotion control from the magnetic nanomotors. Such bioinspired nanorobots thus holds considerable promise for diverse biomedical and biodefense applications.

Bibliography

[1] A. S. Fauci and D. M. Morens, “The perpetual challenge of infectious diseases,” *N. Engl. J. Med.*, vol. 366, pp. 454–461, Feb 2012.

[2] P. E. Farmer, “Shattuck Lecture. Chronic infectious disease and the future of health care delivery,” *N. Engl. J. Med.*, vol. 369, pp. 2424–2436, Dec 2013.

[3] L. A. Baxt, A. C. Garza-Mayers, and M. B. Goldberg, “Bacterial subversion of host innate immune pathways,” *Science*, vol. 340, pp. 697–701, May 2013.

[4] R. L. Modlin and B. R. Bloom, “TB or not TB: that is no longer the question,” *Sci Transl Med*, vol. 5, p. 213sr6, Nov 2013.

[5] P. C. Appelbaum and P. A. Hunter, “The fluoroquinolone antibacterials: past, present and future perspectives,” *Int. J. Antimicrob. Agents*, vol. 16, pp. 5–15, Sep 2000.

[6] P. Poulikakos and M. E. Falagas, “Aminoglycoside therapy in infectious diseases,” *Expert Opin Pharmacother*, vol. 14, pp. 1585–1597, Aug 2013.

[7] D. M. Morens, G. K. Folkers, and A. S. Fauci, “The challenge of emerging and re-emerging infectious diseases,” *Nature*, vol. 430, pp. 242–249, Jul 2004.

[8] B. Spellberg, J. G. Bartlett, and D. N. Gilbert, “The future of antibiotics and resistance,” *N. Engl. J. Med.*, vol. 368, pp. 299–302, Jan 2013.

[9] R. C. Moellering, “Discovering new antimicrobial agents,” *Int. J. Antimicrob. Agents*, vol. 37, pp. 2–9, Jan 2011.

[10] O. C. Farokhzad and R. Langer, “Impact of nanotechnology on drug delivery,” *ACS Nano*, vol. 3, pp. 16–20, Jan 2009.

[11] B. P. Timko, K. Whitehead, W. Gao, D. S. Kohane, O. Farokhzad, D. Anderson, and R. Langer, “Advances in drug delivery,” *Annual Review of Materials Research*, vol. 41, pp. 1–20, 2011.

[12] R. A. Petros and J. M. DeSimone, “Strategies in the design of nanoparticles for therapeutic applications,” *Nat Rev Drug Discov*, vol. 9, pp. 615–627, Aug 2010.

[13] M. E. Davis, Z. G. Chen, and D. M. Shin, “Nanoparticle therapeutics: an emerging treatment modality for cancer,” *Nat Rev Drug Discov*, vol. 7, pp. 771–782, Sep 2008.

[14] L. Zhang, D. Pornpattananangku, C. M. Hu, and C. M. Huang, “Development of nanoparticles for antimicrobial drug delivery,” *Curr. Med. Chem.*, vol. 17, no. 6, pp. 585–594, 2010.

[15] W. L. Lee and W. C. Liles, “Endothelial activation, dysfunction and permeability during severe infections,” *Curr. Opin. Hematol.*, vol. 18, pp. 191–196, May 2011.

[16] S. L. Taylor, V. Wahl-Jensen, A. M. Copeland, P. B. Jahrling, and C. S. Schmaljohn, “Endothelial cell permeability during hantavirus infection involves factor XII-dependent increased activation of the kallikrein-kinin system,” *PLoS Pathog.*, vol. 9, no. 7, p. e1003470, 2013.

[17] M. R. DiStasi and K. Ley, “Opening the flood-gates: how neutrophil-endothelial interactions regulate permeability,” *Trends in immunology*, vol. 30, no. 11, pp. 547–556, 2009.

[18] M. N. Swartz, “Clinical practice. Cellulitis,” *N. Engl. J. Med.*, vol. 350, pp. 904–912, Feb 2004.

[19] E. A. Azzopardi, E. L. Ferguson, and D. W. Thomas, “The enhanced permeability retention effect: a new paradigm for drug targeting in infection,” *J. Antimicrob. Chemother.*, vol. 68, pp. 257–274, Feb 2013.

[20] O. C. Boerman, G. Storm, W. J. Oyen, L. van Bloois, J. W. van der Meer, R. A. Claessens, D. J. Crommelin, and F. H. Corstens, “Sterically stabilized liposomes labeled with indium-111 to image focal infection,” *J. Nucl. Med.*, vol. 36, pp. 1639–1644, Sep 1995.

[21] W. J. Oyen, O. C. Boerman, G. Storm, L. van Bloois, E. B. Koenders, R. A. Claessens, R. M. Perenboom, D. J. Crommelin, J. W. van der Meer, and F. H. Corstens, "Detecting infection and inflammation with technetium-99m-labeled Stealth liposomes," *J. Nucl. Med.*, vol. 37, pp. 1392–1397, Aug 1996.

[22] O. C. Boerman, W. J. Oyen, L. van Bloois, E. B. Koenders, J. W. van der Meer, F. H. Corstens, and G. Storm, "Optimization of technetium-99m-labeled PEG liposomes to image focal infection: effects of particle size and circulation time," *J. Nucl. Med.*, vol. 38, pp. 489–493, Mar 1997.

[23] P. Laverman, E. T. Dams, G. Storm, T. G. Hafmans, H. J. Croes, W. J. Oyen, F. H. Corstens, and O. C. Boerman, "Microscopic localization of PEG-liposomes in a rat model of focal infection," *J Control Release*, vol. 75, pp. 347–355, Aug 2001.

[24] A. H. Kaim, T. Wischer, T. O'Reilly, G. Jundt, J. Frohlich, G. K. von Schulthess, and P. R. Allegrini, "MR imaging with ultrasmall superparamagnetic iron oxide particles in experimental soft-tissue infections in rats," *Radiology*, vol. 225, pp. 808–814, Dec 2002.

[25] K. Dillen, C. Bridts, P. Van der Veken, P. Cos, J. Vandervoort, K. Augustyns, W. Stevens, and A. Ludwig, "Adhesion of PLGA or Eudragit/PLGA nanoparticles to Staphylococcus and Pseudomonas," *Int J Pharm*, vol. 349, pp. 234–240, Feb 2008.

[26] V. Sambhy, B. R. Peterson, and A. Sen, "Antibacterial and hemolytic activities of pyridinium polymers as a function of the spatial relationship between the positive charge and the pendant alkyl tail," *Angew. Chem. Int. Ed. Engl.*, vol. 47, no. 7, pp. 1250–1254, 2008.

[27] e. l. R. Kenawy, S. D. Worley, and R. Broughton, "The chemistry and applications of antimicrobial polymers: a state-of-the-art review," *Biomacromolecules*, vol. 8, pp. 1359–1384, May 2007.

[28] L. Liu, K. Xu, H. Wang, P. K. Tan, W. Fan, S. S. Venkatraman, L. Li, and Y. Y. Yang, "Self-assembled cationic peptide nanoparticles as an efficient antimicrobial agent," *Nat Nanotechnol*, vol. 4, pp. 457–463, Jul 2009.

[29] F. Nederberg, Y. Zhang, J. P. Tan, K. Xu, H. Wang, C. Yang, S. Gao, X. D. Guo, K. Fukushima, L. Li, J. L. Hedrick, and Y. Y. Yang, "Biodegradable

nanostructures with selective lysis of microbial membranes," *Nat Chem*, vol. 3, pp. 409–414, May 2011.

[30] S. K. Choi, A. Myc, J. E. Silpe, M. Sumit, P. T. Wong, K. McCarthy, A. M. Desai, T. P. Thomas, A. Kotlyar, M. M. Holl, B. G. Orr, and J. R. Baker, "Dendrimer-based multivalent vancomycin nanoplatform for targeting the drug-resistant bacterial surface," *ACS Nano*, vol. 7, pp. 214–228, Jan 2013.

[31] K. H. Choi, H. J. Lee, B. J. Park, K. K. Wang, E. P. Shin, J. C. Park, Y. K. Kim, M. K. Oh, and Y. R. Kim, "Photosensitizer and vancomycin-conjugated novel multifunctional magnetic particles as photoinactivation agents for selective killing of pathogenic bacteria," *Chem. Commun. (Camb.)*, vol. 48, pp. 4591–4593, May 2012.

[32] H. Gu, P. Ho, E. Tong, L. Wang, and B. Xu, "Presenting vancomycin on nanoparticles to enhance antimicrobial activities," *Nano letters*, vol. 3, no. 9, pp. 1261–1263, 2003.

[33] G. Qi, L. Li, F. Yu, and H. Wang, "Vancomycin-modified mesoporous silica nanoparticles for selective recognition and killing of pathogenic gram-positive bacteria over macrophage-like cells," *ACS Appl Mater Interfaces*, vol. 5, pp. 10874–10881, Nov 2013.

[34] A. J. Kell, G. Stewart, S. Ryan, R. Peytavi, M. Boissinot, A. Huletsky, M. G. Bergeron, and B. Simard, "Vancomycin-modified nanoparticles for efficient targeting and preconcentration of Gram-positive and Gram-negative bacteria," *ACS Nano*, vol. 2, pp. 1777–1788, Sep 2008.

[35] J. Chen, C. Zhang, Q. Liu, X. Shao, C. Feng, Y. Shen, Q. Zhang, and X. Jiang, "Solanum tuberosum lectin-conjugated PLGA nanoparticles for nose-to-brain delivery: in vivo and in vitro evaluations," *J Drug Target*, vol. 20, pp. 174–184, Feb 2012.

[36] R. B. Umamaheshwari and N. K. Jain, "Receptor mediated targeting of lectin conjugated gliadin nanoparticles in the treatment of Helicobacter pylori," *J Drug Target*, vol. 11, pp. 415–423, Aug 2003.

[37] P. J. Huang, L. L. Tay, J. Tanha, S. Ryan, and L. K. Chau, "Single-domain antibody-conjugated nanoaggregate-embedded beads for targeted detection of pathogenic bacteria," *Chemistry*, vol. 15, pp. 9330–9334, Sep 2009.

[38] L.-L. Tay, P.-J. Huang, J. Tanha, S. Ryan, X. Wu, J. Hulse, and L.-K. Chau, "Silica encapsulated sers nanoprobe conjugated to the bacteriophage tailspike protein for targeted detection of salmonella," *Chemical Communications*, vol. 48, no. 7, pp. 1024–1026, 2012.

[39] F. Chen, J. Zhou, F. Luo, A. B. Mohammed, and X. L. Zhang, "Aptamer from whole-bacterium SELEX as new therapeutic reagent against virulent Mycobacterium tuberculosis," *Biochem. Biophys. Res. Commun.*, vol. 357, pp. 743–748, Jun 2007.

[40] N. Duan, S. Wu, X. Chen, Y. Huang, Y. Xia, X. Ma, and Z. Wang, "Selection and characterization of aptamers against Salmonella typhimurium using whole-bacterium Systemic Evolution of Ligands by Exponential Enrichment (SELEX)," *J. Agric. Food Chem.*, vol. 61, pp. 3229–3234, Apr 2013.

[41] M. Deysine, A. Chua, and A. Gerboth, "Selective delivery of antibiotics to experimental infection by autologous white blood cells," *Surg Forum*, vol. 30, pp. 38–39, 1979.

[42] R. T. Mehta, T. J. McQueen, A. Keyhani, and G. Lopez-Berestein, "Phagocyte transport as mechanism for enhanced therapeutic activity of liposomal amphotericin B," *Chemotherapy*, vol. 40, no. 4, pp. 256–264, 1994.

[43] E. Briones, C. I. Colino, and J. M. Lanao, "Delivery systems to increase the selectivity of antibiotics in phagocytic cells," *J Control Release*, vol. 125, pp. 210–227, Feb 2008.

[44] F. Chellat, Y. Merhi, A. Moreau, and L. Yahia, "Therapeutic potential of nanoparticulate systems for macrophage targeting," *Biomaterials*, vol. 26, pp. 7260–7275, Dec 2005.

[45] C. Kelly, C. Jefferies, and S. A. Cryan, "Targeted liposomal drug delivery to monocytes and macrophages," *J Drug Deliv*, vol. 2011, p. 727241, 2011.

[46] S. P. Vyas, M. E. Kannan, S. Jain, V. Mishra, and P. Singh, "Design of liposomal aerosols for improved delivery of rifampicin to alveolar macrophages," *Int J Pharm*, vol. 269, pp. 37–49, Jan 2004.

[47] M. H. Xiong, Y. J. Li, Y. Bao, X. Z. Yang, B. Hu, and J. Wang, "Bacteria-responsive multifunctional nanogel for targeted antibiotic delivery," *Adv. Mater. Weinheim*, vol. 24, pp. 6175–6180, Dec 2012.

[48] W. Gao, J. M. Chan, and O. C. Farokhzad, “pH-Responsive nanoparticles for drug delivery,” *Mol. Pharm.*, vol. 7, pp. 1913–1920, Dec 2010.

[49] T. T. Kararli, “Comparison of the gastrointestinal anatomy, physiology, and biochemistry of humans and commonly used laboratory animals,” *Biopharm Drug Dispos*, vol. 16, pp. 351–380, Jul 1995.

[50] M. H. Schmid-Wendtner and H. C. Korting, “The pH of the skin surface and its impact on the barrier function,” *Skin Pharmacol Physiol*, vol. 19, no. 6, pp. 296–302, 2006.

[51] S. Simoes, V. Slepushkin, N. Duzgunes, and M. C. Pedroso de Lima, “On the mechanisms of internalization and intracellular delivery mediated by pH-sensitive liposomes,” *Biochim. Biophys. Acta*, vol. 1515, pp. 23–37, Nov 2001.

[52] E. Imbuluzqueta, C. Gamazo, J. Ariza, and M. J. Blanco-Prieto, “Drug delivery systems for potential treatment of intracellular bacterial infections.,” 2010.

[53] C. J. Chu, J. Dijkstra, M. Z. Lai, K. Hong, and F. C. Szoka, “Efficiency of cytoplasmic delivery by pH-sensitive liposomes to cells in culture,” *Pharm. Res.*, vol. 7, pp. 824–834, Aug 1990.

[54] V. A. Slepushkin, S. Simoes, P. Dazin, M. S. Newman, L. S. Guo, M. C. Pedroso de Lima, and N. Duzgunes, “Sterically stabilized pH-sensitive liposomes. Intracellular delivery of aqueous contents and prolonged circulation in vivo,” *J. Biol. Chem.*, vol. 272, pp. 2382–2388, Jan 1997.

[55] S. Simoes, J. N. Moreira, C. Fonseca, N. Duzgunes, and M. C. de Lima, “On the formulation of pH-sensitive liposomes with long circulation times,” *Adv. Drug Deliv. Rev.*, vol. 56, pp. 947–965, Apr 2004.

[56] P. Lutwyche, C. Cordeiro, D. J. Wiseman, M. St-Louis, M. Uh, M. J. Hope, M. S. Webb, and B. B. Finlay, “Intracellular delivery and antibacterial activity of gentamicin encapsulated in pH-sensitive liposomes,” *Antimicrob. Agents Chemother.*, vol. 42, pp. 2511–2520, Oct 1998.

[57] C. Cordeiro, D. J. Wiseman, P. Lutwyche, M. Uh, J. C. Evans, B. B. Finlay, and M. S. Webb, “Antibacterial efficacy of gentamicin encapsulated in pH-sensitive liposomes against an in vivo Salmonella enterica serovar typhimurium intracellular infection model,” *Antimicrob. Agents Chemother.*, vol. 44, pp. 533–539, Mar 2000.

[58] B. C. Ponnappa, I. Dey, G. C. Tu, F. Zhou, M. Aini, Q. N. Cao, and Y. Israel, "In vivo delivery of antisense oligonucleotides in pH-sensitive liposomes inhibits lipopolysaccharide-induced production of tumor necrosis factor-alpha in rats," *J. Pharmacol. Exp. Ther.*, vol. 297, pp. 1129–1136, Jun 2001.

[59] K. Tschaikowsky, "Protein kinase C inhibitors suppress LPS-induced TNF production in alveolar macrophages and in whole blood: the role of encapsulation into liposomes," *Biochim. Biophys. Acta*, vol. 1222, pp. 113–121, May 1994.

[60] K. D. Lee, Y. K. Oh, D. A. Portnoy, and J. A. Swanson, "Delivery of macromolecules into cytosol using liposomes containing hemolysin from Listeria monocytogenes," *J. Biol. Chem.*, vol. 271, pp. 7249–7252, Mar 1996.

[61] K. E. Beauregard, K. D. Lee, R. J. Collier, and J. A. Swanson, "pH-dependent perforation of macrophage phagosomes by listeriolysin O from Listeria monocytogenes," *J. Exp. Med.*, vol. 186, pp. 1159–1163, Oct 1997.

[62] L. Zhang and S. Granick, "How to stabilize phospholipid liposomes (using nanoparticles)," *Nano Lett.*, vol. 6, pp. 694–698, Apr 2006.

[63] L. Zhang, L. Hong, Y. Yu, S. C. Bae, and S. Granick, "Nanoparticle-assisted surface immobilization of phospholipid liposomes," *J. Am. Chem. Soc.*, vol. 128, pp. 9026–9027, Jul 2006.

[64] D. Pornpattananangkul, S. Olson, S. Aryal, M. Sartor, C. M. Huang, K. Vecchio, and L. Zhang, "Stimuli-responsive liposome fusion mediated by gold nanoparticles," *ACS Nano*, vol. 4, pp. 1935–1942, Apr 2010.

[65] S. Thamphiwatana, V. Fu, J. Zhu, D. Lu, W. Gao, and L. Zhang, "Nanoparticle-stabilized liposomes for pH-responsive gastric drug delivery," *Langmuir*, vol. 29, pp. 12228–12233, Oct 2013.

[66] D. Pornpattananangkul, L. Zhang, S. Olson, S. Aryal, M. Obonyo, K. Vecchio, C. M. Huang, and L. Zhang, "Bacterial toxin-triggered drug release from gold nanoparticle-stabilized liposomes for the treatment of bacterial infection," *J. Am. Chem. Soc.*, vol. 133, pp. 4132–4139, Mar 2011.

[67] W. Gao, D. Vecchio, J. Li, J. Zhu, Q. Zhang, V. Fu, J. Li, S. Thamphiwatana, D. Lu, and L. Zhang, "Hydrogel containing nanoparticle-stabilized liposomes for topical antimicrobial delivery," *ACS Nano*, vol. 8, pp. 2900–2907, Mar 2014.

[68] A. F. Radovic-Moreno, T. K. Lu, V. A. Puscasu, C. J. Yoon, R. Langer, and O. C. Farokhzad, “Surface charge-switching polymeric nanoparticles for bacterial cell wall-targeted delivery of antibiotics,” *ACS Nano*, vol. 6, pp. 4279–4287, May 2012.

[69] Y. H. Lin, C. H. Chang, Y. S. Wu, Y. M. Hsu, S. F. Chiou, and Y. J. Chen, “Development of pH-responsive chitosan/heparin nanoparticles for stomach-specific anti-Helicobacter pylori therapy,” *Biomaterials*, vol. 30, pp. 3332–3342, Jul 2009.

[70] M. H. Xiong, Y. Bao, X. Z. Yang, Y. C. Wang, B. Sun, and J. Wang, “Lipase-sensitive polymeric triple-layered nanogel for "on-demand" drug delivery,” *J. Am. Chem. Soc.*, vol. 134, pp. 4355–4362, Mar 2012.

[71] C. M. Hu, S. Aryal, and L. Zhang, “Nanoparticle-assisted combination therapies for effective cancer treatment,” *Ther Deliv*, vol. 1, pp. 323–334, Aug 2010.

[72] P. Deol, G. K. Khuller, and K. Joshi, “Therapeutic efficacies of isoniazid and rifampin encapsulated in lung-specific stealth liposomes against Mycobacterium tuberculosis infection induced in mice,” *Antimicrob. Agents Chemother.*, vol. 41, pp. 1211–1214, Jun 1997.

[73] S. Labana, R. Pandey, S. Sharma, and G. K. Khuller, “Chemotherapeutic activity against murine tuberculosis of once weekly administered drugs (isoniazid and rifampicin) encapsulated in liposomes,” *Int. J. Antimicrob. Agents*, vol. 20, pp. 301–304, Oct 2002.

[74] A. Gursoy, E. Kut, and S. Ozkirimli, “Co-encapsulation of isoniazid and rifampicin in liposomes and characterization of liposomes by derivative spectroscopy,” *Int J Pharm*, vol. 271, pp. 115–123, Mar 2004.

[75] E. Banin, A. Lozinski, K. M. Brady, E. Berenshtein, P. W. Butterfield, M. Moshe, M. Chevion, E. P. Greenberg, and E. Banin, “The potential of desferrioxamine-gallium as an anti-Pseudomonas therapeutic agent,” *Proc. Natl. Acad. Sci. U.S.A.*, vol. 105, pp. 16761–16766, Oct 2008.

[76] M. Halwani, B. Yebio, Z. E. Suntres, M. Alipour, A. O. Azghani, and A. Omri, “Co-encapsulation of gallium with gentamicin in liposomes enhances antimicrobial activity of gentamicin against Pseudomonas aeruginosa,” *J. Antimicrob. Chemother.*, vol. 62, pp. 1291–1297, Dec 2008.

[77] M. Halwani, S. Blomme, Z. E. Suntres, M. Alipour, A. O. Azghani, A. Kumar, and A. Omri, “Liposomal bismuth-ethanedithiol formulation enhances antimicrobial activity of tobramycin,” *Int J Pharm*, vol. 358, pp. 278–284, Jun 2008.

[78] M. Alipour, Z. E. Suntres, R. M. Lafrenie, and A. Omri, “Attenuation of Pseudomonas aeruginosa virulence factors and biofilms by co-encapsulation of bismuth-ethanedithiol with tobramycin in liposomes,” *J. Antimicrob. Chemother.*, vol. 65, pp. 684–693, Apr 2010.

[79] M. Alipour, C. Dorval, Z. E. Suntres, and A. Omri, “Bismuth-ethanedithiol incorporated in a liposome-loaded tobramycin formulation modulates the alginate levels in mucoid Pseudomonas aeruginosa,” *J. Pharm. Pharmacol.*, vol. 63, pp. 999–1007, Aug 2011.

[80] M. Alhariri and A. Omri, “Efficacy of liposomal bismuth-ethanedithiol-loaded tobramycin after intratracheal administration in rats with pulmonary Pseudomonas aeruginosa infection,” *Antimicrob. Agents Chemother.*, vol. 57, pp. 569–578, Jan 2013.

[81] R. M. Schiffelers, G. Storm, M. T. ten Kate, L. E. Stearne-Cullen, J. G. den Hollander, H. A. Verbrugh, and I. A. Bakker-Woudenberg, “Liposome-enabled synergistic interaction of antimicrobial agents,” *J Liposome Res*, vol. 12, no. 1-2, pp. 121–127, 2002.

[82] R. M. Schiffelers, G. Storm, M. T. ten Kate, L. E. Stearne-Cullen, J. G. den Hollander, H. A. Verbrugh, and I. A. Bakker-Woudenberg, “In vivo synergistic interaction of liposome-coencapsulated gentamicin and ceftazidime,” *J. Pharmacol. Exp. Ther.*, vol. 298, pp. 369–375, Jul 2001.

[83] A. A. Kadry, S. A. Al-Suwayeh, A. R. Abd-Allah, and M. A. Bayomi, “Treatment of experimental osteomyelitis by liposomal antibiotics,” *J. Antimicrob. Chemother.*, vol. 54, pp. 1103–1108, Dec 2004.

[84] H. Li, W. Sparks, and B. Bonning, “Protocols for microapplicator-assisted infection of lepidopteran larvae with baculovirus,” *J Vis Exp*, Aug 2008.

[85] C. O. Onyeji, C. H. Nightingale, D. P. Nicolau, and R. Quintiliani, “Efficacies of liposome-encapsulated clarithromycin and ofloxacin against Mycobacterium avium-M. intracellulare complex in human macrophages,” *Antimicrob. Agents Chemother.*, vol. 38, pp. 523–527, Mar 1994.

[86] S. Majumdar, D. Flasher, D. S. Friend, P. Nassos, D. Yajko, W. K. Hadley, and N. Duzgunes, "Efficacies of liposome-encapsulated streptomycin and ciprofloxacin against Mycobacterium avium-M. intracellulare complex infections in human peripheral blood monocyte/macrophages," *Antimicrob. Agents Chemother.*, vol. 36, pp. 2808–2815, Dec 1992.

[87] D. Y. Singh and N. K. Prasad, "Double liposomes mediated dual drug targeting for treatment of Helicobacter pylori infections," *Pharmazie*, vol. 66, pp. 368–373, May 2011.

[88] P. Jain, S. Jain, K. N. Prasad, S. K. Jain, and S. P. Vyas, "Polyelectrolyte coated multilayered liposomes (nanocapsules) for the treatment of Helicobacter pylori infection," *Mol. Pharm.*, vol. 6, no. 2, pp. 593–603, 2009.

[89] S. Sengupta, D. Eavarone, I. Capila, G. Zhao, N. Watson, T. Kiziltepe, and R. Sasisekharan, "Temporal targeting of tumour cells and neovasculature with a nanoscale delivery system," *Nature*, vol. 436, pp. 568–572, Jul 2005.

[90] S. Aryal, C. M. Hu, and L. Zhang, "Combinatorial drug conjugation enables nanoparticle dual-drug delivery," *Small*, vol. 6, pp. 1442–1448, Jul 2010.

[91] S. Aryal, C. M. Hu, and L. Zhang, "Polymeric nanoparticles with precise ratiometric control over drug loading for combination therapy," *Mol. Pharm.*, vol. 8, pp. 1401–1407, Aug 2011.

[92] L. Zhang, A. F. Radovic-Moreno, F. Alexis, F. X. Gu, P. A. Basto, V. Bagalkot, S. Jon, R. S. Langer, and O. C. Farokhzad, "Co-delivery of hydrophobic and hydrophilic drugs from nanoparticle-aptamer bioconjugates," *ChemMedChem*, vol. 2, pp. 1268–1271, Sep 2007.

[93] N. Kolishetti, S. Dhar, P. M. Valencia, L. Q. Lin, R. Karnik, S. J. Lippard, R. Langer, and O. C. Farokhzad, "Engineering of self-assembled nanoparticle platform for precisely controlled combination drug therapy," *Proc. Natl. Acad. Sci. U.S.A.*, vol. 107, pp. 17939–17944, Oct 2010.

[94] U. S. Toti, B. R. Guru, M. Hali, C. M. McPharlin, S. M. Wykes, J. Panyam, and J. A. Whittum-Hudson, "Targeted delivery of antibiotics to intracellular chlamydial infections using PLGA nanoparticles," *Biomaterials*, vol. 32, pp. 6606–6613, Sep 2011.

[95] S. Ramteke, N. Ganesh, S. Bhattacharya, and N. K. Jain, "Triple therapy-based targeted nanoparticles for the treatment of Helicobacter pylori," *J Drug Target*, vol. 16, pp. 694–705, Nov 2008.

[96] S. Ramteke, N. Ganesh, S. Bhattacharya, and N. K. Jain, "Amoxicillin, clarithromycin, and omeprazole based targeted nanoparticles for the treatment of H. pylori," *J Drug Target*, vol. 17, pp. 225–234, Apr 2009.

[97] S. Ramteke and N. K. Jain, "Clarithromycin- and omeprazole-containing gliadin nanoparticles for the treatment of Helicobacter pylori," *J Drug Target*, vol. 16, pp. 65–72, Jan 2008.

[98] R. Pandey and G. K. Khuller, "Oral nanoparticle-based antituberculosis drug delivery to the brain in an experimental model," *J. Antimicrob. Chemother.*, vol. 57, pp. 1146–1152, Jun 2006.

[99] Z. Ahmad, R. Pandey, S. Sharma, and G. K. Khuller, "Alginate nanoparticles as antituberculosis drug carriers: formulation development, pharmacokinetics and therapeutic potential," *Indian J Chest Dis Allied Sci*, vol. 48, no. 3, pp. 171–176, 2006.

[100] S. A. Plotkin, "Vaccines: past, present and future," *Nat. Med.*, vol. 11, pp. 5–11, Apr 2005.

[101] R. N. Germain, "Vaccines and the future of human immunology," *Immunity*, vol. 33, pp. 441–450, Oct 2010.

[102] R. P. Wenzel and M. B. Edmond, "Managing antibiotic resistance," *N. Engl. J. Med.*, vol. 343, pp. 1961–1963, Dec 2000.

[103] R. P. Mishra, E. Oviedo-Orta, P. Prachi, R. Rappuoli, and F. Bagnoli, "Vaccines and antibiotic resistance," *Curr. Opin. Microbiol.*, vol. 15, pp. 596–602, Oct 2012.

[104] R. P. Mishra, E. Oviedo-Orta, P. Prachi, R. Rappuoli, and F. Bagnoli, "Vaccines and antibiotic resistance," *Curr. Opin. Microbiol.*, vol. 15, pp. 596–602, Oct 2012.

[105] A. S. Fauci and D. M. Morens, "The perpetual challenge of infectious diseases," *N. Engl. J. Med.*, vol. 366, pp. 454–461, Feb 2012.

[106] M. A. Swartz, S. Hirosue, and J. A. Hubbell, “Engineering approaches to immunotherapy,” *Science translational medicine*, vol. 4, no. 148, pp. 148rv9–148rv9, 2012.

[107] D. J. Irvine, M. A. Swartz, and G. L. Szeto, “Engineering synthetic vaccines using cues from natural immunity,” *Nat Mater*, vol. 12, pp. 978–990, Nov 2013.

[108] M. L. Tan, P. F. Choong, and C. R. Dass, “Recent developments in liposomes, microparticles and nanoparticles for protein and peptide drug delivery,” *Peptides*, vol. 31, pp. 184–193, Jan 2010.

[109] Z. Gu, A. Biswas, M. Zhao, and Y. Tang, “Tailoring nanocarriers for intracellular protein delivery,” *Chem Soc Rev*, vol. 40, pp. 3638–3655, Jul 2011.

[110] C. H. Villa, T. Dao, I. Ahearn, N. Fehrenbacher, E. Casey, D. A. Rey, T. Korontsvit, V. Zakhaleva, C. A. Batt, M. R. Philips, and D. A. Scheinberg, “Single-walled carbon nanotubes deliver peptide antigen into dendritic cells and enhance IgG responses to tumor-associated antigens,” *ACS Nano*, vol. 5, pp. 5300–5311, Jul 2011.

[111] C. Nembrini, A. Stano, K. Y. Dane, M. Ballester, A. J. van der Vlies, B. J. Marsland, M. A. Swartz, and J. A. Hubbell, “Nanoparticle conjugation of antigen enhances cytotoxic T-cell responses in pulmonary vaccination,” *Proc. Natl. Acad. Sci. U.S.A.*, vol. 108, pp. E989–997, Nov 2011.

[112] R. De Rose, A. N. Zelikin, A. P. Johnston, A. Sexton, S.-F. Chong, C. Cortez, W. Mulholland, F. Caruso, and S. J. Kent, “Binding, internalization, and antigen presentation of vaccine-loaded nanoengineered capsules in blood,” *Advanced Materials*, vol. 20, no. 24, pp. 4698–4703, 2008.

[113] B. G. De Geest, M. A. Willart, B. N. Lambrecht, C. Pollard, C. Vervaet, J. P. Remon, J. Grooten, and S. De Koker, “Surface-engineered polyelectrolyte multilayer capsules: synthetic vaccines mimicking microbial structure and function,” *Angew. Chem. Int. Ed. Engl.*, vol. 51, pp. 3862–3866, Apr 2012.

[114] M. Dierendonck, S. De Koker, C. Cuvelier, J. Grooten, C. Vervaet, J. P. Remon, and B. G. De Geest, “Facile two-step synthesis of porous antigen-loaded degradable polyelectrolyte microspheres,” *Angew. Chem. Int. Ed. Engl.*, vol. 49, pp. 8620–8624, Nov 2010.

[115] J. L. Perry, K. P. Herlihy, M. E. Napier, and J. M. Desimone, "PRINT: a novel platform toward shape and size specific nanoparticle theranostics," *Acc. Chem. Res.*, vol. 44, pp. 990–998, Oct 2011.

[116] C. M. Hu, L. Zhang, S. Aryal, C. Cheung, R. H. Fang, and L. Zhang, "Erythrocyte membrane-camouflaged polymeric nanoparticles as a biomimetic delivery platform," *Proc. Natl. Acad. Sci. U.S.A.*, vol. 108, pp. 10980–10985, Jul 2011.

[117] C. M. Hu, R. H. Fang, J. Copp, B. T. Luk, and L. Zhang, "A biomimetic nanosponge that absorbs pore-forming toxins," *Nat Nanotechnol*, vol. 8, pp. 336–340, May 2013.

[118] C. M. Hu, R. H. Fang, B. T. Luk, and L. Zhang, "Nanoparticle-detained toxins for safe and effective vaccination," *Nat Nanotechnol*, vol. 8, pp. 933–938, Dec 2013.

[119] L. J. Peek, C. R. Middaugh, and C. Berkland, "Nanotechnology in vaccine delivery," *Adv. Drug Deliv. Rev.*, vol. 60, pp. 915–928, May 2008.

[120] S. R. Little, "Reorienting our view of particle-based adjuvants for subunit vaccines," *Proc. Natl. Acad. Sci. U.S.A.*, vol. 109, pp. 999–1000, Jan 2012.

[121] M. Diwan, P. Elamanchili, H. Lane, A. Gainer, and J. Samuel, "Biodegradable nanoparticle mediated antigen delivery to human cord blood derived dendritic cells for induction of primary T cell responses," *J Drug Target*, vol. 11, no. 8-10, pp. 495–507, 2003.

[122] M. Diwan, P. Elamanchili, M. Cao, and J. Samuel, "Dose sparing of CpG oligodeoxynucleotide vaccine adjuvants by nanoparticle delivery," *Curr Drug Deliv*, vol. 1, pp. 405–412, Oct 2004.

[123] A. Heit, F. Schmitz, T. Haas, D. H. Busch, and H. Wagner, "Antigen co-encapsulated with adjuvants efficiently drive protective T cell immunity," *Eur. J. Immunol.*, vol. 37, pp. 2063–2074, Aug 2007.

[124] S. L. Demento, S. C. Eisenbarth, H. G. Foellmer, C. Platt, M. J. Caplan, W. Mark Saltzman, I. Mellman, M. Ledizet, E. Fikrig, R. A. Flavell, and T. M. Fahmy, "Inflammasome-activating nanoparticles as modular systems for optimizing vaccine efficacy," *Vaccine*, vol. 27, pp. 3013–3021, May 2009.

[125] Q. Zhu, C. Egelston, S. Gagnon, Y. Sui, I. M. Belyakov, D. M. Klinman, and J. A. Berzofsky, "Using 3 TLR ligands as a combination adjuvant induces qualitative changes in T cell responses needed for antiviral protection in mice," *J. Clin. Invest.*, vol. 120, pp. 607–616, Feb 2010.

[126] A. Mount, S. Koernig, A. Silva, D. Drane, E. Maraskovsky, and A. B. Morelli, "Combination of adjuvants: the future of vaccine design," *Expert Rev Vaccines*, vol. 12, pp. 733–746, Jul 2013.

[127] M. T. Orr, E. A. Beebe, T. E. Hudson, J. J. Moon, C. B. Fox, S. G. Reed, and R. N. Coler, "A dual TLR agonist adjuvant enhances the immunogenicity and protective efficacy of the tuberculosis vaccine antigen ID93," *PLoS ONE*, vol. 9, no. 1, p. e83884, 2014.

[128] E. Schlosser, M. Mueller, S. Fischer, S. Basta, D. H. Busch, B. Gander, and M. Groettrup, "TLR ligands and antigen need to be coencapsulated into the same biodegradable microsphere for the generation of potent cytotoxic T lymphocyte responses," *Vaccine*, vol. 26, pp. 1626–1637, Mar 2008.

[129] J. M. Blander and R. Medzhitov, "Regulation of phagosome maturation by signals from toll-like receptors," *Science*, vol. 304, pp. 1014–1018, May 2004.

[130] J. M. Blander and R. Medzhitov, "Toll-dependent selection of microbial antigens for presentation by dendritic cells," *Nature*, vol. 440, pp. 808–812, Apr 2006.

[131] S. P. Kasturi, I. Skountzou, R. A. Albrecht, D. Koutsonanos, T. Hua, H. I. Nakaya, R. Ravindran, S. Stewart, M. Alam, M. Kwissa, F. Villinger, N. Murthy, J. Steel, J. Jacob, R. J. Hogan, A. Garcia-Sastre, R. Compans, and B. Pulendran, "Programming the magnitude and persistence of antibody responses with innate immunity," *Nature*, vol. 470, pp. 543–547, Feb 2011.

[132] W. Gao, C.-M. J. Hu, R. H. Fang, and L. Zhang, "Liposome-like nanostructures for drug delivery," *Journal of Materials Chemistry B*, vol. 1, no. 48, pp. 6569–6585, 2013.

[133] J. J. Moon, H. Suh, A. Bershteyn, M. T. Stephan, H. Liu, B. Huang, M. Sohail, S. Luo, S. H. Um, H. Khant, J. T. Goodwin, J. Ramos, W. Chiu, and D. J. Irvine, "Interbilayer-crosslinked multilamellar vesicles as synthetic vaccines for potent humoral and cellular immune responses," *Nat Mater*, vol. 10, pp. 243–251, Mar 2011.

[134] T. Nochi, Y. Yuki, H. Takahashi, S. Sawada, M. Mejima, T. Kohda, N. Harada, I. G. Kong, A. Sato, N. Kataoka, D. Tokuhara, S. Kurokawa, Y. Takahashi, H. Tsukada, S. Kozaki, K. Akiyoshi, and H. Kiyono, "Nanogel antigenic protein-delivery system for adjuvant-free intranasal vaccines," *Nat Mater*, vol. 9, pp. 572–578, Jul 2010.

[135] Q. Zhu, J. Talton, G. Zhang, T. Cunningham, Z. Wang, R. C. Waters, J. Kirk, B. Eppler, D. M. Klinman, Y. Sui, S. Gagnon, I. M. Belyakov, R. J. Mumper, and J. A. Berzofsky, "Large intestine-targeted, nanoparticle-releasing oral vaccine to control genitorectal viral infection," *Nat. Med.*, vol. 18, pp. 1291–1296, Aug 2012.

[136] Y. Fujkuyama, D. Tokuhara, K. Kataoka, R. S. Gilbert, J. R. McGhee, Y. Yuki, H. Kiyono, and K. Fujihashi, "Novel vaccine development strategies for inducing mucosal immunity," *Expert Rev Vaccines*, vol. 11, pp. 367–379, Mar 2012.

[137] S. T. Reddy, A. J. van der Vlies, E. Simeoni, V. Angeli, G. J. Randolph, C. P. O'Neil, L. K. Lee, M. A. Swartz, and J. A. Hubbell, "Exploiting lymphatic transport and complement activation in nanoparticle vaccines," *Nat. Biotechnol.*, vol. 25, pp. 1159–1164, Oct 2007.

[138] C. M. Jewell, S. C. Lopez, and D. J. Irvine, "In situ engineering of the lymph node microenvironment via intranodal injection of adjuvant-releasing polymer particles," *Proc. Natl. Acad. Sci. U.S.A.*, vol. 108, pp. 15745–15750, Sep 2011.

[139] Y. Hu, T. Litwin, A. R. Nagaraja, B. Kwong, J. Katz, N. Watson, and D. J. Irvine, "Cytosolic delivery of membrane-impermeable molecules in dendritic cells using pH-responsive core-shell nanoparticles," *Nano Lett.*, vol. 7, pp. 3056–3064, Oct 2007.

[140] H. Yue, W. Wei, B. Fan, Z. Yue, L. Wang, G. Ma, and Z. Su, "The orchestration of cellular and humoral responses is facilitated by divergent intracellular antigen trafficking in nanoparticle-based therapeutic vaccine," *Pharmacol. Res.*, vol. 65, pp. 189–197, Feb 2012.

[141] A. E. Vasdekis, E. A. Scott, C. P. O'Neil, D. Psaltis, and J. A. Hubbell, "Precision intracellular delivery based on optofluidic polymersome rupture," *ACS Nano*, vol. 6, pp. 7850–7857, Sep 2012.

[142] M. Klompas and D. S. Yokoe, "Automated surveillance of health care-associated infections," *Clin. Infect. Dis.*, vol. 48, pp. 1268–1275, May 2009.

[143] B. Allegranzi, S. Bagheri Nejad, C. Combescure, W. Graafmans, H. Attar, L. Donaldson, and D. Pittet, "Burden of endemic health-care-associated infection in developing countries: systematic review and meta-analysis," *Lancet*, vol. 377, pp. 228–241, Jan 2011.

[144] E. A. Ottesen, J. W. Hong, S. R. Quake, and J. R. Leadbetter, "Microfluidic digital PCR enables multigene analysis of individual environmental bacteria," *Science*, vol. 314, pp. 1464–1467, Dec 2006.

[145] P. M. Dark, P. Dean, and G. Warhurst, "Bench-to-bedside review: the promise of rapid infection diagnosis during sepsis using polymerase chain reaction-based pathogen detection," *Crit Care*, vol. 13, no. 4, p. 217, 2009.

[146] A. Niemz, T. M. Ferguson, and D. S. Boyle, "Point-of-care nucleic acid testing for infectious diseases," *Trends Biotechnol.*, vol. 29, pp. 240–250, May 2011.

[147] N. J. Loman, R. V. Misra, T. J. Dallman, C. Constantinidou, S. E. Gharbia, J. Wain, and M. J. Pallen, "Performance comparison of benchtop high-throughput sequencing platforms," *Nat. Biotechnol.*, vol. 30, pp. 434–439, May 2012.

[148] K. K. Jain, "Nanotechnology in clinical laboratory diagnostics," *Clin. Chim. Acta*, vol. 358, pp. 37–54, Aug 2005.

[149] P. Tallury, A. Malhotra, L. M. Byrne, and S. Santra, "Nanobioimaging and sensing of infectious diseases," *Adv. Drug Deliv. Rev.*, vol. 62, pp. 424–437, Mar 2010.

[150] X. Zhao, L. R. Hilliard, S. J. Mechery, Y. Wang, R. P. Bagwe, S. Jin, and W. Tan, "A rapid bioassay for single bacterial cell quantitation using bioconjugated nanoparticles," *Proc. Natl. Acad. Sci. U.S.A.*, vol. 101, pp. 15027–15032, Oct 2004.

[151] P. Alivisatos, "The use of nanocrystals in biological detection," *Nat. Biotechnol.*, vol. 22, pp. 47–52, Jan 2004.

[152] M. A. Hahn, J. S. Tabb, and T. D. Krauss, "Detection of single bacterial pathogens with semiconductor quantum dots," *Anal. Chem.*, vol. 77, pp. 4861–4869, Aug 2005.

[153] C. Paquet, S. Ryan, S. Zou, A. Kell, J. Tanha, J. Hulse, L. L. Tay, and B. Simard, "Multifunctional nanoprobes for pathogen-selective capture and detection," *Chem. Commun. (Camb.)*, vol. 48, pp. 561–563, Jan 2012.

[154] H. N. Abdelhamid and H.-F. Wu, "Probing the interactions of chitosan capped cds quantum dots with pathogenic bacteria and their biosensing application," *Journal of Materials Chemistry B*, vol. 1, no. 44, pp. 6094–6106, 2013.

[155] W. M. Leevy, T. N. Lambert, J. R. Johnson, J. Morris, and B. D. Smith, "Quantum dot probes for bacteria distinguish Escherichia coli mutants and permit in vivo imaging," *Chem. Commun. (Camb.)*, pp. 2331–2333, May 2008.

[156] R. Edgar, M. McKinstry, J. Hwang, A. B. Oppenheim, R. A. Fekete, G. Giulian, C. Merril, K. Nagashima, and S. Adhya, "High-sensitivity bacterial detection using biotin-tagged phage and quantum-dot nanocomplexes," *Proc. Natl. Acad. Sci. U.S.A.*, vol. 103, pp. 4841–4845, Mar 2006.

[157] E. Katz and I. Willner, "Integrated nanoparticle-biomolecule hybrid systems: synthesis, properties, and applications," *Angew. Chem. Int. Ed. Engl.*, vol. 43, pp. 6042–6108, Nov 2004.

[158] J. Gao, H. Gu, and B. Xu, "Multifunctional magnetic nanoparticles: design, synthesis, and biomedical applications," *Acc. Chem. Res.*, vol. 42, pp. 1097–1107, Aug 2009.

[159] A. K. Gupta, R. R. Naregalkar, V. D. Vaidya, and M. Gupta, "Recent advances on surface engineering of magnetic iron oxide nanoparticles and their biomedical applications," *Nanomedicine (Lond)*, vol. 2, pp. 23–39, Feb 2007.

[160] J. L. Corchero and A. Villaverde, "Biomedical applications of distally controlled magnetic nanoparticles," *Trends Biotechnol.*, vol. 27, pp. 468–476, Aug 2009.

[161] M. A. Gijs, F. Lacharme, and U. Lehmann, "Microfluidic applications of magnetic particles for biological analysis and catalysis," *Chem. Rev.*, vol. 110, pp. 1518–1563, Mar 2010.

[162] P. M. Valencia, O. C. Farokhzad, R. Karnik, and R. Langer, "Microfluidic technologies for accelerating the clinical translation of nanoparticles," *Nat Nanotechnol*, vol. 7, pp. 623–629, Oct 2012.

[163] R. M. Cooper, D. C. Leslie, K. Domansky, A. Jain, C. Yung, M. Cho, S. Workman, M. Super, and D. E. Ingber, "A microdevice for rapid optical detection of magnetically captured rare blood pathogens," *Lab Chip*, vol. 14, pp. 182–188, Jan 2014.

[164] H. J. Chung, C. M. Castro, H. Im, H. Lee, and R. Weissleder, "A magneto-DNA nanoparticle system for rapid detection and phenotyping of bacteria," *Nat Nanotechnol*, vol. 8, pp. 369–375, May 2013.

[165] V. Hoerr, L. Tuchscherr, J. Huve, N. Nippe, K. Loser, N. Glyvuk, Y. Tsytsyura, M. Holtkamp, C. Sunderkotter, U. Karst, J. Klingauf, G. Peters, B. Loffler, and C. Faber, "Bacteria tracking by in vivo magnetic resonance imaging," *BMC Biol.*, vol. 11, p. 63, May 2013.

[166] P. V. Baptista, M. Koziol-Montewka, J. Paluch-Oles, G. Doria, and R. Franco, "Gold-nanoparticle-probe-based assay for rapid and direct detection of Mycobacterium tuberculosis DNA in clinical samples," *Clin. Chem.*, vol. 52, pp. 1433–1434, Jul 2006.

[167] S. Lim, O. K. Koo, Y. S. You, Y. E. Lee, M. S. Kim, P. S. Chang, D. H. Kang, J. H. Yu, Y. J. Choi, and S. Gunasekaran, "Enhancing nanoparticle-based visible detection by controlling the extent of aggregation," *Sci Rep*, vol. 2, p. 456, 2012.

[168] R. L. Phillips, O. R. Miranda, C. C. You, V. M. Rotello, and U. H. Bunz, "Rapid and efficient identification of bacteria using gold-nanoparticle-poly(paraphenyleneethynylene) constructs," *Angew. Chem. Int. Ed. Engl.*, vol. 47, no. 14, pp. 2590–2594, 2008.

[169] G. M. Whitesides, "The origins and the future of microfluidics," *Nature*, vol. 442, pp. 368–373, Jul 2006.

[170] P. Yager, T. Edwards, E. Fu, K. Helton, K. Nelson, M. R. Tam, and B. H. Weigl, "Microfluidic diagnostic technologies for global public health," *Nature*, vol. 442, pp. 412–418, Jul 2006.

[171] A. O'connor, C. A. O'morain, and A. C. Ford, "Population screening and treatment of helicobacter pylori infection," *Nature Reviews Gastroenterology and Hepatology*, vol. 14, no. 4, p. 230, 2017.

[172] N. R. Salama, M. L. Hartung, and A. Müller, "Life in the human stomach: persistence strategies of the bacterial pathogen helicobacter pylori," *Nature Reviews Microbiology*, vol. 11, no. 6, p. 385, 2013.

[173] Y. Yamaoka, "Mechanisms of disease: Helicobacter pylori virulence factors," *Nature Reviews Gastroenterology and Hepatology*, vol. 7, no. 11, p. 629, 2010.

[174] D. Ertem, "Clinical practice: Helicobacter pylori infection in childhood," *European journal of pediatrics*, vol. 172, no. 11, pp. 1427–1434, 2013.

[175] C. Alba, A. Blanco, and T. Alarcon, "Antibiotic resistance in Helicobacter pylori," *Curr. Opin. Infect. Dis.*, vol. 30, pp. 489–497, Oct 2017.

[176] Y. Hu, M. Zhang, B. Lu, and J. Dai, "Helicobacter pylori and antibiotic resistance, a continuing and intractable problem," *Helicobacter*, vol. 21, no. 5, pp. 349–363, 2016.

[177] M. Zhang, "High antibiotic resistance rate: A difficult issue for Helicobacter pylori eradication treatment," *World J. Gastroenterol.*, vol. 21, pp. 13432–13437, Dec 2015.

[178] S. D. Georgopoulos, V. Papastergiou, and S. Karatapanis, "Treatment of Helicobacter Pylori infection: optimization strategies in a high resistance era," *Expert Opin Pharmacother*, vol. 16, no. 15, pp. 2307–2317, 2015.

[179] Y. Hu, Y. Zhu, and N. H. Lu, "Novel and Effective Therapeutic Regimens for Helicobacter pylori in an Era of Increasing Antibiotic Resistance," *Front Cell Infect Microbiol*, vol. 7, p. 168, 2017.

[180] S. Ramteke, N. Ganesh, S. Bhattacharya, and N. K. Jain, "Amoxicillin, clarithromycin, and omeprazole based targeted nanoparticles for the treatment of H. pylori," *J Drug Target*, vol. 17, pp. 225–234, Apr 2009.

[181] S. Ramteke, N. Ganesh, S. Bhattacharya, and N. K. Jain, "Triple therapy-based targeted nanoparticles for the treatment of Helicobacter pylori," *J Drug Target*, vol. 16, pp. 694–705, Nov 2008.

[182] Y. H. Lin, C. H. Chang, Y. S. Wu, Y. M. Hsu, S. F. Chiou, and Y. J. Chen, "Development of pH-responsive chitosan/heparin nanoparticles for stomach-specific anti-Helicobacter pylori therapy," *Biomaterials*, vol. 30, pp. 3332–3342, Jul 2009.

[183] W. Gao, D. Vecchio, J. Li, J. Zhu, Q. Zhang, V. Fu, J. Li, S. Thamphiwatana, D. Lu, and L. Zhang, "Hydrogel containing nanoparticle-stabilized liposomes for topical antimicrobial delivery," *ACS Nano*, vol. 8, pp. 2900–2907, Mar 2014.

[184] S. Thamphiwatana, W. Gao, D. Pornpattananangkul, Q. Zhang, V. Fu, J. Li, J. Li, M. Obonyo, and L. Zhang, “Phospholipase A2-responsive antibiotic delivery via nanoparticle-stabilized liposomes for the treatment of bacterial infection,” *J Mater Chem B*, vol. 2, pp. 8201–8207, Dec 2014.

[185] R. B. Umamaheshwari and N. K. Jain, “Receptor mediated targeting of lectin conjugated gliadin nanoparticles in the treatment of Helicobacter pylori,” *J Drug Target*, vol. 11, pp. 415–423, Aug 2003.

[186] M. Obonyo, L. Zhang, S. Thamphiwatana, D. Pornpattananangkul, V. Fu, and L. Zhang, “Antibacterial activities of liposomal linolenic acids against antibiotic-resistant Helicobacter pylori,” *Mol. Pharm.*, vol. 9, pp. 2677–2685, Sep 2012.

[187] S. Thamphiwatana, W. Gao, M. Obonyo, and L. Zhang, “In vivo treatment of helicobacter pylori infection with liposomal linolenic acid reduces colonization and ameliorates inflammation,” *Proceedings of the National Academy of Sciences*, vol. 111, no. 49, pp. 17600–17605, 2014.

[188] S. W. Jung, S. Thamphiwatana, L. Zhang, and M. Obonyo, “Mechanism of antibacterial activity of liposomal linolenic acid against helicobacter pylori,” *PloS one*, vol. 10, no. 3, p. e0116519, 2015.

[189] W. Gao, S. Thamphiwatana, P. Angsantikul, and L. Zhang, “Nanoparticle approaches against bacterial infections,” *Wiley Interdisciplinary Reviews: Nanomedicine and Nanobiotechnology*, vol. 6, no. 6, pp. 532–547, 2014.

[190] B. Kumar, K. Jalodia, P. Kumar, and H. K. Gautam, “Recent advances in nanoparticle-mediated drug delivery,” *Journal of Drug Delivery Science and Technology*, vol. 41, pp. 260–268, 2017.

[191] W. Gao, Y. Chen, Y. Zhang, Q. Zhang, and L. Zhang, “Nanoparticle-based local antimicrobial drug delivery,” *Adv. Drug Deliv. Rev.*, Sep 2017.

[192] R. H. Fang, A. V. Kroll, W. Gao, and L. Zhang, “Cell Membrane Coating Nanotechnology,” *Adv. Mater. Weinheim*, p. e1706759, Mar 2018.

[193] W. Gao and L. Zhang, “Coating nanoparticles with cell membranes for targeted drug delivery,” *J Drug Target*, vol. 23, no. 7-8, pp. 619–626, 2015.

[194] R. H. Fang, C. M. Hu, B. T. Luk, W. Gao, J. A. Copp, Y. Tai, D. E. O'Connor, and L. Zhang, "Cancer cell membrane-coated nanoparticles for anticancer vaccination and drug delivery," *Nano Lett.*, vol. 14, no. 4, pp. 2181–2188, 2014.

[195] C. M. Hu, R. H. Fang, K. C. Wang, B. T. Luk, S. Thamphiwatana, D. Dehaini, P. Nguyen, P. Angsantikul, C. H. Wen, A. V. Kroll, C. Carpenter, M. Ramesh, V. Qu, S. H. Patel, J. Zhu, W. Shi, F. M. Hofman, T. C. Chen, W. Gao, K. Zhang, S. Chien, and L. Zhang, "Nanoparticle biointerfacing by platelet membrane cloaking," *Nature*, vol. 526, pp. 118–121, Oct 2015.

[196] Q. Hu, W. Sun, C. Qian, C. Wang, H. N. Bomba, and Z. Gu, "Anticancer Platelet-Mimicking Nanovehicles," *Adv. Mater. Weinheim*, vol. 27, pp. 7043–7050, Nov 2015.

[197] D. N. Sgouras, T. T. Trang, and Y. Yamaoka, "Pathogenesis of Helicobacter pylori Infection," *Helicobacter*, vol. 20 Suppl 1, pp. 8–16, Sep 2015.

[198] B. Kaplan-Turkoz, L. F. Jimenez-Soto, C. Dian, C. Ertl, H. Remaut, A. Louche, T. Tosi, R. Haas, and L. Terradot, "Structural insights into Helicobacter pylori oncoprotein CagA interaction with Îš1 integrin," *Proc. Natl. Acad. Sci. U.S.A.*, vol. 109, pp. 14640–14645, Sep 2012.

[199] T. Koelblen, C. Berge, M. V. Cherrier, K. Brillet, L. Jimenez-Soto, L. Ballut, J. Takagi, R. Montserret, P. Rousselle, W. Fischer, R. Haas, R. Fronzes, and L. Terradot, "Molecular dissection of protein-protein interactions between integrin Îś5Îš1 and the Helicobacter pylori Cag type IV secretion system," *FEBS J.*, vol. 284, pp. 4143–4157, 12 2017.

[200] Y. Y. Fei, A. Schmidt, G. Bylund, D. X. Johansson, S. Henriksson, C. Lebrilla, J. V. Solnick, T. BorÃĺn, and X. D. Zhu, "Use of real-time, label-free analysis in revealing low-affinity binding to blood group antigens by helicobacter pylori," *Analytical Chemistry*, vol. 83, no. 16, pp. 6336–6341, 2011.

[201] P. Parreira, Q. Shi, A. Magalhaes, C. A. Reis, J. Bugaytsova, T. Boren, D. Leckband, and M. C. Martins, "Atomic force microscopy measurements reveal multiple bonds between Helicobacter pylori blood group antigen binding adhesin and Lewis b ligand," *J R Soc Interface*, vol. 11, p. 20141040, Dec 2014.

[202] V. Koniger, L. Holsten, U. Harrison, B. Busch, E. Loell, Q. Zhao, D. A. Bonsor, A. Roth, A. Kengmo-Tchoupa, S. I. Smith, S. Mueller, E. J. Sundberg, W. Zimmermann, W. Fischer, C. R. Hauck, and R. Haas, "Helicobacter pylori

exploits human CEACAMs via HopQ for adherence and translocation of CagA," *Nat Microbiol*, vol. 2, p. 16188, 10 2016.

[203] S. Thamphiwatana, P. Angsantikul, T. Escajadillo, Q. Zhang, J. Olson, B. T. Luk, S. Zhang, R. H. Fang, W. Gao, V. Nizet, and L. Zhang, "Macrophage-like nanoparticles concurrently absorbing endotoxins and proinflammatory cytokines for sepsis management," *Proc. Natl. Acad. Sci. U.S.A.*, vol. 114, pp. 11488–11493, Oct 2017.

[204] S. Aryal, C. M. Hu, R. H. Fang, D. Dehaini, C. Carpenter, D. E. Zhang, and L. Zhang, "Erythrocyte membrane-cloaked polymeric nanoparticles for controlled drug loading and release," *Nanomedicine (Lond)*, vol. 8, pp. 1271–1280, Aug 2013.

[205] M. Obonyo, D. G. Guiney, J. Harwood, J. Fierer, and S. P. Cole, "Role of gamma interferon in Helicobacter pylori induction of inflammatory mediators during murine infection," *Infect. Immun.*, vol. 70, pp. 3295–3299, Jun 2002.

[206] K. Hase, M. Murakami, M. Iimura, S. P. Cole, Y. Horibe, T. Ohtake, M. Obonyo, R. L. Gallo, L. Eckmann, and M. F. Kagnoff, "Expression of LL-37 by human gastric epithelial cells as a potential host defense mechanism against Helicobacter pylori," *Gastroenterology*, vol. 125, pp. 1613–1625, Dec 2003.

[207] P. J. Jenks, R. L. Ferrero, J. Tankovic, J. M. Thiberge, and A. Labigne, "Evaluation of nitrofurantoin combination therapy of metronidazole-sensitive and -resistant Helicobacter pylori infections in mice," *Antimicrob. Agents Chemother.*, vol. 44, pp. 2623–2629, Oct 2000.

[208] S. J. van Zanten, T. Kolesnikow, V. Leung, J. L. O'Rourke, and A. Lee, "Gastric transitional zones, areas where Helicobacter treatment fails: results of a treatment trial using the Sydney strain mouse model," *Antimicrob. Agents Chemother.*, vol. 47, pp. 2249–2255, Jul 2003.

[209] J. R. Fitzgerald, T. J. Foster, and D. Cox, "The interaction of bacterial pathogens with platelets," *Nat. Rev. Microbiol.*, vol. 4, pp. 445–457, Jun 2006.

[210] J. Pizarro-Cerda and P. Cossart, "Bacterial adhesion and entry into host cells," *Cell*, vol. 124, pp. 715–727, Feb 2006.

[211] N. Zmora, D. Zeevi, T. Korem, E. Segal, and E. Elinav, "Taking it Personally: Personalized Utilization of the Human Microbiome in Health and Disease," *Cell Host Microbe*, vol. 19, pp. 12–20, Jan 2016.

[212] H. K. Makadia and S. J. Siegel, "Poly lactic-co-glycolic acid (plga) as biodegradable controlled drug delivery carrier," *Polymers*, vol. 3, no. 3, pp. 1377–1397, 2011.

[213] T. Yu, Y. Y. Wang, M. Yang, C. Schneider, W. Zhong, S. Pulicare, W. J. Choi, O. Mert, J. Fu, S. K. Lai, and J. Hanes, "Biodegradable mucus-penetrating nanoparticles composed of diblock copolymers of polyethylene glycol and poly(lactic-co-glycolic acid)," *Drug Deliv Transl Res*, vol. 2, Apr 2012.

[214] F. Wang, W. Gao, S. Thamphiwatana, B. T. Luk, P. Angsantikul, Q. Zhang, C. M. Hu, R. H. Fang, J. A. Copp, D. Pornpattananangkul, W. Lu, and L. Zhang, "Hydrogel Retaining Toxin-Absorbing Nanosponges for Local Treatment of Methicillin-Resistant Staphylococcus aureus Infection," *Adv. Mater. Weinheim*, vol. 27, pp. 3437–3443, Jun 2015.

[215] Y. Zhang, W. Gao, Y. Chen, T. Escajadillo, J. Ungerleider, R. H. Fang, K. Christman, V. Nizet, and L. Zhang, "Self-Assembled Colloidal Gel Using Cell Membrane-Coated Nanosponges as Building Blocks," *ACS Nano*, vol. 11, pp. 11923–11930, Dec 2017.

[216] J. Zhang, W. Gao, R. H. Fang, A. Dong, and L. Zhang, "Synthesis of Nanogels via Cell Membrane-Templated Polymerization," *Small*, vol. 11, pp. 4309–4313, Sep 2015.

[217] H. Yu, W. Chen, C. Li, D. Lin, J. Liu, Z. Yang, J. Yang, Y. Sun, and D. Ma, "Large scale ex vivo expansion of clinical-grade effector cells for adoptive immunotherapy," *Exp Ther Med*, vol. 14, pp. 5678–5686, Dec 2017.

[218] T. Lambrechts, M. Sonnaert, J. Schrooten, F. P. Luyten, J. M. Aerts, and I. Papantoniou, "Large-Scale Mesenchymal Stem/Stromal Cell Expansion: A Visualization Tool for Bioprocess Comparison," *Tissue Eng Part B Rev*, vol. 22, pp. 485–498, 12 2016.

[219] A. P. Gee, "Manufacturing genetically modified T cells for clinical trials," *Cancer Gene Ther.*, vol. 22, pp. 67–71, Mar 2015.

[220] C. M. Hu, R. H. Fang, J. Copp, B. T. Luk, and L. Zhang, "A biomimetic nanosponge that absorbs pore-forming toxins," *Nat Nanotechnol*, vol. 8, pp. 336–340, May 2013.

[221] Y. Chen, M. Chen, Y. Zhang, J. H. Lee, T. Escajadillo, H. Gong, R. H. Fang, W. Gao, V. Nizet, and L. Zhang, "Broad-Spectrum Neutralization of Pore-Forming Toxins with Human Erythrocyte Membrane-Coated Nanosponges," *Adv Healthc Mater*, Feb 2018.

[222] C. M. Hu, R. H. Fang, B. T. Luk, and L. Zhang, "Nanoparticle-detained toxins for safe and effective vaccination," *Nat Nanotechnol*, vol. 8, pp. 933–938, Dec 2013.

[223] X. Wei, J. Gao, F. Wang, M. Ying, P. Angsantikul, A. V. Kroll, J. Zhou, W. Gao, W. Lu, R. H. Fang, and L. Zhang, "In Situ Capture of Bacterial Toxins for Antivirulence Vaccination," *Adv. Mater. Weinheim*, vol. 29, Sep 2017.

[224] L. Olbe, E. Carlsson, and P. Lindberg, "A proton-pump inhibitor expedition: the case histories of omeprazole and esomeprazole," *Nat Rev Drug Discov*, vol. 2, pp. 132–139, Feb 2003.

[225] P. Richardson, C. J. Hawkey, and W. A. Stack, "Proton pump inhibitors. Pharmacology and rationale for use in gastrointestinal disorders," *Drugs*, vol. 56, pp. 307–335, Sep 1998.

[226] P. Moayyedi and G. I. Leontiadis, "The risks of PPI therapy," *Nat Rev Gastroenterol Hepatol*, vol. 9, pp. 132–139, Feb 2012.

[227] P. M. Ho, T. M. Maddox, L. Wang, S. D. Fihn, R. L. Jesse, E. D. Peterson, and J. S. Rumsfeld, "Risk of adverse outcomes associated with concomitant use of clopidogrel and proton pump inhibitors following acute coronary syndrome," *JAMA*, vol. 301, pp. 937–944, Mar 2009.

[228] E. Sheen and G. Triadafilopoulos, "Adverse effects of long-term proton pump inhibitor therapy," *Dig. Dis. Sci.*, vol. 56, pp. 931–950, Apr 2011.

[229] Y. X. Yang, J. D. Lewis, S. Epstein, and D. C. Metz, "Long-term proton pump inhibitor therapy and risk of hip fracture," *JAMA*, vol. 296, pp. 2947–2953, Dec 2006.

[230] H. Blume, F. Donath, A. Warnke, and B. S. Schug, "Pharmacokinetic drug interaction profiles of proton pump inhibitors," *Drug Saf*, vol. 29, no. 9, pp. 769–784, 2006.

[231] D. N. Juurlink, T. Gomes, D. T. Ko, P. E. Szmitko, P. C. Austin, J. V. Tu, D. A. Henry, A. Kopp, and M. M. Mamdani, "A population-based study of the drug interaction between proton pump inhibitors and clopidogrel," *CMAJ*, vol. 180, pp. 713–718, Mar 2009.

[232] S. Ganta, H. Devalapally, A. Shahiwala, and M. Amiji, "A review of stimuli-responsive nanocarriers for drug and gene delivery," *J Control Release*, vol. 126, pp. 187–204, Mar 2008.

[233] Y. Lu, A. A. Aimetti, R. Langer, and Z. Gu, "Bioresponsive materials," *Nature Reviews Materials*, vol. 2, no. 1, p. 16075, 2017.

[234] S. Mura, J. Nicolas, and P. Couvreur, "Stimuli-responsive nanocarriers for drug delivery," *Nat Mater*, vol. 12, pp. 991–1003, Nov 2013.

[235] D. Peer, J. M. Karp, S. Hong, O. C. Farokhzad, R. Margalit, and R. Langer, "Nanocarriers as an emerging platform for cancer therapy," *Nat Nanotechnol*, vol. 2, pp. 751–760, Dec 2007.

[236] J. Wang, *Nanomachines: fundamentals and applications.* John Wiley & Sons, 2013.

[237] M. Guix, C. C. Mayorga-Martinez, and A. Merkoci, "Nano/micromotors in (bio)chemical science applications," *Chem. Rev.*, vol. 114, pp. 6285–6322, Jun 2014.

[238] S. Sanchez, L. Soler, and J. Katuri, "Chemically powered micro- and nanomotors," *Angew. Chem. Int. Ed. Engl.*, vol. 54, pp. 1414–1444, Jan 2015.

[239] Y. Mei, A. A. Solovev, S. Sanchez, and O. G. Schmidt, "Rolled-up nanotech on polymers: from basic perception to self-propelled catalytic microengines," *Chem Soc Rev*, vol. 40, pp. 2109–2119, May 2011.

[240] S. Palagi, A. G. Mark, S. Y. Reigh, K. Melde, T. Qiu, H. Zeng, C. Parmeggiani, D. Martella, A. Sanchez-Castillo, N. Kapernaum, F. Giesselmann, D. S. Wiersma, E. Lauga, and P. Fischer, "Structured light enables biomimetic swimming and versatile locomotion of photoresponsive soft microrobots," *Nat Mater*, vol. 15, pp. 647–653, 06 2016.

[241] J. Li, I. Rozen, and J. Wang, "Rocket Science at the Nanoscale," *ACS Nano*, vol. 10, pp. 5619–5634, Jun 2016.

[242] D. A. Wilson, R. J. Nolte, and J. C. van Hest, “Autonomous movement of platinum-loaded stomatocytes,” *Nat Chem*, vol. 4, pp. 268–274, Feb 2012.

[243] H. Wang and M. Pumera, “Fabrication of Micro/Nanoscale Motors,” *Chem. Rev.*, vol. 115, pp. 8704–8735, Aug 2015.

[244] J. Li, W. Gao, R. Dong, A. Pei, S. Sattayasamitsathit, and J. Wang, “Nanomotor lithography,” *Nat Commun*, vol. 5, p. 5026, Sep 2014.

[245] T. E. Mallouk and A. Sen, “Powering nanorobots,” *Sci. Am.*, vol. 300, pp. 72–77, May 2009.

[246] W. Gao, D. Kagan, O. S. Pak, C. Clawson, S. Campuzano, E. Chuluun-Erdene, E. Shipton, E. E. Fullerton, L. Zhang, E. Lauga, and J. Wang, “Cargo-towing fuel-free magnetic nanoswimmers for targeted drug delivery,” *Small*, vol. 8, pp. 460–467, Feb 2012.

[247] Z. Wu, Y. Wu, W. He, X. Lin, J. Sun, and Q. He, “Self-propelled polymer-based multilayer nanorockets for transportation and drug release,” *Angew. Chem. Int. Ed. Engl.*, vol. 52, pp. 7000–7003, Jul 2013.

[248] F. Mou, C. Chen, Q. Zhong, Y. Yin, H. Ma, and J. Guan, “Autonomous motion and temperature-controlled drug delivery of Mg/Pt-poly(N-isopropylacrylamide) Janus micromotors driven by simulated body fluid and blood plasma,” *ACS Appl Mater Interfaces*, vol. 6, pp. 9897–9903, Jun 2014.

[249] L. K. Abdelmohsen, M. Nijemeisland, G. M. Pawar, G. J. Janssen, R. J. Nolte, J. C. van Hest, and D. A. Wilson, “Dynamic Loading and Unloading of Proteins in Polymeric Stomatocytes: Formation of an Enzyme-Loaded Supramolecular Nanomotor,” *ACS Nano*, vol. 10, pp. 2652–2660, Feb 2016.

[250] W. Z. Teo and M. Pumera, “Motion Control of Micro-/Nanomotors,” *Chemistry*, vol. 22, pp. 14796–14804, Oct 2016.

[251] J. G. Moo, H. Wang, and M. Pumera, “Influence of pH on the Motion of Catalytic Janus Particles and Tubular Bubble-Propelled Micromotors,” *Chemistry*, vol. 22, pp. 355–360, Jan 2016.

[252] Z. Wu, X. Lin, Y. Wu, T. Si, J. Sun, and Q. He, “Near-infrared light-triggered "on/off" motion of polymer multilayer rockets,” *ACS Nano*, vol. 8, pp. 6097–6105, Jun 2014.

[253] Z. Wu, X. Lin, T. Si, and Q. He, “Recent Progress on Bioinspired Self-Propelled Micro/Nanomotors via Controlled Molecular Self-Assembly,” *Small*, vol. 12, pp. 3080–3093, Jun 2016.

[254] W. Gao, R. Dong, S. Thamphiwatana, J. Li, W. Gao, L. Zhang, and J. Wang, “Artificial micromotors in the mouse’s stomach: a step toward in vivo use of synthetic motors,” *ACS Nano*, vol. 9, pp. 117–123, Jan 2015.

[255] J. Li, S. Thamphiwatana, W. Liu, B. Esteban-Fernandez de Avila, P. Angsantikul, E. Sandraz, J. Wang, T. Xu, F. Soto, V. Ramez, X. Wang, W. Gao, L. Zhang, and J. Wang, “Enteric Micromotor Can Selectively Position and Spontaneously Propel in the Gastrointestinal Tract,” *ACS Nano*, Sep 2016.

[256] W. Gao, X. Feng, A. Pei, Y. Gu, J. Li, and J. Wang, “Seawater-driven magnesium based Janus micromotors for environmental remediation,” *Nanoscale*, vol. 5, pp. 4696–4700, Jun 2013.

[257] J. Vormann, “Magnesium: nutrition and metabolism,” *Mol. Aspects Med.*, vol. 24, no. 1-3, pp. 27–37, 2003.

[258] M. C. Daniel and D. Astruc, “Gold nanoparticles: assembly, supramolecular chemistry, quantum-size-related properties, and applications toward biology, catalysis, and nanotechnology,” *Chem. Rev.*, vol. 104, pp. 293–346, Jan 2004.

[259] J. Orozco, G. Cheng, D. Vilela, S. Sattayasamitsathit, R. Vazquez-Duhalt, G. Valdes-Ramirez, O. S. Pak, A. Escarpa, C. Kan, and J. Wang, “Micromotor-based high-yielding fast oxidative detoxification of chemical threats,” *Angew. Chem. Int. Ed. Engl.*, vol. 52, pp. 13276–13279, Dec 2013.

[260] W. Zhiguang, L. Jinxing, de ÃĄvila Berta EstebanâĂŘFernÃąndez, L. Tianlong, G. Weiwei, H. Qiang, Z. Liangfang, and W. Joseph, “WaterâĂŘpowered cellâĂŘmimicking janus micromotor,” *Advanced Functional Materials*, vol. 25, no. 48, pp. 7497–7501.

[261] J. Wang, *Nanomachines: fundamentals and applications.* John Wiley & Sons, 2013.

[262] M. Guix, C. C. Mayorga-Martinez, and A. Merkoci, “Nano/micromotors in (bio)chemical science applications,” *Chem. Rev.*, vol. 114, pp. 6285–6322, Jun 2014.

[263] Y. Mei, A. A. Solovev, S. Sanchez, and O. G. Schmidt, “Rolled-up nanotech on polymers: from basic perception to self-propelled catalytic microengines,” *Chem Soc Rev*, vol. 40, pp. 2109–2119, May 2011.

[264] S. Sanchez, L. Soler, and J. Katuri, “Chemically powered micro- and nanomotors,” *Angew. Chem. Int. Ed. Engl.*, vol. 54, pp. 1414–1444, Jan 2015.

[265] B. J. Nelson, I. K. Kaliakatsos, and J. J. Abbott, “Microrobots for minimally invasive medicine,” *Annu Rev Biomed Eng*, vol. 12, pp. 55–85, Aug 2010.

[266] J. Li, I. Rozen, and J. Wang, “Rocket Science at the Nanoscale,” *ACS Nano*, vol. 10, pp. 5619–5634, Jun 2016.

[267] L. K. E. A. Abdelmohsen, F. Peng, Y. Tu, and D. A. Wilson, “Micro- and nanomotors for biomedical applications,” *J. Mater. Chem. B*, vol. 2, pp. 2395–2408, 2014.

[268] S. Sundararajan, P. E. Lammert, A. W. Zudans, V. H. Crespi, and A. Sen, “Catalytic motors for transport of colloidal cargo,” *Nano Lett.*, vol. 8, pp. 1271–1276, May 2008.

[269] W. Zhiguang, W. Yingjie, H. Wenping, L. Xiankun, S. Jianmin, and H. Qiang, “Self-ĂŘpropelled polymer-ĂŘbased multilayer nanorockets for transportation and drug release,” *Angewandte Chemie International Edition*, vol. 52, no. 27, pp. 7000–7003.

[270] W. Gao and J. Wang, “Synthetic micro/nanomotors in drug delivery,” *Nanoscale*, vol. 6, pp. 10486–10494, Sep 2014.

[271] A. Servant, F. Qiu, M. Mazza, K. Kostarelos, and B. J. Nelson, “Controlled in vivo swimming of a swarm of bacteria-like microrobotic flagella,” *Adv. Mater. Weinheim*, vol. 27, pp. 2981–2988, May 2015.

[272] O. Felfoul, M. Mohammadi, S. Taherkhani, D. de Lanauze, Y. Zhong Xu, D. Loghin, S. Essa, S. Jancik, D. Houle, M. Lafleur, L. Gaboury, M. Tabrizian, N. Kaou, M. Atkin, T. Vuong, G. Batist, N. Beauchemin, D. Radzioch, and S. Martel, “Magneto-aerotactic bacteria deliver drug-containing nanoliposomes to tumour hypoxic regions,” *Nat Nanotechnol*, vol. 11, pp. 941–947, Nov 2016.

[273] B. Esteban-Fernandez de Avila, C. Angell, F. Soto, M. A. Lopez-Ramirez, D. F. Baez, S. Xie, J. Wang, and Y. Chen, “Acoustically Propelled Nanomotors for Intracellular siRNA Delivery,” *ACS Nano*, vol. 10, pp. 4997–5005, May 2016.

[274] D. Kagan, M. J. Benchimol, J. C. Claussen, E. Chuluun-Erdene, S. Esener, and J. Wang, "Acoustic droplet vaporization and propulsion of perfluorocarbon-loaded microbullets for targeted tissue penetration and deformation," *Angew. Chem. Int. Ed. Engl.*, vol. 51, pp. 7519–7522, Jul 2012.

[275] T. G. Leong, C. L. Randall, B. R. Benson, N. Bassik, G. M. Stern, and D. H. Gracias, "Tetherless thermobiochemically actuated microgrippers," *Proc. Natl. Acad. Sci. U.S.A.*, vol. 106, pp. 703–708, Jan 2009.

[276] S. Balasubramanian, D. Kagan, C. M. Hu, S. Campuzano, M. J. Lobo-Castanon, N. Lim, D. Y. Kang, M. Zimmerman, L. Zhang, and J. Wang, "Micromachine-enabled capture and isolation of cancer cells in complex media," *Angew. Chem. Int. Ed. Engl.*, vol. 50, pp. 4161–4164, Apr 2011.

[277] T. E. Mallouk and A. Sen, "Powering nanorobots," *Sci. Am.*, vol. 300, pp. 72–77, May 2009.

[278] B. Esteban-Fernandez de Avila, A. Martin, F. Soto, M. A. Lopez-Ramirez, S. Campuzano, G. M. Vasquez-Machado, W. Gao, L. Zhang, and J. Wang, "Single Cell Real-Time miRNAs Sensing Based on Nanomotors," *ACS Nano*, vol. 9, pp. 6756–6764, Jul 2015.

[279] S. K. Srivastava, M. Guix, and O. G. Schmidt, "Wastewater Mediated Activation of Micromotors for Efficient Water Cleaning," *Nano Lett.*, vol. 16, pp. 817–821, Jan 2016.

[280] H. Marcus, S. Yang, C. XiangâĂŘZhong, M. Fajer, I. L. M., S. M. S., P. Andrew, L. M. J., N. B. J., and P. Salvador, "Magnetically driven silverâĂŘcoated nanocoils for efficient bacterial contact killing," *Advanced Functional Materials*, vol. 26, no. 7, pp. 1063–1069.

[281] L. Soler, V. Magdanz, V. M. Fomin, S. Sanchez, and O. G. Schmidt, "Self-propelled micromotors for cleaning polluted water," *ACS Nano*, vol. 7, pp. 9611–9620, Nov 2013.

[282] W. Gao, R. Dong, S. Thamphiwatana, J. Li, W. Gao, L. Zhang, and J. Wang, "Artificial micromotors in the mouse's stomach: a step toward in vivo use of synthetic motors," *ACS Nano*, vol. 9, pp. 117–123, Jan 2015.

[283] J. Li, S. Thamphiwatana, W. Liu, B. Esteban-Fernandez de Avila, P. Angsantikul, E. Sandraz, J. Wang, T. Xu, F. Soto, V. Ramez, X. Wang, W. Gao,

L. Zhang, and J. Wang, “Enteric Micromotor Can Selectively Position and Spontaneously Propel in the Gastrointestinal Tract,” *ACS Nano*, Sep 2016.

[284] J. Li, P. Angsantikul, W. Liu, B. Esteban-Fernandez de Avila, S. Thamphiwatana, M. Xu, E. Sandraz, X. Wang, J. Delezuk, W. Gao, L. Zhang, and J. Wang, “Micromotors Spontaneously Neutralize Gastric Acid for pH-Responsive Payload Release,” *Angew. Chem. Int. Ed. Engl.*, vol. 56, pp. 2156–2161, Feb 2017.

[285] D. Walker, B. T. Kasdorf, H. H. Jeong, O. Lieleg, and P. Fischer, “Enzymatically active biomimetic micropropellers for the penetration of mucin gels,” *Sci Adv*, vol. 1, p. e1500501, Dec 2015.

[286] N. R. Salama, M. L. Hartung, and A. Muller, “Life in the human stomach: persistence strategies of the bacterial pathogen Helicobacter pylori,” *Nat. Rev. Microbiol.*, vol. 11, pp. 385–399, Jun 2013.

[287] G. Sachs, D. L. Weeks, K. Melchers, and D. R. Scott, “The gastric biology of Helicobacter pylori,” *Annu. Rev. Physiol.*, vol. 65, pp. 349–369, 2003.

[288] G. Holtmann, C. Cain, and P. Malfertheiner, “Gastric Helicobacter pylori infection accelerates healing of reflux esophagitis during treatment with the proton pump inhibitor pantoprazole,” *Gastroenterology*, vol. 117, pp. 11–16, Jul 1999.

[289] L. Olbe, E. Carlsson, and P. Lindberg, “A proton-pump inhibitor expedition: the case histories of omeprazole and esomeprazole,” *Nat Rev Drug Discov*, vol. 2, pp. 132–139, Feb 2003.

[290] P. Richardson, C. J. Hawkey, and W. A. Stack, “Proton pump inhibitors. Pharmacology and rationale for use in gastrointestinal disorders,” *Drugs*, vol. 56, pp. 307–335, Sep 1998.

[291] P. Moayyedi and G. I. Leontiadis, “The risks of PPI therapy,” *Nat Rev Gastroenterol Hepatol*, vol. 9, pp. 132–139, Feb 2012.

[292] P. M. Ho, T. M. Maddox, L. Wang, S. D. Fihn, R. L. Jesse, E. D. Peterson, and J. S. Rumsfeld, “Risk of adverse outcomes associated with concomitant use of clopidogrel and proton pump inhibitors following acute coronary syndrome,” *JAMA*, vol. 301, pp. 937–944, Mar 2009.

[293] E. Sheen and G. Triadafilopoulos, “Adverse effects of long-term proton pump inhibitor therapy,” *Dig. Dis. Sci.*, vol. 56, pp. 931–950, Apr 2011.

[294] Y. X. Yang, J. D. Lewis, S. Epstein, and D. C. Metz, “Long-term proton pump inhibitor therapy and risk of hip fracture,” *JAMA*, vol. 296, pp. 2947–2953, Dec 2006.

[295] A. Martirosyan, M. J. Olesen, and K. A. Howard, “Chitosan-based nanoparticles for mucosal delivery of RNAi therapeutics,” *Adv. Genet.*, vol. 88, pp. 325–352, 2014.

[296] S. Thamphiwatana, W. Gao, M. Obonyo, and L. Zhang, “In vivo treatment of Helicobacter pylori infection with liposomal linolenic acid reduces colonization and ameliorates inflammation,” *Proc. Natl. Acad. Sci. U.S.A.*, vol. 111, pp. 17600–17605, Dec 2014.

[297] A. L. Lameris, M. W. Hess, I. van Kruijsbergen, J. G. Hoenderop, and R. J. Bindels, “Omeprazole enhances the colonic expression of the Mg(2+) transporter TRPM6,” *Pflugers Arch.*, vol. 465, pp. 1613–1620, Nov 2013.

[298] M. Correia, V. Michel, A. A. Matos, P. Carvalho, M. J. Oliveira, R. M. Ferreira, M. A. Dillies, M. Huerre, R. Seruca, C. Figueiredo, J. C. Machado, and E. Touati, “Docosahexaenoic acid inhibits Helicobacter pylori growth in vitro and mice gastric mucosa colonization,” *PLoS ONE*, vol. 7, no. 4, p. e35072, 2012.

[299] C. D. Tran, S. Kritas, M. A. Campbell, H. Q. Huynh, S. S. Lee, and R. N. Butler, “Novel combination therapy for the eradication of Helicobacter pylori infection in a mouse model,” *Scand. J. Gastroenterol.*, vol. 45, pp. 1424–1430, Dec 2010.

[300] Y. Ping, X. Hu, Q. Yao, Q. Hu, S. Amini, A. Miserez, and G. Tang, “Engineering bioinspired bacteria-adhesive clay nanoparticles with a membrane-disruptive property for the treatment of Helicobacter pylori infection,” *Nanoscale*, vol. 8, pp. 16486–16498, Sep 2016.

[301] Y. H. Lin, C. L. Feng, C. H. Lai, J. H. Lin, and H. Y. Chen, “Preparation of epigallocatechin gallate-loaded nanoparticles and characterization of their inhibitory effects on Helicobacter pylori growth in vitro and in vivo,” *Sci Technol Adv Mater*, vol. 15, p. 045006, Aug 2014.

[302] Y. H. Lin, S. C. Tsai, C. H. Lai, C. H. Lee, Z. S. He, and G. C. Tseng, "Genipin-cross-linked fucose-chitosan/heparin nanoparticles for the eradication of Helicobacter pylori," *Biomaterials*, vol. 34, pp. 4466–4479, Jun 2013.

[303] J. Li, V. V. Singh, S. Sattayasamitsathit, J. Orozco, K. Kaufmann, R. Dong, W. Gao, B. Jurado-Sanchez, Y. Fedorak, and J. Wang, "Water-driven micromotors for rapid photocatalytic degradation of biological and chemical warfare agents," *ACS Nano*, vol. 8, pp. 11118–11125, Nov 2014.

[304] M. Obonyo, D. G. Guiney, J. Harwood, J. Fierer, and S. P. Cole, "Role of gamma interferon in Helicobacter pylori induction of inflammatory mediators during murine infection," *Infect. Immun.*, vol. 70, pp. 3295–3299, Jun 2002.

[305] F. Mou, C. Chen, Q. Zhong, Y. Yin, H. Ma, and J. Guan, "Autonomous motion and temperature-controlled drug delivery of Mg/Pt-poly(N-isopropylacrylamide) Janus micromotors driven by simulated body fluid and blood plasma," *ACS Appl Mater Interfaces*, vol. 6, pp. 9897–9903, Jun 2014.

[306] K. K. Dey, X. Zhao, B. M. Tansi, W. J. Mendez-Ortiz, U. M. Cordova-Figueroa, R. Golestanian, and A. Sen, "Micromotors Powered by Enzyme Catalysis," *Nano Lett.*, vol. 15, pp. 8311–8315, Dec 2015.

[307] G. Subbiahdoss, S. Sharifi, D. W. Grijpma, S. Laurent, H. C. van der Mei, M. Mahmoudi, and H. J. Busscher, "Magnetic targeting of surface-modified superparamagnetic iron oxide nanoparticles yields antibacterial efficacy against biofilms of gentamicin-resistant staphylococci," *Acta Biomater*, vol. 8, pp. 2047–2055, Jul 2012.

[308] D. Davies, "Understanding biofilm resistance to antibacterial agents," *Nat Rev Drug Discov*, vol. 2, pp. 114–122, Feb 2003.

[309] H. C. Gugnani, "Some emerging food and water borne pathogens," *J Commun Dis*, vol. 31, pp. 65–72, Jun 1999.

[310] N. authors listed, "Surveillance for foodborne disease outbreaks–United States, 2009-2010," *MMWR Morb. Mortal. Wkly. Rep.*, vol. 62, pp. 41–47, Jan 2013.

[311] F. Chowdhury, M. A. Rahman, Y. A. Begum, A. I. Khan, A. S. Faruque, N. C. Saha, N. I. Baby, M. A. Malek, A. R. Kumar, A. M. Svennerholm, M. Pietroni, A. Cravioto, and F. Qadri, "Impact of rapid urbanization on the rates of infection by Vibrio cholerae O1 and enterotoxigenic Escherichia coli in Dhaka, Bangladesh," *PLoS Negl Trop Dis*, vol. 5, p. e999, Apr 2011.

[312] N. Hirschhorn, J. L. Kinzie, D. B. Sachar, R. S. Northrup, J. O. Taylor, S. Z. Ahmad, and R. A. Phillips, "Decrease in net stool output in cholera during intestinal perfusion with glucose-containing solutions," *N. Engl. J. Med.*, vol. 279, pp. 176–181, Jul 1968.

[313] J. D. Clemens, G. B. Nair, T. Ahmed, F. Qadri, and J. Holmgren, "Cholera," *Lancet*, vol. 390, pp. 1539–1549, Sep 2017.

[314] A. N. Atia and A. L. Buchman, "Oral rehydration solutions in non-cholera diarrhea: a review," *Am. J. Gastroenterol.*, vol. 104, pp. 2596–2604, Oct 2009.

[315] C. K. Wallace, P. N. Anderson, T. C. Brown, S. R. Khanra, G. W. Lewis, N. F. Pierce, S. N. Sanyal, G. V. Segre, and R. H. Waldman, "Optimal antibiotic therapy in cholera," *Bull. World Health Organ.*, vol. 39, no. 2, pp. 239–245, 1968.

[316] D. I. Andersson and D. Hughes, "Microbiological effects of sublethal levels of antibiotics," *Nat. Rev. Microbiol.*, vol. 12, pp. 465–478, Jul 2014.

[317] B. D. Spangler, "Structure and function of cholera toxin and the related Escherichia coli heat-labile enterotoxin," *Microbiol. Rev.*, vol. 56, pp. 622–647, Dec 1992.

[318] J. Holmgren, I. Lonnroth, J. Mansson, and L. Svennerholm, "Interaction of cholera toxin and membrane GM1 ganglioside of small intestine," *Proc. Natl. Acad. Sci. U.S.A.*, vol. 72, pp. 2520–2524, Jul 1975.

[319] B. Tsai and T. A. Rapoport, "Unfolded cholera toxin is transferred to the ER membrane and released from protein disulfide isomerase upon oxidation by Ero1," *J. Cell Biol.*, vol. 159, pp. 207–216, Oct 2002.

[320] C. J. O'Neal, M. G. Jobling, R. K. Holmes, and W. G. Hol, "Structural basis for the activation of cholera toxin by human ARF6-GTP," *Science*, vol. 309, pp. 1093–1096, Aug 2005.

[321] D. Cassel and Z. Selinger, "Mechanism of adenylate cyclase activation by cholera toxin: inhibition of GTP hydrolysis at the regulatory site," *Proc. Natl. Acad. Sci. U.S.A.*, vol. 74, pp. 3307–3311, Aug 1977.

[322] D. V. Kimberg, M. Field, E. Gershon, and A. Henderson, "Effects of prostaglandins and cholera enterotoxin on intestinal mucosal cyclic AMP accumulation. Evidence against an essential role for prostaglandins in the action of toxin," *J. Clin. Invest.*, vol. 53, pp. 941–949, Mar 1974.

[323] A. W. Paton, R. Morona, and J. C. Paton, “Bioengineered bugs expressing oligosaccharide receptor mimics: toxin-binding probiotics for treatment and prevention of enteric infections,” *Bioeng Bugs*, vol. 1, no. 3, pp. 172–177, 2010.

[324] O. C. Farokhzad and R. Langer, “Impact of nanotechnology on drug delivery,” *ACS Nano*, vol. 3, pp. 16–20, Jan 2009.

[325] R. A. Petros and J. M. DeSimone, “Strategies in the design of nanoparticles for therapeutic applications,” *Nat Rev Drug Discov*, vol. 9, pp. 615–627, Aug 2010.

[326] L. Zhang, J. M. Chan, F. X. Gu, J. W. Rhee, A. Z. Wang, A. F. Radovic-Moreno, F. Alexis, R. Langer, and O. C. Farokhzad, “Self-assembled lipid–polymer hybrid nanoparticles: a robust drug delivery platform,” *ACS Nano*, vol. 2, pp. 1696–1702, Aug 2008.

[327] R. H. Fang, B. T. Luk, C. M. Hu, and L. Zhang, “Engineered nanoparticles mimicking cell membranes for toxin neutralization,” *Adv. Drug Deliv. Rev.*, vol. 90, pp. 69–80, Aug 2015.

[328] C. M. Hu, R. H. Fang, J. Copp, B. T. Luk, and L. Zhang, “A biomimetic nanosponge that absorbs pore-forming toxins,” *Nat Nanotechnol*, vol. 8, pp. 336–340, May 2013.

[329] J. M. Chan, L. Zhang, K. P. Yuet, G. Liao, J. W. Rhee, R. Langer, and O. C. Farokhzad, “PLGA-lecithin-PEG core-shell nanoparticles for controlled drug delivery,” *Biomaterials*, vol. 30, pp. 1627–1634, Mar 2009.

[330] K. M. Lee, Y. Park, W. Bari, M. Y. Yoon, J. Go, S. C. Kim, H. I. Lee, and S. S. Yoon, “Activation of cholera toxin production by anaerobic respiration of trimethylamine N-oxide in Vibrio cholerae,” *J. Biol. Chem.*, vol. 287, pp. 39742–39752, Nov 2012.

[331] S. Sawasvirojwong, P. Srimanote, V. Chatsudthipong, and C. Muanprasat, “An Adult Mouse Model of Vibrio cholerae-induced Diarrhea for Studying Pathogenesis and Potential Therapy of Cholera,” *PLoS Negl Trop Dis*, vol. 7, p. e2293, Jun 2013.

[332] J. A. Copp, R. H. Fang, B. T. Luk, C. M. Hu, W. Gao, K. Zhang, and L. Zhang, “Clearance of pathological antibodies using biomimetic nanoparticles,” *Proc. Natl. Acad. Sci. U.S.A.*, vol. 111, pp. 13481–13486, Sep 2014.

[333] S. Bouillot, I. Attree, and P. Huber, "Pharmacological activation of Rap1 antagonizes the endothelial barrier disruption induced by exotoxins ExoS and ExoT of Pseudomonas aeruginosa," *Infect. Immun.*, vol. 83, pp. 1820–1829, May 2015.

[334] A. Cabrera, J. E. Lepage, K. M. Sullivan, and S. M. Seed, "Vaxchora: A Single-Dose Oral Cholera Vaccine," *Ann Pharmacother*, vol. 51, pp. 584–589, Jul 2017.

[335] A. Focareta, J. C. Paton, R. Morona, J. Cook, and A. W. Paton, "A recombinant probiotic for treatment and prevention of cholera," *Gastroenterology*, vol. 130, pp. 1688–1695, May 2006.

[336] E. Tuomola, R. Crittenden, M. Playne, E. Isolauri, and S. Salminen, "Quality assurance criteria for probiotic bacteria," *Am. J. Clin. Nutr.*, vol. 73, pp. 393S–398S, 02 2001.

[337] D. T. Riglar, T. W. Giessen, M. Baym, S. J. Kerns, M. J. Niederhuber, R. T. Bronson, J. W. Kotula, G. K. Gerber, J. C. Way, and P. A. Silver, "Engineered bacteria can function in the mammalian gut long-term as live diagnostics of inflammation," *Nat. Biotechnol.*, vol. 35, pp. 653–658, Jul 2017.

[338] P. H. Fishman, T. Pacuszka, and P. A. Orlandi, "Gangliosides as receptors for bacterial enterotoxins," *Adv. Lipid Res.*, vol. 25, pp. 165–187, 1993.

[339] D. Pandita, S. Kumar, and V. Lather, "Hybrid poly(lactic-co-glycolic acid) nanoparticles: design and delivery prospectives," *Drug Discov. Today*, vol. 20, pp. 95–104, Jan 2015.

[340] Y. Li, H. Wu, X. Yang, M. Jia, Y. Li, Y. Huang, J. Lin, S. Wu, and Z. Hou, "Mitomycin C-soybean phosphatidylcholine complex-loaded self-assembled PEG-lipid-PLA hybrid nanoparticles for targeted drug delivery and dual-controlled drug release," *Mol. Pharm.*, vol. 11, pp. 2915–2927, Aug 2014.

[341] B. Mandal, N. K. Mittal, P. Balabathula, L. A. Thoma, and G. C. Wood, "Development and in vitro evaluation of core-shell type lipid-polymer hybrid nanoparticles for the delivery of erlotinib in non-small cell lung cancer," *Eur J Pharm Sci*, vol. 81, pp. 162–171, Jan 2016.

[342] L. Guo, B. Chen, R. Liu, G. Xia, Y. Wang, X. Li, C. Wei, X. Wang, and H. Jiang, "Biocompatibility Assessment of Polyethylene Glycol-Poly L-Lysine-Poly Lactic-Co-Glycolic Acid Nanoparticles In Vitro and In Vivo," *J Nanosci Nanotechnol*, vol. 15, pp. 3710–3719, May 2015.

[343] H. K. Makadia and S. J. Siegel, "Poly Lactic-co-Glycolic Acid (PLGA) as Biodegradable Controlled Drug Delivery Carrier," *Polymers (Basel)*, vol. 3, pp. 1377–1397, Sep 2011.

[344] J. M. Lu, X. Wang, C. Marin-Muller, H. Wang, P. H. Lin, Q. Yao, and C. Chen, "Current advances in research and clinical applications of PLGA-based nanotechnology," *Expert Rev. Mol. Diagn.*, vol. 9, pp. 325–341, May 2009.

[345] K. Ohashi, T. Kabasawa, T. Ozeki, and H. Okada, "One-step preparation of rifampicin/poly(lactic-co-glycolic acid) nanoparticle-containing mannitol microspheres using a four-fluid nozzle spray drier for inhalation therapy of tuberculosis," *J Control Release*, vol. 135, pp. 19–24, Apr 2009.

[346] D. S. Jung, T. H. Hwang, S. B. Park, and J. W. Choi, "Spray drying method for large-scale and high-performance silicon negative electrodes in Li-ion batteries," *Nano Lett.*, vol. 13, pp. 2092–2097, May 2013.

[347] J. L. Perry, K. P. Herlihy, M. E. Napier, and J. M. Desimone, "PRINT: a novel platform toward shape and size specific nanoparticle theranostics," *Acc. Chem. Res.*, vol. 44, pp. 990–998, Oct 2011.

[348] B. Moulari, A. Beduneau, Y. Pellequer, and A. Lamprecht, "Lectin-decorated nanoparticles enhance binding to the inflamed tissue in experimental colitis," *J Control Release*, vol. 188, pp. 9–17, Aug 2014.

[349] A. Makhlof, M. Werle, Y. Tozuka, and H. Takeuchi, "A mucoadhesive nanoparticulate system for the simultaneous delivery of macromolecules and permeation enhancers to the intestinal mucosa," *J Control Release*, vol. 149, pp. 81–88, Jan 2011.

[350] K. Sonaje, Y. J. Chen, H. L. Chen, S. P. Wey, J. H. Juang, H. N. Nguyen, C. W. Hsu, K. J. Lin, and H. W. Sung, "Enteric-coated capsules filled with freeze-dried chitosan/poly(gamma-glutamic acid) nanoparticles for oral insulin delivery," *Biomaterials*, vol. 31, pp. 3384–3394, Apr 2010.

[351] Z. M. Wu, L. Zhou, X. D. Guo, W. Jiang, L. Ling, Y. Qian, K. Q. Luo, and L. J. Zhang, "HP55-coated capsule containing PLGA/RS nanoparticles for oral delivery of insulin," *Int J Pharm*, vol. 425, pp. 1–8, Apr 2012.

[352] M. J. Barea, M. J. Jenkins, Y. S. Lee, P. Johnson, and R. H. Bridson, "Encapsulation of Liposomes within pH Responsive Microspheres for Oral Colonic Drug Delivery," *Int J Biomater*, vol. 2012, p. 458712, 2012.

[353] J. Moss, J. C. Osborne, P. H. Fishman, S. Nakaya, and D. C. Robertson, "Escherichia coli heat-labile enterotoxin. Ganglioside specificity and ADP-ribosyltransferase activity," *J. Biol. Chem.*, vol. 256, pp. 12861–12865, Dec 1981.

[354] E. A. Merritt, T. K. Sixma, K. H. Kalk, B. A. van Zanten, and W. G. Hol, "Galactose-binding site in Escherichia coli heat-labile enterotoxin (LT) and cholera toxin (CT)," *Mol. Microbiol.*, vol. 13, pp. 745–753, Aug 1994.

[355] M. S. Lee, S. Koo, D. G. Jeong, and V. L. Tesh, "Shiga Toxins as Multi-Functional Proteins: Induction of Host Cellular Stress Responses, Role in Pathogenesis and Therapeutic Applications," *Toxins (Basel)*, vol. 8, Mar 2016.

[356] D. C. Angus and T. van der Poll, "Severe sepsis and septic shock," *N. Engl. J. Med.*, vol. 369, pp. 840–851, Aug 2013.

[357] J. Cohen, "The immunopathogenesis of sepsis," *Nature*, vol. 420, no. 6917, pp. 885–891, 2002.

[358] D. Rittirsch, M. A. Flierl, and P. A. Ward, "Harmful molecular mechanisms in sepsis," *Nat. Rev. Immunol.*, vol. 8, pp. 776–787, Oct 2008.

[359] V. M. Ranieri, B. T. Thompson, P. S. Barie, J. F. Dhainaut, I. S. Douglas, S. Finfer, B. Gardlund, J. C. Marshall, A. Rhodes, A. Artigas, D. Payen, J. Tenhunen, H. R. Al-Khalidi, V. Thompson, J. Janes, W. L. Macias, B. Vangerow, M. D. Williams, V. Ranieri, B. Thompson, P. S. Barie, J. F. Dhainaut, I. S. Douglas, S. Finfer, B. Gardlund, J. C. Marshall, A. Rhodes, J. Janes, W. L. Macias, B. Vangerow, M. D. Williams, A. S. Slutsky, G. Guyatt, D. Angus, T. Evans, R. Carroll, C. Weijer, R. Boots, D. Ernest, P. Harrigan, M. Chapman, R. Bellomo, S. Finfer, C. Wright, T. Crozier, A. Davies, C. French, N. Orford, A. Leditschke, M. Reade, C. MacIsaac, T. Dugernier, P. Jorens, M. Vander Laenen, M. Malbrain, W. Meersseman, W. Stockman, F. Damas, J. Raemaekers, A. M. Dive, P. Damas, P. Rogiers, P. F. Laterre, S. M. Lobo, J. O. Auler, C. M.

Carvalho, M. Caldeira, F. S. Dias, F. B. de Carvalho, F. Machado, P. Aslanian, J. G. Guimond, N. Ferguson, D. Zuege, D. Zuege, D. Chittock, V. Dhingra, D. Chittock, P. Rico, A. Kumar, B. Paunovic, R. Fowler, O. Lesur, W. Anderson, N. Sne, R. Light, V. Sramek, J. Neiser, J. Pachl, P. Sevcik, I. Burget, V. Cerny, R. Parizkova, E. Kasal, M. Balik, P. Dlouhy, J. Tenhunen, J. Kurola, I. Parviainen, R. Laru-Sompa, P. Loisa, A. Kuitunen, V. Pettila, M. Kaukonen, K. Saarinen, C. Santre, G. Hilbert, E. Azoulay, H. Mentec, B. Levy, D. Villers, G. Bernardin, D. Payen, J. L. Diehl, P. Montravers, J. Duranteau, Y. Cohen, Y. Malledant, A. LePape, F. Zeni, J. Y. Lefrant, J. P. Quenot, J. Durand-Gasselin, P. Guiot, M. Ferrandiere, Y. Le Tulzo, Q. Lu, S. Jaber, C. Gatecel, K. Asehnoune, B. de Jonghe, J. L. Ricome, P. Asfar, B. Francois, A. Desachy, E. Mercier, L. Martin-Lefevre, R. Robert, B. Allaouchiche, H. Gerlach, J. Motsch, U. Jaschinski, R. Kuhlen, S. Kubitza, S. Kluge, J. Barth, G. Marx, W. Hartl, N. Weiler, S. Jog, M. Gadkari, R. Gupta, V. K. Chopra, A. Varma, A. Oomman, R. Reddy, O. Singh, H. Thacker, M. K. Ramesh, G. Tulli, R. Fumagalli, G. Gagliardi, M. Ranieri, R. Urbino, G. Minoja, B. Panascia, G. Castiglione, D. Salaris, M. Antonelli, F. Della Corte, M. N. Poblano Morales, J. S. Aguirre Sanchez, F. D. Aguilera Almazan, J. G. Dominguez Cherit, S. Henderson, R. Ure, F. Van Haren, C. McArthur, T. Williams, R. Moreno, P. Povoa, J. A. Paiva, N. Catorze, J. Blanco, J. C. Ruiz-Rodriguez, F. Alvarez, J. Rello, A. Rodriguez, M. J. Lopez, C. Perez, A. Betbese, A. Artigas, J. Ibanez, S. Ruiz-Santana, J. I. Gomez, J. Rico, M. Sanchez, A. Esteban, G. Gonzalez, J. Cambronero, G. Sirgo, R. Claramonte, T. Guzman, M. Maggiorini, G. R. Kleger, R. Malacrida, H. van Leeuwen, A. van Zanten, P. Pickkers, J. Schouten, A. Mallick, T. Quasim, M. Zuleika, P. Sarkar, D. Pogson, P. MacNaughton, A. Rhodes, T. Whitehouse, M. Margarson, M. Jonas, J. Bewley, D. Arawwawala, S. McLellan, A. Davidson, R. S. Harris, J. Samuel, R. Birkhahn, D. Willms, B. Ardolic, B. Hahn, I. Douglas, R. Albert, J. Charchaflieh, S. Djurkovic, J. Barney, D. Striker, F. Koura, M. McNellis, S. Chang, G. Frendl, C. Morrison, M. Kelly, K. Dishman, A. Anzueto, D. Hagg, M. Barram, N. Ettinger, C. Fruci, G. Bayasi, A. Kumar, W. Abel, M. Tanios, R. Wunderink, R. Rains, B. Young, W. Bekemeyer, K. Krell, T. Lo, P. Wright, M. Wilson, R. Rains, and P. Wright, "Drotrecogin alfa (activated) in adults with septic shock," *N. Engl. J. Med.*, vol. 366, pp. 2055–2064, May 2012.

[360] D. F. Gaieski, J. M. Edwards, M. J. Kallan, and B. G. Carr, "Benchmarking the incidence and mortality of severe sepsis in the United States," *Crit. Care Med.*, vol. 41, pp. 1167–1174, May 2013.

[361] M. Yaroustovsky, M. Plyushch, D. Popov, N. Samsonova, M. Abramyan, Z. Popok, and N. Krotenko, “Prognostic value of endotoxin activity assay in patients with severe sepsis after cardiac surgery,” *J Inflamm (Lond)*, vol. 10, p. 8, Mar 2013.

[362] U. Grandel and F. Grimminger, “Endothelial responses to bacterial toxins in sepsis,” *Crit. Rev. Immunol.*, vol. 23, no. 4, pp. 267–299, 2003.

[363] K. Peters, R. E. Unger, J. Brunner, and C. J. Kirkpatrick, “Molecular basis of endothelial dysfunction in sepsis,” *Cardiovasc. Res.*, vol. 60, pp. 49–57, Oct 2003.

[364] Y. Wang, “Attenuation of berberine on lipopolysaccharide-induced inflammatory and apoptosis responses in Îš-cells via TLR4-independent JNK/NF-ÎžB pathway,” *Pharm Biol*, Nov 2013.

[365] K. Nishio, M. Horie, Y. Akazawa, M. Shichiri, H. Iwahashi, Y. Hagihara, Y. Yoshida, and E. Niki, “Attenuation of lipopolysaccharide (LPS)-induced cytotoxicity by tocopherols and tocotrienols,” *Redox Biol*, vol. 1, pp. 97–103, 2013.

[366] K. Brandenburg and A. Wiese, “Endotoxins: relationships between structure, function, and activity,” *Curr Top Med Chem*, vol. 4, no. 11, pp. 1127–1146, 2004.

[367] L. Gabrielli, A. Capitoli, D. Bini, F. Taraballi, C. Lupo, L. Russo, and L. Cipolla, “Recent approaches to novel antibacterials designed after LPS structure and biochemistry,” *Curr Drug Targets*, vol. 13, pp. 1458–1471, Oct 2012.

[368] T. Kelesidis and M. E. Falagas, “The safety of polymyxin antibiotics,” *Expert Opin Drug Saf*, vol. 14, no. 11, pp. 1687–1701, 2015.

[369] J. A. Justo and J. A. Bosso, “Adverse reactions associated with systemic polymyxin therapy,” *Pharmacotherapy*, vol. 35, pp. 28–33, Jan 2015.

[370] J. M. Cavaillon, “Polymyxin B for endotoxin removal in sepsis,” *Lancet Infect Dis*, vol. 11, pp. 426–427, Jun 2011.

[371] T. Fujii, R. Ganeko, Y. Kataoka, R. Featherstone, S. M. Bagshaw, and T. A. Furukawa, “Polymyxin B-immobilised haemoperfusion and mortality in critically ill patients with sepsis/septic shock: a protocol for a systematic review and meta-analysis,” *BMJ Open*, vol. 6, p. e012908, 11 2016.

[372] R. Raghavan, "When access to chronic dialysis is limited: one center's approach to emergent hemodialysis," *Semin Dial*, vol. 25, pp. 267–271, May 2012.

[373] L. Zhang and J. C. Leroux, "Current and forthcoming approaches for systemic detoxification," *Adv. Drug Deliv. Rev.*, vol. 90, pp. 1–2, Aug 2015.

[374] C. M. Hu, R. H. Fang, K. C. Wang, B. T. Luk, S. Thamphiwatana, D. Dehaini, P. Nguyen, P. Angsantikul, C. H. Wen, A. V. Kroll, C. Carpenter, M. Ramesh, V. Qu, S. H. Patel, J. Zhu, W. Shi, F. M. Hofman, T. C. Chen, W. Gao, K. Zhang, S. Chien, and L. Zhang, "Nanoparticle biointerfacing by platelet membrane cloaking," *Nature*, vol. 526, pp. 118–121, Oct 2015.

[375] C. M. Hu, R. H. Fang, J. Copp, B. T. Luk, and L. Zhang, "A biomimetic nanosponge that absorbs pore-forming toxins," *Nat Nanotechnol*, vol. 8, pp. 336–340, May 2013.

[376] T. Escajadillo, J. Olson, B. T. Luk, L. Zhang, and V. Nizet, "A Red Blood Cell Membrane-Camouflaged Nanoparticle Counteracts Streptolysin O-Mediated Virulence Phenotypes of Invasive Group A Streptococcus," *Front Pharmacol*, vol. 8, p. 477, 2017.

[377] J. A. Copp, R. H. Fang, B. T. Luk, C. M. Hu, W. Gao, K. Zhang, and L. Zhang, "Clearance of pathological antibodies using biomimetic nanoparticles," *Proc. Natl. Acad. Sci. U.S.A.*, vol. 111, pp. 13481–13486, Sep 2014.

[378] Z. Pang, C. M. Hu, R. H. Fang, B. T. Luk, W. Gao, F. Wang, E. Chuluun, P. Angsantikul, S. Thamphiwatana, W. Lu, X. Jiang, and L. Zhang, "Detoxification of Organophosphate Poisoning Using Nanoparticle Bioscavengers," *ACS Nano*, vol. 9, pp. 6450–6458, Jun 2015.

[379] S. Akira, K. Takeda, and T. Kaisho, "Toll-like receptors: critical proteins linking innate and acquired immunity," *Nat. Immunol.*, vol. 2, pp. 675–680, Aug 2001.

[380] R. Medzhitov, "Toll-like receptors and innate immunity," *Nat. Rev. Immunol.*, vol. 1, pp. 135–145, Nov 2001.

[381] C. Schutt, "Fighting infection: the role of lipopolysaccharide binding proteins CD14 and LBP," *Pathobiology*, vol. 67, no. 5-6, pp. 227–229, 1999.

[382] M. Triantafilou and K. Triantafilou, "Lipopolysaccharide recognition: CD14, TLRs and the LPS-activation cluster," *Trends Immunol.*, vol. 23, pp. 301–304, Jun 2002.

[383] I. Zanoni, R. Ostuni, L. R. Marek, S. Barresi, R. Barbalat, G. M. Barton, F. Granucci, and J. C. Kagan, "CD14 controls the LPS-induced endocytosis of Toll-like receptor 4," *Cell*, vol. 147, pp. 868–880, Nov 2011.

[384] J. D. Schilling, H. M. Machkovech, L. He, A. Diwan, and J. E. Schaffer, "TLR4 activation under lipotoxic conditions leads to synergistic macrophage cell death through a TRIF-dependent pathway," *J. Immunol.*, vol. 190, pp. 1285–1296, Feb 2013.

[385] J. A. Hagar, D. A. Powell, Y. Aachoui, R. K. Ernst, and E. A. Miao, "Cytoplasmic LPS activates caspase-11: implications in TLR4-independent endotoxic shock," *Science*, vol. 341, pp. 1250–1253, Sep 2013.

[386] F. Martinon, X. Chen, A. H. Lee, and L. H. Glimcher, "TLR activation of the transcription factor XBP1 regulates innate immune responses in macrophages," *Nat. Immunol.*, vol. 11, pp. 411–418, May 2010.

[387] S. Spence, M. K. Greene, F. Fay, E. Hams, S. P. Saunders, U. Hamid, M. Fitzgerald, J. Beck, B. K. Bains, P. Smyth, E. Themistou, D. M. Small, D. Schmid, C. M. O'Kane, D. C. Fitzgerald, S. M. Abdelghany, J. A. Johnston, P. G. Fallon, J. F. Burrows, D. F. McAuley, A. Kissenpfennig, and C. J. Scott, "Targeting Siglecs with a sialic acid-decorated nanoparticle abrogates inflammation," *Sci Transl Med*, vol. 7, p. 303ra140, Sep 2015.

[388] R. H. Fang, C. M. Hu, B. T. Luk, W. Gao, J. A. Copp, Y. Tai, D. E. O'Connor, and L. Zhang, "Cancer cell membrane-coated nanoparticles for anticancer vaccination and drug delivery," *Nano Lett.*, vol. 14, no. 4, pp. 2181–2188, 2014.

[389] S. E. Gratton, P. D. Pohlhaus, J. Lee, J. Guo, M. J. Cho, and J. M. Desimone, "Nanofabricated particles for engineered drug therapies: a preliminary biodistribution study of PRINT nanoparticles," *J Control Release*, vol. 121, pp. 10–18, Aug 2007.

[390] C. M. Hu, L. Zhang, S. Aryal, C. Cheung, R. H. Fang, and L. Zhang, "Erythrocyte membrane-camouflaged polymeric nanoparticles as a biomimetic delivery platform," *Proc. Natl. Acad. Sci. U.S.A.*, vol. 108, pp. 10980–10985, Jul 2011.

[391] R. E. Unger, K. Peters, A. Sartoris, C. Freese, and C. J. Kirkpatrick, "Human endothelial cell-based assay for endotoxin as sensitive as the conventional Limulus Amebocyte Lysate assay," *Biomaterials*, vol. 35, pp. 3180–3187, Mar 2014.

[392] T. Roger, C. Froidevaux, D. Le Roy, M. K. Reymond, A. L. Chanson, D. Mauri, K. Burns, B. M. Riederer, S. Akira, and T. Calandra, "Protection from lethal gram-negative bacterial sepsis by targeting Toll-like receptor 4," *Proc. Natl. Acad. Sci. U.S.A.*, vol. 106, pp. 2348–2352, Feb 2009.

[393] J. H. Kang, M. Super, C. W. Yung, R. M. Cooper, K. Domansky, A. R. Graveline, T. Mammoto, J. B. Berthet, H. Tobin, M. J. Cartwright, A. L. Watters, M. Rottman, A. Waterhouse, A. Mammoto, N. Gamini, M. J. Rodas, A. Kole, A. Jiang, T. M. Valentin, A. Diaz, K. Takahashi, and D. E. Ingber, "An extracorporeal blood-cleansing device for sepsis therapy," *Nat. Med.*, vol. 20, pp. 1211–1216, Oct 2014.

[394] R. H. Fang, C. M. Hu, K. N. Chen, B. T. Luk, C. W. Carpenter, W. Gao, S. Li, D. E. Zhang, W. Lu, and L. Zhang, "Lipid-insertion enables targeting functionalization of erythrocyte membrane-cloaked nanoparticles," *Nanoscale*, vol. 5, pp. 8884–8888, Oct 2013.

[395] D. Dehaini, X. Wei, R. H. Fang, S. Masson, P. Angsantikul, B. T. Luk, Y. Zhang, M. Ying, Y. Jiang, A. V. Kroll, W. Gao, and L. Zhang, "Erythrocyte-Platelet Hybrid Membrane Coating for Enhanced Nanoparticle Functionalization," *Adv. Mater. Weinheim*, vol. 29, Apr 2017.

[396] J. Wang, *Nanomachines: fundamentals and applications.* John Wiley & Sons, 2013.

[397] Y. Mei, A. A. Solovev, S. Sanchez, and O. G. Schmidt, "Rolled-up nanotech on polymers: from basic perception to self-propelled catalytic microengines," *Chemical Society Reviews*, vol. 40, no. 5, pp. 2109–2119, 2011.

[398] B. J. Nelson, I. K. Kaliakatsos, and J. J. Abbott, "Microrobots for minimally invasive medicine," *Annual review of biomedical engineering*, vol. 12, pp. 55–85, 2010.

[399] S. Sánchez, L. Soler, and J. Katuri, "Chemically powered micro-and nanomotors," *Angewandte Chemie International Edition*, vol. 54, no. 5, pp. 1414–1444, 2015.

[400] M. Guix, C. C. Mayorga-Martinez, and A. Merkoçi, "Nano/micromotors in (bio) chemical science applications," *Chemical reviews*, vol. 114, no. 12, pp. 6285–6322, 2014.

[401] K. Kim, J. Guo, X. Xu, and D. Fan, "Recent progress on man-made inorganic nanomachines," *Small*, vol. 11, no. 33, pp. 4037–4057, 2015.

[402] H. Wang and M. Pumera, “Fabrication of micro/nanoscale motors,” *Chemical reviews*, vol. 115, no. 16, pp. 8704–8735, 2015.

[403] W. Wang, W. Duan, S. Ahmed, T. E. Mallouk, and A. Sen, “Small power: Autonomous nano-and micromotors propelled by self-generated gradients,” *Nano Today*, vol. 8, no. 5, pp. 531–554, 2013.

[404] Z. Wu, X. Lin, T. Si, and Q. He, “Recent Progress on Bioinspired Self-Propelled Micro/Nanomotors via Controlled Molecular Self-Assembly,” *Small*, vol. 12, pp. 3080–3093, Jun 2016.

[405] L. K. Abdelmohsen, F. Peng, Y. Tu, and D. A. Wilson, “Micro-and nano-motors for biomedical applications,” *Journal of Materials Chemistry B*, vol. 2, no. 17, pp. 2395–2408, 2014.

[406] A. A. Solovev, Y. Mei, E. Bermúdez Ureña, G. Huang, and O. G. Schmidt, “Catalytic microtubular jet engines self-propelled by accumulated gas bubbles,” *Small*, vol. 5, no. 14, pp. 1688–1692, 2009.

[407] Z. Wu, X. Lin, Y. Wu, T. Si, J. Sun, and Q. He, “Near-infrared light-triggered "on/off" motion of polymer multilayer rockets,” *ACS Nano*, vol. 8, pp. 6097–6105, Jun 2014.

[408] G. Loget and A. Kuhn, “Electric field-induced chemical locomotion of conducting objects,” *Nature communications*, vol. 2, p. 535, 2011.

[409] W. F. Paxton, K. C. Kistler, C. C. Olmeda, A. Sen, S. K. St. Angelo, Y. Cao, T. E. Mallouk, P. E. Lammert, and V. H. Crespi, “Catalytic nanomotors: autonomous movement of striped nanorods,” *Journal of the American Chemical Society*, vol. 126, no. 41, pp. 13424–13431, 2004.

[410] D. Fan, Z. Yin, R. Cheong, F. Q. Zhu, R. C. Cammarata, C. Chien, and A. Levchenko, “Subcellular-resolution delivery of a cytokine through precisely manipulated nanowires,” *Nature nanotechnology*, vol. 5, no. 7, p. 545, 2010.

[411] S. Palagi, A. G. Mark, S. Y. Reigh, K. Melde, T. Qiu, H. Zeng, C. Parmeggiani, D. Martella, A. Sanchez-Castillo, N. Kapernaum, *et al.*, “Structured light enables biomimetic swimming and versatile locomotion of photoresponsive soft microrobots,” *Nature materials*, vol. 15, no. 6, p. 647, 2016.

[412] W. Wang, L. A. Castro, M. Hoyos, and T. E. Mallouk, "Autonomous motion of metallic microrods propelled by ultrasound," *ACS nano*, vol. 6, no. 7, pp. 6122–6132, 2012.

[413] J. Li, I. Rozen, and J. Wang, "Rocket science at the nanoscale," *ACS Nano*, vol. 10, no. 6, pp. 5619–5634, 2016.

[414] K. E. Peyer, L. Zhang, and B. J. Nelson, "Bio-inspired magnetic swimming microrobots for biomedical applications," *Nanoscale*, vol. 5, no. 4, pp. 1259–1272, 2013.

[415] O. Felfoul, M. Mohammadi, S. Taherkhani, D. De Lanauze, Y. Z. Xu, D. Loghin, S. Essa, S. Jancik, D. Houle, M. Lafleur, *et al.*, "Magneto-aerotactic bacteria deliver drug-containing nanoliposomes to tumour hypoxic regions," *Nature nanotechnology*, vol. 11, no. 11, p. 941, 2016.

[416] L. Soler and S. Sánchez, "Catalytic nanomotors for environmental monitoring and water remediation," *Nanoscale*, vol. 6, no. 13, pp. 7175–7182, 2014.

[417] V. V. Singh and J. Wang, "Nano/micromotors for security/defense applications. A review," *Nanoscale*, vol. 7, pp. 19377–19389, Dec 2015.

[418] J. Li, W. Gao, R. Dong, A. Pei, S. Sattayasamitsathit, and J. Wang, "Nanomotor lithography," *Nature Communications*, vol. 5, p. 5026, 2014.

[419] J. Li, W. Liu, T. Li, I. Rozen, J. Zhao, B. Bahari, B. Kante, and J. Wang, "Swimming Microrobot Optical Nanoscopy," *Nano Lett.*, vol. 16, pp. 6604–6609, Oct 2016.

[420] J. Li, B. E.-F. de Ávila, W. Gao, L. Zhang, and J. Wang, "Micro/nanorobots for biomedicine: Delivery, surgery, sensing, and detoxification," *Science Robotics*, vol. 2, no. 4, p. eaam6431, 2017.

[421] J. Wang, "Can man-made nanomachines compete with nature biomotors?," *ACS nano*, vol. 3, no. 1, pp. 4–9, 2009.

[422] M. Garcia, J. Orozco, M. Guix, W. Gao, S. Sattayasamitsathit, A. Escarpa, A. Merkoci, and J. Wang, "Micromotor-based lab-on-chip immunoassays," *Nanoscale*, vol. 5, pp. 1325–1331, Feb 2013.

[423] J. W. Yoo, D. J. Irvine, D. E. Discher, and S. Mitragotri, "Bio-inspired, bioengineered and biomimetic drug delivery carriers," *Nat Rev Drug Discov*, vol. 10, pp. 521–535, Jul 2011.

[424] C. M. Hu, R. H. Fang, J. Copp, B. T. Luk, and L. Zhang, "A biomimetic nanosponge that absorbs pore-forming toxins," *Nat Nanotechnol*, vol. 8, pp. 336–340, May 2013.

[425] M. Olsson, P. Bruhns, W. A. Frazier, J. V. Ravetch, and P. A. Oldenborg, "Platelet homeostasis is regulated by platelet expression of CD47 under normal conditions and in passive immune thrombocytopenia," *Blood*, vol. 105, pp. 3577–3582, May 2005.

[426] P. J. Sims, S. A. Rollins, and T. Wiedmer, "Regulatory control of complement on blood platelets. Modulation of platelet procoagulant responses by a membrane inhibitor of the C5b-9 complex," *J. Biol. Chem.*, vol. 264, pp. 19228–19235, Nov 1989.

[427] B. Nieswandt and S. P. Watson, "Platelet-collagen interaction: is GPVI the central receptor?," *Blood*, vol. 102, pp. 449–461, Jul 2003.

[428] N. Kieffer and D. R. Phillips, "Platelet membrane glycoproteins: functions in cellular interactions," *Annu. Rev. Cell Biol.*, vol. 6, pp. 329–357, 1990.

[429] M. R. Yeaman, "Platelets in defense against bacterial pathogens," *Cell. Mol. Life Sci.*, vol. 67, pp. 525–544, Feb 2010.

[430] J. R. Fitzgerald, T. J. Foster, and D. Cox, "The interaction of bacterial pathogens with platelets," *Nature Reviews Microbiology*, vol. 4, no. 6, p. 445, 2006.

[431] P. N. Walsh, "Platelet coagulant activities and hemostasis: a hypothesis," *Blood*, vol. 43, no. 4, pp. 597–605, 1974.

[432] C. M. Hu, R. H. Fang, K. C. Wang, B. T. Luk, S. Thamphiwatana, D. Dehaini, P. Nguyen, P. Angsantikul, C. H. Wen, A. V. Kroll, C. Carpenter, M. Ramesh, V. Qu, S. H. Patel, J. Zhu, W. Shi, F. M. Hofman, T. C. Chen, W. Gao, K. Zhang, S. Chien, and L. Zhang, "Nanoparticle biointerfacing by platelet membrane cloaking," *Nature*, vol. 526, pp. 118–121, Oct 2015.

[433] J. Li, T. Li, T. Xu, M. Kiristi, W. Liu, Z. Wu, and J. Wang, "Magneto-Acoustic Hybrid Nanomotor," *Nano Lett.*, vol. 15, pp. 4814–4821, Jul 2015.

[434] J. Li, S. Sattayasamitsathit, R. Dong, W. Gao, R. Tam, X. Feng, S. Ai, and J. Wang, "Template electrosynthesis of tailored-made helical nanoswimmers," *Nanoscale*, vol. 6, pp. 9415–9420, Aug 2014.

[435] W. Gao, C. M. Hu, R. H. Fang, B. T. Luk, J. Su, and L. Zhang, "Surface functionalization of gold nanoparticles with red blood cell membranes," *Adv. Mater. Weinheim*, vol. 25, pp. 3549–3553, Jul 2013.

[436] W. Gao, C. M. Hu, R. H. Fang, B. T. Luk, J. Su, and L. Zhang, "Surface functionalization of gold nanoparticles with red blood cell membranes," *Adv. Mater. Weinheim*, vol. 25, pp. 3549–3553, Jul 2013.

[437] P. I. Tarr, C. A. Gordon, and W. L. Chandler, "Shiga-toxin-producing Escherichia coli and haemolytic uraemic syndrome," *Lancet*, vol. 365, no. 9464, pp. 1073–1086, 2005.

[438] J. C. Paton and A. W. Paton, "Pathogenesis and diagnosis of Shiga toxin-producing Escherichia coli infections," *Clin. Microbiol. Rev.*, vol. 11, pp. 450–479, Jul 1998.

[439] L. L. Cooling, K. E. Walker, T. Gille, and T. A. Koerner, "Shiga toxin binds human platelets via globotriaosylceramide (Pk antigen) and a novel platelet glycosphingolipid," *Infect. Immun.*, vol. 66, pp. 4355–4366, Sep 1998.

[440] T. Sekino, N. Kiyokawa, T. Taguchi, H. Takenouchi, J. Matsui, W. R. Tang, T. Suzuki, H. Nakajima, M. Saito, K. Ohmi, Y. U. Katagiri, H. Okita, H. Nakao, T. Takeda, and J. Fujimoto, "Characterization of a shiga-toxin 1-resistant stock of vero cells," *Microbiol. Immunol.*, vol. 48, no. 5, pp. 377–387, 2004.

[441] L. O'Brien, S. W. Kerrigan, G. Kaw, M. Hogan, J. Penades, D. Litt, D. J. Fitzgerald, T. J. Foster, and D. Cox, "Multiple mechanisms for the activation of human platelet aggregation by Staphylococcus aureus: roles for the clumping factors ClfA and ClfB, the serine-aspartate repeat protein SdrE and protein A," *Mol. Microbiol.*, vol. 44, pp. 1033–1044, May 2002.

[442] S. W. Kerrigan, I. Douglas, A. Wray, J. Heath, M. F. Byrne, D. Fitzgerald, and D. Cox, "A role for glycoprotein Ib in Streptococcus sanguis-induced platelet aggregation," *Blood*, vol. 100, pp. 509–516, Jul 2002.

[443] I. R. Siboo, H. F. Chambers, and P. M. Sullam, "Role of SraP, a Serine-Rich Surface Protein of Staphylococcus aureus, in binding to human platelets," *Infect. Immun.*, vol. 73, pp. 2273–2280, Apr 2005.